Influence of Frenkel Excitons and Charge Transfer States on the Spectroscopic Properties of Organic Molecular Crystals

Linus Gisslén

Abstract

Organic semiconductors represent a large group of materials consisting of small molecules or longer polymer chains. In the condensed phase, these polyaromatic molecules are held together by relatively weak interactions between their electric quadropoles and by van der Waals forces. Perylene and its derivatives have attracted significant interest as active layers for light harvesting, photovoltaics, and photoinduced charge and energy transfer processes. This thesis focuses mainly on crystals of perylene-based molecules because these substances are among the best characterized organic materials. Perylene derivatives are robust organic dyes absorbing and emitting light in the visible range and in the near infrared. They display a strong tendency to self-assemble into molecular aggregates, liquid crystals, or even crystals. In order to increase their efficiency and stability, these materials have been studied quite intensively. In particular, their possible application in solar-cells needs insight into optical excitation and charge transport processes. The vision is that in the near future organic electronics will successfully compete with inorganic electronics for applications that require mechanical flexibility, high area coverage, and low cost mass production.

The performance of these materials as charge or energy transport materials does not arise exclusively from the electronic properties of the individual molecules, but it depends as well on favorable intermolecular interactions, such as π stacking. In fact it can be shown that many perylene derivatives display very similar optical spectra as dissolved monomers, whereas in their crystalline phase, the interactions between the π orbitals of adjacent molecules result in quite diversified optical properties. The interactions between these π orbitals depend strongly on the side wings attached to the perylene core since different side groups result in different stacking geometries. This difference in geometric overlap governs the level of interactions between neutral excitons and charge transfer states, so that it becomes the starting point for understanding the microscopic processes involved.

After a careful investigation of electronic excitations in a single molecule, this thesis develops theoretical tools allowing to quantify intermolecular interactions and their impact onto the optical properties of molecular crystals. As the deformation of a relaxed excited molecule defines the vibronic progressions observed in absorption and photoluminescence, the relation between electronic excitations, deformation patterns and the elongation of molecular vibrations are studied for a monomer. The deformation of positively or negatively charged molecular ions with respect to the neutral ground state is calculated with density functional theory (DFT), and the geometry in the optically excited state is de-

duced from constrained DFT and time-dependent DFT. These deformations are then projected onto the vibrational eigenvectors, allowing in turn to compare calculated absorption, photoluminescence, and resonant Raman spectra to experimental observations. For later use in an exciton model addressing molecular crystals, all of these deformations are reinterpreted in terms of the elongation of an effective internal vibration.

In the crystalline phase, neutral molecular excitations and charge transfer between adjacent molecules are coupled via electron and hole transfer, two quantities relating directly to the width of the conduction and valence band. Based on the crystal structure determined by X-ray diffraction, DFT and Hartree-Fock are used for the calculation of the electronic states of a dimer of stacked molecules. The resulting transfer parameters for electron and hole are inserted into the exciton model for the coupling between Frenkel excitons and charge transfer states.

A comparison between the calculated dielectric tensor and the observed optical spectra allows to deduce the relative energetic positions of Frenkel excitons and the charge-transfer state involving stack neighbors, a key parameter for various electronic and optoelectronic device application. Irrespective of the energetic ordering of these two types of excitations, the exciton model provides a new sum rule for the second moment of the optical response, giving a direct measure of the impact of electron and hole transfer onto the observed absorption spectra of molecular crystals.

For six out of seven perylene pigments studied, the exciton model results in excellent agreement between calculated and observed optical properties, and for the seventh compound, the agreement was still within acceptable range. Moreover, the model calculations described in this thesis have revealed that the published dielectric tensor of one of these molecular crystals (PTCDA) has resulted from an erroneous evaluation of ellipsometry data, but a refined analysis of these spectra gives experimental line shapes that can indeed be reproduced by the exciton model. Among the materials studied, PTCDA is the only compound where the charge transfer state along the stacking direction has an energy far below the neutral molecular excitation. Therefore, photoluminescence excitation spectroscopy with photon energy below the main absoption features allows the selective excitation of photoluminescence from charge transfer states. The dispersion branches arising from the exciton model corroborate previous interpretations of the radiative recombination mechanisms, and they allow to assign the respective excitation resonances to specific charge transfer states.

In conclusion, we have demonstrated a successful realization of a theoretical approach describing the fundamental interactions influencing on exciton transfer in crystalline perylene pigments. Furthermore, the microscopic parameter set obtained has allowed to calculate an optical response congruent with experimental spectra, quantifying several intrinsic variables of the molecular crystals for the first time.

Zusammenfassung

Organische Halbleiter sind eine sehr vielfältige Klasse von Materialien, die sich aus kleinen Molekülen und langen Polymerketten zusammensetzen können. Die aus polyaromatischen Molekülen aufgebauten Festkörper entstehen durch relativ schwache attraktive Kräfte zwischen den Molekülen, die auf ihren elektrischen Quadrupolmomenten und der van der Waals Wechselwirkung beruhen. Insbesondere Perylen und seine Derivate finden Anwendungen als aktive Materialien für Solarzellen, Lichtsensoren und lichtinduzierten Ladungs- und Energietransport. Die vorliegende Dissertation beschäftigt sich hauptsächlich mit kristallinen Perylen-Pigmenten, weil diese Substanzen zu den am besten charakterisierten organischen Materialien gehören.

Derivate von Perylen sind besonders stabile organische Farbstoffe, die im Sichtbaren und Nahinfrarot Licht emittieren und absorbieren. Sie tendieren dazu, Molekülaggregate, flüssigkristalline Phasen und sogar kristalline Festkörpern zu bilden. Diese Materialien wurden bereits intensiv untersucht, um ihren Wirkungsgrad und ihre Beständigkeit zu verbessern. In Bereichen, die hohe mechanische Flexibilität und niedrige Produktionskosten auf großen Flächen voraussetzen, werden organische Halbleiter in absehbarer Zukunft erfolgreich mit anorganischen Halbleitern konkurrieren. Allerdings erfordern insbesondere Anwendungen als Solarzellen ein tieferes theoretisches Verständnis der optischen Anregungen, der Bildung von Elektron-Loch-Paaren, sowie des Transports von Ladungsträgern.

Der Ladungs- und Energietransport in diesen Materialien hängt nicht nur von den elektronischen Eigenschaften einzelner Moleküle ab, sondern vielmehr auch von den Wechselwirkungen zwischen benachbarten Molekülen (z.B. π stacking). Tatsächlich kann man zeigen, dass viele Perylenderivate in Form gelöster Monomere sehr ähnliche optische Spektren zeigen. Im Gegensatz dazu bewirken die Wechselwirkungen zwischen den π Orbitalen benachbarter Moleküle deutlich verschiedene optischen Eigenschaften.

Die Wechselwirkungen zwischen diesen π Orbitalen hängen stark davon ab, welche Seitengruppen am Perylenmolekül angebunden sind, da verschiedene Seitengruppen verschiedene Kristallgeometrien nach sich ziehen. Deren unterschiedliche Geometrie verändert sowohl die Wechselwirkungen zwischen neutralen Exzitonen als auch die elektronischen Zustände, die am Ladungstransfer beteiligt sind. Daher ist die Kristallgeometrie der Ausgangspunkt, um sämtliche mikroskopischen Prozesse zu verstehen.

Die mechanische Verformung von elektronisch angeregten Molekülen bestimmt die vibronische Progression, die bei Lichtabsorptions- und Photolumineszenzexperimenten beobachtet wird. Daher untersuchen wir die Beziehung zwischen den elektronischen Anregungen, den Verformungen und den Vibrationen am Monomer. Wir berechnen die Ver-

formung der Molekülionen im Vergleich zum neutralen Grundzustand mittels der Dichtefunktionaltheorie (DFT). Außerdem schließen wir aus Ergebnissen der eingeschränkten DFT und der zeitabhängigen DFT auf die Molekülgeometrie im optisch angeregten Zustand. Indem wir Verformungen auf die Eigenvektoren der Vibrationen projizieren, können wir unsere berechneten Absorptions-, Photolumineszenz- und resonanten Ramanspektren mit experimentellen Daten vergleichen. Im Hinblick auf die spätere Anwendung in einem Exzitonenmodell für die kristalline Phase werden diese Auslenkungen verschiedener Vibrationsmoden zu einer effektiven internen Vibrationsmode zusammengefasst.

In Kristallen sind Anregungen neutraler Moleküle mit den Ladungstransferzuständen zwischen benachbarten Molekülen über den Elektronen- und Lochtransfer gekoppelt. Die dafür benötigten Transferparameter hängen direkt mit der Breite des Leitungs- und Valenzbandes zusammen. Ausgehend von Röntgenstrukturmessungen der Kristalle verwenden wir die DFT und Hartree-Fock Methode, um die elektronischen Zustände eines Dimers von gestapelten Molekülen zu berechnen. Wir setzen dann die sich daraus ergebenden Transferparameter der Elektronen und Löcher in unser Modell für die Kopplung zwischen Frenkelexzitonen und Ladungstransferzuständen ein.

Wir vergleichen unsere theoretischen Ergebnisse für den dielektrischen Tensor mit dem experimentell beobachteten optischen Spektrum und können damit die Energieunterschiede zwischen Frenkelexzitonen und ladungstrennenden Zuständen benachbarter Moleküle bestimmen. Dies ist ein Schlüsselergebnis für verschiedenste elektronische und optoelektronische Anwendungen. Aus dem Exzitonenmodell folgt eine bisher nicht bekannte Summenregel für das zweite Moment der optischen Absorption, die zwar nicht von der energetischen Lage neutraler molekularer Anregungen und Ladungstransferanregungen abhängt, aber ein eindeutiges Maß für den Einfluss von Elektron- und Lochtransfer auf die optischen Eigenschaften darstellt.

In sechs von sieben untersuchten Perylenfarbstoffen finden wir eine exzellente Übereinstimmung unserer Rechnungen mit gemessenen optischen Eigenschaften. Für die siebte Perylenverbindung ist die Übereinstimmung immerhin noch akzeptabel. Außerdem haben die Berechnungen in dieser Arbeit gezeigt, dass der bisher veröffentlichte dielektrische Tensor eines dieser Molekülkristalle (PTCDA) aus einer fehlerhaften Auswertung von Ellipsometriedaten herrührt. Eine genauere Auswertung der Spektren hat eine exzellente Übereinstimmung mit unseren Vorhersagen ergeben. Unter allen von uns untersuchten Materialien ist PTCDA die einzige Verbindung, in der der Ladungstransferzustand entlang der Stapelrichtung signifikant unterhalb der neutralen Molecülanregung liegt. Daher erlaubt die Photolumineszenzspektroskopie mit Photonenenergien unterhalb der niedrigsten starken Absorptionsbande die gezielte Anregung von ladungstrennenden Zuständen. Die Dispersionskurven, die sich aus unserem Exzitonenmodell ergeben, bekräftigen frühere Interpretationen der strahlenden Rekombinationsmechanismen und ermöglichen es uns, die jeweiligen Anregungsresonanzen bestimmten ladungstrennenden Zuständen zuzuweisen.

Wir haben in dieser Arbeit ein neues theoretisches Modell für die wesentlichen Wechselwirkungen zwischen Exzitonen in kristallinen Perylenfarbstoffen entwickelt. Mit Hilfe dieses Modells ist es uns gelungen, experimentelle Daten für die optischen Eigen-

schaften von etlichen Perlyenverbindungen zu reproduzieren. Die außerordentlich gute Übereinstimmung unseres Modells mit dem Experiment hat es uns erlaubt, einige wichtige Parameter zu quantifizieren, die bisher weder in Experimenten zugänglich sind noch vergleichbar genau berechnet werden können.

Contents

Chapter 1

Introduction

One of the most recent research topics in the field of optical devices is based on organic molecules, and it receives much attention both from the scientific community and from its commercial counterpart. Organic molecules show promising properties, such as excellent light fastness [1, 2, 3], emission bands in the visible range and efficient transport of charge between adjacent molecules [4]. Together with their flexibility and heat resistance, to name a few advantages over silicon based devices, they have the potential to replace traditional inorganic devices in many applications. Moreover, organic light-emitting diodes have a higher power efficiency than III-V semiconductors. One example for new applications are heads-up displays integrated in the windscreen, where both transparency and flexibility are required. The market for devices based on organic molecules is still under development and during the next few years it has a large potential for growth. Besides light-emitting devices, recent applications include photovoltaic cells [5, 6], field effect transistors [7], erasable optical disks [8], sensors [9] and xerographic photoreceptors [10].

In this thesis the main focus will be on a specific class of molecular crystals called perylene pigments. This refers to a class of high performance pigments made up of N, N'-disubstituted perylene-3,4,9,10-tetracarboxylic acid diimides or perylene-3,4,9,10-tetracarboxylic acid dianhydride. The perylene core is the base for different derivatives which are typically characterized by their different side groups attached to the core, compare Fig. 1.1. The choice of different side groups results in a large diversity of perylene compounds, and as a consequence, in quite different properties of their crystalline phases.

An interesting feature of perylene molecules is how their optical properties change when they form crystalline pigments. When the molecules are dissolved, the mean distances between them are large enough to consider each monomer to be isolated, so that its spectroscopic properties can be determined from the internal dynamics of a single molecule. Irrespective of the different side groups, the dissolved molecules have very similar absorption line shapes. This similarity arises from the fact that these molecules have the same backbone where the optical processes take place, and therefore the spectra are independent of the size and configuration of the side wings. In the crystal phase, the prox-
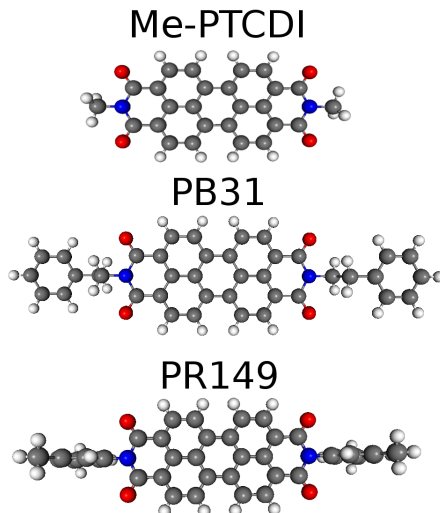
Figure 1.1: Three perylene pigments: Me-PTCDI (N,N-dimethyl-3,4,9,10-perylene-tetracarboxylic diimide), PB31 (N,N-bis(2-phenylethyl) - perylene-3,4,9,10-bis (dicarboximide)), PR149 (N,N-bis(3,5-xylyl)perylene-3,4,9,10-bis (dicarboximide)).

imity to other molecules results in interactions which include intermolecular transfer of excitations. The regular arrangement of adjacent molecules into stacks with intermolecular distances resembling graphite results in substantial interactions between the π-orbitals of stack neighbors. Since these are the orbitals mainly involved in charge transport and in the optical response, their intermolecular interactions induce significant changes in these properties. These features can be exemplified by the spectra of three perylene diimide molecules in Fig. 1.2. From this figure it is clear that the spectra for dissolved perylene compounds are very similar, but in their crystal phases, the optical properties differ substantially. Such a dependence of color on crystal packing is a phenomenon known as crystallochromy. However, even in their crystalline state some perylene materials have relatively little geometric overlap between neighboring molecules which gives spectra resembling dissolved molecules, *e.g.* for diindenoperylene (DIP) [11]. In most other cases, the interactions between adjacent molecules in the crystal phase result in strong modifications of the optical response [12, 13, 14, 15].

Early studies attempting to derive the color of perylene-based pigments from their crystal structure were performed using purely phenomenological parameterizations [16]. Hädicke and Graser studied more than twenty crystalline perylene pigments by X-ray diffraction. They concluded that the color of each pigment is related to both the area of overlap and the distance between adjacent perylene molecules in the crystal [2, 3]. However, at this stage, the perylenes were not understood so well that a complete correlation between structure and color could be established. To get a deeper understanding, theoretical models including the transfer of optical excitations have to be developed. Previous models have contributed significantly to the understanding of excitonic interactions by
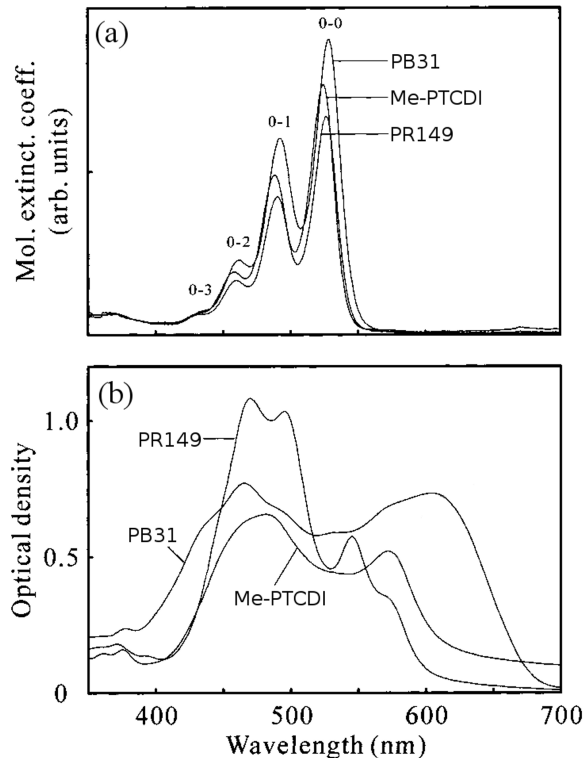
Figure 1.2: Optical spectra for three perylene diimide molecules, (a) in solution and (b) in their crystalline phase [14].

including small radius neutral excitons, also referred to as Frenkel excitons, and charge transfer (CT) states.

The purpose of this thesis is to describe the optical properties of molecular crystals by developing a microscopic model allowing to investigate the impact of the Frenkel excitons and charge transfer states on the optical properties. We investigate a set of perylene compounds, all having a perylene backbone but displaying very different optical properties in their crystalline state. Both for the single molecule and for the molecules in their crystalline phase, we derive several microscopic parameters from *ab initio* methods, and we test their quality on experimental results where this is possible. We find that the exciton model can reproduce the optical spectra of several different perylene molecules very accurately, confirming that Frenkel and CT type states mix substantially via electron transfer and hole transfer. The comparison between calculated and observed optical spectra allows to deduce the energetic difference between neutral molecular excitations and CT states within a precision of 0.05 eV. As this difference plays a key role for optoelectronic applications of molecular semiconductors, the analysis of optical spectra with a microscopically founded exciton model is of direct relevance for devices.

Furthermore, in order to obtain a more comprehensive picture of the optical properties

arising for polyaromatic molecules, we investigate the interplay between vibrational modes and optical response for further molecules with applications in semiconducting devices: pentacene, rubrene and TPD (N, N'-diphenyl-N, N'-bis(3-methylphenyl)-(1,1'-biphenyl)-4,4'-diamine). For TPD, the substantial Stokes shift can be deduced quantitatively from the calculations. This parameter is particular interesting since it governs the transparency to emitted photoluminescence, favoring applications as a lasing material.

This thesis is organized as follows. In Chap. 2 we will discuss the properties of an isolated molecule, such as vibrations and reorganization energies of excited states, Huang-Rhys factors, and resonant Raman spectra. In Chap. 3 the crystalline phase of molecular materials will be discussed, involving intermolecular interactions such as electron and hole transfer and the optical excitations in a pair of molecules in a stacking geometry compatible with the crystalline phase. Chap. 4 is devoted to the development of an exciton model accounting for neutral excitations and intermolecular charge transfer. In Chap. 5 this approach is applied to several perylene compounds, including a detailed comparison with observed spectra. The main achievements of this thesis are summarized in Chap. 6.

Chapter 2

Molecular properties and quantum chemical analysis

Since the attraction between the molecules in the crystalline phase arises mainly from relatively weak van der Waals forces, electronic interactions between adjacent sites remain rather small. Therefore, the excitations of the crystal can be interpreted as being located on a single molecule or a pair of molecules. This will simplify the calculations without a significant loss of accuracy. In this chapter, the single molecule will be examined, including bond geometries, orbitals, and vibrational modes, covering the key ingredients governing its optical properties. This including internal vibrations and their Huang-Rhys factors for neutral excitations, and for anionic and cationic states.

Besides the perylene compounds, this chapter addresses pentacene, TPD and rubrene, partially as a further test of our method of analysis, and partially because they are popular organic semiconductors with a wide range of applications.

In this thesis, most microscopic parameters are calculated with *ab initio* methods, and a detailed comparison with experimental measurements allows to test the validity of different computational schemes. In the next section we will present theoretical foundations of the quantum chemical methods used.

2.1   Quantum chemistry and computational methods

Even though experimental measurements and observations are crucial for the field of small organic molecules, there are shortcomings of this approach and there are mainly two reason for this. Firstly, the accuracy of experiments depends on the precision of the tools that are used. Although incredible progress has been achieved there will always be a limit to which resolution the instruments can detect. Secondly, even though an observation can be done, it is not certain that one understands the physics behind a particular event. To compensate these shortcomings researchers have developed analytical and numerical methods to understand the physical processes on a very fundamental level instruments cannot reach. *Quantum chemistry* (QC) is a unifying name for this theoretical approach using quantum mechanics and quantum field theory applied to molecular systems. QC

has been used for many decades, however, the big revolution came with the development of the computer and has vastly increased the possible size and complexity of systems that can be handled. In principle, QC can be an exceptionally precise method, but due to limitations of time and computational resources, much of the concern in QC is to find an approximation that can describe the physics as accurately as possible with as little computational effort as possible. In this thesis, QC calculations are used to approximate parameters that otherwise would remain unknown because there exists no measurements for some of the materials investigated. The following section will discuss the most common QC methods which will be used in the subsequent parts of this thesis to compute molecular properties.

2.1.1 Hartree-Fock and Slater determinants

The description of the electronic structures of molecules is complex and not yet fully understood. However, its appearance and properties can be described very precisely within the quantum mechanical theory by applying a set of simplifying approximations. If one restricts to smaller atoms, and thus can neglect relativistic effects, the task is to find approximate solutions of the non-relativistic Schrödinger equation

$$\hat{H}|\Psi\rangle = E|\Psi\rangle, \tag{2.1}$$

where $\hat{H}$ is the full Hamiltonian for a system of nuclei and electrons, and $|\Psi\rangle$ is the wave function describing the system.

The most basic approximation is the Born-Oppenheimer (BO) approximation [17] which uses the fact that the nuclei have a much larger mass than the electron, with a mass ratio exceeding 1000:1. Therefore, the nucleus will not relocate itself fast enough to affect the electronic part of the wavefunction noticeably. From this follows that the wave function of the electrons can be obtained for fixed nuclei, and the nuclei move on a potential energy surface determined from the solution of the electronic Schrödinger equation. In a first step, within this approximation, the kinetic energy of the nuclei can be neglected and the repulsion between them can be considered constant in $\hat{H}$ from eq. (2.1). The second step addresses the motion of the nuclei in the potential derived from the electron density, resulting in the vibrational properties. As a results, the BO approximation allows the total wavefunction $|\Psi\rangle$ to be separated into an electronic and a nuclear wave function. Not including the nuclear part, the formal way to write the time-independent Schrödinger equation is

$$\hat{H}_e|\Psi_e\rangle = E|\Psi_e\rangle. \tag{2.2}$$

where $|\Psi_e\rangle$ is the electronic wave function describing the motion of the electrons and $\hat{H}_e$ is the electronic Hamiltonian:

$$\hat{H}_e = -\sum_{i=1}^{n} \frac{\hbar^2 \nabla_i^2}{2m_i} - \sum_{i=1}^{n}\sum_{A=1}^{M} \frac{Z_A e^2}{4\pi\epsilon_0 r_{iA}} + \sum_{i=1}^{n}\sum_{j>i}^{n} \frac{e^2}{4\pi\epsilon_0 r_{ij}} \tag{2.3}$$

$$\Psi_e = \Psi_e(\{\mathbf{r}_i\}; \{\mathbf{R}_A\}) \tag{2.4}$$

where ∇_i^2 is the Laplacian operator, Z_A is the the atomic number of nucleus A and r_{ij} is the distance between electrons i and j. The wave function Ψ_e depends explicitly on the electron coordinates $\mathbf{r}_i$ but only parametrically[1] on the nuclear coordinates $\mathbf{R}_A$. The nuclear part of $\hat{H}$ in eq. (2.1) can be solved under the same assumption as used to formulate the electronic problem. A key feature here is to replace the electronic coordinates by their mean values, which is averaged over the electronic wave function, using the fact that the electrons move much faster than the nuclei. Therefore, the nuclei in the BO approximation moves on a potential surface obtained by solving the electronic problem.

To describe the full interactions among the electrons, it is necessary to define a wave function for a single particle, or orbital, which includes the spin feature. The spin orbitals consist of a spatial wave function $\psi(\mathbf{r})$ and an independent spin wave function which can be either spin up $\alpha(\sigma)$ or spin down $\beta(\sigma)$:

$$\psi_i(x) = \psi_i(\mathbf{r}, \sigma) = \begin{cases} \psi_i(\mathbf{r})\alpha(\sigma) \\ \psi_i(\mathbf{r})\beta(\sigma) \end{cases} \tag{2.5}$$

The electrons have a spin of $1/2$ and the total wave function must be antisymmetric, *i.e.* when two electrons change coordinates the sign of the wave function changes. This can be fulfilled by building the wave function of *Slater determinants* which are antisymmetrized product states composed of single particle wave functions ψ called spin orbitals:

$$\Phi_{SD} = \frac{1}{\sqrt{N!}} \begin{vmatrix} \psi_1(x_1) & \psi_2(x_1) & \dots & \psi_n(x_1) \\ \psi_1(x_2) & \psi_2(x_2) & \dots & \psi_n(x_2) \\ \vdots & \vdots & \ddots & \vdots \\ \psi_1(x_n) & \psi_2(x_n) & \dots & \psi_n(x_n) \end{vmatrix}. \tag{2.6}$$

The columns in the Slater determinant are single electron functions, or orbitals, and the rows represent the electron coordinates. When setting two columns equivalent, thus giving two electrons the same single particle orbitals, the determinant vanishes as required by the Pauli principle.

From a minimization of the energy of a single Slater determinant, one can derive a set of equations for single particle spin orbitals. This is commonly referred to as the Hartree-Fock approximation. Since these single electron orbitals are described as wave functions, their energy eigenvalues are explicitly related to the orbital they occupy. The HF approximation concerns only ground state wave functions, but it is a central concept in quantum chemistry, and it is a common ground for a number of more advanced methods.

It can be shown [18, 19] that the Hartree-Fock equation is an eigenvalue equation of the form

$$\hat{f}_i\psi(\mathbf{x}_i) = \epsilon_i\psi(\mathbf{x}_i) \tag{2.7}$$

---

[1]In this case parametrical dependence means that for different nuclear geometries $\mathbf{R}_A$, Ψ_e is a different function of the electronic coordinates $\mathbf{r}_i$.

where $\hat{f}_i$ is an effective one-electron operator, called the Fock operator

$$\hat{f}_i = -\frac{\hbar}{2m_i}\nabla_i^2 - \sum_{A=1}^{n}\frac{Z_A e^2}{4\pi\epsilon_0 r_{iA}} + v_i^{HF}, \tag{2.8}$$

which includes the kinetic energy, the Coloumb interaction of the electrons with the nuclei and where v_i^{HF} is the Hartree-Fock potential representing the average potential arising from the presence of the other electrons. As discussed before, in this expression resides the approximation to remove the many-electron interaction and to replace it by a one-electron problem. The potential part in the Fock operator depends on the average potential of all the electrons affecting an electron i so that the electron-electron repulsion is treated in an average way. Therefore, the Hartree-Fock potential of $\hat{f}_i$ depends on the spin orbitals of the other electrons. In other words the Fock operator relies on the knowledge of the single particle orbitals of all other electrons. This requires eq. (2.7) to be solved iteratively, a process which can be very time consuming. This procedure is commonly referred to as the self-consistent-field (SCF) method, for a more in depth discussion consult *e.g.* chapter 2 in Ref. [18].

2.1.2 Density Functional Theory

The foundation of *Density Functional Theory* (DFT) relies on the fact that the total energy of a many electron system can be expressed as a function of the electron density alone [20]. This was first shown by Hohenberg and Kohn (HK) [21] using the Born-Oppenheimer approximation and the variational principle. The base for the use of DFT methods in computational chemistry are the Kohn-Sham (KS) orbitals [22]. The basic idea of the KS formalism is to split the kinetic functional into two parts, one that can be calculated exactly and one small correction term. Since the exact density matrix is unknown in the KS-theory, the HF approximation is applied, so that the calculation of the kinetic energy can be performed under the assumption of non-interacting electrons. Due to the small difference between the exact kinetic energy and the kinetic energy of non-interacting-electrons, this approximation is still relatively accurate. The general DFT energy expression can be written as

$$E_{DFT}[\rho] = T_S[\rho] + E_{ne}[\rho] + J[\rho] + E_{ex}[\rho] \tag{2.9}$$

where $T_S[\rho]$ is the kinetic energy calculated as a functional of the electron density, $E_{ne}[\rho]$ is the attraction between electrons and nuclei, $J[\rho]$ is the functional describing the Coulomb repulsion between electrons, and $E_{ex}[\rho]$ contains exchange and correlation.

A large advantage over pure Hartree-Fock (HF) methods is that it is not necessary to solve the wave function, where for HF the cpu time required scales as N^4 with the number of electrons N. Instead, all relevant information can be obtained from the electron density of the system. Since independently of the number of electrons, the electron density depends only on three coordinates, the cpu time requirements are considerable reduced.

However, a potential drawback is that the electron correlation, above the mean field approximation, is unknown and/or impossible to estimate, so that the error of the exchange-correlation functional has to be measured and controlled for each class of molecules. On our class of molecules these tests have been performed by several groups *e.g.* [23, 24, 25], so we consider typical exchange-correlation functionals to be quite reliable.

The functional mainly used in this report is the B3LYP (Becke, three-parameter, Lee-Yang-Parr), which is a hybrid functional [26]. A hybrid exchange-correlation functional is usually constructed as a linear combination of the Hartree-Fock exact exchange functional (E_{ex}^{HF}) and additional exchange correlation density functionals. Specifically, in B3LYP the exchange-correlation functional is described as

$$E_{ex-corr}^{B3LYP} = E_{ex-corr}^{LDA} + a_{ex}^{HF}(E_{ex}^{HF} - E_{ex}^{LDA}) + a_{ex}^{B88}(E_{ex}^{GGA} - E_{ex}^{LDA}) + a_{corr}(E_{corr}^{GGA} - E_{corr}^{LDA}) \tag{2.10}$$

where E_{ex}^{HF}, E_{ex}^{LDA} and E_{ex}^{GGA} are the HF, *Local density approximation* (LDA), and *Generalized gradient approximation* (GGA) exchange [26], respectively, and E_{corr}^{GGA} and E_{corr}^{LDA} are GGA and LDA correlation. The LDA correlation energy E_{corr}^{LDA} can be determined by Monte Carlo methods for different densities. After test calculations the empirical parameters have been set to $a_{ex}^{HF} = 0.2$, $a_{ex}^{B88} = 0.72$ and $a_{corr} = 0.81$ [27].

The LDA functionals rely on the homogeneous electron gas, requiring that the electron density variation is relatively slow. The exchange correlation energy $E_{ex-corr}^{LDA}$ can be calculated integrating over the electron density ρ and the exchange-correlation energy density $\epsilon_{ex-corr}$

$$E_{ex-corr}^{LDA} = \int \rho(\mathbf{r})\epsilon_{ex-corr}(\rho)d\mathbf{r}. \tag{2.11}$$

The exchange energy for a uniform electron gas is given by the Dirac formula

$$E_{ex}^{LDA} = -\frac{3}{4}(\frac{3}{\pi})^{1/3} \int \rho^{4/3}(\mathbf{r})d\mathbf{r}. \tag{2.12}$$

For the analytic interpolation formula for LDA, B3LYP uses the Vosko-Wilk-Nusair [28] correlation, see chapter 6.1 in [19] for a more in depth discussion about this functional. The GGA is included to consider a non-uniform electron gas where the exchange and correlation is calculated from the derivatives of the electron density. The reason for including it is that it compensates for the tendency of LDA to overestimate the total binding energy, or so-called overbinding.

We have chosen to use DFT with the B3LYP functional for our ground state calculations since this functional is very accurate and allows to describe the wave functions [29] which gives excellent agreement with observed molecular geometries and measured frequencies of vibrational modes [26, 33, 34] with relatively low computational effort. B3LYP has proven to be very reliable when calculating the ground state properties of, for example, naphthalene, anthracene, perylene, and terrylene [30, 31, 32] which are closely related to our materials. The calculations were performed with the TURBOMOLE 5.9 program package developed by Ahlrichs *et al.* [35, 36, 27].

2.1.3 Excited state calculations

For the excited states calculations two methods were applied, the *time-dependent* DFT (TD-DFT) [37, 38, 39] method and a constrained DFT method. As the name implies TD-DFT extends the concept of DFT to time-dependent situations arising for electronic excitations. This method relies on the statement that any interacting quantum system subject to an arbitrary time-dependent potential can be described by the time-dependent Schrödinger equation. It can be determined completely by knowledge of the time-dependent density of the system at a given time [20]. Thus all the physical variables are dependent on the density, and this relation makes it possible to derive information on the particle-to-particle interaction by looking at a density-dependent single-particle potential. This allows to study the time evolution of an interacting system by solving a time-dependent auxiliary single-particle problem

$$i\hbar\frac{\partial\Psi(\mathbf{x},t)}{\partial t} = \hat{H}(t)\Psi(\mathbf{x},t). \tag{2.13}$$

The other method used to describe the lowest excited state is a constrained DFT (*c*-DFT) approach which allows to pick specific electronic configurations to be excited by setting $n_{occupied} = n_{virtual} = 1$. This approach of applying DFT is covered by the Hohenberg-Kohn theorem [21]. In the molecules we are studying the lowest optical transition is dominated by the HOMO to LUMO excitation so that the *c*-DFT method can provide a good approximation of this transition. A schematic visualization of the electronic configurations investigated with the three different variations of DFT can be found in Fig. 2.1.

2.1.4 Basis sets

A variational basis set is a set of functions used to describe, for example, the molecular orbitals (MO). The MO are expanded as linear combination of basis functions, usually atomic orbitals, for example *Slater Type Orbitals* (STOs) or *Gaussian Type Orbitals* (GTOs). In the ideal case, which describes the orbital exactly, the set of functions is complete, which means it contains an infinite number of functions. This is of course impossible to manage, so the selection of a basis set should fit both the accuracy expectations and available resources in terms of computational power and cpu time.

The two types of basis functions have different advantages. The STO has an exponential dependence on the distance, $e^{-\xi r}$, while the GTO has a $e^{-\xi r^2}$ dependence which makes the GTOs inferior to the STOs in two ways. At the nucleus, the GTO has a zero slope, while the STO has a discontinuous derivative, or a "cusp", so GTOs have problems representing the behavior near the nucleus. The other drawback with a GTO is that is falls off too rapidly far from the nucleus, and the tail of the wave function is represented poorly. In order to compensate for these shortcomings, several GTOs are superimposed, up to three per STOs. Nevertheless, since the GTOs require much less computational power they are actually preferred over STOs in our type of configurations.
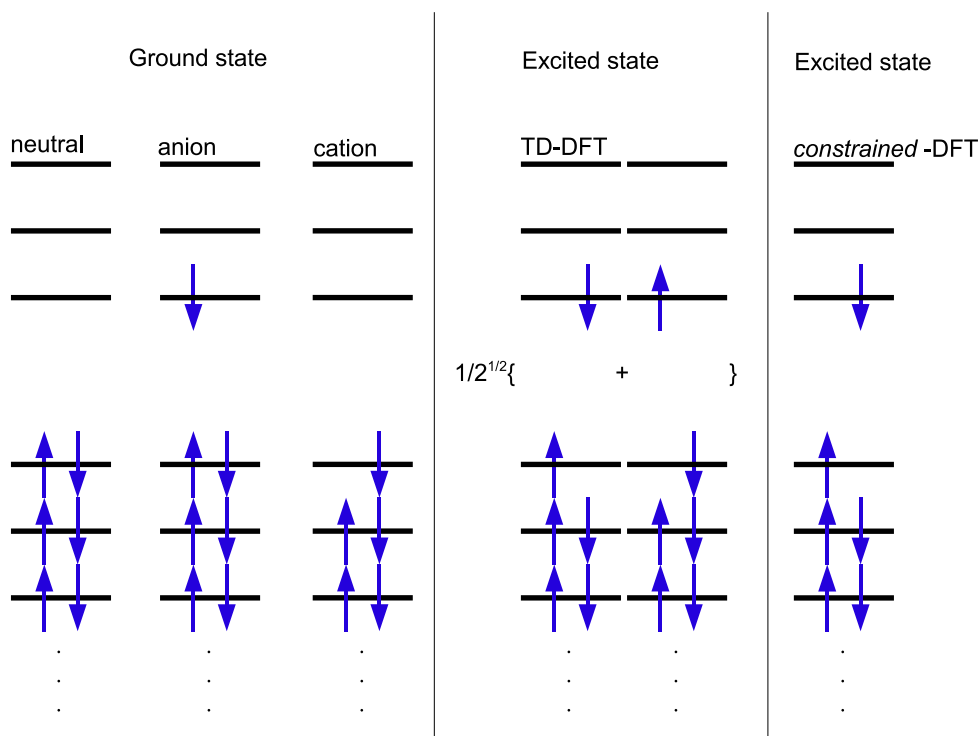
Figure 2.1: Left: visualization of electronic configurations treated with DFT, middle:
lowest excited singlet, as obtained with TD-DFT, right: lowest excited electronic configu-
ration obtained with the constrained DFT approach. The arrows represent electrons with
either spin up or spin down and the horizontal lines the electronic orbitals, both occupied
and unoccupied.

The simplest possible level of basis set corresponds to the lowest number of functions
required to describe all occupied atomic orbitals. This minimal basis set is named STO-nG
(where each Slater orbital required is expressed by a superposition of n Gaussians) for the
program package GAUSSIAN where the n in STO-nG represents the number of primitive
Gaussian functions representing an atomic orbital. The minimal basis set is too small
to be particularly useful for quantitative use, however, the chemical bonds are described
correctly, so that it becomes a suitable starting point for increasing the size of the basis
set. For TURBOMOLE, the SV contractions are obtained from an atom-optimized single-ζ
(SZ) basis set by decontracting valence atomic orbitals. SV contains two uncontracted
Gaussian-type orbitals (GTOs) in the valence shell, and the orbitals in the inner shells
are described by a single basis function.

In TURBOMOLE, the more accurate basis functions are called Double-ζ (DZ) [40],
Triple-ζ (TZ) and Quadruple-ζ (QZ) [41]. They represent the order of increase in functions
compared to the lowest basis set, so DZ contains approximately the double amount of
basis functions compared to the SZ basis function, and similar reasoning applies to the
others. As an illustration, for the carbon atom the basis set for SV in general notation

is (10s,5p)/[4s,1p], for DZ it is (11s,5p)/[6s,2p] and for TZ it is (12s,6p)/[7s,2p] where "(...)" stands for GTOs and "[...]" contracted-GTOs (CGTOs) [40].

There is also an option to add valence polarization (VP) functions which include the polarization for the valence electrons of the atoms. The polarization can arise from non-symmetric interactions between the valence electrons. A basis set with double-ζ functions including valence polarization functions will then be abbreviated DZVP.

2.2 Theory of spectroscopic observables

The optical properties of a molecule depend directly on its internal vibrations and their elongations in the relaxed excited geometry. The Stokes shift, which determines the difference between absorption and emission, and the absorption and PL spectrum itself are related to internal vibrational modes. In order to study the optical properties of an isolated molecule an effective method is to dissolve the molecules in a fluid at sufficiently low concentration, so that intermolecular interaction between molecules of the same kind are replaced by random solute-solvent interactions. By doing this it is possible to get optical spectra which will resemble very accurately the one of a single molecule [12, 15]. In an absorption spectrum, the relative height of the peaks is proportional to the probability of transfer between the ground state and a specific vibronic level in the excited state. This section will summarize the theoretical foundations on which our calculated parameters are based on.

2.2.1 Displaced harmonic oscillator

To describe the theory behind the optical spectra in terms of transition energies and intensities, we use the harmonic approximation. The system in its electronic ground state can be described by the Hamiltonian for a harmonic oscillator

$$H_g = \frac{p^2}{2m} + \frac{m\omega^2}{2}x^2 = (a_g^\dagger a_g + \frac{1}{2})\hbar\omega \qquad (2.14)$$

where $a_g^\dagger$ (a_g) is the creation (annihilation) operator of a vibration in the electronic ground state

$$a_g^\dagger = \frac{1}{\sqrt{2}}\Big(\sqrt{\frac{m\omega}{\hbar}}x + \sqrt{\frac{\hbar}{m\omega}}\frac{\partial}{\partial x}\Big) \qquad (2.15)$$

$$a_g = \frac{1}{\sqrt{2}}\Big(\sqrt{\frac{m\omega}{\hbar}}x - \sqrt{\frac{\hbar}{m\omega}}\frac{\partial}{\partial x}\Big). \qquad (2.16)$$

For vibrational modes with $\hbar\omega >> k_B T$, only the lowest vibrational level $|0_g\rangle$ in the electronic ground state is occupied. In this report we will only include the lowest excited electronic configuration, but vibrational levels are unrestricted. For a large molecule with several internal vibrations, the deformation pattern in the relaxed excited geometry

projected onto the complete set of vibrational eigenvectors defines a coordinate shift q_0 for each mode and a vibronic coupling constant g

$$g = \sqrt{\frac{m\omega}{2\hbar}}q_0. \tag{2.17}$$

The reorganization energy can be written as a function of the vibrational coupling constant

$$\lambda = g^2\hbar\omega = S\hbar\omega, \tag{2.18}$$

where S is known as the Huang-Rhys factor. The creation and annihilation operators in the displaced harmonic potential associated to an excited state are related to the respective operators in the electronic ground state and the vibronic coupling constant:

$$a_e^\dagger = a_g^\dagger - g \tag{2.19}$$

$$a_e = a_g - g \tag{2.20}$$

According to Glauber [42], these relations allow to express the lowest vibrational level in the electronic ground state by a superposition of the vibrational levels in the excited state:

$$|0_g\rangle = e^{-g^2/2}e^{-ga_e^\dagger}|0_e\rangle = e^{-g^2/2}\sum_\nu^\infty \frac{(-g)^\nu}{\nu!}\sqrt{\nu!}|\nu_e\rangle. \tag{2.21}$$

As a result, all Franck-Condon factors $\langle \nu_e \mid 0_g \rangle$ can be read off as $\langle \nu_e|0_g\rangle = e^{-g^2/2}\frac{(-g)^\nu}{\sqrt{\nu!}}$, so that the relative intensities in the vibronic progression are given by a Poisson progression.

The overlap between a displaced oscillator function with quantum number ν and the quantum number μ in the ground state potential was first discussed by Franck [43] and later by Condon, hence named the Franck-Condon overlap factor. The Franck-Condon factor describes the overlap between two vibronic functions, one in the electronic excited state $|\chi^{e\nu}\rangle$ and one in the electronic ground state $|\chi^{g\mu}\rangle$. The relative contribution of different vibronic sublevels to the optical excitation of the monomer is given by the square of the Franck-Condon overlap factors, which can be obtained (see Appendix A for details) using the operators stated

$$S_{\mu\nu} = \langle \chi^{g\mu} \mid \chi^{e\nu}\rangle = \langle \frac{1}{\sqrt{\mu!}}(a_g^\dagger)^\mu \chi^{g0} \mid \frac{1}{\sqrt{\nu!}}(a_g^\dagger - g)^\nu e^{-g^2/2}e^{g(a_g^\dagger)}\chi^{g0}\rangle =$$

$$= \frac{e^{-g^2/2}}{\sqrt{\nu!\mu!}}\sum_{i=0}^{min(\nu,\mu)} \frac{(-1)^{\nu-i}g^{\mu+\nu-2i}\mu!\nu!}{i!(\mu-i)!(\nu-i)!}. \tag{2.22}$$

When the transitions start from the lowest vibrational level $|\chi^{0_g}\rangle$ in the electronic ground state to an arbitrary vibronic level $|\chi^{\nu_e}\rangle$ in the electronic excited state, the squared overlap can be expressed as

$$S_{0_g\nu_e}^2 = |\langle \chi^{\nu_e}|\chi^{0_g}\rangle|^2 = e^{-S}\frac{S^{\nu_e}}{\nu_e!} = P_{\nu_e}(S) \tag{2.23}$$

where P_{ν_e} is a Poisson progression with argument $S = g^2$. These equations show that the size of the Huang-Rhys factor defines the overlap between $|\chi^{0_g}\rangle$ and vibronic levels $|\chi^{\nu_e}\rangle$, hence the larger the overlap the larger the probability of a transition to that state. If the factor S is less than 1.0, the zero-to-zero vibronic transition is most probable and the probability decreases for each transition higher level. Therefore, for $S < 1$, we can restrict our model to include only a small number of vibronic levels without receiving measurable deviations from completeness. *E.g.* when the highest mode included is $\nu_e = 8$, for $S = 1$ the smallest probability included is $S^2_{0_g\nu_e} = |\langle\chi^{\nu_e}|\chi^{0_g}\rangle|^2 < 10^{-5}$, according to eq. (2.23).

2.2.2 Solution spectra

A simple picture for the vibrational levels and their relation to the optical spectra can be sketched as in Fig. 2.2. The thermal motion of the solvent molecules modulate the electronic transition energy, giving rise to a broadening of the peaks. The width of the peaks is described by Gaussian functions, so the contribution of each sublevel to the dielectric function of a dilute solution is modelled with a normalized Gaussian. By using this scheme the energy spacing $\hbar\omega$ and the Huang-Rhys factor S can be extracted from measurements by fitting the observed spectra to a Poisson progression with variable Gaussian broadening [11]

$$\Im(\epsilon) = \epsilon_2 = y_0 + A_0 \sum_{\nu=0}^{\nu_{max}} \frac{S^\nu}{\nu!\sigma_\nu\sqrt{\pi}} e^{-(\frac{E-E_\nu}{\sigma_\nu})^2}, \tag{2.24}$$

where y_0 is an offset, A_0 is the amplitude, E_ν the energy and σ_ν the width of the νth Gaussian corresponding to a broadened $0 - \nu$ transition.

The absorption is directly related to the dielectric function of the material and at sufficiently low concentration the influence of the solute on the refractive index of the solution can be neglected, so that the observed absorption coefficient can then be written as

$$\alpha(E) = \frac{E}{\hbar c}\frac{\Im(\epsilon)}{n_{solvent}}. \tag{2.25}$$

2.2.3 Raman spectroscopy of organic molecules

In order to verify our *ab initio* calculations we will compare the results to Raman data. Therefore, in the following, the relation between Franck-Condon factors and Raman spectra will be described.

The Raman theory applies the specific attributes of a molecule, including bond lengths, bond types and atomic mass in order to extract information on the scattering cross section of specific vibrations. A laser exciting a molecule will mostly render elastically scattered photons, so called Rayleigh scattering. However, a small fraction of the photons, about 1 in 10^7, will give a molecule-specific inelastic scattering pattern. This process is named Raman scattering effect after its discoverer [44]. The energy difference between the incident photon and the scattered photon corresponds to the energy of the molecular vibration
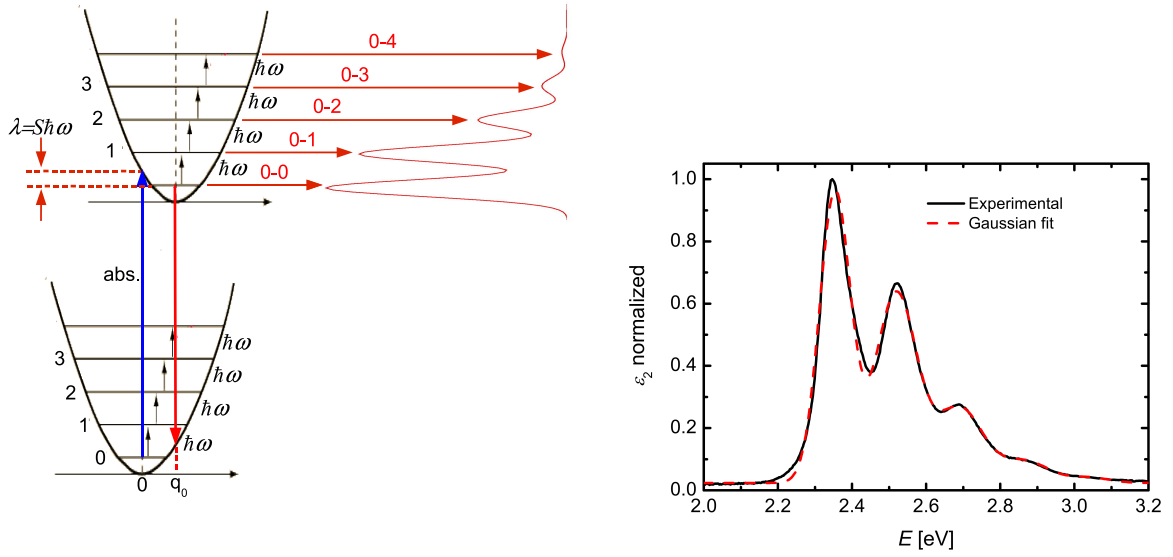
Figure 2.2: Relation between vibronic levels and optical spectra. The left picture is a visualization of the excitations of a single molecule and how they correspond to the optical spectra shown besides. The right picture is modelled with Gaussians superimposed to an experimental spectrum of DIP using a Huang-Rhys factor of $S = 0.87$ and an effective mode of $\hbar\omega_{\text{eff}} = 0.17$ eV [11], with variable Gaussian broadening.

that has scattered the photon. Thus the Raman spectrum is a plot of relative intensity as a function of energy difference. The scattering process can be divided into two steps, the first is an excitation when the molecule is excited from the initial state $|i\rangle$ to a virtual state $|m\rangle$, the second step is the recombination to the final state $|f\rangle$. $|m\rangle$ represents any state that has a transition dipole coupling it to $|i\rangle$ and $|f\rangle$. In the following, we will restrict the discussion to the excitation of a single internal vibration k after the scattering process. The three states are defined as

$$|i\rangle = |g\rangle \prod_j |0_j^g\rangle \tag{2.26}$$

$$|m\rangle = |e\rangle |m_k^e\rangle \prod_{j \neq k} |m_j^e\rangle \tag{2.27}$$

$$|f\rangle = |g\rangle |1_k^g\rangle \prod_{j \neq k} |0_j^g\rangle. \tag{2.28}$$

A schematic view of the transitions involved is depicted in Fig. 2.3. The states can be compared with the single vibrational modes in Sec. 2.2.1. However, for readability the notation for multi-vibrational states will be somewhat altered, therefore state $|n_j^g\rangle$ corresponds to state $|\chi^{n_g}\rangle$, and similar for the excited state, throughout this section. The energy difference between $|i\rangle$ and $|f\rangle$ vibrational levels can be expressed as

$$E_{shift} = E_f - E_i \tag{2.29}$$

19
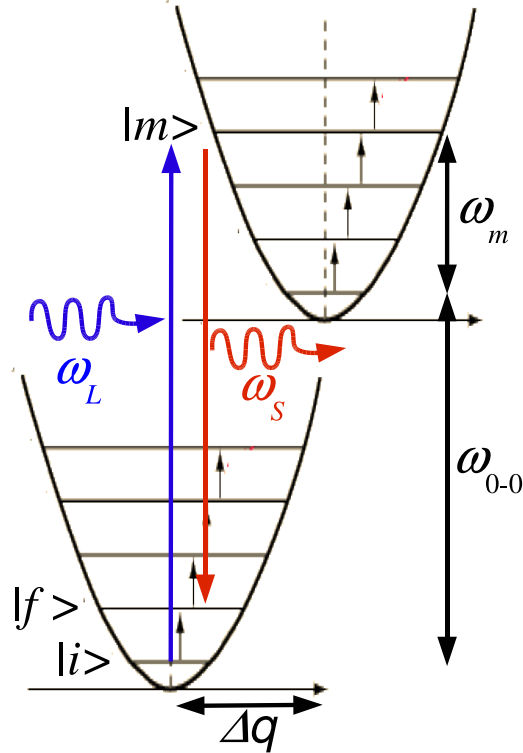
Figure 2.3: Visualization of the transfers involved in resonance Raman scattering.

where E_i is the energy of the photons in the laser and E_f is the energy of the scattered photons. In aromatic molecules, some typical Raman active modes include C-C stretching modes in the region 1300-1600 cm^{-1} and C-H bending modes in the range 1000-1300 cm^{-1}. Typically, at smaller energies, one finds breathing modes where the entire molecule is expanded or compressed in phase, so that the elongation pattern resembles acoustic phonons of graphite, with a wavelength corresponding to twice the size of the molecules. A more detailed discussion is contained in earlier work on resonant Raman theory published in the 1970s [45, 46, 47].

In the harmonic approximation the intensity of a Raman band is determined by the derivative of the polarizability with respect to a normal coordinate:

$$R \propto \left(\frac{\partial \alpha}{\partial q} \right)^2 . \tag{2.30}$$

A non-linear molecule composed of n atoms has $3n - 6$ normal modes of vibration. However, in experimental setups not all of them are visible, many modes have zero or negligible intensity due to selection rules giving vanishing derivatives in eq. (2.30). If a given vibration does not affect the polarizability, according to eq. (2.30), the Raman band will also be negligible. In order to see asymmetric stretching modes one can apply *e.g.* infra red (IR) spectroscopy.

The cross section is the probability of observing a scattered photon in a given quantum state at a given angle. For resonant Raman the cross section is expressed as [48, 49, 46, 50]

$$\frac{d\sigma(\omega_L)}{d\Omega} = \sum_f \frac{\omega_L \omega_S^3}{16\pi^2 \epsilon_0^2 \hbar^2 c^4} \cdot$$

$$\sum_i P_i \times \left| \sum_m \left[\frac{\langle f | \boldsymbol{e}_S \cdot \hat{\boldsymbol{\mu}} | m \rangle \langle m | \boldsymbol{e}_L \cdot \hat{\boldsymbol{\mu}} | i \rangle}{\omega_m - \omega_i - \omega_L - i\gamma} + \frac{\langle f | \boldsymbol{e}_S \cdot \hat{\boldsymbol{\mu}} | m \rangle \langle m | \boldsymbol{e}_L \cdot \hat{\boldsymbol{\mu}} | i \rangle}{\omega_m - \omega_i + \omega_L + i\gamma} \right] \right|^2, \tag{2.31}$$

where ω_L is the incident laser photon frequency and ω_S is the frequency of the scattered photons and ω_m and ω_i are the frequencies of the intermediate and initial state, respectively. $\hat{\boldsymbol{\mu}}$ is the dipole operator that connects the intermediate vibrational level $|m\rangle$ in the excited electronic state to the electronic ground state, and γ is the inverse of the dephasing time. If we limit the model to vanishing temperature, only the lowest vibrational level $|i\rangle$ in the electronic ground state $|g\rangle$ occurs with the probability $P_i = 1$ and therefore the sum over initial states can be skipped. An overview visualizing the states involved in eq. (2.31) is visualized in Fig. 2.3.

Under the assumption that the transition dipoles are independent of the positions of the atoms, the matrix elements in eq. (2.31) can be decomposed into contributions of different internal modes,

$$\langle m | \hat{\boldsymbol{\mu}} | i \rangle = \boldsymbol{\mu}_{eg} \langle m_k^e | 0_k^g \rangle \prod_{j \neq k} \langle m_j^e | 0_j^g \rangle \tag{2.32}$$

$$\langle f | \hat{\boldsymbol{\mu}} | m \rangle = \boldsymbol{\mu}_{ge} \langle 1_k^g | m_k^e \rangle \prod_{j \neq k} \langle 0_j^g | m_j^e \rangle, \tag{2.33}$$

where $\boldsymbol{\mu}_{eg} = \langle e | \hat{\boldsymbol{\mu}} | g \rangle$ is the transition dipole and similar for $\boldsymbol{\mu}_{ge}$. According to [50] the overlap factors of the vibrational mode excited by the scattering process are defined as

$$\langle 1_k^g | m_k^e \rangle \langle m_k^e | 0_k^g \rangle = e^{-S_k} \sqrt{S_k} \frac{S_k^{m_k^e} - m_k^e S_k^{m_k^e - 1}}{m_k^e!} \tag{2.34}$$

where S_k is the Huang-Rhys factor of the mode k excited after the scattering process. As the other modes, $j \neq k$, return to their vibrational ground states, they give a contribution similar to the Franck-Condon factor in absorption:

$$|\langle m_j^e | 0_j^g \rangle|^2 = \frac{e^{-S_j} S_j^{m_j^e}}{m_j^e!}. \tag{2.35}$$

For the denominator in eq. (2.31) we can rewrite the excitation frequency since we let the intermediate excited state $|m\rangle$ be able to contain an arbitrary number j of excited quanta of several internal modes

$$\omega_m - \omega_i = \omega_{00} + m_k^e \omega_k^e + \sum_{j \neq k} m_j^e \omega_j^e \tag{2.36}$$

where, for simplicity, we assume vanishing Dushinsky rotation so that the vibrational mode of the ground and excited state coincide $\omega_k = \omega_k^e = \omega_k^g$. The full denominator can now be rewritten using a detuning δ

$$\delta = \underbrace{\omega_{00} + \sum_{j \neq k} m_j^e \omega_j}_{\omega_m - \omega_i - m_k^e \omega_k} - \omega_L. \tag{2.37}$$

For off-resonant or pre-resonant laser line, the ratio between $m_k^e \omega_k$ and δ is small. This allows to expand the denominator in eq. (2.31) into a Taylor series

$$\frac{1}{\omega_m - \omega_i - \omega_L - i\gamma} = \frac{1}{\delta} \frac{1}{1 + \frac{m_k^e \omega_k}{\delta}} \approx \frac{1}{\delta} \left(1 - \frac{m_k^e \omega_k}{\delta} \right). \tag{2.38}$$

By replacing the numerator and denominator in eq. (2.31) by eq. (2.34) and the Taylor expansion, it is clear the the zero order term in the Taylor expansion gives a vanishing contribution. The first order term yields

$$e^{-S_k} \sqrt{S_k} \sum_{m_k^e} \frac{m_k^e \omega_k}{\delta^2} \frac{S_k^{m_k^e} - m_k^e S_k^{m_k^{e-1}}}{m_k^e!} = e^{-S_k} \sqrt{S_k} \frac{\omega_k}{\delta^2} e^{S_k} = \sqrt{S_k} \frac{\omega_k}{\delta^2}. \tag{2.39}$$

This gives then a cross section proportional to

$$\frac{d\sigma(\omega_L)}{d\Omega} \propto S_k \omega_k^2 \langle \frac{1}{\delta^2} \rangle^2. \tag{2.40}$$

At finite temperature there will be an increase in cross section due to the thermal occupation of each mode according to

$$\frac{d\sigma(\omega_L)}{d\Omega} \propto S_k \omega_k^2 [1 + n_{th}(\hbar\omega_k, k_B T)] \langle \frac{1}{\delta^2} \rangle^2. \tag{2.41}$$

In the case of the fully resonant case the Taylor series expansion used in eq. (2.37) is not applicable and the cross section has a more complex resonance profile. Since the cross section is proportional to $\langle \frac{1}{\delta^2} \rangle^2$, it shows a large resonance enhancement of the Raman signal when the detuning from full resonance is decreased.

From eqs. (2.40) and (2.41) it is clear that the cross sections are proportional to their Huang-Rhys factor. Therefore, the decomposition of the calculated deformation in the relaxed excited geometry of a molecule into contributions of different internal modes allows for a quantitative comparison between measured and calculated Raman cross sections.

Molecules with a specific symmetry can be classified into different point groups. This geometry remain will be unchanged under all the symmetry operations of that group. The molecules investigated in the following belong to either the D_{2h} or C_{2h} point group. D_n represents the dihedral group which is the group of symmetries of a regular polygon with n undirected sides, and C_n represents the cyclic group of a regular polygon with n directed

sides. A molecule with D_{2h} (C_{2h}) symmetry has 8 (4) irreducible representations, but only A_g modes are elongated when the molecule is excited, resulting in a non-vanishing Huang-Rhys factor. As the elongation of the A_g modes of rectangular D_{2h}-symmetric molecules is intimately related to the vibronic progression in absorption and PL, in the following we will mainly concentrate on computational schemes addressing these modes. B_g modes are Raman-active too, but they can only be excited if their elongation changes the transition dipole $\mu_{eg} = \langle e|\mu|g \rangle$ between the electronic states involved in the virtual transition, so that most of these modes have Raman cross section much smaller than the A_g modes.

2.3 Perylene compounds

The main aim of this thesis is the development of a comprehensive exciton model for molecular crystals. Due to very detailed experimental studies of various crystalline pigments based on perylene compounds, this specific class of organic semiconductors will be used for validating this exciton model. In order to have a sound basis for these methological developments, we need to start from the photophysics of the respective molecules. The following set of perylene chromophores will be addressed: 3,4,9,10-perylene tetracarboxylic dianhydride (**PTCDA**, pigment classification name red pigment PR224), 5,15-Diaza-6,16,dihydroxy- tetrabenzo[*b,e,k,n*]perylene (**DDTP**) N,N-dimethyl-3,4,9,10-perylene-tetracarboxylic diimide (red/maroon pigment PR179 or **Me-PTCDI**), N,N-bis(3,5-xylyl)perylene-3,4,9,10-bis (dicarboximide) (red pigment **PR149**), N,N-bis(2-phenylethyl) - perylene-3,4,9,10-bis (dicarboximide) (black pigment **PB31**), 3,4,9,10-perylene-bis(dicarboximide) (**PTCDI**, violet pigment PV29) and diindenoperylene (**DIP**), for a visualization see Fig. 2.4. The bold font indicates under which abbreviation they will be referred to in the subsequent parts of this thesis. The molecules, except for DDTP and DIP, share a common geometrical feature, which is the perylene backbone surrounded by two identical functional groups involving oxygen (PTCDA) or an imide group with a sidegroup of varying size, ranging from a hydrogen atom (PTCDI) to a larger extension consisting of *e.g.* -CH_2-CH_2-phenyl (PB31). In all these cases the HOMO and LUMO have a node plane along the long axis, so that the size of the sidegroup has little effect on the optical properties of each chromophore. This can be verified by studying the spectra of dissolved molecules, which show great similarities, consolidating the idea that the side wings have a small influence on the frontier orbitals and thus the optical properties in the single molecule.

2.3.1 Molecular properties

PTCDA

PTCDA is a well investigated planar molecule consisting of 38 atoms, compare Fig. 2.4. It can crystallize in two monoclinic bulk phases, called α and β. The point group of the isolated molecule is D_{2h}, while the experimental PTCDA geometry in the crystal shows
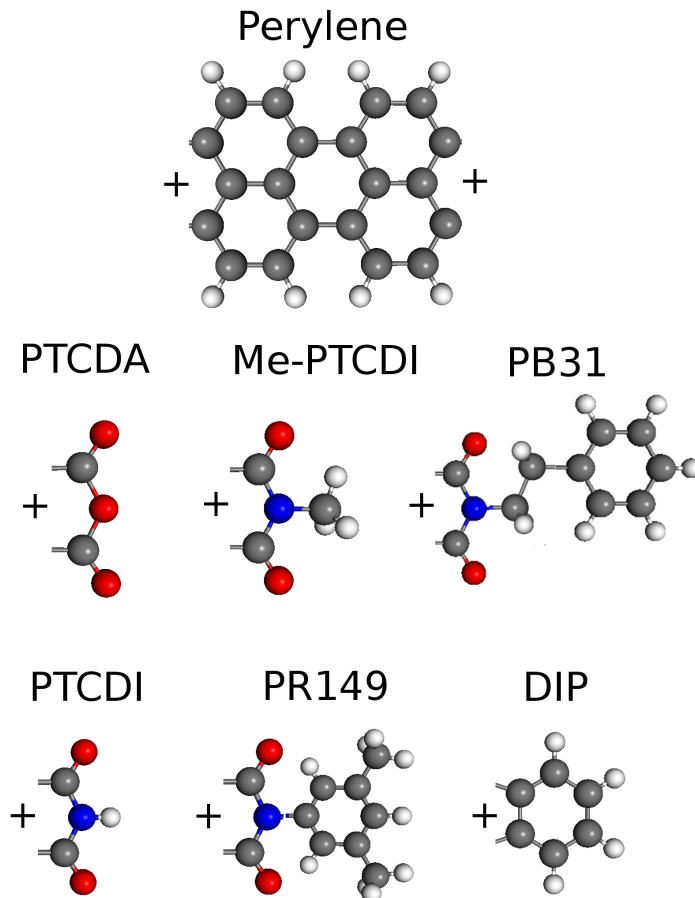
Figure 2.4: Perylene compounds studied in the present work PTCDA, Me-PTCDI, PB31, PTCDI, PR149 and DIP. The plus signs indicates where the sidegroups are attached. For clarity, the side wings in PB31 and PR149 are rotated by 90° after the first connection.

some deviations from the full D_{2h} symmetry due to distortions of the anhydride groups. In the PTCDA monomer, the lowest transition at 2.44 eV is the strongest one, with oscillator strength $f_{osc} = 0.657$ calculated with a B3LYP/TZ scheme. Further prominent transitions have energies 3.65 eV ($f_{osc} = 0.076$) and 5.57 eV ($f_{osc} = 0.517$).

DDTP

The DDTP molecule deviates from the other perylene compounds in several respects. First, the polyaromatic structure is extended by an additional hexagonal ring attached to each corner of the perylene core, second, along the long axis of the core, there is no additional ring like in the six compounds analyzed, and third, two OH groups are attached to the perylene part. As a result, this compound looks like two pentacene molecules crossing each other at an angle of 60°, with two additional OH groups attached to one of them.
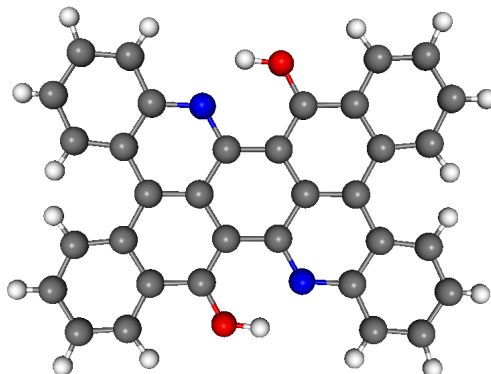
Figure 2.5: Perylene compound DDTP.

DDTP is a violet/purple pigment based on the diaza-perylene skeleton with 56 atoms, compare Fig. 2.5. It was found to exhibit two distinct colors in evaporated films: violet and reddish-purple. In the DDTP monomer, the lowest transition at 2.14 eV is the strongest one, with oscillator strength $f_{osc} = 0.594$ calculated with a B3LYP/TZ scheme.

Me-PTCDI

The Me-PTCDI molecule consists of 46 atoms and the point group of the isolated molecule is C_{2h}. B3LYP/TZ calculations show a very strong lowest excitation at 2.40 eV with B_u symmetry ($f_{osc} = 0.728$) and a weaker one at 3.73 eV ($f_{osc} = 0.110$), see Table 2.1.

transition	energy (eV)	f_{osc} (1)
$1B_u(x)$	2.403	0.728
$1A_u(z)$	3.062	0.000
$2B_u(y)$	3.446	0.000
$2A_u(z)$	3.553	0.000
$3B_u(y)$	3.725	0.110
$3A_u(z)$	4.592	0.000
$4B_u(y)$	4.746	0.066
$5B_u(y)$	4.828	0.000
$6B_u(x)$	4.920	0.037

Table 2.1: Lowest dipole-active transition energies for Me-PTCDI in C_{2h} geometry. B_u $\pi \rightarrow \pi^*$ transitions have their transition dipole along the long (x) and short (y) axis of the molecule, and $\pi \rightarrow \sigma^*$ transitions along the molecule normal (z).

DIP

DIP has two indeno groups in the planar aromatic region, resulting in a spreading of HOMO and LUMO over the entire molecule [11]. Nevertheless, the larger extension of the DIP frontier orbitals compared to the other molecules does not give rise to a significant red shift with respect to the other compounds. The crystal state of DIP is radically different from the others in this group of perylene compounds since the geometric overlap between stack neighbors is much smaller than for the others. However, the ordering in its crystal phase is very well defined and it has been found to give rise to a rather high mobility of charge carriers [51, 52, 53]. TZVP calculations for a single DIP give the strongest transition $1B_{1u}(x)$ at 2.347 eV with an oscillator strength of $f_{osc} = 0.764$. Between the lowest transition and 4 eV, the calculations give some relative weak transitions, but above 4 eV there are several strong transitions, all with transition dipoles along the long axis of DIP.

transition	energy (eV)	f_{osc} (1)
$1B_{1u}(x)$	2.347	0.764
$1B_{2u}(y)$	2.970	0.001
$2B_{2u}(y)$	3.711	0.036
$2B_{1u}(x)$	3.944	0.051
$3B_{2u}(y)$	3.995	0.022
$3B_{1u}(x)$	4.220	0.587
$4B_{2u}(y)$	4.308	0.059
$4B_{1u}(x)$	4.514	0.640
$5B_{2u}(y)$	4.809	0.070
$5B_{1u}(x)$	4.908	0.321

Table 2.2: Lowest dipole-active transition energies for DIP in rectangular D_{2h} geometry. B_{1u} $\pi \to \pi^*$ transitions have their transition dipole along the long (x) axis of the molecule, and B_{2u} $\pi \to \pi^*$ transitions along the short (y) axis. B_{3u} transitions with transition dipole along the molecule normal (z) do not occur in the energetic range reported. The lowest dipole-forbidden transition $1B_{1g}$ at 2.333 eV is nearly degenerate with the $1B_{1u}$ HOMO-LUMO transition.

Allowing for a typical solvent shift of -0.15 eV, the lowest calculated dipole-active $1B_{1u}$ transition would be red-shifted to a vertical transition energy of about 2.2 eV in solution, or about 0.3 eV below the observed vertical transition energy $\langle E \rangle = 2.50$ eV. This rather small deviation indicates that gap estimates for DIP based on the hybrid functional B3LYP with its admixture of exact exchange are more reliable than pure density functionals [54], in agreement with previous studies of transitions in aromatic molecules [23].

2.3.2 Effective vibrational mode in solution spectra

In solution, the energetic distance between subsequent vibronic bands is found to be constant over the lower vibronic levels. In this work we treat only the lowest few vibronic levels of the oscillations, so that the potential can be approximated by a parabolic shape corresponding to a *harmonic oscillator*. In order to simplify calculations, a single effective mode of $\hbar\omega_{\text{eff}}$ is introduced, replacing several high-frequency internal vibrations elongated in the relaxed excited state of a molecule. $\hbar\omega_{\text{eff}}$ then corresponds to the energetic difference between vibronic subbands in the optical absorption of dissolved molecules [13]. Assuming that this is a valid approximation, the energy difference between the lowest vibronic level in the ground state and an arbitrary vibronic level ν_e in the excited state would then be

$$E_{0\nu_e} \approx E_{00} + \nu_e \hbar\omega_{\text{eff}}. \tag{2.42}$$

where E_{00} is the distance between the two lowest vibronic levels of each electronic state.

The fitting procedure gives vibronic subbands which are approximately equally spaced, $E_{0n} \approx E_{00} + n\hbar\omega$, and the experimental effective mode reported in Table 2.3 is defined as $\hbar\omega = (E_{02} - E_{00})/2$. The fits of the observed spectra demonstrate that the sidegroups have only a marginal influence on the optical response.

2.3.3 Calculation of effective internal mode

The effective vibrational modes for the perylene compounds were calculated using TD-DFT and *c*-DFT with B3LYP as functional and TZ as basis set. The ground state vibronic modes were used, this can be done since we assume that the molecular geometry is conserved on the time scale of the electronic transition according to the Franck-Condon principle. We found calculated values of approximately $\hbar\omega$=0.17 eV for all compounds, the exact calculated values can be found in Table 2.3.

Our analysis of experimental spectra with a calculated vibronic effective mode results in good agreement. For PTCDA, the measured value $\hbar\omega_{exp} = 0.172$ eV compares well with the calculated one of $\hbar\omega_{calc} = 0.171$ eV and for Me-PTCDI, a measured value of $\hbar\omega_{exp} = 0.173$ eV is well reproduced by the calculated value $\hbar\omega_{calc} = 0.170$ eV. For DIP, the results can be compared to measurements made by Heinemeyer *et al.* where the measured value in solution can be estimated to $\hbar\omega_{exp} = 0.167$ eV [11], again in good agreement with the calculated value of $\hbar\omega_{calc} = 0.165$ eV. For PTCDI and DDTP, we have no data from measurements, but as the other compounds show a maximum deviation between calculated and experimental effective mode of only a few meV, we can assume that the calculated value for them are realistic.

2.3.4 Geometry optimization and reorganization energies for different electronic configurations

The geometric structure of a molecule depends on its electronic configuration and therefore a deformation in an excited state arises in a natural way from the minimum of the new

compound		c-DFT $\hbar\omega$ eV	exp. $\hbar\omega$ eV
PTCDA	[15]	0.171	0.172
DDTP		0.167	
Me-PTCDI	[15]	0.170	0.173
PB31	[14]	0.170	0.169
PTCDI		0.175	
PR149	[14]	0.170	0.170
DIP	[11]	0.165	0.167

Table 2.3: Effective internal vibration for the perylene compounds obtained with constrained DFT at the B3LYP/TZ level, scaled by a factor of 0.973 adequate for this functional [34]. The experimental values are obtained from a fit to solution spectra according to eq. (2.24).

potential energy surface associated to the new configuration. The deformation is directly related to the bonding and anti-bonding regions of the frontier orbitals. As an explanation of the deformation after exciting a HOMO electron into the LUMO, for Me-PTCDI these orbitals are displayed in Fig. 2.6 together with the resulting deformation. Since the excitation transfers one valence electron from the HOMO to the LUMO, the horizontal bonds in the central rings will get stronger and contract the molecule in this direction while the molecule loses binding strength in the vertical direction. The molecule as a whole tends to become shorter and broader, and this is generally true for all of our perylene compounds because of their similar backbone. For calculations of the excited states we use both the TD-DFT and the c-DFT method. For both approaches the deformation patterns are similar, but the size of the deformation of TD-DFT is significantly smaller. For the optimization for the charged states we have used DFT where $n_{\mathrm{HOMO}} = 2, n_{\mathrm{LUMO}} = 1$ corresponds to the anion and $n_{\mathrm{HOMO}} = 1, n_{\mathrm{LUMO}} = 0$ corresponds to the cation.

Immediately after a transition to an excited state the molecule has its ground state geometry configuration according to the BO approximation. The reorganization energy λ is defined as the difference in energy between vertical excitation from the ground state geometry and the energy in the relaxed excited state. Our calculations show that the reorganization energy for the neutral excited states are higher than for the ionic states, and the anionic state has a higher value than the cationic state, thus $\lambda > \lambda_- > \lambda_+$, see Table 2.4.

2.3.5 Huang-Rhys factors for neutral excited molecules and ionized states

When analyzing the spectra from dissolved chromophores, the various internal vibrations are not resolved, but instead they merge into a single vibronic progression with a
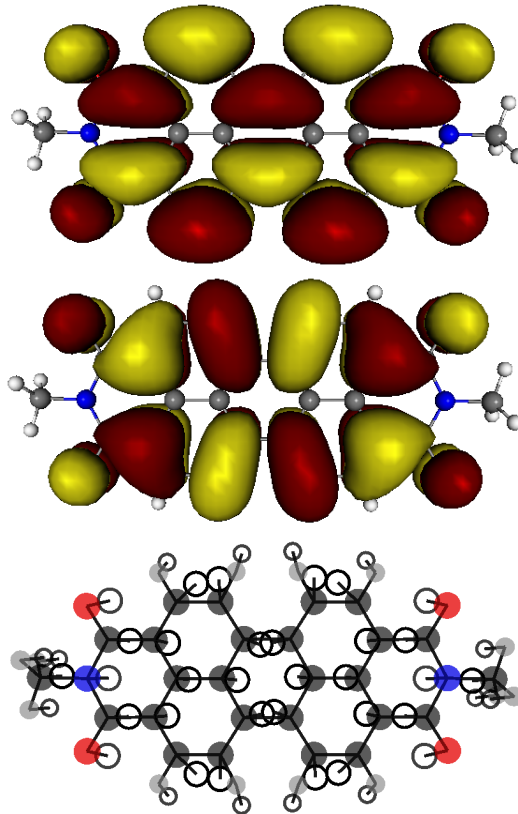
Figure 2.6: LUMO (top), HOMO (middle) and deformation in the relaxed excited electronic state (bottom) of Me-PTCDI. The deformed geometry is visualized by the open circles with a scaling factor of 30 and the ground state relaxed geometry is represented by the filled and colored circles. The relaxed geometry has been calculated with the constraint $n_{HOMO} = n_{LUMO} = 1$ at the B3LYP/TZ level.

large Gaussian broadening coming from geometric fluctuations of the surrounding solvent molecules. By a projection of the deformation patterns onto the vibrational eigenvectors one can define individual Huang-Rhys factors for each internal A_g mode. In a second step, several strongly elongated modes in the region 900 and 1800 cm^{-1} are replaced by an effective mode with an effective Huang-Rhys factor:

$$S = \sum_j S_j \tag{2.43}$$

$$\hbar\omega = \frac{1}{S} \sum_j S_j \hbar\omega_j \tag{2.44}$$

This scheme is applicable to both ionized and excited states since the energies of the effective modes deduced from the different deformation patterns are quite similar. However, in ionized states, the deformation is generally smaller, which results in smaller Huang-Rhys factors than for a neutral excited state.

	cation λ_+ eV	anion λ_- eV	c-DFT λ eV	TD-DFT λ eV
PTCDA	0.068	0.127	0.180	0.112
DDTP	0.095	0.103	0.162	0.113
Me-PTCDI	0.074	0.131	0.177	0.110
PB31	0.038	0.137	0.178	0.110
PTCDI	0.069	0.119	0.171	0.110
PR149	0.039	0.128	0.174	0.109
DIP	0.055	0.104	0.188	0.121

Table 2.4: Reorganization energies for the molecules in their relaxed geometries in the cationic, anionic, and neutral excited electronic configurations. The values are calculated at the B3LYP/TZ and they are unscaled.

For the studies of a single molecule we use a well converged triple-ζ variational basis for the electronic orbitals [41] with DFT, TD-DFT and constrained DFT. For molecules with a relatively small number of valence electrons this basis is expected to show good agreement with experimental results. In order to validate the calculated Huang-Rhys factors we have performed rigorous studies of the vibrational modes in molecules and compared them with experimental results.

We found that the constrained theory estimates accurately the effective Huang-Rhys factors, while TD-DFT tends to underestimate its values. In general the effective Huang-Rhys factor calculated with the constraint $n_{\mathrm{HOMO}} = n_{\mathrm{LUMO}} = 1$ is overestimated by less than 10 %, while TD-DFT underestimates it by up to 30 % compared to observed values extracted from solution spectra. This gives a motivation to use the constrained DFT values when calculating the parameters used for the exciton model in Chap. 4. For the internal vibrations of aromatic molecules, it is common practice to reduce the values obtained with the B3LYP functional by a scaling factor of 0.973 [34]. This factor comes from problems handling the electron correlation, neglect of the anharmonicity of the potentials, and/or basis set truncation, resulting in an overestimate of the vibrational modes. When keeping the reorganization energies fixed, this gives a rescaling of the Huang-Rhys factor by $1/0.973$.

While information on neutral excited states for perylene molecules is relatively easy to find, measurements on the anionic and cationic states and their spectra are more scarce. However, earlier experimental work on photoionization spectra of pentacene, interpreted with DFT [55], was showing that B3LYP calculations reproduce these results for anionic states well. This serves as a motivation to trust the calculated deformations of ionized states. In all cases, we find that the reorganization energy of the positively charged ionized state is smaller than for the anionic state, and that the relaxed excited state is deformed even more, fulfilling $S > S_- > S_+$ for the molecules, just like for the total reorganization energies, and the approximate sum rule $S_- + S_+ \approx S$. The calculated Huang-Rhys factors can be found in Table 2.5. In the next subsections we discuss the results based on the

compound	cation S_+	anion S_-	excited S
	1	1	1
PTCDA	0.35	0.65	0.88
DDTP	0.38	0.46	0.72
Me-PTCDI	0.34	0.62	0.87
PB31	0.17	0.64	0.87
PTCDI	0.28	0.55	0.82
PR149	0.19	0.73	0.88
DIP	0.31	0.56	0.90

Table 2.5: Huang-Rhys factors S_- and S_+ of the ionized states obtained with DFT, and the Huang-Rhys factor in the relaxed excited geometry with constrained DFT, all at the B3LYP/TZ level. All values have been scaled by 1/0.973.

theory introduced in Sec. 2.2.

PTCDA

Earlier works on PTCDA calculated with DFT reports values of $S_+ = 0.72$ and $S_- = 0.34$ indicating a distribution of reorganization energies consistent with $S_+ > S_-$ [56]. Hoffmann *et al.* found $S = 0.77$ for PTCDA which was obtained from solution spectra of Me-PTCDI where the absorption spectrum of PTCDA was identical within graphical accuracy [57]. Their Huang-Rhys factors for ionized states where assigned to half of the value of the neutral state, $S_+ = S_- = S/2$.

PTCDA has 108 internal vibrational modes including 54 Raman- and 46 infrared-active modes. Their calculated individual contribution to the Huang-Rhys factors can be found in Table 2.6 where the B3LYP calculation gives a scaled Huang-Rhys factor of $S = 0.88$ for the excited state, and for the ions $S_- = 0.65$ and $S_+ = 0.35$, with two large contributions from modes at 1299 and 1552 cm^{-1}, see Table 2.6. The value for S is within the range of previous estimates between 0.77 [59, 13] and 1.18 [60]. The individual Huang-Rhys factors of the breathing modes compare favorably with measured Raman cross sections [60], compare Fig. 2.7 for a visualization.

Me-PTCDI

A single molecule of Me-PTCDI has 138 internal vibrations of which 6 are silent, 66 infrared-active and 66 Raman-active and their individual calculated contribution to the Huang-Rhys factor and their vibronic modes can be found in Table A.1. The results show one large contribution for a mode at 1299 cm^{-1} and one at 1552 cm^{-1}, which together contribute to more than 60% to the effective Huang-Rhys factor. We found values for the three excited states with *c*-DFT to be $S = 0.88$, $S_- = 0.65$, and $S_+ = 0.35$. This can be compared to data by Hoffmann *et al.* finding a value of $S = 0.77$ [57] from fitting to

mode		Cation		Anion		neutral		neutral	
B3LYP	Raman [58]	DFT		DFT		c-DFT		TD-DFT	
		λ_j	S_j	λ_j	S_j	λ_j	S_j	λ_j	S_j
(cm^{-1})	(cm^{-1})	(cm^{-1})	(1)	(cm^{-1})	(1)	(cm^{-1})	(1)	(cm^{-1})	(1)
225	233	26	0.123	14	0.066	86	0.404	61	0.286
380	388	14	0.038	24	0.067	2	0.005	2	0.006
457	476	12	0.028	3	0.008	4	0.008	2	0.005
520	538	1	0.001	54	0.109	40	0.081	39	0.080
605	625	28	0.048	2	0.004	33	0.057	27	0.048
709	724	4	0.006	0	0.000	5	0.007	6	0.009
819	856	4	0.005	2	0.003	0	0.000	0	0.000
1013	1050	41	0.042	1	0.001	25	0.026	14	0.014
1111	1149	36	0.034	37	0.036	0	0.000	2	0.002
1232	1280	6	0.005	69	0.059	26	0.022	15	0.013
1299	1303	181	0.147	158	0.128	497	0.404	315	0.257
1325	1381	3	0.002	49	0.039	25	0.020	22	0.017
1357	1390	21	0.016	100	0.078	155	0.120	82	0.063
1423	1451	13	0.010	22	0.016	42	0.032	26	0.020
1552	1572	65	0.044	177	0.121	319	0.217	224	0.152
1567	1590	1	0.001	125	0.084	56	0.038	36	0.024
1669	1773	76	0.048	137	0.087	2	0.001	2	0.001
Sum:			0.349		0.649		0.880		0.562

Table 2.6: Calculated A_g breathing modes for PTCDA in the electric ground state together with the corresponding contribution to the reorganization energy and vibronic coupling constants using B3LYP/TZ. The first section contains the mode frequency in cm^{-1} compared to measured Raman, the second to fourth section contains the reorganization energy and Huang-Rhys factor for the cation, anion, neutral excited state calculated with constrained DFT and neutral excited state calculated with TD-DFT, respectively. The effective mode and its Huang-Rhys factors are obtained from a summation over modes between 900 and 1800 cm^{-1}. The table has been truncated for reorganization energies below 1 cm^{-1}. For all entries, the mode frequencies are scaled by 0.973 and the Huang-Rhys factors by 1/0.973.

solution spectra. Our calculated modes and their relative strength in the neutral excited state have been compared with experimental Raman cross sections from Akers *et al.* [61], resulting in good agreement, see Figs. 2.7 and 2.8. More details can be found in chapter 13 in [62] and in [63].

PTCDI

PTCDI has 114 vibrational normal modes where 54 are Raman active ($20A_g + 7B_{1g} + 11B_{2g} + 19B_{3g}$), 49 are IR active and the other are silent modes. The calculated vibrational
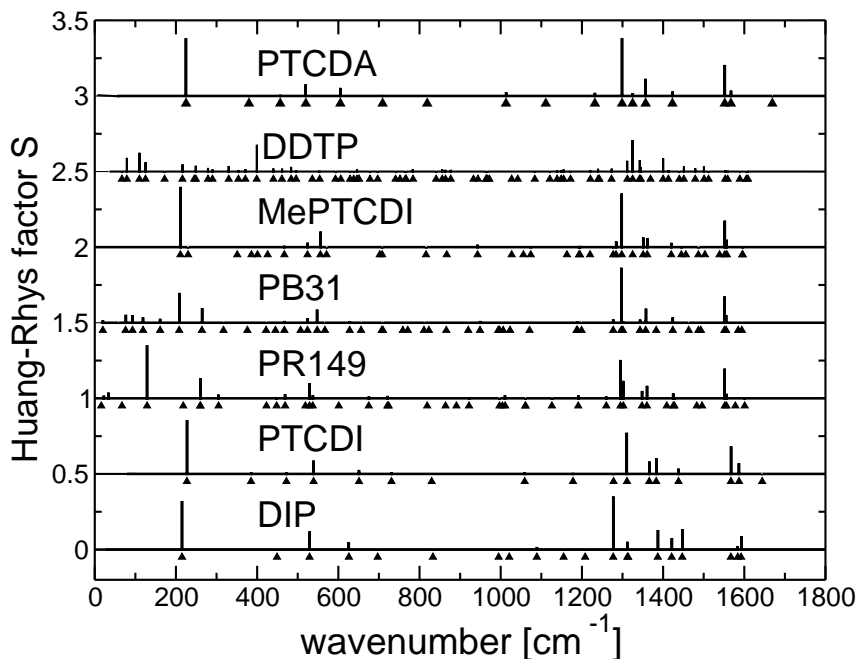
Figure 2.7: Huang-Rhys factors for neutral excitation of the perylene compounds, obtained at the B3LYP/TZ level, with base lines shifted for clarity. All mode energies have been scaled by a factor of 0.973 adequate for the B3LYP functional [35], and the Huang-Rhys factors by 1/0.973.

modes of PTCDI are in good agreement with experimental results [64], compare Table A.2 in Appendix A.5. The biggest contributing modes to the Huang-Rhys factors are at 1311, 1383 and 1567 cm^{-1}, and the total values are $S = 0.82$, $S_- = 0.55$ and $S_+ = 0.28$.

DIP

For the geometry calculated with TD-DFT we find an effective Huang-Rhys factor of $S = 0.61$ and with the c-DFT method a value of $S = 0.90$, in good agreement with experimental results where $S = 0.87$ was obtained by fitting to spectra from dissolved molecules [11]. The dominating contributions come from vibronic modes 1313 cm^{-1} (S_j=0.361), 1426 cm^{-1} (S_j=0.133), and 1488 cm^{-1} (S_j=0.138).

For the ions with positive and negative charges the deformation is found to be smaller resulting in a Huang-Rhys factor of $S_- = 0.55$ and $S_+ = 0.30$, see Table A.5 for contributions from individual modes.

Summary of Huang-Rhys factors

For DDTP, the visualization of the HR factors of the internal modes in Fig. 2.7 reveals substantial elongations of low frequency internal modes after optical excitation, indicating that the extension of the perylene core by additional peripheral aromatic rings and the
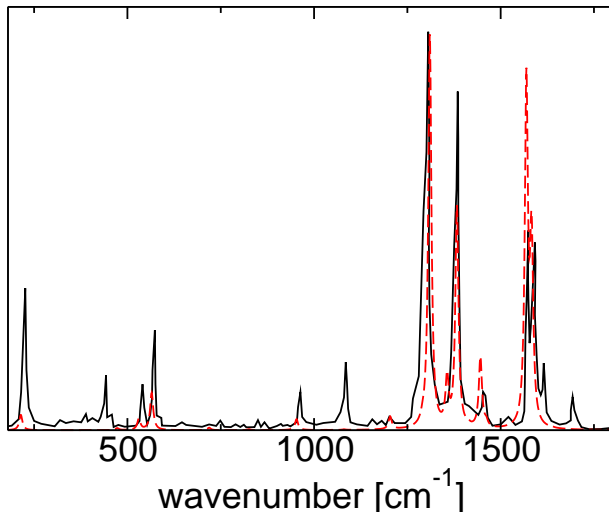
Figure 2.8: Me-PTCDI breathing modes. Experiment [61] (black solid line) and calculated with c-DFT (red dashed line). The functional used was B3LYP/TZ and a scaling of 0.973 was applied to all mode frequencies.

OH groups modifies the mechanical response to the optical excitation substantially. On the other hand, in the region of the high frequency internal modes clustering between 1300 and 1400 cm^{-1}, the vibrational fingerprint differs from the other compounds investigated but the parameters describing the effective internal vibration remain in the same range.

For DDTP, PR149 and PB31, Raman spectra have not been reported yet, so that the calculated mode frequencies and Huang-Rhys factors cannot be validated by a comparsion to measured data. However, since we have strong evidence that for PTCDA, Me-PTCDI, PTCDI and DIP, the B3LYP functional gives accurate results, we expect this to remain valid for similar molecules. Fig. 2.7 contains a comparison of the Huang-Rhys factors of our model compounds. In the high frequency region between 1250 and 1600 cm^{-1}, all molecules contains four carboxylic groups show similar patterns, with a strongly elongated C-H bending mode close to 1300 cm^{-1} and vibrational modes resembling optical phonons of graphite slightly below 1600 cm^{-1}. In DIP, the strongest Raman mode contains again significant C-H bending contributions, but the somewhat different composition of the molecule places this mode at a lower frequency of 1277 cm^{-1}, in good agreement with the observed mode at 1284 cm^{-1}, compare Table A.5.

In general, for all molecules we find that the ions have smaller reorganization energies resulting in lower Huang-Rhys factors, and for all molecules studied the cations have the lowest values. This finding corroborates earlier B3LYP calculations on polyacenes demonstrating that the reorganization energies for the negatively charged molecule were larger than in their cationic state [66, 55]. For the other molecules, the tabulated vibrational mode results from B3LYP/TZVP calculations can be found in the Appendix A.5.

compound		E_{00}	S	$\hbar\omega$	S	$\hbar\omega$	S	$\hbar\omega$
			solution spectra		c-DFT		TD-DFT	
PTCDA	[15]	2.363	**0.86**	0.172	**0.88**	0.171	0.56	0.171
DDTP		-	-	-	**0.72**	0.167	0.49	0.166
Me-PTCDI	[15]	2.363	**0.80**	0.173	**0.87**	0.170	0.56	0.171
PB31	[14]	2.350	**0.80**	0.169	**0.87**	0.170	0.56	0.171
PTCDI		-	-	-	**0.82**	0.175	0.51	0.176
PR149	[14]	2.360	**0.84**	0.170	**0.88**	0.170	0.53	0.171
DIP	[11]	2.351	**0.87**	0.167	**0.93**	0.165	0.64	0.170

Table 2.7: Comparison between observed solution spectra, c-DFT calculations of the deformation pattern in the relaxed excited state, and TD-DFT calculations of this deformation pattern. The experimental spectra are fitted to a Poisson progression for the dielectric response with argument S and vibronic spacing $\hbar\omega$, compare eqs. (2.23, 2.25, 2.24). In both types of DFT calculations, the effective mode $\hbar\omega$ and its Huang-Rhys parameter S are defined via eqs. (2.43, 2.44).

In Table 2.7 we compare the Huang-Rhys factors for neutral excitation obtained from constrained DFT calculations and TD-DFT with the observed vibronic progression in solution spectra of perylene compounds [67, 60], revealing that constrained DFT calculations are in better agreement with the experimental findings.

2.4 Pentacene

Resonant Raman spectra and solution spectra were also obtained on other compounds, including pentacene, rubrene, and triphenyldiamine (TPD) (Fig. 2.9). The calculations summarized in the present section were applied to an analysis of resonant Raman spectra obtained on single crystals of pentacene, grown by J. Pflaum [68]. The non-planar compounds rubrene and TPD will be discussed in Sec. 2.5.

Pentacene has proven to be a very good candidate for organic electronics since it has demonstrated one of the highest electron and hole mobilities of all organic semiconductors investigated so far [69]. Pentacene can be found in diverse fields such as light sensors [70], field effect transistors [71], photovoltaic cells [72, 73, 74, 75, 76], strain sensors [77], and thin film transistors (TFT) [78, 79]. Pentacene can form highly ordered polycrystalline films depending on the growth conditions. Previous studies of the optical properties of pentacene thin films were performed by Hinderhofer *et al.* [80] showing that the material inherits a strong optical anisotropy from the specific arrangement of the two basis molecules in the crystal unit cell.

Vibronic studies on pentacene show that the internal vibrational modes [81] and vibronic coupling to external phonons [82] affect the carrier transportation properties. The particle transport achieved in pentacene has revealed electron and hole mobilities above $1 \text{ cm}^2/\text{Vs}$ [4].
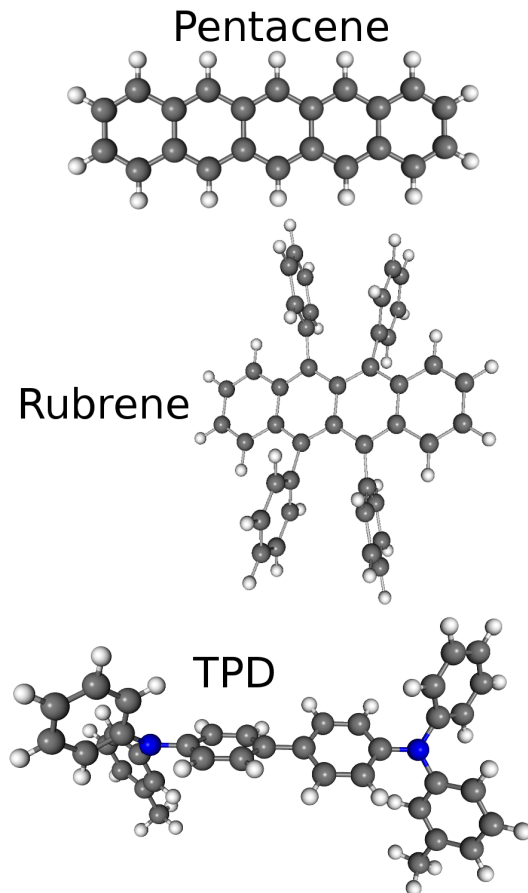
Figure 2.9: The chemical structure of pentacene, rubrene and TPD.

Studies on vibrational properties including papers by Banasiewicz [83, 84] *et al.* report spectroscopic properties on pentacene in solution and in Shpol'skii matrices. Amirav *et al.* studied the out-of-plane vibrational modes of an isolated single molecule via laser spectroscopy [85], Malagoli *et al.* used a multimode analysis to study vibrations of ions [86], and Hartmann *et al.* have investigated pentacene in liquid helium droplets [87].

Resonant Raman and deformation pattern

Previous studies on the lowest excited states have been performed both with optical measurements [84] and theoretical methods [23]. Our study extends these calculations to include higher excitations so that we can analyse Raman spectra in resonance with different electronic excitations. For the lowest transition, we find that our TD-DFT calculation reproduces earlier TD-DFT results and the observed Raman intensity pattern. In Fig. 2.10 we compare the measured Raman spectra excited at 514 nm (2.41 eV), the lowest calculated TD-DFT transition $1B_{2u}$ (1.93 eV) and a constrained approach where only the HOMO to LUMO transition is allowed. We find that both TD-DFT and *c*-DFT are able to produce a deformation pattern compatible with the observed Raman spectra.
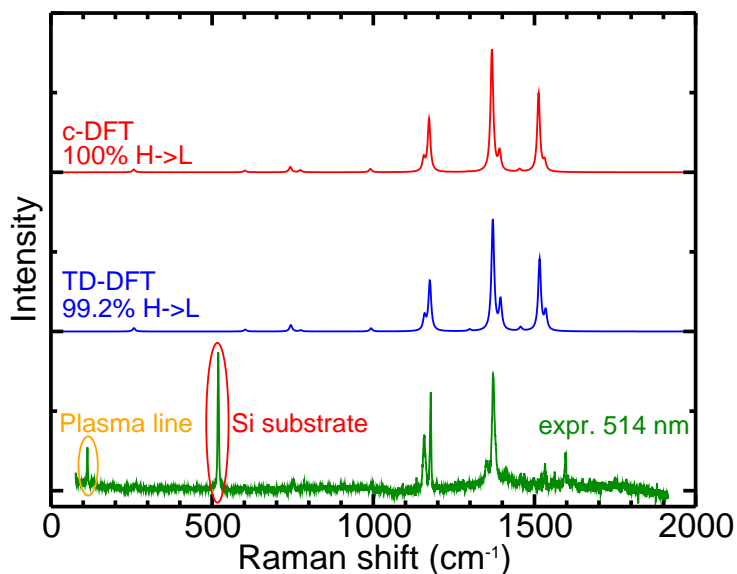
Figure 2.10: Comparsion of measured Raman spectra (lower) close to resonance with the $1B_{2u}$ (1.93 eV) transition with calculated intensities obtained with TD-DFT B3LYP/TZ (middle), and c-DFT (upper). The exciting laser had an energy of 514 nm (2.41 eV). The calculated intensities have been reproduced as $S(\hbar\omega)^2$ for B3LYP vibrational frequencies scaled by a factor of 0.973.

By studying the valence orbitals of pentacene it is possible to obtain an understanding of the deformation that is taking place after the laser excitation. This transition (HOMO→LUMO) gives rise to a stretching of the whole molecule along the long axis. The reason for this can be found in the frontier orbitals: in the ground state, the valence electron contributes to a contraction along the long axis, whereas in the LUMO state the wave function has more repulsive nodes along the long axis but contributes to a contraction along the short axis, see Fig. 2.11.

By using a laser with shorter wavelength it is possible to access transitions of higher energy. Our calculations shows that the next two allowed transitions consist of two different electronic excitations HOMO-2→LUMO and HOMO→LUMO+2. As the transition dipoles of these two excitations are parallel and of similar size, they produce a destructive interference with very low oscillator strength at 3.23 eV ($f_{osc} = 0.005$) and a very strong transition at 4.28 eV with $f_{osc} = 3.333$.

To examine those two superimposed electronic excitations of pentacene, we need to study the two electronic excitations given (HOMO-2→LUMO and HOMO →LUMO+2) separately. To do this, we apply the c-DFT scheme to each of them. The geometric changes can be understood once again by looking at the contributing orbitals. As stated previously the HOMO contributes to a longitudinal contraction. After exciting to LUMO+2, the pronounced node of this orbital along each bond crossing the long axis makes the molecule expand along the short axis, and the increased number of nodes along

37
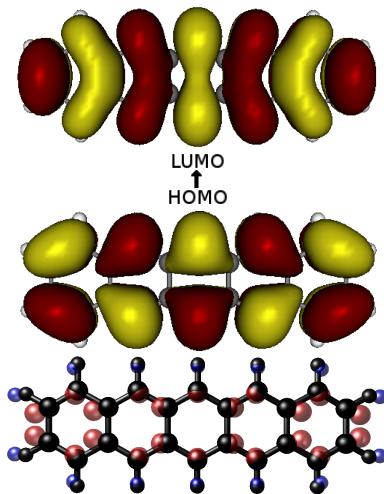
Figure 2.11: Frontier orbitals and deformation pattern for $1B_{2u}$ electronic excitation dominated by $3B_{3g} \to 4B_{1u}$ (HOMO→LUMO), obtained with *c*-DFT B3LYP/TZVP. In the lower panel the black circles represent the ground state and the colored semi-transparent represent the molecule in its relaxed excited geometry. For clarity, the deformation has been increased by a factor of 20.

the long axis increases its length. Altogether, both ingredients contribute to an expansion of the molecular area, see Fig. 2.12. The HOMO-2→LUMO excitation yields a similar deformation pattern because the transverse bonding regions of HOMO-2 are replaced by a weaker bonding LUMO orbital. Again, the increased number of lobes in the LUMO expands the geometry in the longitudinal direction.

From this we conclude that the pre-resonant laser excitation with a wavelength of 325 nm mainly gives rise to HOMO → LUMO+2 and HOMO-2 → LUMO excitations. The measured spectra obtained at 325 nm and the computed vibrational modes together with their Raman intensities proportional to $S(\hbar\omega)^2$ are in very good agreement, see Fig. 2.13 and Table 2.8. The *c*-DFT scheme was found to be an excellent way to study individual contribution of both main transitions involved in this Raman spectra, compare Fig. 2.13. There is clear evidence that the HOMO-2 → LUMO transition contributes more in the lower regions, especially at peaks around 740 cm^{-1} and 1175 cm^{-1}, while the HOMO→LUMO+2 contributes more above 1380 cm^{-1}

From these results we conclude that the lowest dipole-active $1B_{2u}$ transition found in TD-DFT is dominated by HOMO → LUMO excitations (99.2%) resulting in the *c*-DFT and TD-DFT will give essentially equivalent results. However, for higher transitions which are not dominated by a single electronic excitation between a specific pair of Kohn-Sham orbitals, TD-DFT is required to address the specific mixture occuring in the optical excitation.

The most prominent vibrational modes are found at 257 cm^{-1} which is a stretching mode in the long direction, whereas at 742 cm^{-1} there is a stretching mode in the short direction of the molecule. At 1173 cm^{-1} there is a C-H bending mode and at 1368 cm^{-1}
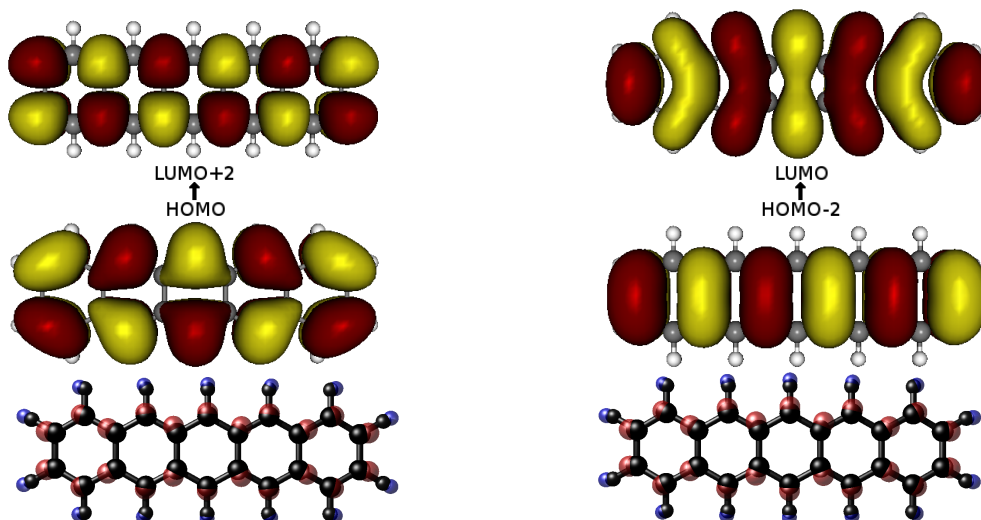
Figure 2.12: Frontier orbitals and deformation pattern for electronic excitations, obtained with c-DFT B3LYP/TZVP. In the lower panel the black circles represent the ground state and the colored semi-transparent represent the molecule in its relaxed excited geometry. For clarity, the deformation has been increased by a factor of 20. Left: Excitation $3B_{3g} \rightarrow 3A_u$ (HOMO→LUMO+2). Right: excitation $3B_{2g} \rightarrow 4B_{1u}$ (HOMO-2→LUMO). Both excitations have a transition dipole along the long axis of pentacene.

and 1513 cm^{-1} there are C-C stretching modes. In Fig. 2.14 these mode are visualized. The elongation of two prominent B_{3g} modes observed at 1598 cm^{-1} and 1628 cm^{-1} cannot be understood from our analysis of rectangular deformations occuring in individual optical transitions. Instead, their Raman activity arises from an off-diagonal coupling between two transitions with orthogonal transition dipoles influenced by elongations of these B_{3g} modes, a coupling mechanism which will not be quantified in the present thesis.

We found that resonant Raman spectra reveal deformations in relaxed excited states where different resonance conditions leads to different transitions and deformation patterns. Two complementary ways to study these transfers are TD-DFT and a constrained DFT scheme, both giving quantitatively reliable deformations patterns. Their specific advantages is that TD-DFT gives the actual mixture occurring in the optical excitation while c-DFT gives access to the individual transitions. Further details of this refined interpretation of Raman spectra in resonance with higher lying transitions will be discussed elsewhere [68].

As a further note, photoionization spectra of pentacene have been interpreted with DFT [55], and as our computational scheme reproduces these results for the cationic state together with a larger deformation of the anionic molecule, we are confident that the B3LYP functional is well suited for ionized perylene compounds as well, compare Sec. 2.3.5.
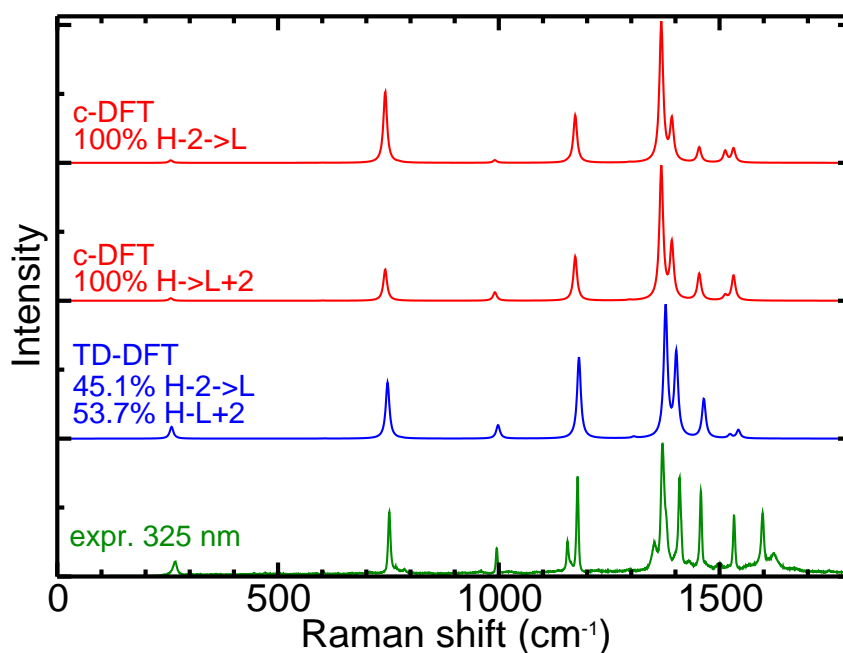
Figure 2.13: Comparsion of measured Raman spectra (lower, green line) close to resonance with the $2B_{3u}$ (4.28 eV) transition obtained with TD-DFT B3LYP/TZ (second lowest, blue line), and c-DFT (two upper, red lines). The exciting laser had an energy of 325 nm (3.82 eV). The calculated intensities have been reproduced as $S(\hbar\omega)^2$ for B3LYP vibrational frequencies scaled by a factor of 0.973.
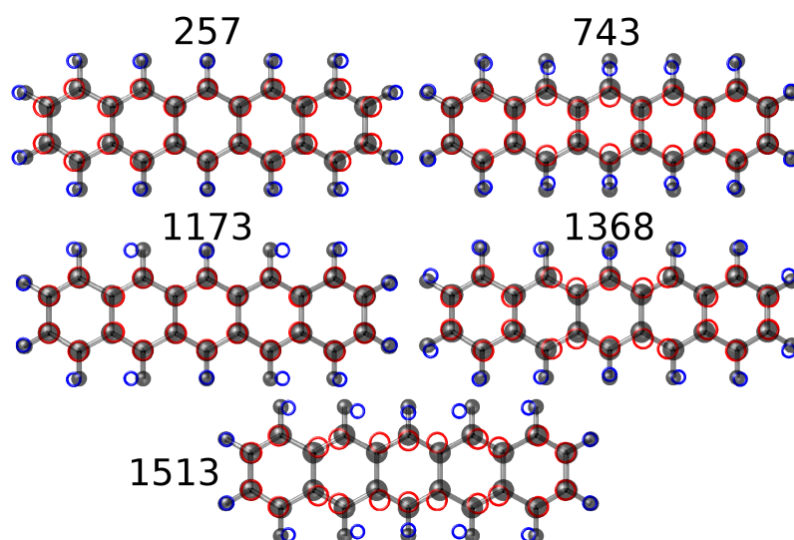
Figure 2.14: Visualization of the five most prominent Raman-active modes of pentacene: 257 cm^{-1}, 743 cm^{-1}, 1173 cm^{-1}, 1368 cm^{-1}, and 1513 cm^{-1}.

	experimental 514 nm		calculated $1B_{2u}$		experimental 325 nm		calculated $2B_{3u}$	
	mode cm^{-1}	intensity (arb.)	mode cm^{-1}	intensity (arb.)	mode cm^{-1}	intensity (arb.)	mode (arb.)	intensity
A_g	-	-	**257**	0.029	268	0.111	**257**	0.087
A_g	-	-	**743**	0.057	752	0.486	**743**	0.419
A_g	-	-	995	0.213	991	0.029	995	0.101
A_g	1158	0.486	1156	0.164	1156	0.265	1156	0.002
A_g	1178	0.855	**1173**	0.453	1178	0.748	**1173**	0.538
A_g	1372	1.000	**1368**	1.000	1371	1.000	**1368**	1.000
A_g	1412	0.208	1392	0.302	1410	0.745	1392	0.646
A_g	1458	0.151	1454	0.044	1458	0.641	1454	0.298
A_g	1533	0.239	**1513**	0.209	1533	0.459	**1513**	0.066
B_{3g}	1598	0.278	-	-	1598	0.4775	-	-
B_{3g}	-	-	-	-	1622	0.1743	-	-
B_{3g}	-	-	-	-	1931	0.0670	-	-

Table 2.8: Observed dominant Raman peaks at measurements with 514 nm and 325 nm laser, with their relative intensities compared to calculated modes, obtained with B3LYP/TZVP and scaled by 0.973. The relative intensity has been normalized to the observed mode at 1371 cm^{-1}. Modes visualized in Fig. 2.14 are highlighted.

mode	TD-DFT		*c*-DFT		
	$1B_{2u}$	$2B_{3u}$	HOMO→ LUMO	HOMO→ LUMO+2	HOMO-2→ LUMO
$\hbar\omega_j$ (cm^{-1})	S_j (1)	S_j (1)	S_j (1)	S_j (1)	S_j (1)
257	0.238	0.135	0.231	0.069	0.059
602	0.025	0.000	0.026	0.001	0.001
631	0.001	0.000	0.001	0.000	0.000
743	0.054	0.077	0.052	0.103	0.201
774	0.010	0.000	0.019	0.000	0.001
991	0.015	0.010	0.018	0.016	0.004
1156	0.050	0.000	0.052	0.000	0.001
1173	0.171	0.045	0.208	0.058	0.054
1296	0.005	0.001	0.001	0.001	0.000
1368	0.279	0.053	0.354	0.129	0.117
1392	0.071	0.033	0.052	0.051	0.033
1454	0.008	0.014	0.007	0.023	0.011
1513	0.146	0.001	0.187	0.004	0.008
1532	0.037	0.003	0.022	0.019	0.009
sum	0.781	0.160	0.900	0.300	0.236

Table 2.9: Internal vibrations of pentacene. The first column are the calculated vibrational modes scaled by 0.973 [34], the other columns are the Huang-Rhys factor for each mode calculated with TD-DFT and *c*-DFT, scaled with 1/0.973. The modes where both types of Huang-Rhys factors are below 0.001 are not shown. Modes visualized in Fig. 2.14 are highlighted.

2.5 Spectroscopic properties of non-planar molecules

2.5.1 TPD

N, N'-diphenyl-N, N'-bis(3-methylphenyl)-(1,1'-biphenyl)-4,4'-diamine (TPD, see Fig. 2.9), has recently attracted attention due to its rather high hole mobility, allowing to use it as a hole-conducting layer in light-emitting diodes [88, 89, 90, 91]. The Stokes shift of 0.5 eV is large enough to make it transparent to its own photoluminescence, so that it becomes a promising material for laser applications [90, 92, 93, 94]. It has been found that the intermolecular distances in the crystalline phase are rather large, without stacking of the aromatic rings. Thus, in sharp contrast to perylene pigments or pentacene, the intermolecular interactions should not play a dominating role in the photophysics. We have performed studies on TPD with the objective to provide an *ab initio* interpretation of the experimentally observed Stokes shift. The DFT calculations were carried out with the hybrid functional B3LYP where the molecular geometry was optimized at the DZ level, and the vertical excitation energies were obtained with TD-DFT in the adiabatic approximation, using the same functional and basis set.
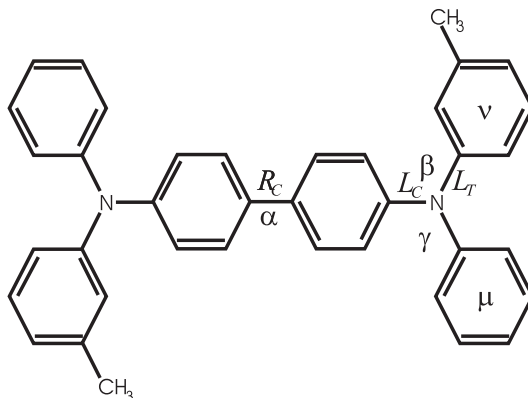
Figure 2.15: Trans isomer of N, N'-diphenyl-N, N'-bis(3-methylphenyl)-(1,1'-biphenyl)-4,4'-diamine (TPD).

Raman activity

The overall Stokes shift was obtained from a TD-DFT optimization of the geometry in the excited state [24], and for the Raman activity of the internal modes, a projection of the deformation in the relaxed excited state onto the vibrational eigenvectors defined the Huang-Rhys factors S_k for each internal mode $\hbar\omega_k$, as described in Sec. 2.2. For an assignment of the measured Raman-active modes to calculated internal vibrations, we determined their contributions to the reorganization energies. The procedure is described previously in Sec. 2.2.3, and the experimental details can be found in [95, 96].

The calculated vibrational modes are compared with Raman measurements, see also [96]. The calculated resonant Raman spectra in Fig. 2.16 are defined by eq. (2.41) and

visualized with a Lorentzian broadening of FWHM=10 cm^{-1} similar to the measured linewidths. The elongations of the internal modes in the relaxed excited geometry are obtained from two complementary projection schemes. However, from the very large changes of some dihedral angles in the excited geometry, compare Table 2.10, one projection scheme suffers from non-orthogonality problems related to the modified orientations of the various phenyl rings. The large change of the dihedral angle α produces a cross-talk between torsional modes, out-of-plane wagging modes and low frequency in-plane bending modes, resulting in rather large features in the range 700 - 800 cm^{-1} where the experimental Raman spectra do not contain substantial cross sections, see [96] for details.
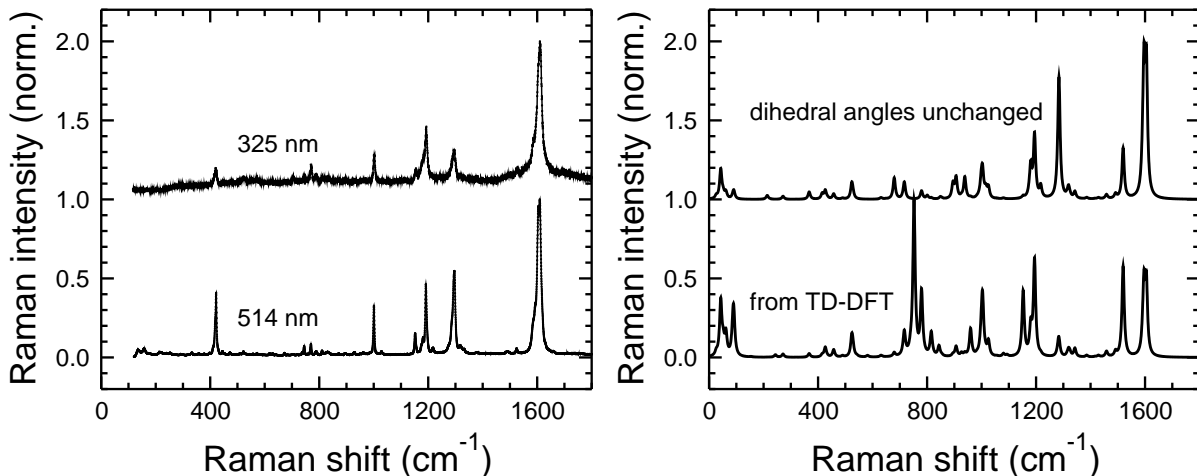
Figure 2.16: Left: Raman spectra of pure TPD powder with pre-resonant measurement of TPD powder using a laser line at 514 nm (2.41 eV), and resonant Raman spectra obtained with a laser line at 325 nm (3.81 eV). Right: calculated resonant Raman spectra according to eq. (2.41), with B3LYP frequencies scaled down by a factor of 0.973. The computed spectra are visualized with Lorentzian lineshapes with a FWHM of 10 cm^{-1}.

Absorption and PL

The absorption spectra of TPD consist of two distinct peaks at 3.4 and 4.0 eV. The dominating one is always the lower regardless of the type of solvent or substrate (see Fig. 2.17). The PL exhibits a strong redshift with an intensity maximum around 3.1 eV followed by several shoulders at lower energy. As shown in [96], these sidebands arise from a vibronic progression over an effective internal mode with $\hbar\omega_{eff} = 158$ meV (1278 cm^{-1}), calculated as an average over the most strongly elongated in-plane modes. The peaks of absorption and PL are clearly separated in all solvents, see Fig. 2.17. The spectra for TPD dissolved in toluene have a separation between the maxima of absorption and PL of approximately 0.38 eV, whereas the Stokes shift between the average over the first absorption peak and the center of mass of the PL band is 0.57 eV, defined after eliminating the prefactors E in absorption and E^3 in PL, respectively [97].
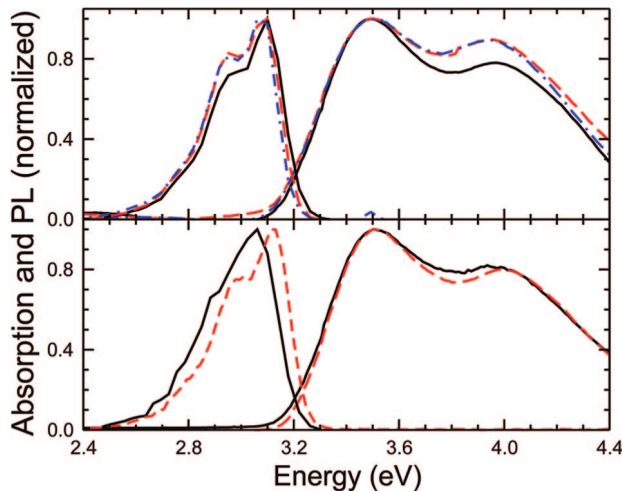
Figure 2.17: Measured linear absorption and PL of TPD at room temperature. Top: PS films doped with varying amounts of TPD: 20% (solid black line), 50% (dashed red line) and 80%(dot-dashed blue line). Bottom: TPD dissolved in chloroform (solid black line) and toluene (red dashed line) at a concentration of 5×10^{-5} mol/L in a 1-cm-thick quartz cuvette.

Optimized Geometry in electronic ground and excited state

The molecular structure of the *trans* isomer of TPD is displayed in Fig. 2.15. It consists of a central biphenyl core and two twisted diphenylamine terminal wings, where the methyl groups of the tolyl rings point into the same direction. The geometric parameters in the electronic ground state and in the lowest excited state are reported in Table 2.10.

isomer, state	R_c [Å]	α	β, γ	μ	ν
cis, ground	1.484	32.8°	40.3°	43.3°	42.8°
cis, excited	1.444	4.7°	55.5°	32.8°	32.7°
trans, ground	1.484	32.9°	40.3°	43.2°	42.8°
trans, excited	1.444	−3.5°	53.6°	33.3°	33.3°

Table 2.10: Optimized geometries of the *cis* and *trans* isomers of TPD in their electronic ground and excited states obtained at the B3LYP/DZ level, using DFT for the electronic ground state and TD-DFT for the excited state. R_c - length of central bond; α - central dihedral angle; β, γ - dihedral angles of the terminal rings; ν, μ - torsion angles of the terminal rings, compare Fig. 2.15.

The twisting in the electronic ground state is quite pronounced, as shown by the value of the central dihedral angle $\alpha = 32.8°$, see Table 2.10. The twisted geometry obtained with B3LYP/DZ is in a good agreement with the results of previous DFT calculations [98, 95]. However, the calculated shape does not correspond precisely to the experimental

structure in a crystalline environment, as obtained by X-ray diffraction measurements on single crystals [99]. In the crystalline phase, the peripheral wings adopt considerably different conformations, thus breaking the C_2 symmetry which can be realized in the free molecule. After excitation TPD becomes nearly planar with the central angle reduced to 4.7° and with the central bond length significantly shortened, see Table 2.10. A similar tendency was observed in previous calculations based on Hartree-Fock and CIS [100, 95]. The change of the dihedral angle in the center of the molecule can be understood from the node patterns of the orbitals reported in [96].

Transition Energies and Reorganization Processes

The present TD-DFT analysis shows that additional transitions with significant coupling strengths occur below the measured ionization potential of 6.69 eV. In the ground state geometry, time-dependent DFT calculations at the B3LYP/DZ level find the lowest transition at 3.39 eV with an oscillator strength of $f_{osc} = 1.06$, as well as several transitions between 3.75 and 5 eV with a total oscillator strength of $f_{osc} = 0.65$, see [96] for details.

isomer, PES	geometry		reorganization energy	
	ground	excited		
cis, ground	0.	0.224	$\lambda^g =$	0.224
cis, excited	3.390	3.118	$\lambda^e =$	0.272
cis, transition	3.390	2.894	$\lambda^g + \lambda^e =$	0.496
trans, ground	0.	0.209	$\lambda^g =$	0.209
trans, excited	3.391	3.119	$\lambda^e =$	0.272
trans, transition	3.391	2.910	$\lambda^g + \lambda^e =$	0.481

Table 2.11: Energies (in eV) of the potential energy surfaces in the electronic ground state and the lowest excited state, for the relaxed geometries of the *cis* and *trans* isomers. The ground state energies have been obtained with DFT, and the excited state energies with TD-DFT, both at the B3LYP/DZ level. For each isomer, the reference energy relates to the geometry in the electronic ground state. On an absolute scale, the ground state energies of both isomers differ by less than 1 meV.

The Raman cross sections of high frequency modes are defined on a time scale faster than the twisting motion, so that they can be quantified from the modified excited geometry where the dihedral angles are frozen to their values in the electronic ground state. This projection scheme improves the agreement with the measured Raman spectra in the range 1002 - 1605 cm^{-1}, where the vibrations are dominated by elongation patterns in the plane of the various phenyl rings. The four strongest observed features at about 1600 cm^{-1}, 1296 cm^{-1}, 1186 cm^{-1} and 1002 cm^{-1} are reproduced quantitatively, with a reasonable relative size of the respective cross sections.

Calculated absorption and PL line shapes

According to the scheme introduced for the perylene compounds, the internal vibrations in the range 900 cm^{-1} to 1800 cm^{-1} were replaced by an effective mode at 1278 cm^{-1} (158 meV) with an effective Huang-Rhys factor of S=0.72. The Stokes shift consists of the sum of the reorganization energies on the potential energy surface of the electronic ground state and the excited state, $\lambda_S = \lambda^g + \lambda^e$. The total Stokes shift of 0.49 eV composed of $\lambda^g = 0.22$ eV and $\lambda^e = 0.27$ eV is in good agreement with the experimental value of 0.57 eV.
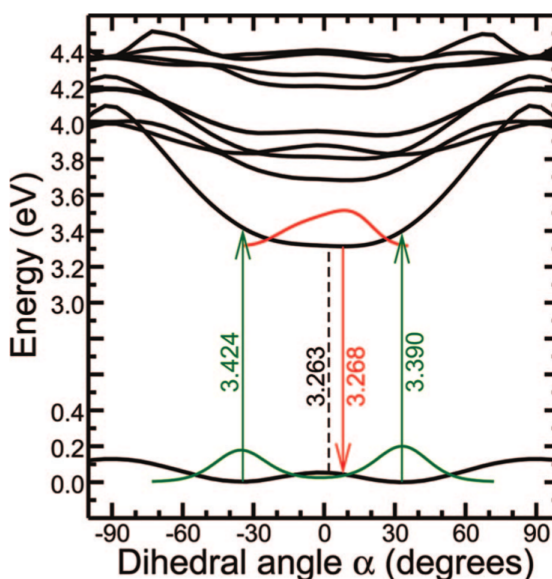
Figure 2.18: PES for rotation of the two halves of TPD around the dihedral angle α, for the electronic ground state and the lowest 10 excited states. The colored lines visualize Boltzmann distributions at $T = 300$ K around the minima of the lowest two PESs and the transition energies starting from the minima of the two PESs. The dashed vertical line indicates the lowest transition energy.

For low-frequency modes with $\hbar\omega_k \ll k_B T$, including especially those involving a twisting of the bond connecting the two rings of the central biphenyl group, we compare the elongation patterns and harmonic frequencies of the modes at the minimum of the potential energy surface (PES) of the excited state with the modes in the electronic ground state, compare Fig. 2.18. For these modes, we find substantial differences, reflecting directly the different shape of the two PES along selected twisting angles, especially around the bond connecting the central biphenyl group. Therefore, instead of using the Huang-Rhys factors of these modes, we model the absorption and PL line shapes starting from a Boltzmann distribution over the twisting angle α around the central bond. The shape of the two PES around this bond results directly in a large asymmetry between the density of states and broadenings involved in absorption and PL. This is also reflected in

different contributions to the respective reorganization energies λ^g and λ^e.

The model curves in Fig. 2.19 are obtained from a Poisson progression over an effective mode at $\hbar\omega_{\text{eff}} = \sum_k S_k \hbar\omega_k / \sum_k S_k = 1278 \text{ cm}^{-1}$ (158 meV) with $S_{\text{eff}} = \sum_k S_k = 0.87$, where the shape of each vibronic subband is defined by the convolution of the respective DOS with a Gaussian of FWHM= 0.15 eV, see [96] for more details.
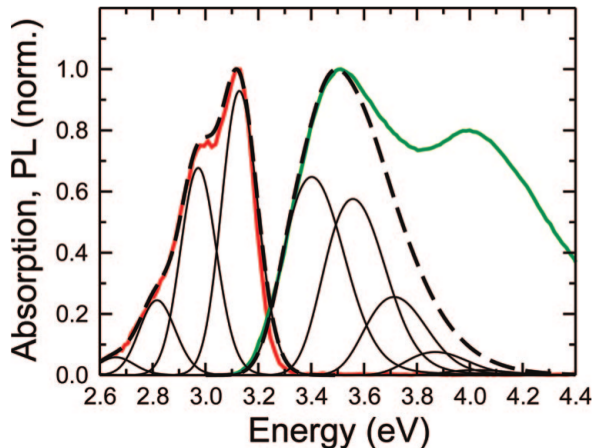
Figure 2.19: Comparison between the measured absorption and PL for TPD dissolved in toluene (green, absorption; red, PL) and the model calculation based on the dihedral angle α, a convolution with a Gaussian having a FWHM of 0.15 eV, a Poisson progression over an effective mode at 158 meV with a Huang-Rhys factor of 0.87, and a rigid shift of the absorption band by $+13$ meV and of the PL band by -162 meV (black, dashed line). In each case, the vibronic subbands resulting from a convolution of the DOS with the Gaussian are shown separately (black thin lines). Altogether, the center of mass of the absorption band is shifted by $+156$ meV against the TD-DFT reference and the PL band by $+81$ meV.

Conclusion

It was found that the twisted shape of the TPD central biphenyl group allows to understand the different linewidth observed in absorption and PL together with an asymmetry between the reorganization energies on the two potential energy surfaces involved. The torsional modes at low frequencies contribute substantially to the broadening of absorption and PL. As a matter of fact, the vibronic subbands of a high frequency effective mode defined as an average over the most strongly elongated high frequency modes can only be observed in PL, but in absorption, the subbands are washed out by the larger broadening arising from the flat ground state potential along the twisting angle around the central bond.

Our detailed model calculations have demonstrated that the photophysics of TPD can be understood from the properties of the molecule itself. The influence of intermolecular

interactions is restricted to a small dependence of the Stokes shift on the solvent or matrix material, but the contribution of the surroundings to the broadening remains much smaller than the influence of the torsional modes of TPD at very low frequency.

2.5.2 Rubrene

In order to investigate the optical properties of rubrene we study the vibronic progression of the first absorption band (lowest $\pi \rightarrow \pi^*$ transition). The *ab initio* calculations are compared with experimental findings concerning absorption in solution and the dielectric functions ε_2, see [101] for more details.

Rubrene mainly forms two isomers, one with a planar backbone and one with a twisted backbone, see Fig. 2.20. Even though the twisted isomer is more stable both as a free molecule and in solution, in the crystalline phase the planar isomer can be stabilized by a beneficial geometric arrangement between neighboring molecules, resulting in a large cohesive energy so that the energetic cost of the planarization is overcompensated by attractive inter-molecular interactions. In the twisted isomer the repulsion between the phenyl sidegroups achieves a rather large distance between them as opposed to the planar isomer, where a relatively small distance between the phenyl groups is enforced by the rigidity of the bond connecting each sidegroup to the tetracene core and by the more restrictive point group C_{2h}. Therefore, the twisted isomer gains a substantial amount of energy through a reduction of these repulsive interactions, allowing eventually to invest a part of this energy into the unfavorable twist of the tetracene backbone. The resulting angle between the two central rings of the tetracene core is 22.8° in the electronic ground state, and the angle between the two final rings 42.0°, compare Fig. 2.20b. In the relaxed excited state these angles increase to 26.7° and 43.6°, respectively.
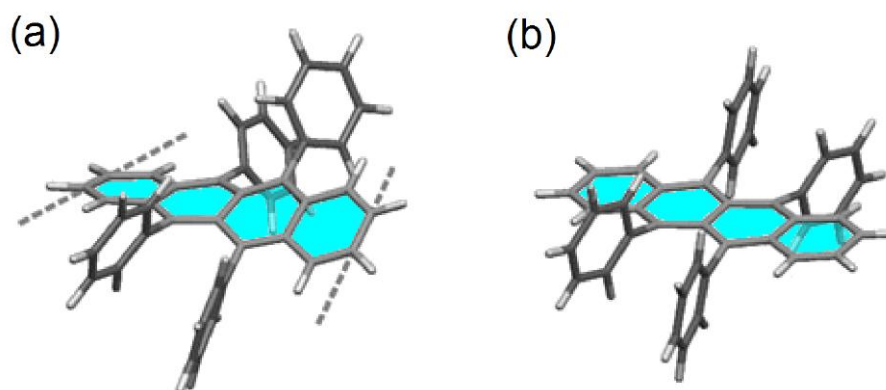
Figure 2.20: (a) Geometry of the most stable rubrene isomer with a twisted tetracene backbone, and (b) planar rubrene isomer, which resembles the geometry in the crystalline phase.

We compare calculations of rubrene in two different conformations, *i.e.* with a twisted or planar tetracene backbone. For both isomers the calculated vibronic progressions de-

	E_{0-0}	E_v	S_{exp}	S_{calc}
Solution	2.359	0.165	0.986	0.985
Thin Film	2.335	0.169	0.974	1.025

Table 2.12: Fit of measured spectra in the region of the first absorption band to the model of the displaced harmonic oscillator, for rubrene in solution and amorphous thin films: Transition energy between the vibrational ground states E_{0-0} (eV), effective vibrational energy $\hbar\omega$ (eV), and effective Huang-Rhys factor S, see [101] for more details.

scribe the observed spectra very well. However, the different calculated transition energies found for the two conformations indicate that the spectrum of amorphous rubrene films is dominated by the twisted isomer. The calculations result in Huang-Rhys factors of ($S_{\text{twist}} = 0.985$, $S_{\text{plan}} = 1.025$) which are in excellent agreement with the experimental results, showing only very small differences between the twisted and the planar isomer. However, the almost coinciding Huang-Rhys factor for the twisted isomer with the observed value should be interpreted cautiously. This agreement is better than for previous applications of the same functional and basis set to the relaxed excited geometry of other polyaromatic molecules. Therefore, a distinction between both isomers on the basis of the Huang-Rhys factors is not possible. However, the same calculations show that the transition energies of the twisted and planar monomer differ significantly with $\Delta E_{\text{abs}} = 0.106$ eV and $\Delta E_{0-0} = 0.120$ eV, respectively. As the observed spectra shows sign of two superimposed Poisson progressions with an energy offset in this range, it can be concluded that one of the isomer dominates in the amorphous films. Due to the much higher stability, this isomer can only correspond to the twisted configuration.

Summary

We have investigated the optical properties of rubrene by examining the vibronic progression of the first absorption band, the lowest $\pi \rightarrow \pi^*$ transition. The analysis of the dielectric function ϵ_2 in solution and thin films was performed using the displaced harmonic oscillator model, from this we could derive the relevant parameters of the vibronic progression. Comparison between experimental data and DFT calculations was done with two different conformations, one with twisted and one with planar tetracene backbone. The calculated values describes the observed spectra very well. The different transition energies found for the two conformations give an indication that the spectrum of amorphous rubrene films is dominated by the twisted isomer.

Chapter 3

Crystal structure of perylene compounds

This chapter concerns the crystalline phase, focusing on the variables that are connected to the exciton model described in Chap. 4, such as transfer integrals and dipole moments. As in Chap. 5 this model will only be applied to perylene-based compounds, other types of molecules discussed in Chap. 2 will not be considered any further.

3.1 Crystal geometry and dielectric response

3.1.1 Transition dipoles of monomers

For molecules with a perylene backbone, in general, the transition dipole of the HOMO to LUMO transition is aligned along the long axis of the molecule. Due to the herringbone structure there are two directions of the molecular transition dipole moment in the crystal, $\boldsymbol{\mu}_A$ and $\boldsymbol{\mu}_B$, one for each basis molecule. In the space group $P2_1/c$, the $\mathbf{b}$ lattice vector defines a C_2 axis followed by a shift of $(\mathbf{b} + \mathbf{c})/2$, with the important consequence that all second order tensors decouple into a 1×1 block for the $\mathbf{b}$ direction, and a 2×2 block governing the plane spanned by the lattice vectors $\mathbf{a}$ and $\mathbf{c}$. In the following, we shall use the convention that the transition dipoles $\boldsymbol{\mu}_A$ and $\boldsymbol{\mu}_B$ of the two basis molecules form an angle δ below 90° with the $\mathbf{b}$ lattice vector, so that their sum $(\boldsymbol{\mu}_A + \boldsymbol{\mu}_B)/\sqrt{2}$ is oriented along $\mathbf{b}$, whereas the difference $(\boldsymbol{\mu}_A - \boldsymbol{\mu}_B)/\sqrt{2}$ is located in the ac-plane, compare fig. 3.1. Discarding the small contributions of intermolecular transition dipoles towards CT states, the ϵ_{yy} is defined by the dielectric tensor along the $\mathbf{b} = (\mu_A + \mu_B)/\sqrt{2}$ direction and ϵ_{xx} along the direction defined by $(\mu_A - \mu_B)/\sqrt{2}$. The angle δ (see Fig. 3.1) can be used to describe the relation between the molecular long axis and the $\mathbf{b}$ lattice vector in the form of $\cos^2 \delta$ and $\sin^2 \delta$, see Table 3.1.
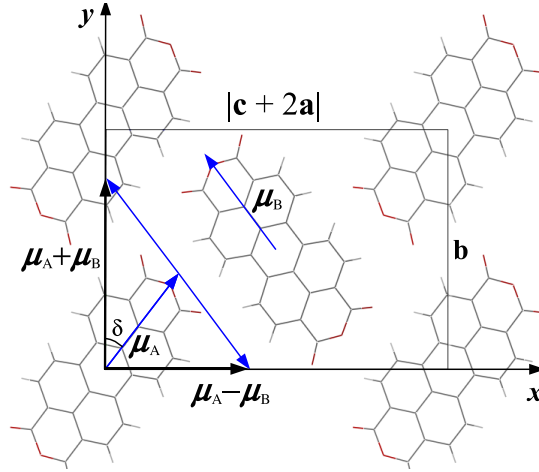
Figure 3.1: Relation between the orientation of the molecules in the unit cell and the xy-plane, defined by the transition dipole $\boldsymbol{\mu}_A$ and $\boldsymbol{\mu}_B$ of the two basis molecules.

compound	δ	ϵ_{yy}	ϵ_{xx}
	(°)	$\cos^2 \delta$	$\sin^2 \delta$
α-PTCDA [102]	41.0	0.57	0.43
DDTP [103]	29.6	0.76	0.24
Me-PTCDI [3]	18.4	0.90	0.10
PB31 [104]	53.1	0.36	0.64
PTCDI [105]	81.5	0.02	0.98
PR149 [106]	83.7	0.01	0.99
DIP [107]	89.3	$1.5 \cdot 10^{-4}$	1.00

Table 3.1: Angle δ between the molecular HOMO-LUMO transition dipole and the lattice vector $\mathbf{b}$, and relative contributions of this transition to the strength of the dielectric response ϵ_{yy} along $y \parallel \mathbf{b}$ and to the component ϵ_{xx} obtained with $x \parallel (\mu_A - \mu_B)/\sqrt{2}$.

3.2 Crystal unit cell

The crystal geometry of perylene compounds is governed by external forces between the stacked molecules, *i.e.* the van der Waals attraction which strives to place the perylene center on top of each other and the Coulomb interaction between charged parts of the molecules. The competition between Coulomb interaction, van der Waals attraction and steric repulsion involving the side wings will displace the positions of the molecules in adjacent layers, so that their centers will not be aligned along the normal of the molecule. Thus, the side wing groups will play a large role in the mutual orientation of the molecules, so that each perylene compound has a specific stacking geometry. There are great diversities in packing for different compounds in their solid state. As an example, for PTCDA and Me-PTCDI which have relatively small side groups, the Coulomb attraction

between differently charged carbon and oxygen atoms is dominant, so that deviations between stacking direction and molecule normal remain small. On the other hand, for the molecules with larger side wings, such as PR149 and PB31, the side groups will contribute largely to displacing the molecules to a position with smaller geometric overlap between the perylene cores.
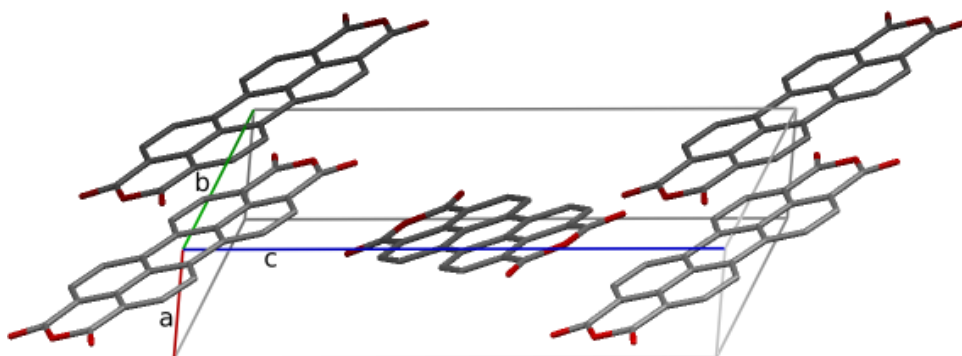
Figure 3.2: 3D view of the unit cell of PTCDA with the lower part invisible for easier view.

parameter	α-PTCDA	DDTP	Me-PTCDI	PB31
Molecular formula	$C_{24}H_8O_6$	$C_{34}O_2N_2H_{18}$	$C_{26}H_{14}N_2O_4$	$C_{40}H_{26}N_2O_4$
Space group	$P2_1/c$	$P2_1/n$	$P2_1/c$	$P2_1/c$
Point group	D_{2h}	-	C_{2h}	C_{2h}
a (Å)	**3.72**	10.56	**3.784**	**4.737**
b (Å)	11.96	**3.78**	15.580	32.45
c (Å)	17.34	26.52	14.597	9.51
β (°)	98.8	95.2	97.65	100.27
Z	2	2	2	2
Volume (Å^3)	762.4	1056.7	873.19	1438.0

Table 3.2: Crystal unit cell data of perylene pigments, ordered according to length of stacking vector: α-PTCDA [102], DDTP [103], Me-PTCDI [3] and PB31 [104]. In the monoclinic space group $P2_1/c$, the lattice vector **b** is orthogonal to the other two, **a** $\perp$ **b** $\perp$ **c**, and β is the angle between the lattice vectors **a** and **c**. Z is the number of molecules per unit cell. The stacking vector is highlighted.

A molecular crystal defines a periodic arrangement, so that all molecules far from the surface experience the same surroundings. Therefore, each unit cell contains the same information as the bulk crystal. Depending on the stacking and the orientation of molecules in the lattice, different numbers of molecules reside in the unit cell. In the case of PTCDA and Me-PTCDI, and many other aromatic molecules, the structure resembles

parameter	PTCDI	PR149	DIP
molecular formula	$C_{24}H_{10}N_2O_4$	$C_{40}H_{36}N_2O_4$	$C_{16}H_8$
Space group	$P2_1/n$	$P2_1/c$	$P2_1/a$
Point group	D_{2h}	C_{2h}	D_{2h}
a (Å)	**4.865**	17.03	**7.171**
b (Å)	14.660	**4.869**	8.550
c (Å)	10.844	17.096	16.798
β (°)	91.33	93.40	92.42
Z	2	2	2
Volume (Å^3)	773.20	1413.0	1029.0

Table 3.3: Crystal unit cell data for PTCDI [105], PR149 [106] and DIP [107]. See caption of Table 3.2 for details.

the body-centered lattice with two molecules per unit cell. However, unlike in an atomic crystal, the molecules are not connected via strong covalent or ionic bonds, but mainly by weak van der Waals forces.

A common feature for all the molecules in the present report is that they have a monoclinic crystal system with $\alpha = \gamma = 90°$, so that the volume of the crystal unit cell is given by

$$V = abc \cdot \sin \beta, \tag{3.1}$$

where a, b, and c are the length of the lattice vectors and α, β, and γ are the angles between them, compare Fig. 3.2, where β is the angle (a $\bigwedge$ c). The volume of the crystal governs the density of the dipole moments, defining in turn the strength of the optical response. The unit cells parameters can be found in tables 3.2 and 3.3.

Some compounds may grow in different phases depending under which conditions they crystallize. In these cases, the best characterized phase was chosen. For PTCDA, the α phase was chosen since there exist several independent X-ray characterizations implying that this phase is the most abundant in polycrystalline films obtained from organic molecular beam deposition (OMDB) at room temperature [102, 108]. PB31 and DIP have a second crystalline phase with a space group including four basis molecules [8, 104, 107]. In order to test the transferability of the exciton model discussed below, these cases will not be analyzed further, concentrating instead on the herringbone structure with two molecules per unit cell. It is defined by a unit cell containing of two identical molecules, A and B, differing by their orientation, compare Figs. 3.3 to 3.9.
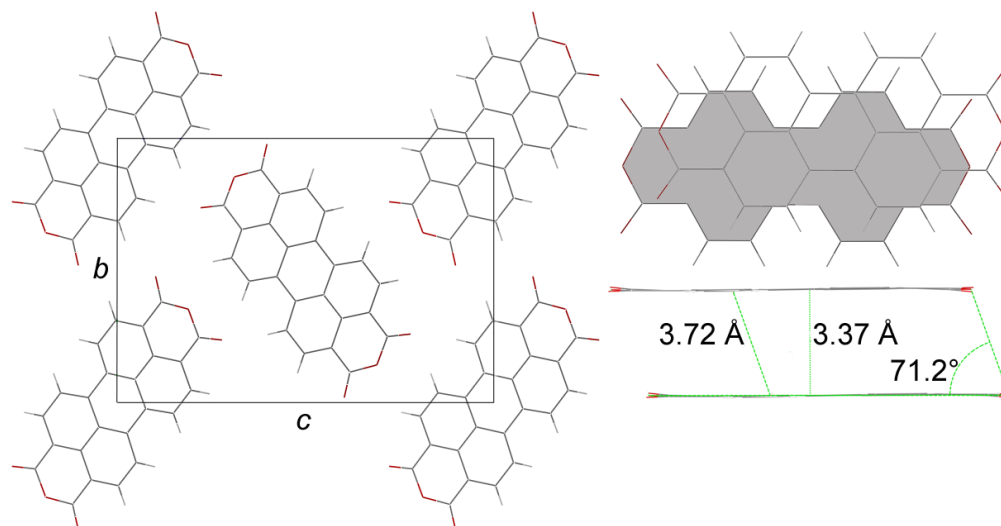
Figure 3.3: Unit cell for the crystalline phase of α-PTCDA, with parameters according to Table 3.2. Left: view along stacking vector **a**, right: view of stacked dimer along molecule normal (top) and along short axis of molecule (bottom).
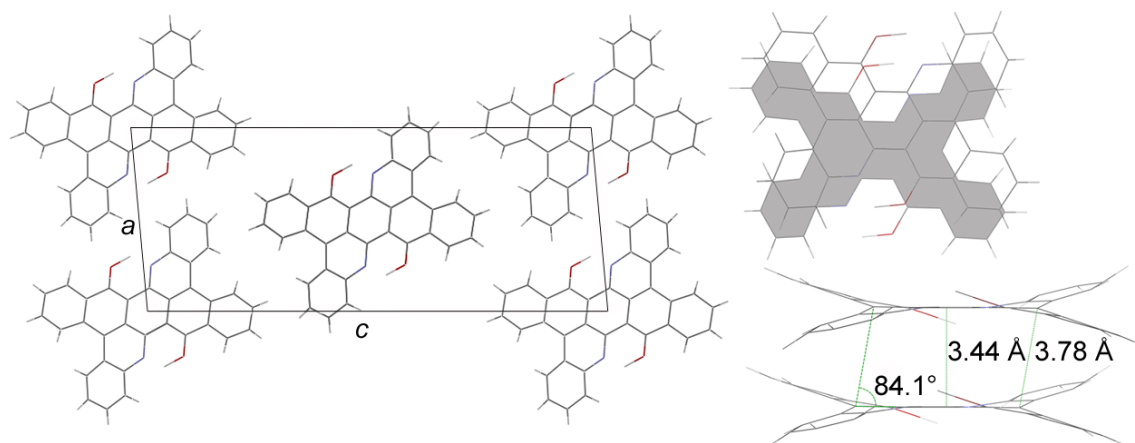
Figure 3.4: Unit cell for the crystalline phase of DDTP, with parameters according to Table 3.2 with projection as in Fig. 3.3.
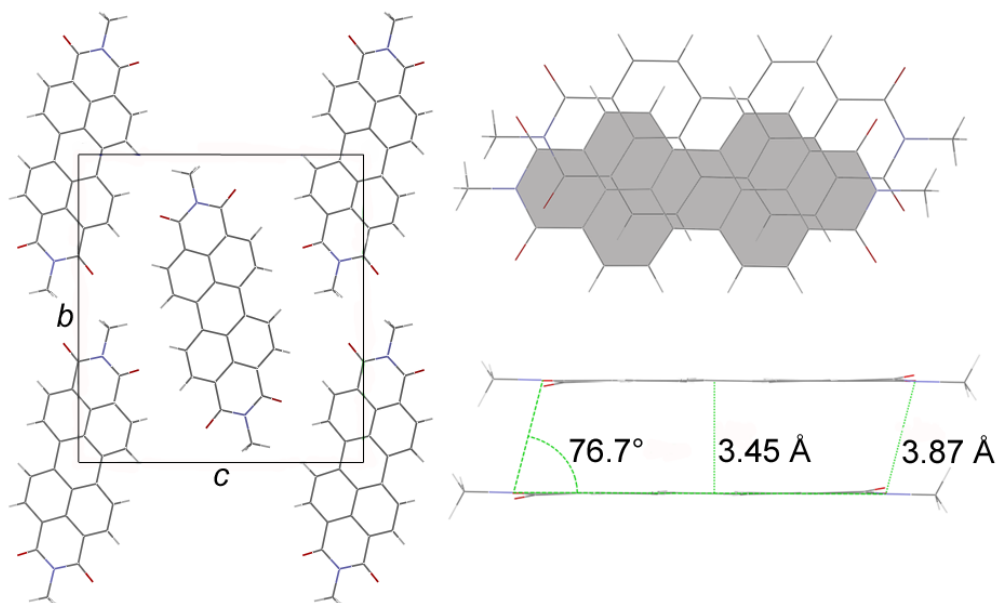
Figure 3.5: Unit cell for the crystalline phase of Me-PTCDI, with parameters according to Table 3.2 with projection as in Fig. 3.3.
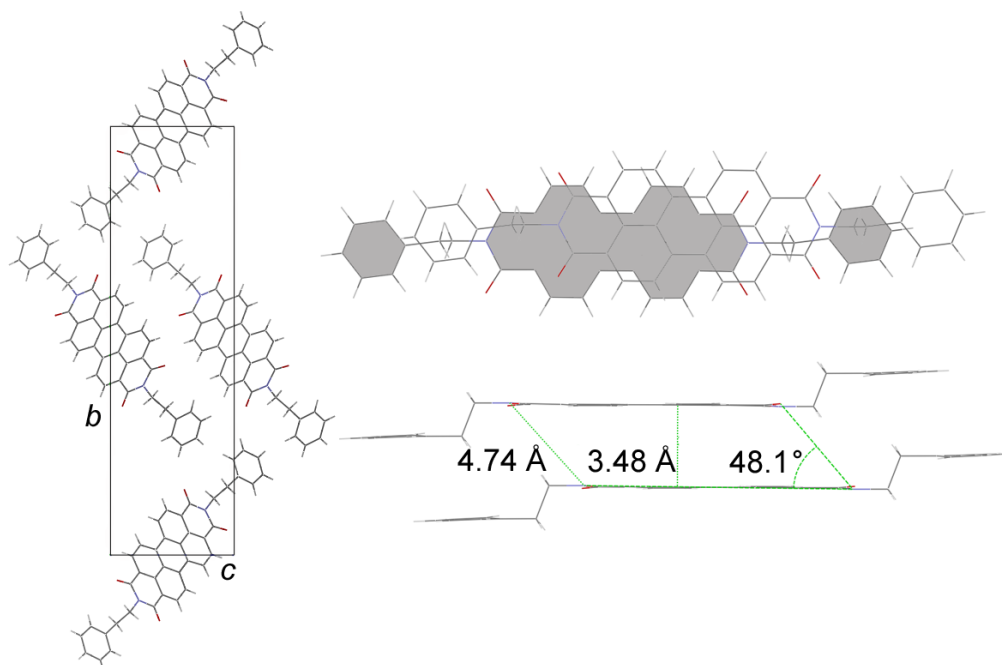
Figure 3.6: Unit cell for the crystalline phase of PB31, with parameters according to Table 3.2 with projection as in Fig. 3.3.
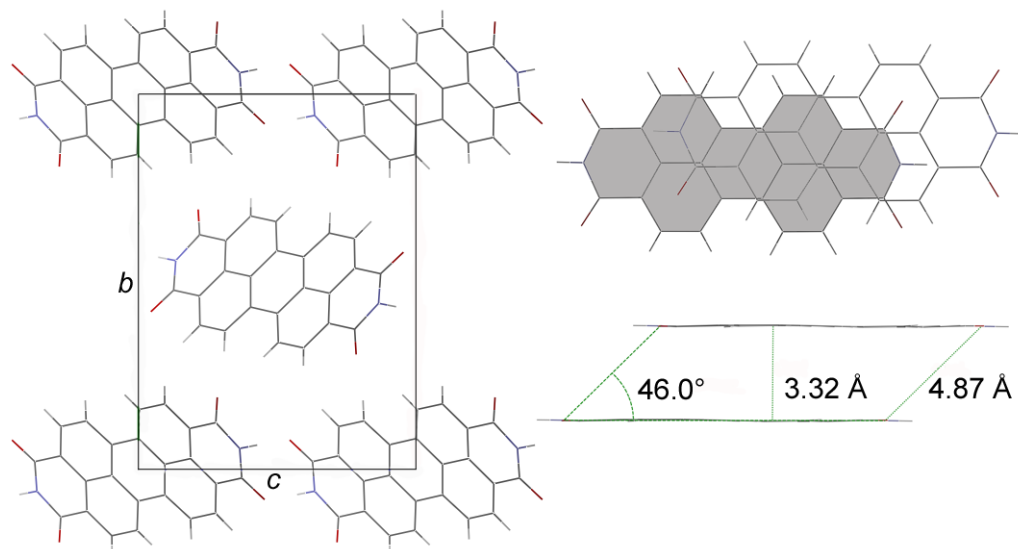
Figure 3.7: Unit cell for the crystalline phase of PTCDI, with parameters according to Table 3.3 with projection as in Fig. 3.3.
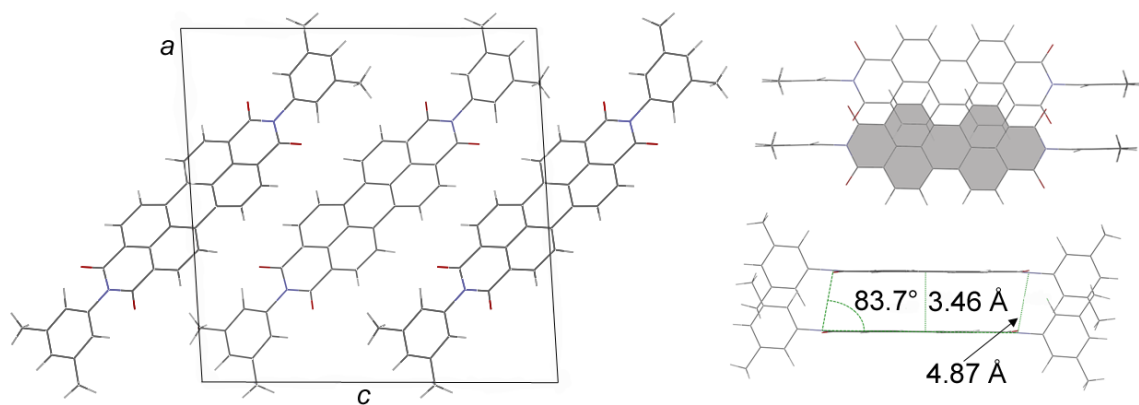
Figure 3.8: Unit cell for the crystalline phase of PR149, with parameters according to Table 3.3 with projection as in Fig. 3.3.
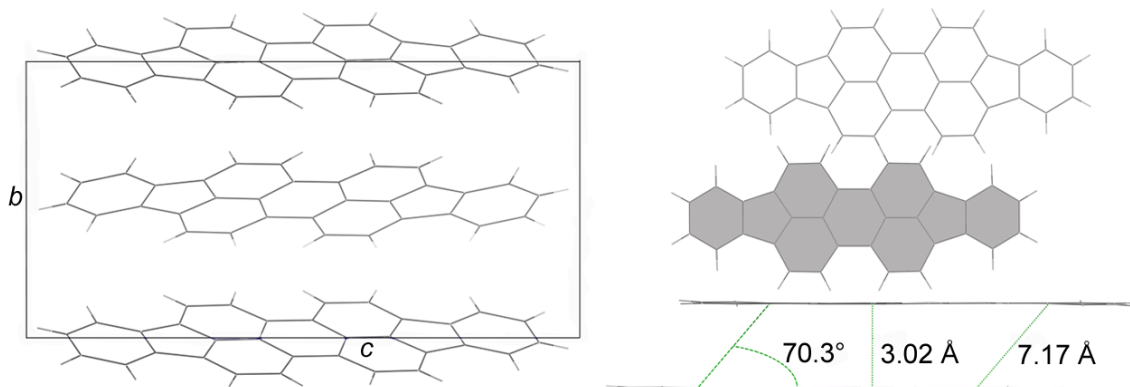
Figure 3.9: Unit cell for the crystalline phase of DIP, with parameters according to Table 3.3 with projection as in Fig. 3.3.

In all crystals except for DIP, the intermolecular distance measured along the normal for the molecular plane resembles graphite (3.35 Å) and shows little dependence on the size of the sidewings, see Table 3.4. This is due to the fact that the distance between the planes is mainly governed by van der Waals interaction between the aromatic cores of the perylenes. In the case of DIP, the perylene cores hardly overlap at all, resulting in the distance approaching the sum of van der Waals radiis of carbon and hydrogen. Generally the stacking vector is much larger than the distance along the normal of the molecular planes, resulting in substantial projections onto the long axis and the short axis of the molecules, compare Table 3.4.

compound	stack Å	long Å	short Å	normal Å	φ (°)
PTCDA	3.703	1.19	1.04	3.35	82.1
DDTP	3.775	0.45	1.49	3.44	-
Me-PTCDI	3.874	0.89	1.52	3.45	36.8
PB31	4.737	3.16	0.74	3.45	73.7
PTCDI	4.865	3.38	1.10	3.32	17.1
PR149	4.869	0.54	3.38	3.46	12.7
DIP	7.171	2.42	6.03	3.02	3.1

Table 3.4: Geometric arrangement of stacked chromophores with respect to each other: The second column contains the stacking vectors, the third and fourth the sliding along long or short axis and the fifth the distance along the molecular normal. φ is the angle between the long axes of the 2 basis molecules, coinciding with the direction of the HOMO-LUMO transition dipoles. Compare Figs. 3.3 to 3.9 for a visualization of the crystal structures realized for these perylene compounds.

3.3   Electronic interaction between stacked molecules

In a crystal, the interaction between molecules is rather small, the largest occurring between neighbors along the stacking direction. As the distances between the molecular planes along the stacking direction are relatively short compared to the in-plane distance between adjacent sites, these types of crystals can be classified as quasi 1D crystals. Combined with the fact that the π-orbitals overlap along the molecular normal, electronic interactions along the stack are expected to be stronger than between other neighboring sites. By using these facts, a convenient way to simplify calculations when investigating transfers is to introduce a supermolecule approach, where the supermolecule will only represent the interaction of one molecule and one of its closest neighbors in the stacking direction, compare Fig. 3.10.
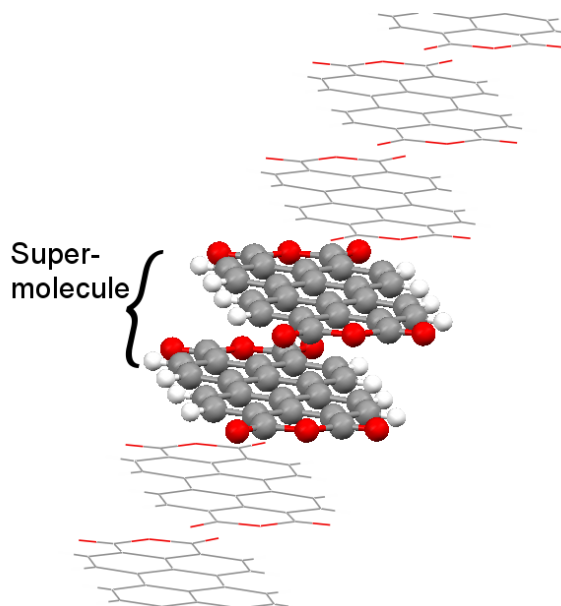
Figure 3.10: Stack alignment in α-PTCDA and visualization of a supermolecule which consisting of the two molecules drawn with balls and sticks.

3.3.1   Fermionic transfer integrals

The values for the transfer parameters can be deduced from a DFT or HF calculation for a supermolecule. The pairs of frontier orbitals are governed by Hamiltonians

$$H_{LUMO} = \begin{pmatrix} E_L & t_L \\ t_L & E_L \end{pmatrix}, \tag{3.2}$$

$$H_{HOMO} = \begin{pmatrix} E_H & t_H \\ t_H & E_H \end{pmatrix}, \tag{3.3}$$

where eigenstates are defined by symmetric or anti-symmetric superpositions of the molecular orbitals,

$$\psi_{LUMO}^{\pm} = \frac{1}{\sqrt{2}} \begin{pmatrix} 1 \\ \pm 1 \end{pmatrix} \tag{3.4}$$

$$\psi_{HOMO}^{\pm} = \frac{1}{\sqrt{2}} \begin{pmatrix} 1 \\ \pm 1 \end{pmatrix} \tag{3.5}$$

with eigenvalues of $E_{LUMO}^{\pm} = E_L \pm t_L$ and $E_{HOMO}^{\pm} = E_H \pm t_H$. In Fig. 3.11 and 3.12, the frontier orbitals are shown for PTCDA and Me-PTCDI. By analyzing the signs of the wave functions it is possible to get information about the signs of the transfer parameters $t_L = t_e$ and $t_H = -t_h$. Using Me-PTCDI as an example, from Fig. 3.12, it is clear the the LUMO is the state ψ_{LUMO}^{+} with the eigenvalue $E_{LUMO}^{+} = E_L + t_L$. We know that E_{LUMO}^{+} is the lower eigenvalue, thus t_L has to be negative in order to achieve that. Furthermore the HOMO in Fig. 3.12 is the state ψ_{HOMO}^{+} with eigenvalue $E_{HOMO}^{+} = E_H + t_H$, requiring a positive t_H.
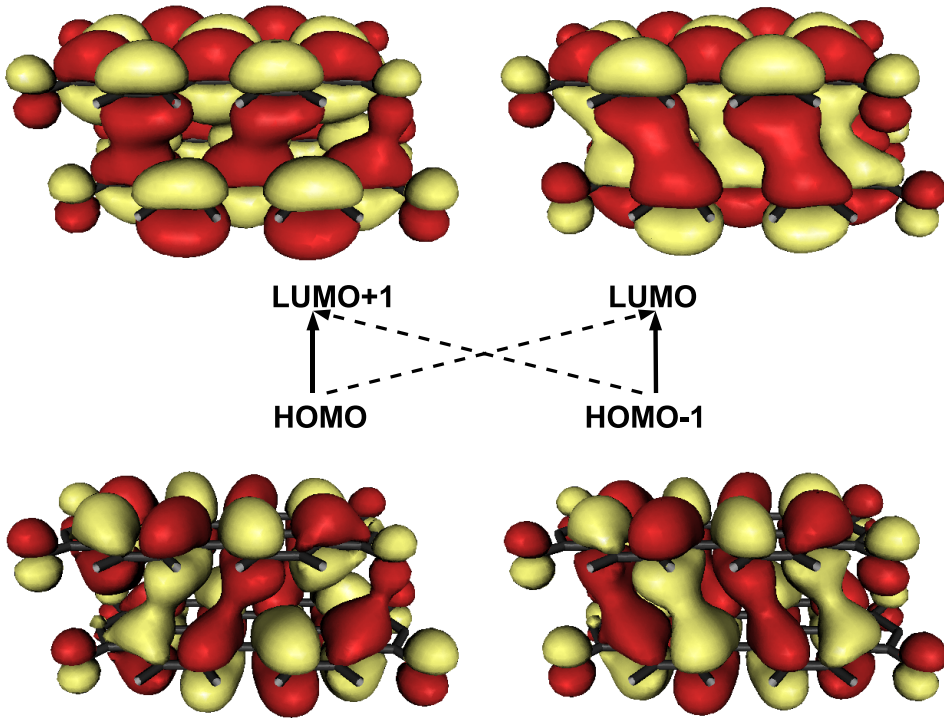
Figure 3.11: Visualization of LUMO+1, LUMO, HOMO and HOMO-1 orbitals of PTCDA, where the different colors of the orbitals represent different signs of the electronic wave functions. The solid black arrows represent allowed transitions between the orbitals, and the dotted arrows represent forbidden transitions. The calculations were performed at the B3LYP/TZ level.

Each stacked pair is governed by the point group C_i since it has a center of inversion. Therefore, the four Kohn-Sham orbitals closest to the gap form the following dimer or-
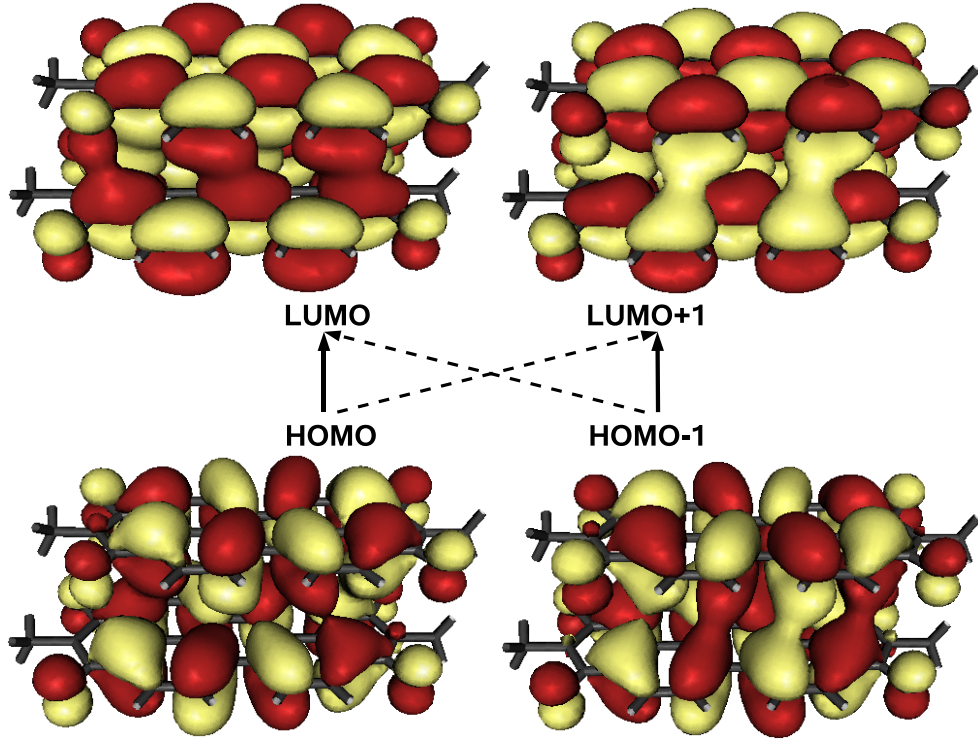
Figure 3.12: As Fig. 3.11, but for Me-PTCDI.

bitals: H_g, H_u, L_g and L_u. The B3LYP values for this subset of orbitals can be found in Table 3.5. With these orbitals we can construct excited configurations with well defined parity, either dipole-allowed or dipole-forbidden, see Figs. 3.11 3.12 and 3.17.

$$|H_u \rightarrow L_g\rangle, \qquad |H_g \rightarrow L_u\rangle: \qquad (A_u) \tag{3.6}$$

$$|H_u \rightarrow L_u\rangle, \qquad |H_g \rightarrow L_g\rangle: \qquad (A_g) \tag{3.7}$$

where only the A_u-symmetric transitions are allowed, whereas A_g transitions are forbidden. From the numerical eigenvalues the relation between energetic splitting and transfer integrals can be obtained from the difference of the Kohn-Sham orbital energies as

$$t_L = t_e = \frac{1}{2}\Big(E(L_g) - E(L_u)\Big) \tag{3.8}$$

$$t_H = -t_h = \frac{1}{2}\Big(E(H_u) - E(H_g)\Big) \tag{3.9}$$

As these stack calculations are performed for the entire chromophores including their side groups, they are more accurate than estimates based on Figs. 3.14 and 3.14. Nevertheless, for all perylene pigments investigated, the signs of $t_L = t_e$ and $t_H = -t_e$ coincide with these figures. Table 3.6 compares the results derived from HF and B3LYP calculations with different variational basis sets, DZ and TZ [40, 41]. The signs are independent

compound	H_g	H_u	L_u	L_g
PTCDA	-7.107	-7.039	-4.468	-4.421
DDTP	-5.321	-5.105	-2.382	-2.327
Me-PTCDI	-6.386	-6.305	-3.640	-3.847
PB31	-6.137	-6.424	-3.849	-3.682
PTCDI	-6.376	-6.578	-3.884	-3.847
PR149	-6.132	-6.299	-3.655	-3.616
DIP	-5.374	-5.242	-2.715	-2.781

Table 3.5: Kohn-Sham orbital energy levels obtained with DFT calculations at the B3LYP/TZ level.

compound		HF/DZ	HF/TZ	B3LYP/DZ	B3LYP/TZ
PTCDA	t_h	-0.052	-0.054	-0.031	-0.034
	t_e	0.021	0.037	0.014	0.024
DDTP	t_h		0.044		0.028
	t_e		-0.172		-0.108
Me-PTCDI	t_h	-0.071	-0.073	-0.038	-0.041
	t_e	-0.160	-0.148	-0.111	-0.104
PB31	t_h	0.216	0.218	0.140	0.144
	t_e	0.117	0.128	0.078	0.083
PTCDI	t_h	0.150	0.151	0.098	0.102
	t_e	0.018	0.024	0.017	0.019
PR149	t_h	0.136	0.137	0.090	0.083
	t_e	0.035	0.030	0.022	0.020
DIP	t_h	-0.097	-0.099	-0.065	-0.066
	t_e	-0.042	-0.041	-0.034	-0.033

Table 3.6: Comparison of calculated transfer parameters t_h and t_e dispersion with different functionals (HF and B3-LYP) and basis sets (DZ and TZ).

of the computational method and basis set but the size of the transfer parameters varies considerably. Transfer parameters deduced from B3LYP/TZ are systematically smaller than the respective HF values. This indicates that the short range correlation included in the B3LYP functional produces more localized orbitals resulting in a reduction of the intermolecular transfer integrals. Furthermore DFT-based methods are less sensitive to the size of the variational basis, so that he energies obtained in a finite basis are better converged than the HF values.

Experimental results for the transfer parameters can be found for PTCDA [111] and Me-PTCDI [112] where the width of the valence bands has been measured. This band width corresponds to $4t_h$. Together with the shape of the valence band, the observations reveal also the sign of the transfer parameter, resulting in values of $t_h = -0.05$ eV for PTCDA and $t_h = -0.04$ eV for Me-PTCDI. Unfortunately the experimental values give

little indication which of the computational approaches produces the best results: for PTCDA, Hartree-Fock comes closer to the measured value, while calculations on Me-PTCDI suggest that it is B3LYP.

The visualization of the stacking geometries in the various pigments indicates that the center of a molecule avoids a position above the center of a hexagon in the underlying molecule, a situation resembling graphite. In the following we will examine how the transfer parameters are governed by the stacking parameters of adjacent unit cell. Since the geometric overlap between the molecules influences on the interaction between the orbitals, there are also changes in the size and sign of the transfer parameters t_e and t_h as a function of the sliding of adjacent molecules along their long and short axes. Earlier work investigating sliding exclusively along the short or long axis showed a relationship between stack geometry and size and sign of the transfer parameters. These were then used to determine the width of the conduction and valence bands in simplified model geometries [145].
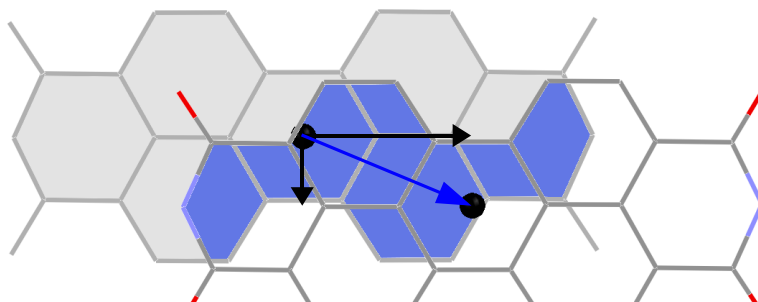
Figure 3.13: Two PTCDI molecules where the darker area shows the geometric overlap between the aromatic rings of the two molecules, the black dots display their centers and the arrows indicate the direction to which one molecule was moved. In the calculations, the starting point is were the black dots overlap completely.

To study the sign and size of the transfer parameters, it is convenient to introduce a scheme where each geometric arrangement, within a certain span, can be studied. In all cases, the displacement between layers is a combination of both orthonormal directions in the molecular plane. Therefore, calculations in two dimensions are needed to pinpoint where exactly the transfer parameters change sign. In the following, this question is investigated for model geometries consisting of two planar D_{2h}-symmetric PTCDI. The individual geometries were optimized at the B3LYP/DZ level and the molecules were placed above each other with a distance of 3.4 Å in the direction along the molecular normal. From that starting position the molecules were moved, at a constant normal distance from each other, along different directions, see Fig. 3.13 for a schematic description of the sliding. The positions of the sign changes are plotted in Fig. 3.14.

By studying the frontier orbitals of PTCDI (see Fig. 3.15) it is possible to interpret the results. For the LUMO orbitals, which govern the sign and size of the electron transfer

t_e, the node planes along the long axis imply sign changes at shifts of about 1 Å and 3 Å along the short axis, but no sign change occurs for sliding along the long axis. The HOMO node plane along the long axis generates sign changes at shifts of about 1.6 Å and 3.9 Å along the long axis, whereas, along the short axis, a sign change occurs around 2 Å of displacement. We find that sign changes occur in an approximately periodic pattern starting from the point with maximal overlap. We find that in all pigments, the signs of the transfer parameters in Fig. 3.14 are well defined because the stacking geometries are never close to $t_h = 0$ or $t_e = 0$. A more precise method of calculating the transfer parameters for each compound has been discussed above.
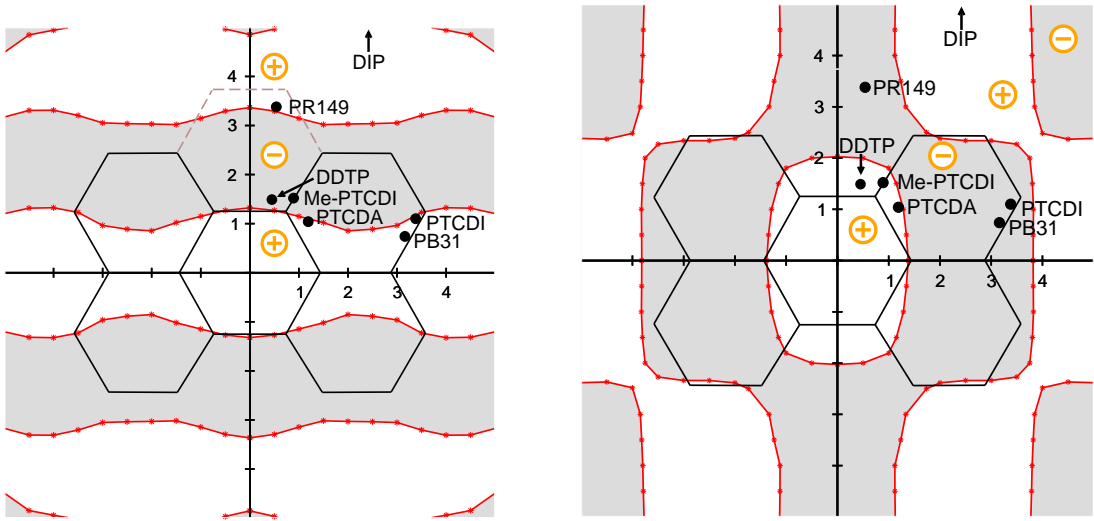
Figure 3.14: Left: Calculated signs of the transfer parameter $t_L = t_e$ for two stacked PTCDI molecules at a distance of 3.4 Å along their normal: Regions of positive transfer parameter (white), negative transfer parameter (gray), and contour lines of the sign changes (red). The dots represent the geometric offset with respect to the next molecule in the stack for α-PTCDA, DDTP, Me-PTCDI, PB31, PTCDI, and PR149, as annotated. The DIP location is indicated by an arrow since the lateral offset is outside the range of the figure. Right: the same but for the transfer $t_H = -t_h$ between the HOMO states of two stacked PTCDI molecules.

3.3.2 Electronic band structure

The electronic band structure arising from transfer along the stacking direction has the following dispersion:

$$E_{\text{HOMO}}(\mathbf{k}) = E_{\text{H}} + 2t_{\text{H}} \cos \mathbf{k} \cdot \mathbf{a}, \tag{3.10}$$

$$E_{\text{LUMO}}(\mathbf{k}) = E_{\text{L}} + 2t_{\text{L}} \cos \mathbf{k} \cdot \mathbf{a}, \tag{3.11}$$

$$E_{\text{gap}}(\mathbf{k}) = E_{\text{L}} - E_{\text{H}} + 2(t_{\text{L}} - t_{\text{H}}) \cos \mathbf{k} \cdot \mathbf{a}. \tag{3.12}$$
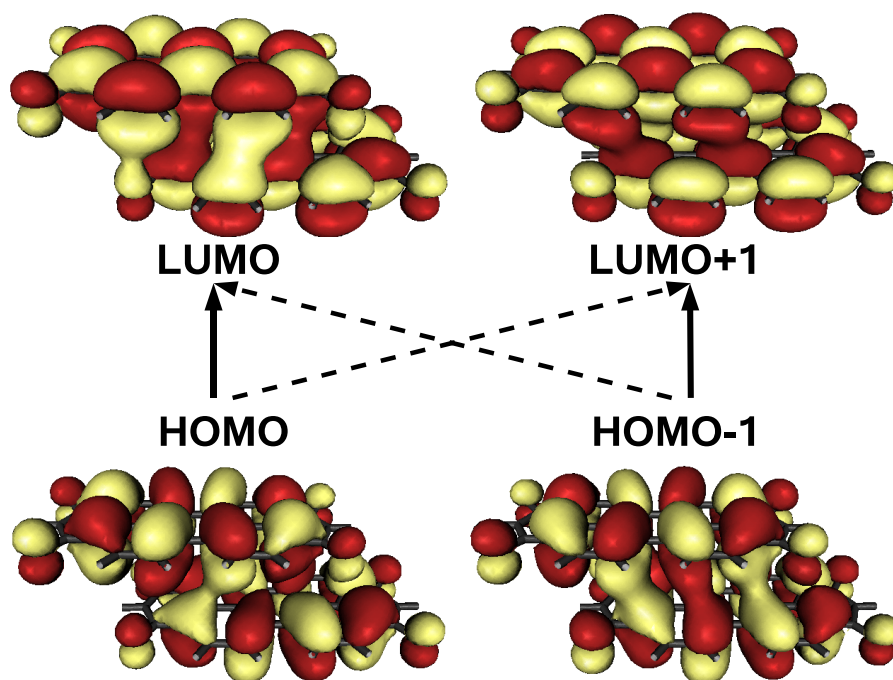
Figure 3.15: As Fig. 3.11, but for PTCDI
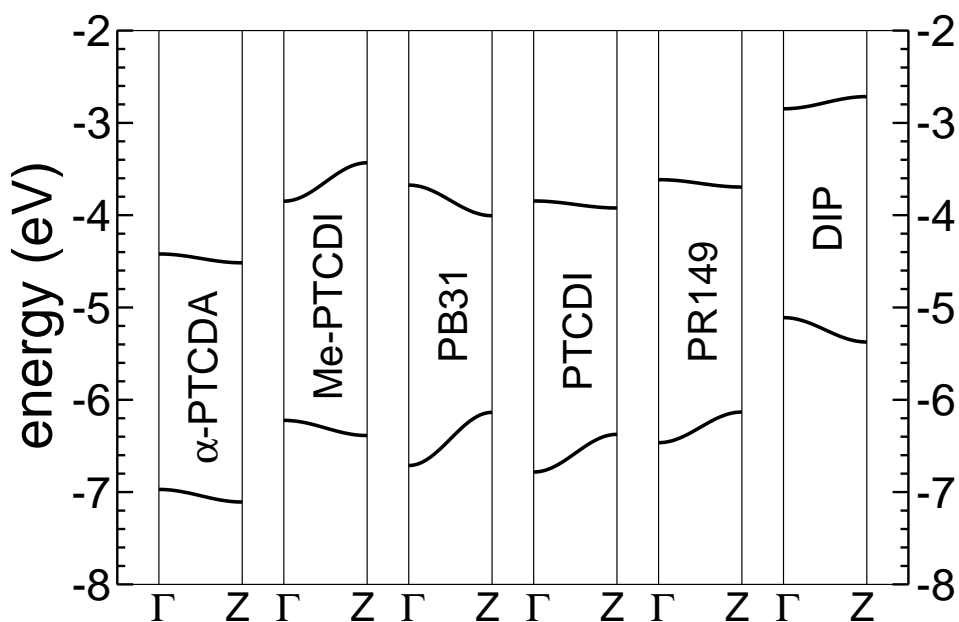
Figure 3.16: Electronic band structure of the model compounds based on B3LYP/TZ calculations for a stacked dimer in a geometry compatible with the respective crystalline phase.

For the model compounds, Fig. 3.16 visualizes the resulting valence band $E_{\mathrm{HOMO}}(\mathbf{k})$ and the conduction band $E_{\mathrm{LUMO}}(\mathbf{k})$ over the first Brillouin zone. The energies E_{H} and E_{L} are defined as the average energies of the pairs of frontier orbitals in a stack with a geometry compatible to the crystalline phase and the transfer parameters correspond to half of their splitting calculated with B3LYP/TZ; compare Table 3.6. PTCDA is the only material where the two transfer parameters t_{H} and t_{L} have the same sign, so that the gap between valence and conduction band has a particularly small dispersion.

In a single particle picture, optical excitations correspond to vertical transition between valence and conduction band with the following first and second moments:

$$\langle E_{\mathrm{gap}} \rangle = E_{\mathrm{L}} - E_{\mathrm{H}}, \tag{3.13}$$

$$\langle (\Delta E_{\mathrm{gap}})^2 \rangle = 2(t_{\mathrm{L}} - t_{\mathrm{H}})^2. \tag{3.14}$$

In Sec. 4.5, we shall discuss sum rules arising from our exciton model and compare them with eqs. (3.13) and (3.14).

3.3.3 Transition dipoles in stacked dimers

Using TD-DFT, the transition energies and transition dipoles are calculated in a frozen geometry relying on the Born-Oppenheimer approximation which gives eigenvalues without influence of the internal vibrational modes. Following the same reasoning as Ishikawa *et al.* [113] it is possible to write a Hamiltonian for the resulting transition energies between localized HOMO and LUMO states in the dimer as

$$H = \begin{pmatrix} E_F & W & t_e & t_h \\ W & E_F & t_h & t_e \\ t_e & t_h & E_{CT} & V \\ t_h & t_e & V & E_{CT} \end{pmatrix} \tag{3.15}$$

where E_F and E_{CT} are the energies of the Frenkel and CT exciton transition, respectively. The matrix elements W and V describe the transfer of a neutral excitation and of a CT exciton, respectively. A basis change to orbitals with well-defined parity can be performed with a transformation matrix

$$T = \frac{1}{\sqrt{2}} \begin{pmatrix} 1 & -1 & 0 & 0 \\ 1 & 1 & 0 & 0 \\ 0 & 0 & 1 & -1 \\ 0 & 0 & 1 & 1 \end{pmatrix}. \tag{3.16}$$

giving a transformed Hamiltonian

$$H' = T^{\dagger} H T = \begin{pmatrix} E_F + W & 0 & t_e + t_h & 0 \\ 0 & E_F - W & 0 & t_e - t_h \\ t_e + t_h & 0 & E_{CT} + V & 0 \\ 0 & t_e - t_h & 0 & E_{CT} - V \end{pmatrix}. \tag{3.17}$$

This Hamiltonian can now be decoupled into two independent subblocks, one for dipole-allowed transitions and one for dipole-forbidden transitions,

$$H_{all.}^{(P=-1)} = \begin{pmatrix} E_F + W & t_e + t_h \\ t_e + t_h & E_{CT} \end{pmatrix}, \tag{3.18}$$

$$H_{forb.}^{(P=+1)} = \begin{pmatrix} E_F - W & t_e - t_h \\ t_e - t_h & E_{CT} \end{pmatrix}. \tag{3.19}$$

This gives four independent equations which together with the calculated transfer integrals can be used to calculate all elements of the Hamiltonian matrix. The solutions of the two Hamiltonians give the eigenvalues

$$E_{1,2}^{all.} = \frac{E_F + E_{CT} + W + V}{2} \pm \frac{1}{2}\sqrt{(E_F + W - E_{CT} - V)^2 + 4(t_e + t_h)^2} \tag{3.20}$$

$$E_{1,2}^{forb.} = \frac{E_F + E_{CT} - W - V}{2} \pm \frac{1}{2}\sqrt{(E_F - W - E_{CT} + V)^2 + 4(t_e - t_h)^2} \tag{3.21}$$

By using TD-DFT values for the transition energies $E_{1,2}$ and transfer integrals from Table 3.6 we obtain all the matrix elements for each one, see Table 3.7.

compound	E_F (eV)	E_{CT} (eV)	W (eV)	V (eV)
PTCDA	2.466	2.104	0.152	0.012
DDTP	2.570	2.343	0.163	0.004
Me-PTCDI	2.448	2.086	0.145	0.006
PB31	2.380	2.025	0.105	0.010
PTCDI	2.465	2.117	0.108	0.010
PR149	2.455	2.145	0.110	0.002
DIP	2.379	2.183	0.057	0.001

Table 3.7: Elements of the matrix (3.18) and (3.19) obtained at the B3LYP/TZ level, except for PR149 which was obtained at the B3LYP/DZ level.

3.3.4 Transition dipoles derived from TD-DFT

In the configuration interaction of singlets (CIS) scheme, the singlets can be determined by the spatial orbitals $\psi_i(\mathbf{r}, \sigma)$ according to

$$|S_{o,u}\rangle = |\psi_o \rightarrow \psi_u\rangle = \frac{1}{\sqrt{2}}\Big\{ |\psi_1(\mathbf{r}, \alpha)\psi_1(\mathbf{r}, \beta) \dots \psi_u(\mathbf{r}, \alpha)\psi_o(\mathbf{r}, \beta) \dots \rangle^{(-)} +$$

$$|\psi_1(\mathbf{r}, \alpha)\psi_1(\mathbf{r}, \beta) \dots \psi_o(\mathbf{r}, \alpha)\psi_u(\mathbf{r}, \beta) \dots \rangle^{(-)} \Big\} \tag{3.22}$$

and the molecular singlet states can be expressed as

$$|S_f\rangle = \sum_{o,u} C_{o,u}|\psi_o \to \psi_u\rangle \tag{3.23}$$

where $C_{o,u}$ are the coefficients where o runs over all occupied spatial MOs and u over all unoccupied ones (compare [18], page 103). With this, it is possible to construct four transitions in a molecule pair which are a sum of these transitions expressed in terms of the electronic orbitals. Within the same parity, these transitions are allowed to mix

$$|S_u^{w/s}\rangle = C_{1u}^{w/s}|H_u \to L_g\rangle + C_{2u}^{w/s}|H_g \to L_u\rangle \tag{3.24}$$

$$|S_g\rangle = C_{1g}|H_u \to L_u\rangle + C_{2g}|H_g \to L_g\rangle \tag{3.25}$$

where $C_{1/2,u/g}^{w/s}$ is the configuration interaction (CI) coefficients for respective transfers, $\{u, g\}$ represents the parities *ungerade* and *gerade*, respectively, and w/s denoted the weak and strong interactions. The contribution from other orbitals is less than 3% except for PR149. In PR149 dimers, the specific orientation of the functional groups mixes transitions based on HOMO and LUMO of the monomers with transitions involving HOMO-1 and HOMO-2 states, so that an assignment of the transition dipoles from the B3LYP/TZ TD-DFT calculations would require a larger model Hamiltonian than eq. 3.15. As this problem is less disturbing in a smaller DZ variational basis, we have analyzed this specific compound with TD-DFT calculations at the B3LYP/DZ level.

For a pair of stacked molecules, the transition energies and the transition dipoles can be obtained from different computational schemes, including configuration interaction of singles (CIS), time-dependent Hartree-Fock (TD-HF), or TD-DFT, as reported in Table 3.8 for α-PTCDA. The two Hartree-Fock based schemes place the CT states well above the neutral excitation with the large oscillator strength, whereas TD-DFT with the B3LYP hybrid functional results in a CT transition below the neutral excitation, and from the exciton model discussed in Chaps. 4 and 5 we find the CT states in a range of about ± 0.25 eV around the neutral excitations. From the large differences between different *ab initio* schemes for the computation of the transition energies, it is clear that all three attempts to compare a calculation for a pair of molecules to the crystalline phase have their weaknesses, resulting both from the incomplete geometric model and from known systematic deficiencies of the methods used.

As an example, the calculated orbitals and transitions in α-PTCDA with TD-DFT calculations at the B3LYP/TZ level, are having the configuration:

$$\left.\begin{array}{llll} |C_{1u}^w|^2 = 50.1\% & H_g = \text{HOMO} - 1 & \to & L_u = \text{LUMO} \\ |C_{2u}^w|^2 = 49.7\% & H_u = \text{HOMO} & \to & L_g = \text{LUMO} + 1 \end{array}\right\} f_{osc.} = 0.015,\ \text{E=2.116 eV}$$

$$\left.\begin{array}{llll} |C_{1u}^s|^2 = 48.8\% & H_u = \text{HOMO} & \to & L_g = \text{LUMO} + 1 \\ |C_{2u}^s|^2 = 48.3\% & H_g = \text{HOMO} - 1 & \to & L_u = \text{LUMO} \end{array}\right\} f_{osc.} = 0.956,\ \text{E=2.618 eV}$$

where transitions with coefficients below 1% are not reported.
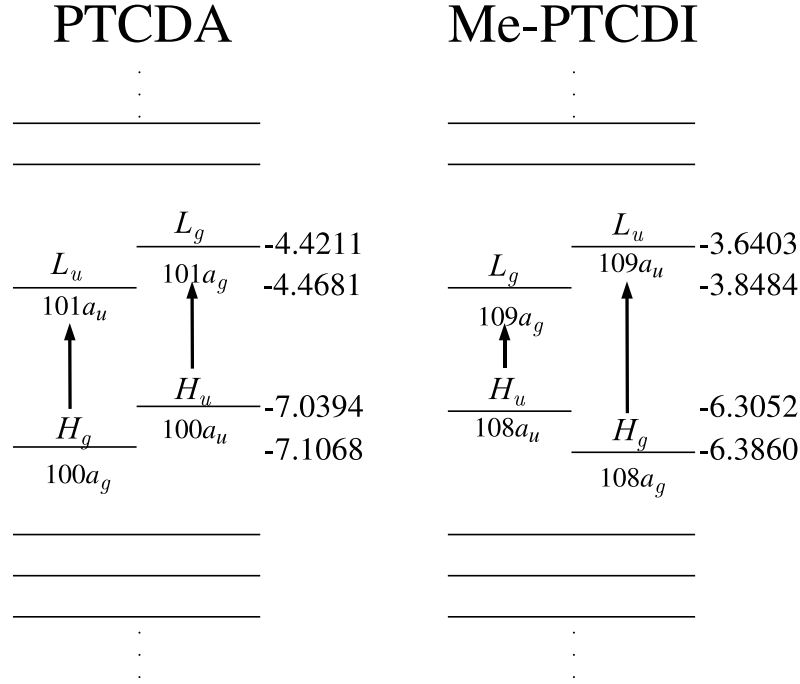
PTCDA

Me-PTCDI

Figure 3.17: The energies of the Kohn-Sham orbitals closest to the bandgap for PTCDA and Me-PTCDI, in eV. The black arrows indicate the allowed transitions and the horizontal lines represent further occupied and unoccupied electronic orbitals.

Due to symmetry reasons only the a_u states can have a non-vanishing transition dipole. The electronic transition dipole for the two allowed states can be derived by using eqs. (3.24,3.25)

$$\boldsymbol{\mu}^w = C_{1u}^w \langle L_g | \hat{\boldsymbol{\mu}} | H_u \rangle + C_{2u}^w \langle L_u | \hat{\boldsymbol{\mu}} | H_g \rangle \tag{3.26}$$

$$\boldsymbol{\mu}^s = C_{1u}^s \langle L_u | \hat{\boldsymbol{\mu}} | H_g \rangle + C_{2u}^s \langle L_g | \hat{\boldsymbol{\mu}} | H_u \rangle \tag{3.27}$$

where the H and L orbitals always have different parities.

compound	dipole-allowed				forbidden	
	E	f_{osc}	E	f_{osc}	E	E
	eV	1	eV	1	eV	eV
CIS	3.586	2.013	4.211	0.040	3.201	4.217
TD-HF	3.270	1.489	4.166	0.036	2.954	4.190
TD-DFT	2.116	0.015	2.618	0.956	2.078	2.328

Table 3.8: Transition energies in a stack of two PTCDA molecules, obtained with CIS, TD-HF and TD-DFT based on the B3LYP hybrid functional, using a TZ variational basis.

Inside the crystal, the polarization of the surroundings induces a red shift of CT transitions by about 2 eV with respect to an isolated dimer [114, 115, 116]. Moreover, the neutral molecular excitations in the crystal are red-shifted by nearly 0.5 eV with respect to a monomer in weakly interacting surroundings [117], and with TD-DFT it can be investigated how different neighbors contribute to this effect [118]. For any microscopic investigation of a stacked dimer, the resulting transition energies will necessarily suffer from large energetic offsets with respect to a more complete description of the crystalline phase, so that approaches like CIS, TD-HF and TD-DFT can only generate raw data which will require further interpretation.

For TD-DFT, it is well known that the wrong asymptotics of the exchange-correlation functional is responsible for a distance dependence of the CT energy deviating from the $-1/r$ behavior expected from the Coulomb interaction [119]. However, from Table 3.8, it is clear that this systematic deficiency of TD-DFT together with the missing polarizable surroundings brings the weakly absorbing CT states rather close to the strongly absorbing neutral excitation, resembling the situation in the crystal discussed in Chaps. 4 and 5. Due to this compensation of errors, TD-DFT calculations of an isolated dimer become a quantitatively meaningful approach for an investigation of basic features of neutral excitations and CT states in the crystalline phase. Moreover, they have the advantage that the transitions of interest are well approximated by the HOMO-LUMO based Hamiltonian (3.15), whereas in the HF based schemes, one of the lowest dipole-allowed transitions has more than 10% admixture of transitions arising from other pairs of molecular orbitals.

compound	dipole-allowed				forbidden	
	E	$f_{\rm osc}$	E	$f_{\rm osc}$	E	E
	eV	1	eV	1	eV	eV
α-PTCDA	2.116	0.015	2.618	0.956	2.078	2.328
DDTP	2.332	0.043	2.616	0.637	2.233	2.514
Me-PTCDI	2.064	0.067	2.622	1.021	2.057	2.326
PB31	1.957	0.221	2.564	1.195	2.004	2.286
PTCDI	2.101	0.098	2.598	1.066	2.083	2.382
PR149	2.127	0.062	2.586	0.852	2.125	2.363
DIP	2.150	0.116	2.469	1.141	2.714	2.328

Table 3.9: Vertical transition energies in a stack of two molecules, in a geometry compatible with the monoclinic crystal phase, obtained with TD-DFT at the B3LYP/TZ level, except for PR149, which has been calculated with B3LYP/DZ.

In Table 3.9, we report the transition energies in stacked dimers of different perylene compounds, obtained with TD-DFT at the B3LYP/TZ level. Among the two transitions of each parity, the lower is always dominated by CT transitions, and the higher by neutral molecular excitations, in keeping with the large difference between the respective oscillator strengths of the dipole-allowed transitions. Together with the projection of the transitions onto pairs of Kohn-Sham orbitals, the TD-DFT results allow for the determination of

the matrix elements W and V in eqs. (3.15, 3.18, 3.19) and for an assignment of the transition dipoles between the localized frontier orbitals of the two molecules, compare the visualization for PTCDA and Me-PTCDI in Figs. 3.18 and 3.19. In all compounds except for PTCDA, both dipole-allowed transitions in Table 3.9 derive the main part of their oscillator strength from the large transition dipoles of the neutral molecular excitations. Thus, in general the weaker among the two dipole-allowed transitions is not a suitable measure for the transition dipole of the CT states. For Me-PTCDI, the four coplanar transition dipoles in Fig. 3.19 reveal the specific linear superpositions of μ_F and μ_{CT} realized in the dimer transitions in Table 3.9. The orientation of the transition dipoles follows intuitive expectations: For the strong molecular transitions, they are aligned with the long axis of the molecule, just like the molecular HOMO-LUMO transition dipole, whereas the transition dipole of the CT state has an orientation rather close to the stacking direction, compare Table 3.10. Due to the larger off-diagonal matrix element $(t_e + t_h)$ in eq. (3.18) with respect to PTCDA, the strongest transition obtained in TD-DFT carries a larger contribution from $\boldsymbol{\mu}^{CT}$, so that the angle between its transition dipole and $\boldsymbol{\mu}^F$ is somewhat larger.

compound	neutral excitation			CT state		
	E_F	μ_F	α_{long}	E_{CT}	μ_{CT}	α_{stack}
	eV	Debye	deg.	eV	Debye	deg.
α-PTCDA	2.470	6.93	1.8	2.101	0.94	15.0
DDTP	2.499	5.86	4.6	2.347	0.42	62.2
Me-PTCDI	2.429	7.42	1.6	2.106	0.68	18.4
PB31	2.440	8.62	1.1	1.965	1.06	5.2
PTCDI	2.453	7.69	3.0	2.129	1.05	13.6
PR149	2.452	6.76	0.6	2.149	0.37	15.5
DIP	2.390	8.20	2.0	2.171	0.03	63.9

Table 3.10: Vertical transition energies and transition dipoles of neutral molecular excitations and CT states in a stacked dimer determined from the values in Table 3.9, together with the orientation of the transition dipoles, expressed in terms of the angle α_{long} between $\boldsymbol{\mu}^F$ and the long axis of the molecules and the angle α_{stack} between $\boldsymbol{\mu}^{CT}$ and the stacking direction.

For all compounds, the transition dipoles obtained with TD-DFT can be found in Table 3.11. For the case of α-PTCDA dipole allowed transitions are illustrated in Fig. 3.18. In this figure, we can see that the transition dipole of the neutral excitation $\boldsymbol{\mu}^F$ is directed along the long axis of the molecule, whereas the transition dipole of the charge transfer state, $\boldsymbol{\mu}^{CT}$, is mainly contributing along the stacking direction.

In DIP, the transition dipole of the CT state is very small, and as opposed to the other compounds, it forms a rather large angle with the stacking direction, two features arising from the small geometric overlap between the molecules in the stack. Residual deviations from the ideal orientation of the transition dipoles for neutral excitation can be related
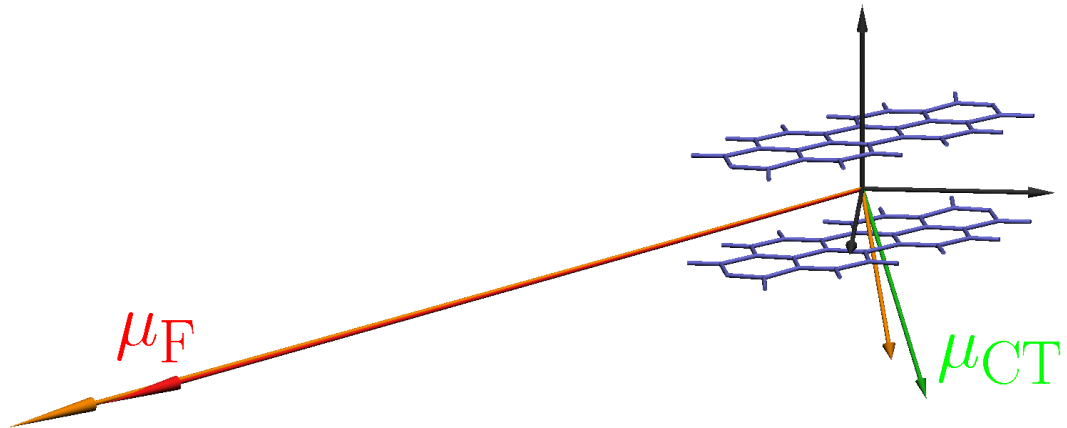
Figure 3.18: Transition dipoles in a stacked dimer of PTCDA. Red: transition dipole μ_F of neutral molecular excitation, green: transition dipole μ_{CT} of CT transition, orange: transition dipoles calculated with TD-DFT.
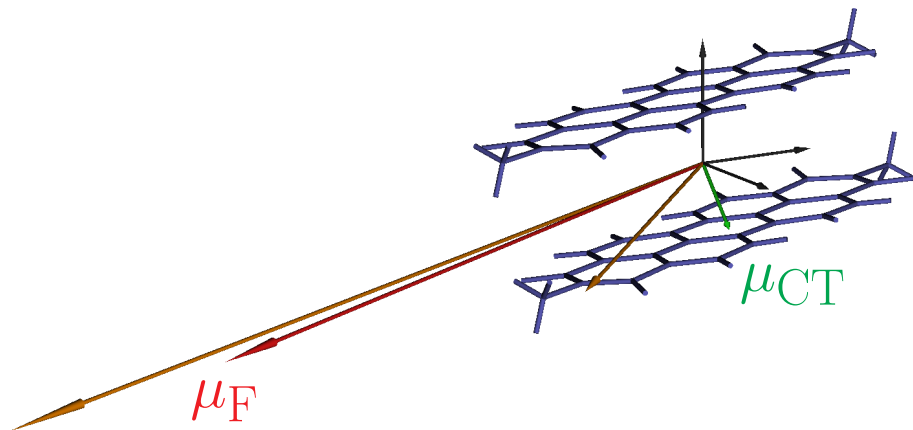
Figure 3.19: Transition dipoles in a stacked dimer of Me-PTCDI. Red: transition dipole μ_F of neutral molecular excitation, green: transition dipole μ_{CT} of CT transition, orange: transition dipoles calculated with TD-DFT.

to the incomplete covering of the lowest transitions found in TD-DFT by the four states underlying eqs. (3.15, 3.18, 3.19.)

In the exciton model developed in the following, the ratio of the transition dipoles μ_{CT}/μ_F will be taken from the values in Table 3.11. Concerning the direction of these dipoles, we shall assume that the neutral excitation has a transition dipole oriented exactly along the long axis of the molecule, whereas the CT states are handled with an orientation of their transition dipoles deduced from TD-DFT. As will be explained in Chaps. 4 and 5 in more detail, absolute values of the transition dipoles in the exciton model will be determined from a comparison to spectroscopic observations.

compound	μ_{xx}^{F}	μ_{yy}^{F}	μ_{zz}^{F}	μ_{xx}^{CT}	μ_{yy}^{CT}	μ_{zz}^{CT}
PTCDA	4.653	5.135	-0.165	0.541	-0.167	-0.756
DDTP	3.383	4.985	-0.018	0.3495	-0.12	-0.172
Me-PTCDI	2.441	7.002	-0.172	0.473	0.115	-0.471
PB31	6.964	5.082	0.116	0.654	0.201	-0.816
PTCDI	7.553	1.268	-0.371	0.609	-0.317	-0.790
PR149	6.716	0.809	0.028	0.092	0.221	-0.282
DIP	8.194	0.380	-0.053	-0.015	0.010	-0.024

Table 3.11: Transition dipoles obtained with TD-DFT calculations at the B3LYP/TZ level, except for PR149 where B3LYP/DZ was used.

3.4 Exciton transfer

The approximate magnitude of the Frenkel transfer integral between two molecules in the crystal $T_{\mathbf{n}\alpha;\mathbf{m}\beta}$ can be estimated by using the unscreened Coulomb interaction between the transition dipoles $\mathbf{d}_\alpha$ and $\mathbf{d}_\beta$ in the point-dipole approximation [120, 121]

$$T_{\mathbf{n}\alpha;\mathbf{m}\beta}(\mathbf{r}) = \frac{1}{4\pi\epsilon_0\epsilon(\mathbf{r})r^5}\left((\mathbf{d}_\alpha \cdot \mathbf{b}_\beta)\mathbf{r}^2 - 3(\mathbf{d}_\alpha \cdot \mathbf{r})(\mathbf{d}_\beta \cdot \mathbf{r})\right) \qquad (3.28)$$

where $\mathbf{r} = \mathbf{R}_{\mathbf{n}\alpha;\mathbf{m}\beta}$ is the vector between the molecule α in unit cell $\mathbf{n}$ and molecule β in unit cell $\mathbf{m}$.

In an anisotropic dielectric medium, a generalization to the screened interaction between point dipoles can most easily be defined by resolving the transition dipole $\mathbf{d}_\alpha$ into a distribution of atomic overlap charges $q_{i\alpha}$ on atom i in the molecule α. For PTCDA, this generalization has been discussed already [122]

$$T_{\mathbf{n}\alpha;\mathbf{m}\beta} = \frac{1}{4\pi\epsilon_0\sqrt{\epsilon_{xx}\epsilon_{yy}\epsilon_{zz}}}\sum_{i,j}\frac{q_{i\alpha}q_{j\beta}}{\left(\frac{x_{i\alpha,j\beta}^2}{\epsilon_{xx}} + \frac{y_{i\alpha,j\beta}^2}{\epsilon_{yy}} + \frac{z_{i\alpha,j\beta}^2}{\epsilon_{zz}}\right)^{1/2}} \qquad (3.29)$$

where $x_{i\alpha,j\beta} = x_{i\alpha} - x_{j\beta}$, etc. are the Cartesian components of the distance between i-th atom in the molecule, and the j-th atom in the molecule β. The evaluation of this expression requires well founded values for the diagonal elements of the anisotropic dielectric tensor [123]. To the best of our knowledge, experimental observations of the anisotropy of the dielectric tensor exist only for PTCDA so that a similar calculation is not possible for other compounds. Therefore, in the exciton model, the exciton transfer parameters will not be calculated microscopically but they will be obtained from a sum rule (Sec. 4.5) applied to the observed data. In all compounds, the values derived from the sum rule will be somewhat smaller than the upper limit of the interaction between point dipoles according to tabulated values in Table 3.11.

Chapter 4

Exciton Model

In this chapter, an exciton model involving Frenkel excitons and charge transfer states will be introduced. As an overview, other related models will be discussed in the first section 4.1. In the following section 4.2 the pure Frenkel Hamiltonian of the model will be constructed and fundamental concepts will be discussed such as transformation into wave-vector representation. In the subsequent section 4.3, the charge transfer states and their mixing with the Frenkel excitons is added to the pure Frenkel model. For the construction of the F-CT Hamiltonian, a set of CT operators will be introduced which will be Fourier transformed to Bloch waves. In section 4.4 the transition dipole moments for the model will be derived using these new operators presented in previous sections. On that basis, calculated optical properties, such as dielectric function and refractive index *etc.* will be discussed and also the implementation process of the model into a numerical code.

4.1 Overview

For a single molecule, the calculation of the optical properties is fairly easy since the dielectric function and the absorption are based on simple Poisson distributions over internal vibrations discussed in Chap. 2. However, in a crystalline molecular pigment, the possible transitions are modified by inter-molecular interactions, including new excitation channels like charge transfer between neighboring sites. Due to the complexity of this task, several approximate models have been discussed in the literature, highlighting the importance of specific phenomena under simplifying assumptions.

Early attempts to analyze the spectroscopic properties of PTCDA used 3D Wannier-Mott excitons to model optical absorption [124] and electroabsorption [125] in thin films confined between other molecular materials. For a large dielectric constant, the electron-hole interaction in the Wannier-Mott exciton is screened, resulting in an exciton binding energy of the order of 0.1 eV. This results in an exciton Bohr radius of 12 Å which would require an exciton distribution over several molecular layers. This approach is suitable for inorganic semiconductors where covalent bonds allow the electrons to spread over a larger volume.

Since the weak intermolecular interactions do not allow for transfers over long distances, an improved approach found was a small radius exciton model. Such an approach to organic materials was introduced when Bulovic *et al.* presented a model using self trapped excitons and CT excitons [12]. Soos *et al.* [126] and Hennessy *et al.* [59] further developed this and introduced the concept of mixing of the Frenkel and the CT states for a pair of molecules. Later on, this dimer model was extended by Hoffmann *et al.* [127, 128] to a 1D stack geometry and the elongations of an effective internal vibration in the isolated configuration.

Vragovíc *et al.* [129, 122] found that for PTCDA, the exciton transfer between different basis molecules of the crystal lattice results in different shapes of the diagonal elements of the dielectric function, in qualitative agreement with ellipsometry data obtained on single crystals [130]. By introducing a pure Frenkel model with two molecules per unit cell it was possible to reproduce the main features of the optical spectrum and of the photoluminescence spectra observed at low temperature. This leads to the question under which conditions the CT states becomes important for modelling perylene derivatives. The dipole moment of the CT state is very small compared to the HOMO-LUMO transition within a molecule. Nevertheless, since the CT states couple to neutral excitations, the resulting mixed states are able to inherit oscillator strength from the Frenkel contributions [131, 127]. This will increase the importance of the CT states if they are close to resonant with neutral excitations. The mixing depends on the size of electron and hole transfer. In Chap. 3 we found that these transfers are particularly small in PTCDA, so that Frenkel and CT states are hardly coupled. However, even though PTCDA does not have large enough transfer integrals to generate an efficient coupling between Frenkel and CT states, Table 3.6 shows that the situation in other pigments will be different. For similar molecules, such as Me-PTCDI [57] and DIP [11], it was demonstrated that a pure Frenkel model cannot reproduce the optical observables.

Previous microscopic calculations of dielectric function and PL spectra raise the fundamental question under which conditions separate F and CT states or their mixing via electron or hole transfer determine the optical observables. In the following, we extend a Frenkel-CT approach developed earlier for a one-dimensional stack to a crystal model accounting for both basis molecules in the unit cell, combining two key ingredients applied earlier to the calculation of the anisotropic optical response of perylene compounds [127, 57, 129, 122]. The deformation of each molecule in its anionic, cationic and optically excited states is deduced from DFT calculations, parameterized in terms of the elongation of an effective internal vibration. DFT and Hartree-Fock calculations applied to a pair of stacked molecules reveal intermolecular parameters like electron transfer and hole transfer. In such a stacked dimer, the transition dipole between the electronic ground state and the CT state and the transition dipole of neutral molecular excitations can be derived from DFT and TD-DFT calculations. The transfer of a neutral molecular excitation towards different sites is constrained by a sum rule relating the center of mass of the absorption band to the molecular deformation and excitation transfer, so that the required transfer parameter can be deduced in a controlled way from the observed spectra [132, 133, 134]. Based on these constraints for the quantities entering the exciton model,

we use the energies of neutral excitations and CT states as the only free parameters. Our approach is limited to transitions arising from the highest molecular orbital (HOMO) and lowest occupied molecular orbitals (LUMO). For DIP, higher transitions and the respective CT states seem to have a minor influence on the lowest absorption band [11], but for the other perylene compounds investigated in the present work, we found little evidence for a similar phenomenon.

4.2 Frenkel Hamiltonian

The Frenkel exciton, named after the Russian physicist Yakov Frenkel, can be applied when the dielectric function of the material is small and the Coulomb interaction between electrons and holes is very strong. This results in a relatively small exciton size, of the same order as a crystal unit cell. Applied to molecular materials, this model indicates that electron and hole reside on the same molecule with a binding energy in the range of 1 eV. Therefore the Frenkel exciton fulfills the criteria of a small radius model. As will be discussed below, in the present context a Frenkel exciton is a Bloch wave composed of localized molecular excitations.

The starting point of the model is a crystal in its lowest energy state where all molecules in the system are in their electronic and vibronic ground state. Within the effective mode model, as a consequence of the BO-approximation, it is possible to factorize the electronic ground state of the crystal into the product of the ground state wave function of the constituting molecules,

$$| \, g \rangle = \prod_{\mathbf{n}\alpha} | \, \phi^g_{\mathbf{n}\alpha} \chi^{0_g}_{\mathbf{n}\alpha} \rangle, \tag{4.1}$$

where $\phi^g_{\mathbf{n}\alpha}$ is the electronic wave function in the ground state of molecule $\alpha \in \{A, B\}$ in unit cell $\mathbf{n}$ and $\chi^{0_g}_{\mathbf{n}\alpha}$ the lowest vibronic eigenstate of an effective internal vibration. The factorized ground state $| \, g \rangle$ makes it possible to analyze optical excitations in terms of localized molecular transitions towards vibronic eigenstates associated with the excited electron state. We introduce creation operators which excite a specific molecule into the electronic excited state

$$b^\dagger_{\mathbf{n}\alpha\nu_e} | \, \phi^g_{\mathbf{n}\alpha} \chi^{0_g}_{\mathbf{n}\alpha} \rangle = | \, \phi^e_{\mathbf{n}\alpha} \chi^{\nu_e}_{\mathbf{n}\alpha} \rangle, \tag{4.2}$$

where $\phi^e_{\mathbf{n}\alpha}$ is the electronic part of the wave function in the excited electronic configuration, and $\chi^{e\nu_e}_{\mathbf{n}\alpha}$ the ν_eth vibrational state in the excited state potential of molecule α in the unit cell $\mathbf{n}$. The application of this creation operator to a system in its ground state results in a factorization of the excited state into molecular wave functions

$$b^\dagger_{\mathbf{n}\alpha\nu_e} | \, g \rangle = | \, \phi^e_{\mathbf{n}\alpha} \chi^{\nu_e}_{\mathbf{n}\alpha} \rangle \, | \, \phi^g_{\mathbf{n}\beta} \chi^{0_g}_{\mathbf{n}\beta} \rangle \times \prod_{\mathbf{m}\neq\mathbf{n}} | \, \phi^g_{\mathbf{m}\alpha} \chi^{0_g}_{\mathbf{m}\alpha} \, | \, \phi^g_{\mathbf{m}\beta} \chi^{0_g}_{\mathbf{m}\beta} \rangle, \tag{4.3}$$

where $\alpha \neq \beta$, see Fig. 4.1 for a visualization. In the Heitler-London approximation [120, 135], these product states form the basis of our formulation of the Frenkel exciton Hamiltonian. In this model we assume that both the basis for the electronic transition and the internal molecular vibration reside on the same molecule [127] because of the

relatively large value of the exciton-phonon coupling constant (≈ 1), thus neglecting any configuration in which they are placed on different molecular sites [57, 136, 137].
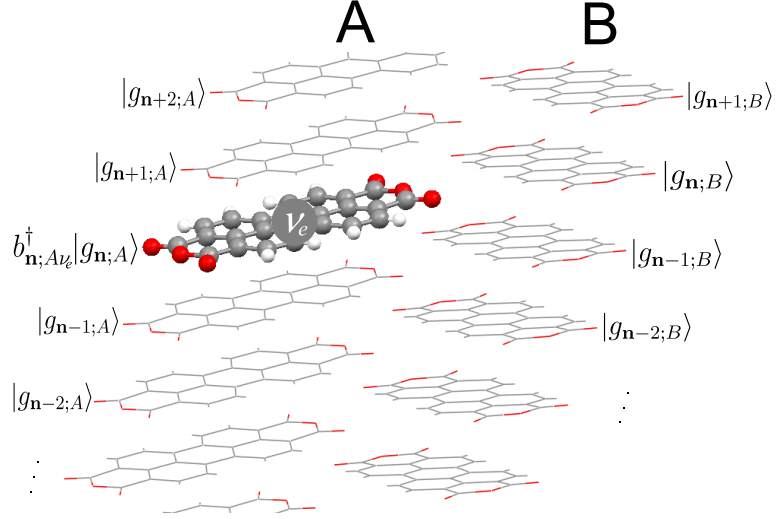
Figure 4.1: Visualization of the operator $b^{\dagger}_{\mathbf{n};A\nu_e}$ operating on a PTCDA crystal in its ground state $|g\rangle$. The molecule in unit cell $\mathbf{n}$ in stack A is excited to the first excited state with vibronic level ν_e. The molecules still in their ground state are depicted with wires and the excited molecule is visualized by a ball-and-stick scheme.

The resulting pure Frenkel exciton Hamiltonian for the 3D molecular crystal, with two molecules per unit cell, reads

$$H^{\mathrm{F}} = \sum_{\mathbf{n}} \sum_{\alpha=A,B} \sum_{\nu_e} E^{\mathrm{F}}_{0_g\nu_e} b^{\dagger}_{\mathbf{n}\alpha\nu_e} b_{\mathbf{n}\alpha\nu_e} + \sum_{\mathbf{n}\alpha\nu_e} \sum_{\mathbf{m}\beta\mu_e} t_{\mathbf{n}\alpha\nu_e,\mathbf{m}\beta\mu_e} b^{\dagger}_{\mathbf{n}\alpha\nu_e} b_{\mathbf{m}\beta\mu_e} \tag{4.4}$$

where $E^{\mathrm{F}}_{0_g\nu_e} = E^{\mathrm{F}}_{0_g0_e} + \nu_e\hbar\omega_{\mathrm{eff}}$ is the exciton on-site energy in the ν_eth vibronic level. $E^{\mathrm{F}}_{0_g0_e}$ is the transition energy between the lowest vibronic levels $|\chi^{0_g}_{\mathbf{n}\alpha}\rangle$ and $|\chi^{0_e}_{\mathbf{n}\alpha}\rangle$ of the free molecule α in cell $\mathbf{n}$, corresponding to excitation between the two harmonic oscillators potentials in Fig. 2.2. In this notation, the gas-to-crystal shift shall be included by a suitable choice of the lowest molecular transition energy $E^{\mathrm{F}}_{0_g0_e}$. The last term, $\nu_e\hbar\omega_{\mathrm{eff}}$, is the vibronic energy of the vibronic level ν_e, where $\hbar\omega_{\mathrm{eff}}$ is the energy difference between consecutive vibronic levels, compare Fig. 2.2. The Hamiltonian H^{F} is based on localized transitions in eq. (4.3) excited from the ground state $|\,g\rangle$ in eq. (4.1) using the exciton creation operators in eq. (4.2). This corresponds to the realistic assumption that $k_BT \ll \hbar\omega_{\mathrm{eff}}$ since the single exciton state is still referring to a crystal ground state without any electronic or vibronic excitation.

The rule for the transfer matrix element $t_{\mathbf{n}\alpha\nu_e;\mathbf{m}\beta\mu_e}$ is that it has to return the molecule β in unit cell $\mathbf{m}$ from excited level μ_e into the lowest vibronic level of the electronic ground state, and the molecule α in unit cell $\mathbf{n}$ is moved into an excitonic state in the vibronic

sublevel ν_e of the excited state potential. As before, applying the BO-approximation, it is possible to divide the transfer matrix element into an electronic and a vibronic part

$$t_{\mathbf{n}\alpha\nu_e;\mathbf{m}\beta\mu_e} = \langle g b_{\mathbf{n}\alpha\nu_e} g \mid H^F \mid b_{\mathbf{m}\beta\mu_e}^\dagger g \rangle =$$

$$= \underbrace{\langle \phi_{\mathbf{n}\alpha}^e \phi_{\mathbf{n}\beta}^g \prod_{\mathbf{n}\neq\mathbf{n}'} \phi_{\mathbf{n}'\alpha}^g \phi_{\mathbf{n}'\beta}^g \mid H^F \mid \phi_{\mathbf{m}\alpha}^g \phi_{\mathbf{m}\beta}^e \prod_{\mathbf{m}\neq\mathbf{m}'} \phi_{\mathbf{m}'\alpha}^g \phi_{\mathbf{m}'\beta}^g \rangle}_{T_{\mathbf{n}\alpha;\mathbf{m}\beta}} \underbrace{\langle \chi_{\mathbf{n}\alpha}^{\nu_e} \mid \chi_{\mathbf{n}\alpha}^{0_g} \rangle}_{S_{0_g\nu_e}} \underbrace{\langle \chi_{\mathbf{m}\alpha}^{0_g} \mid \chi_{\mathbf{m}\alpha}^{\mu_e} \rangle}_{S_{\mu_e 0_g}}$$

$$= T_{\mathbf{n}\alpha;\mathbf{m}\beta} S_{0_g\nu_e} S_{\mu_e 0_g}, \tag{4.5}$$

where $S_{0_g\nu_e}$ and $S_{\mu_e 0_g}$ are the vibronic Franck-Condon factors described before and $T_{\mathbf{n}\alpha;\mathbf{m}\beta}$ is the transfer integral of neutral excited excitons discussed in Sec. 3.4.

As the system is periodic we can perform a total Fourier transformation into wave-vector representation. An operator for the excitation of a Bloch wave composed of localized excitations can be introduced as

$$b_{\mathbf{k}\alpha\nu_e}^\dagger = \frac{1}{\sqrt{N}} \sum_{\mathbf{n}} e^{-i\mathbf{k}\mathbf{R}_{\mathbf{n},\alpha}} b_{\mathbf{n}\alpha\nu_e;\mathbf{n}\alpha 0_g}^\dagger, \tag{4.6}$$

where $\mathbf{R}_{\mathbf{n},\alpha} = \mathbf{R}_\mathbf{n} + \mathbf{r}_\alpha$ is the position of the α molecule in the crystal unit cell $\mathbf{n}$. When the Hamiltonian is Fourier transformed, it decouples into independent sub-blocks for different wave vectors $\mathbf{k}$, see Appendix A for a detailed description of the Fourier transform, and the $\mathbf{k}$-space Frenkel Hamiltonian can be written as

$$H^F(\mathbf{k}) = \sum_{\alpha\nu_e} E_{0_g\nu_e}^F b_{\mathbf{k}\alpha\nu_e}^\dagger b_{\mathbf{k}\alpha\nu_e} + \sum_{\alpha\nu_e,\beta\mu_e} S_{0_g\nu_e} S_{0_g\mu_e} T_{\alpha\beta}(\mathbf{k}) b_{\mathbf{k}\alpha\nu_e}^\dagger b_{\mathbf{k}\beta\mu_e} \tag{4.7}$$

where

$$T_{\alpha\beta}(\mathbf{k}) = \sum_{\mathbf{R}_{\mathbf{n}\alpha;\mathbf{m}\beta}\neq 0} e^{-i\mathbf{k}\mathbf{R}_{\mathbf{n}\alpha;\mathbf{m}\beta}} T_{\mathbf{n}\alpha;\mathbf{m}\beta} \tag{4.8}$$

and $\mathbf{R}_{\mathbf{n}\alpha;\mathbf{m}\beta} = \mathbf{R}_{\mathbf{n}\alpha} - \mathbf{R}_{\mathbf{m}\beta}$ is the distance vector between molecules $\mathbf{n}\alpha$ and $\mathbf{m}\beta$. $T_{\alpha\beta}(\mathbf{k})$ is the discrete Fourier transform of the transfer matrix element summed over the relative position $\mathbf{R}_{\mathbf{n}\alpha;\mathbf{m}\beta}$. Since perylene crystals have a center of symmetry the exciton transfer matrix element $T_{\alpha\beta}(\mathbf{k})$ are real and symmetric with respect to the indices α and β [120].

With respect to the basis molecules and their creation operators $b_{\mathbf{k}A\nu_e}^\dagger$ and $b_{\mathbf{k}B\nu_e}^\dagger$ together with the respective annhiliation operators, this Hamiltonian has the following block structure:

$$H^F(\mathbf{k}) = H_{AA}^F(\mathbf{k}) b_{\mathbf{k}A\nu_e}^\dagger b_{\mathbf{k}A\mu_e} + H_{AB}^F(\mathbf{k}) b_{\mathbf{k}A\nu_e}^\dagger b_{\mathbf{k}B\mu_e} +$$

$$H_{BA}^F(\mathbf{k}) b_{\mathbf{k}B\nu_e}^\dagger b_{\mathbf{k}A\mu_e} + H_{BB}^F(\mathbf{k}) b_{\mathbf{k}B\nu_e}^\dagger b_{\mathbf{k}B\mu_e} \tag{4.9}$$

or in terms of the matrix elements involved

$$H^F(\mathbf{k}) = \begin{pmatrix} H_{AA}^F(\mathbf{k}) & H_{BA}^F(\mathbf{k}) \\ H_{AB}^F(\mathbf{k}) & H_{BB}^F(\mathbf{k}) \end{pmatrix}, \tag{4.10}$$

where the block $H_{AA}^{\mathrm{F}}(\mathbf{k})$ contains the possible transfer of the optical excitation from a basis molecule A to all A molecules in the other unit cells, and similarly for the other blocks. Each block can now be written as

$$H_{AA;\nu_e\mu_e}^{\mathrm{F}}(\mathbf{k}) = H_{BB;\nu_e\mu_e}^{\mathrm{F}}(\mathbf{k}) = E_{0_g\nu_e}^{\mathrm{F}}\delta_{\nu_e\mu_e} + S_{0_g\nu_e}S_{0_g\mu_e}T_{AA}(\mathbf{k}), \qquad (4.11)$$

$$H_{AB;\nu_e\mu_e}^{\mathrm{F}}(\mathbf{k}) = H_{BA;\nu_e\mu_e}^{\mathrm{F}}(\mathbf{k}) = S_{0_g\nu_e}S_{0_g\mu_e}T_{AB}(\mathbf{k}) \qquad (4.12)$$

The Frenkel excitons on the A and B basis molecules are coupled by the off-diagonal element $H_{AB}^{\mathrm{F}}(\mathbf{k})$, but a decoupling can be achieved by a superposition of both basis molecules governed by Hamiltonians

$$H_{AA}^{\mathrm{F}}(\mathbf{k}) \pm H_{AB}^{\mathrm{F}}(\mathbf{k}). \qquad (4.13)$$

In terms of the creation operator of Frenkel excitons, this further block diagonalization can be expressed by a superposition of Bloch waves involving A or B basis molecules:

$$b_{\mathbf{k}\xi\nu_e}^{\dagger} = \frac{1}{\sqrt{2}}(b_{\mathbf{k}A\nu_e}^{\dagger} \pm b_{\mathbf{k}B\nu_e}^{\dagger}) \qquad (4.14)$$

where $\xi = y$ governed by the upper sign represents Bloch waves with transition dipoles exclusively along y, coinciding with the screw axis in the monoclinic space group, and the difference indexed $\xi = x$ has molecular transition dipoles along x and CT transition dipoles in the xz plane, compare Fig. 3.1. Because the Hamiltonian (4.10) is invariant under exchange of the two basis molecules A and B, all eigenstates have a well-defined symmetry with respect to this operation. After the rotation the Hamiltonian is separated into two non-zero blocks

$$H^{\mathrm{F}}(\mathbf{k}) = \left(\begin{array}{c|cc} & b_{\mathbf{k}y\nu_e}^{\dagger} & b_{\mathbf{k}x\nu_e}^{\dagger} \\ \hline b_{\mathbf{k}y\nu_e} & H_{AA}^{\mathrm{F}}(\mathbf{k}) + H_{AB}^{\mathrm{F}}(\mathbf{k}) & 0 \\ b_{\mathbf{k}x\nu_e} & 0 & H_{AA}^{\mathrm{F}}(\mathbf{k}) - H_{AB}^{\mathrm{F}}(\mathbf{k}) \end{array} \right) \qquad (4.15)$$

where the upper left block is the block Hamiltonian for transitions with the transition dipole along the y direction and the lower right block for the x direction. With this we achieve a separation of both parts, so that they can be solved independently from each other. Diagonalization of the Hamiltonian (4.15) by unitary transformation with respect to the vibrational sublevels gives

$$b_{\mathbf{k}x\zeta_e}^{\dagger} = \sum_{\nu_e} u_{\nu_e\zeta_e}(\mathbf{k}, x)b_{\mathbf{k}x\nu_e}^{\dagger} \qquad (4.16)$$

and

$$b_{\mathbf{k}y\zeta_e}^{\dagger} = \sum_{\nu_e} u_{\nu_e\zeta_e}(\mathbf{k}, y)b_{\mathbf{k}y\nu_e}^{\dagger} \qquad (4.17)$$

where ζ_e is the vibrational sublevel for the excitons when diagonalizing the sub-blocks of (4.15) and $u_{\nu_e\zeta_e}(\mathbf{k}, y_e)$ are the eigenvectors.

4.3 Interference between Frenkel excitons and CT transitions

As stated before, the Frenkel model is not sufficient for explaining the spectra of certain molecular crystals, especially for those with a large CT influence. One example is the DIP molecule where the mixing of the two states is large enough to have a noticeable impact on the shape of the optical spectra. Fig. 4.2 compares the line shape derived from the pure Frenkel exciton model with the observed spectra of DIP, revealing the limitations of this approach [11].
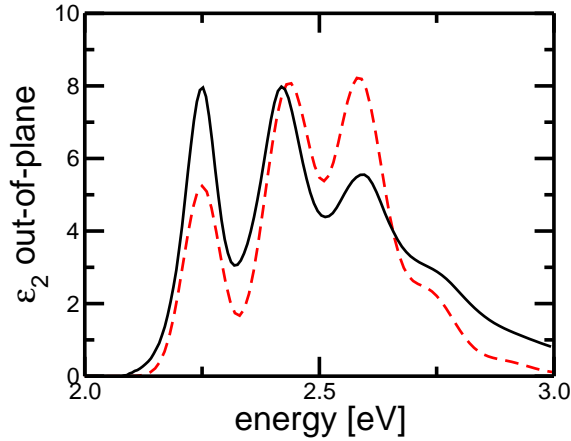
Figure 4.2: Experimental out-of-plane component ϵ_2 of a DIP film deposited on SiO_2 (solid line) and the results of the pure Frenkel model (dashed line) with parameters $E_{00}^F = 2.21$ eV, $\hbar\omega_{\text{eff}} = 0.17$ eV, $S = 0.87$, and $T = 0.142$ eV [11], so that the lowest subband and the average transition energy of the calculated spectra coincide with the measured values.

In this section we will build on the Frenkel model and develop a model including CT states which also allows these two exciton states to interfere. The charge transfers are relative weak over longer distances in the stack. As a result of this we will restrict the CT transfers to closest neighbors along the stacking direction. However, even though we will include transfers to neighboring molecules the model will still be considered a small radius model.

The full Hamiltonian with CT states, and interference between Frenkel and CT states, can be described with a three-part Hamiltonian

$$H^{\text{tot}} = H^{\text{F}} + H^{\text{CT}} + H^{\text{F-CT}}, \tag{4.18}$$

where H^{F} is the pure Frenkel state Hamiltonian given previously in eq. (4.4), H^{CT} the pure CT Hamiltonian, and $H^{\text{F-CT}}$ the part of the Hamiltonian mixing Frenkel and CT

states. In order to excite the crystal ground state into configuration involving opposite charges on adjacent stack neighbors, new operators for the CT states are introduced. An anionic electronic configuration at site $\mathbf{R_n}$ will be denoted as $|\phi_{\mathbf{n}\alpha}^-\rangle$, and a cationic state on the neighboring site $\mathbf{R_{n+a}}$, as $|\phi_{\mathbf{n}\pm1,\alpha}^+\rangle$ together with the vibronic levels η_- and γ_+ on the respective molecules:

$$c_{\mathbf{n}\alpha\eta_-;\mathbf{n}+1,\alpha\gamma_+}^\dagger \mid g\rangle = \mid \phi_{\mathbf{n},\alpha}^- \chi_{\mathbf{n},\alpha}^{\eta_-}\rangle \mid \phi_{\mathbf{n},\beta}^g \chi_{\mathbf{n},\beta}^{0_g}\rangle \mid \phi_{\mathbf{n}+1,\alpha}^+ \chi_{\mathbf{n}+1,\alpha}^{\gamma_+}\rangle \mid \phi_{\mathbf{n}+1,\beta}^g \chi_{\mathbf{n}+1,\beta}^{0_g}\rangle \times$$

$$\prod_{\mathbf{m}\neq\mathbf{n},\mathbf{n+1}} \mid \phi_{\mathbf{m},\alpha}^g \chi_{\mathbf{m},\alpha}^{0_g}\rangle \mid \phi_{\mathbf{m},\beta}^g \chi_{\mathbf{m},\beta}^{0_g}\rangle. \tag{4.19}$$

The operator for a charge separation in the other stack direction is written as

$$c_{\mathbf{n}\alpha\eta_-;\mathbf{n}-1,\alpha\gamma_+}^\dagger \mid g\rangle = \mid \phi_{\mathbf{n}-1,\alpha}^+ \chi_{\mathbf{n}-1,\alpha}^{\gamma_+}\rangle \mid \phi_{\mathbf{n}-1,\beta}^g \chi_{\mathbf{n}-1,\beta}^{0_g}\rangle \mid \phi_{\mathbf{n},\alpha}^- \chi_{\mathbf{n},\alpha}^{\eta_-}\rangle \mid \phi_{\mathbf{n},\beta}^g \chi_{\mathbf{n},\beta}^{0_g}\rangle \times$$

$$\prod_{\mathbf{m}\neq\mathbf{n},\mathbf{n-1}} \mid \phi_{\mathbf{m},\alpha}^g \chi_{\mathbf{m},\alpha}^{0_g}\rangle \mid \phi_{\mathbf{m},\beta}^g \chi_{\mathbf{m},\beta}^{0_g}\rangle. \tag{4.20}$$

where $c_{\mathbf{n}\alpha\eta_-;\mathbf{n}\pm1,\alpha\gamma_+}^\dagger$ $(c_{\mathbf{n}\alpha\eta_-;\mathbf{n}\pm1,\alpha\gamma_+})$ is the creation (annihilation) operator for the CT state with an electron at lattice site $\mathbf{n}$ and a hole at lattice site $\mathbf{n} \pm 1$ in stack α. Based on the Huang-Rhys factors in Table 2.5, setting the cutoff for the squared Franck-Condon factors to 10^{-6}, it is sufficient to include vibronic levels γ_+ in the range $\gamma_+ = 0, 1, \ldots, \gamma_+^{max}$ and vibronic level of the anion $\eta_- = 0, 1, \ldots, \eta_-^{max}$ with $\gamma_+^{max} = \eta_-^{max} = 8$. These operators can be pictured as a transfer of a hole from a basis molecule α in unit cell $\mathbf{n}$ to the same basis molecule in the neighboring unit cell $\mathbf{n} + 1$ or $\mathbf{n} - 1$, involving the vibronic level γ_+ of the cationic molecule and the vibronic level η_- of the anionic molecule, see Fig 4.3. Notice that charge transfer between different basis molecules is not included because it is not expected to be relevant in this specific monoclinic arrangement of the two basis molecules.

The excitations described by the creation operators in eqs. (4.19 and 4.20) are the only states with a transition dipole towards the electronic ground state, whereas states involving vibronic excitations at sites differing from the molecules with modified electronic configurations cannot be excited from the electronic ground state, so that they will be ignored in the following.

The charge transfer Hamiltonian can now be written as

$$H^{\mathrm{CT}} = \sum_\alpha \sum_\mathbf{n} \sum_{\gamma_+\eta_-} E_{\gamma_+\eta_-}^{\mathrm{CT}} \left(c_{\mathbf{n}\alpha\eta_-;\mathbf{n}+1,\alpha\gamma_+}^\dagger c_{\mathbf{n}\alpha\eta_-;\mathbf{n}+1,\alpha\gamma_+} + c_{\mathbf{n}\alpha\eta_-;\mathbf{n}-1,\alpha\gamma_+}^\dagger c_{\mathbf{n}\alpha\eta_-;\mathbf{n}-1,\alpha\gamma_+} \right) \tag{4.21}$$

where $E_{\gamma_+\eta_-}^{\mathrm{CT}} = E_{00}^{\mathrm{CT}} + (\gamma_+ + \eta_-)\hbar\omega$ is the on-site energy of a CT exciton in vibronic levels η_- and γ_+ for the anionic and the cationic sites, and E_{00}^{CT} is the energy difference between the lowest vibronic levels in the electronic ground and excited states. The Hamiltonian which includes mixing between neutral excitations and CT states via electron and hole transfer can be written as

$$H^{\mathrm{F-CT}} = \sum_\alpha \sum_{\mathbf{n}\nu_e} \sum_{\mathbf{m}\gamma_+\eta_-} (c_{\mathbf{m}\alpha\eta_-;\mathbf{m}-1,\alpha\gamma_+}^\dagger b_{\mathbf{n}\alpha\nu_e}(\delta_{\mathbf{mn}}t_h' + \delta_{\mathbf{m}-1,\mathbf{n}}t_e') +$$
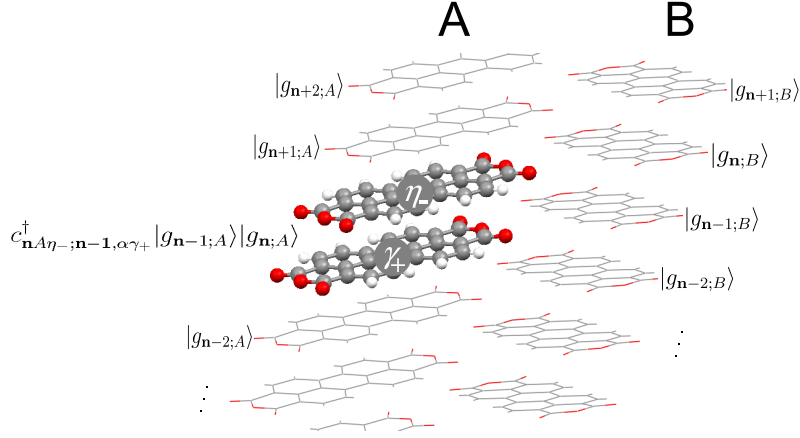
Figure 4.3: Visualization of operator $c^\dagger_{\mathbf{n}A\eta_-;\mathbf{n}-1,A\gamma_+}$ operating on a crystal in the ground state. The A molecule in the $\mathbf{n}$th unit cell is excited to an anionic state with vibronic level η_- and the A molecule in the $(\mathbf{n}-1)$th unit cell is excited to a cationic state with vibronic level γ_+. The molecules in their ground states are depicted with wires and the molecules with modified electronic configurations are visualized by a ball-and-stick scheme.

$$c^\dagger_{\mathbf{m}\alpha\eta_-;\mathbf{m}+1,\alpha\gamma_+} b_{\mathbf{n}\alpha\nu_e}(\delta_{\mathbf{mn}}t'_h + \delta_{\mathbf{m}+1,\mathbf{n}}t'_e)) + h.c. \tag{4.22}$$

where

$$t'_h = \langle c^\dagger_{\mathbf{n}\alpha\eta_-;\mathbf{n}+1,\alpha\gamma_+} g \mid H^{\mathrm{F-CT}} \mid b^\dagger_{\mathbf{n}\alpha\nu_e} g\rangle = \underbrace{\langle \chi^{+\gamma_+}_{\mathbf{n+1}} \mid \chi^{g0_g}_{\mathbf{n+1}}\rangle}_{S^+_{0_g\gamma_+}} \underbrace{\langle \chi^{-\eta_-}_{\mathbf{n}} \mid \chi^{e\nu_e}_{\mathbf{n}}\rangle}_{S^-_{\nu_e\eta_-}} \cdot$$

$$\underbrace{\langle \phi^+_{\mathbf{n+1},\alpha}\phi^-_{\mathbf{n},\alpha}\phi^g_{\mathbf{n+1},\beta}\phi^e_{\mathbf{n},\beta} \prod_{\mathbf{n}'\neq\mathbf{n},\mathbf{n+1}} \phi^{g0}_{\mathbf{n}'\alpha}\phi^{g0}_{\mathbf{n}'\beta} \mid H^{\mathrm{F-CT}} \mid \phi^g_{\mathbf{m}\alpha}\phi^g_{\mathbf{m}\beta}\rangle \langle \prod_{\mathbf{m}'\neq\mathbf{m}} \phi^g_{\mathbf{m}'\alpha}\phi^g_{\mathbf{m}'\beta}\rangle}_{t_h} \tag{4.23}$$

and similar for t'_e, so we receive

$$t'_h = t_h S_{0_g\gamma_+} S_{\nu_e\eta_-} \tag{4.24}$$

$$t'_e = t_e S_{0_g\eta_-} S_{\nu_e\gamma_+} \tag{4.25}$$

where t_h and t_e are the transfer integrals of a hole and an electron, respectively. The transfer of the CT states is neglected here since that would imply transfer of two charge carriers simultaneously, with very small matrix elements. As the Frenkel part H^{F} of the model Hamiltonian is restricted to vibronic states having a transition dipole towards the electronic and vibrational ground state, vibronic overlap factors between an excited vibrational level $|\chi^{\mu_g}\rangle$ in the electronic ground state and a vibronic level $|\chi^{\nu_e}\rangle$ in the excited state do not occur. However, in the interaction part $H^{\mathrm{F-CT}}$ of the Hamiltonian, overlap factors of this kind are required because electron and hole transfer couple all vibronic levels of an excited molecule to the ones of the same molecule in its ionized state.

Within the framework of the same effective internal vibration for the charged state and the excited state of a molecule, the inequality $S_+ < S_- < S$ discussed earlier in Sec. 2.3.5 allows the definition of positive Huang-Rhys factors for the deformation from an ionized state towards the optically excited state as

$$\tilde{S}_+ = (\sqrt{S} - \sqrt{S_+})^2 \tag{4.26}$$

$$\tilde{S}_- = (\sqrt{S} - \sqrt{S_-})^2 \tag{4.27}$$

using the vibronic overlap expression in eq. (2.22).

In a periodic system we can transform the CT operators into their wave vector representation, compare eq. (4.6):

$$c^\dagger_{\mathbf{k}\alpha\eta_-\gamma_+,+} = \frac{1}{\sqrt{N}} \sum_n e^{-i\mathbf{k}\cdot\mathbf{R_n}} c^\dagger_{\mathbf{n}\alpha\eta_-;\mathbf{n}+1,\alpha\gamma_+} \tag{4.28}$$

$$c^\dagger_{\mathbf{k}\alpha\eta_-\gamma_+,-} = \frac{1}{\sqrt{N}} \sum_n e^{-i\mathbf{k}\cdot\mathbf{R_n}} c^\dagger_{\mathbf{n}\alpha\eta_-;\mathbf{n}-1,\alpha\gamma_+} \tag{4.29}$$

where the last index of the operators on the left hand side, $+$ or $-$, addresses the relative position of the cationic molecule with respect to the anionic site, so that the operator $c^\dagger_{\mathbf{k}\alpha\eta_-\gamma_+,+}$ and $c^\dagger_{\mathbf{k}\alpha\eta_-\gamma_+,-}$ describes Bloch waves of the CT states with opposite direction of charge transfer. The annhiliation operators can be expressed by the adjoint of these discrete Fourier transforms.

Building a model Hamiltonian with these operators will result in a decoupling of blocks with different wave vectors $\mathbf{k}$. The resulting Hamiltonian becomes

$$H^{\text{tot}} = \sum_{\mathbf{k}} \left(H^{\text{F}}(\mathbf{k}) + H^{\text{CT}}(\mathbf{k}) + H^{\text{F-CT}}(\mathbf{k}) \right)$$

where $H^{\text{F}}(\mathbf{k})$ is the $\mathbf{k}$-space Frenkel Hamiltonian given before,

$$H^{\text{CT}}(\mathbf{k}) = \sum_\alpha \sum_{\gamma_+\eta_-} E^{\text{CT}}_{\gamma_+\eta_-} (c^\dagger_{\mathbf{k}\alpha\eta_-\gamma_+,-} c_{\mathbf{k}\alpha\eta_-\gamma_+,-} + c^\dagger_{\mathbf{k}\alpha\eta_-\gamma_+,+} c_{\mathbf{k}\alpha\eta_-\gamma_+,+}) \tag{4.30}$$

and the mixing between Frenkel and CT excitations is described as

$$H^{\text{F-CT}}(\mathbf{k}) = \sum_\alpha \sum_{\nu_e} \sum_{\gamma_+\eta_-} \left(c^\dagger_{\mathbf{k}\alpha\eta_-\gamma_+,-} b_{\mathbf{k}\alpha\nu_e}(t'_h + e^{-i\mathbf{k}\cdot\mathbf{a}}t'_e) + c^\dagger_{\mathbf{k}\alpha\eta_-\gamma_+,+} b_{\mathbf{k}\alpha\nu_e}(t'_h + e^{i\mathbf{k}\cdot\mathbf{a}}t'_e) \right) + h.c. \tag{4.31}$$

The total Hamiltonian in its matrix form can be written as

$$H^{\text{tot}}(\mathbf{k}) = \begin{pmatrix} & b^\dagger_{\mathbf{k}A\nu_e} & b^\dagger_{\mathbf{k}B\nu_e} & c^\dagger_{\mathbf{k}A\eta_-\gamma_+\sigma} & c^\dagger_{\mathbf{k}B\eta_-\gamma_+\sigma} \\ \hline b_{\mathbf{k}A\nu_e} & H^{\text{F}}_{AA}(\mathbf{k}) & H^{\text{F}}_{BA}(\mathbf{k}) & H^{\text{F-CT}}_{AA}(\mathbf{k}) & H^{\text{F-CT}}_{BA}(\mathbf{k}) \\ b_{\mathbf{k}B\nu_e} & & H^{\text{F}}_{BB}(\mathbf{k}) & H^{\text{F-CT}}_{AB}(\mathbf{k}) & H^{\text{F-CT}}_{BB}(\mathbf{k}) \\ c_{\mathbf{k}A\eta_-\gamma_+\sigma} & & h.c. & H^{\text{CT}}_{AA}(\mathbf{k}) & 0 \\ c_{\mathbf{k}B\eta_-\gamma_+\sigma} & & & & H^{\text{CT}}_{BB}(\mathbf{k}) \end{pmatrix}$$
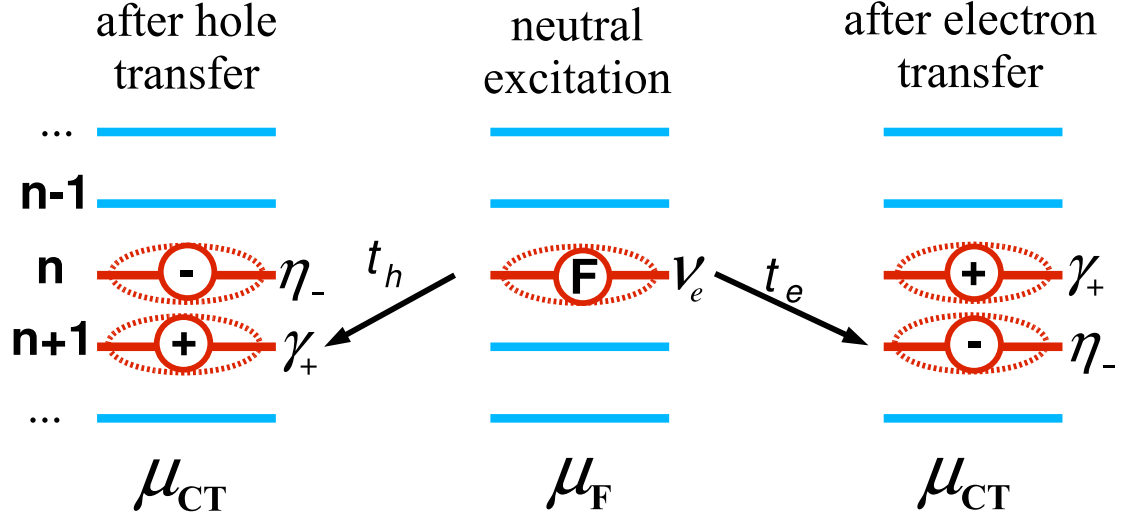
Figure 4.4: Schematic description of included (black arrows) charge transfer in the exciton model. Middle: neutral molecular excitation; left: CT state obtained from the neutral excitation after transferring a hole onto the neighboring site; right: CT state after transferring an electron. Each state can be obtained directly from the electronic ground state by an optical excitation governed by the large transition dipole $\boldsymbol{\mu}^{\mathrm{F}}$ of a molecular HOMO-LUMO transition or by the small intermolecular CT transition dipole $\boldsymbol{\mu}^{\mathrm{CT}}$.

where $H_{\alpha\alpha}^{\mathrm{CT}}(\mathbf{k})$ represents the CT transfer, and $H_{\alpha\alpha}^{\mathrm{F-CT}}(\mathbf{k})$ represents mixing between Frenkel and CT states between equally oriented molecules in the stack α. Since the A and B basis molecules are still subject to operations of the space group transforming them into each other, and to inversion symmetry of each molecule, in analogy with the Frenkel part we have $H_{AA}^{\mathrm{F-CT}}(\mathbf{k}) = H_{BB}^{\mathrm{F-CT}}(\mathbf{k})$ and $H_{AB}^{\mathrm{F-CT}}(\mathbf{k}) = H_{BA}^{\mathrm{F-CT}}(\mathbf{k})$. As a consequence of not including the transfer of charge between both basis molecules, the respective matrix elements are neglected, where $H_{AB}^{\mathrm{CT}}(\mathbf{k}) = 0$ and $H_{AB}^{\mathrm{F-CT}}(\mathbf{k}) = 0$. Fig. 4.4 gives a schematic overview over the transfer mechanisms in this model. The last index + or - indicates the direction of the charge transfer.

The matrix element of the charge transfer Hamiltonian can now be written as

$$H_{AA\pm}^{\mathrm{CT}}(\mathbf{k}) = H_{BB\pm}^{\mathrm{CT}}(\mathbf{k}) = E_{c\gamma_+\eta_-}^{\mathrm{CT}}, \tag{4.32}$$

where γ_+ and η_- represents counters for all the possible CT transitions between the vibronic levels $(0, \dots, \gamma_+^{max})$ and $(0, \dots, \eta_-^{max})$, so that the number of vibronic basis states sums up to $(\gamma_+^{max} + 1) \times (\eta_-^{max} + 1)$.

The matrix elements including mixing of Frenkel and CT states are

$$H_{AA\pm}^{\mathrm{F-CT}}(\mathbf{k}) = H_{BB\pm}^{\mathrm{F-CT}}(\mathbf{k}) = t_h' + e^{\pm i\mathbf{k}}t_e' \tag{4.33}$$

so that electron and hole transfer interfere with a specific **k**-dependent phase. Similar to eq. (4.14) we rotate the Hamiltonian by introducing new operators

$$c^\dagger_{\mathbf{k}x\gamma_+\eta_-\sigma} = \frac{1}{\sqrt{2}}(c^\dagger_{\mathbf{k}A\gamma_+\eta_-\sigma} - c^\dagger_{\mathbf{k}B\gamma_+\eta_-\sigma}) \tag{4.34}$$

$$c^\dagger_{\mathbf{k}y\gamma_+\eta_-\sigma} = \frac{1}{\sqrt{2}}(c^\dagger_{\mathbf{k}A\gamma_+\eta_-\sigma} + c^\dagger_{\mathbf{k}B\gamma_+\eta_-\sigma}) \tag{4.35}$$

where $\sigma = +, -$ represents either of the two directions of charge transfer along the stack, and the operators $c^\dagger_{\mathbf{k}y\gamma_+\eta_-\sigma}$ describe CT transitions with transition dipole along $\mathbf{b}//y$, and $c^\dagger_{\mathbf{k}x\gamma_+\eta_-\sigma}$ CT states with transition dipole in the ac plane.

To summarize, the operators introduced are used to construct a rotated Hamiltonian with the upper left corner containing the y component and the lower right the x component:

$$H^{\text{tot}}(\mathbf{k}) = \begin{pmatrix} H^{\text{F}}_{AA}(\mathbf{k}) + H^{\text{F}}_{BA}(\mathbf{k}) & H^{\text{F--CT}}_{AA\pm}(\mathbf{k}) & 0 & 0 \\ H^{\text{F--CT}}_{AA\pm}(\mathbf{k}) & H^{\text{CT}}_{AA\pm}(\mathbf{k}) & 0 & 0 \\ 0 & 0 & H^{\text{F}}_{AA}(\mathbf{k}) - H^{\text{F}}_{AB}(\mathbf{k}) & H^{\text{F--CT}}_{AA\pm}(\mathbf{k}) \\ 0 & 0 & H^{\text{F--CT}}_{AA\pm}(\mathbf{k}) & H^{\text{CT}}_{AA\pm}(\mathbf{k}) \end{pmatrix} \tag{4.36}$$

The resulting Hamiltonian was diagonalized numerically using the LAPACK routines.

4.4 Dipole moment

In each molecule, the transition dipole moment for transitions from the ground state $|\phi_g\rangle$ to the excited state $|\phi_e\rangle$ is given by the relevant off-diagonal matrix elements of the dipole operator $\hat{\boldsymbol{\mu}}$,

$$\boldsymbol{\mu}_{ge} = \langle \phi_g \mid \hat{\boldsymbol{\mu}} \mid \phi_e \rangle, \tag{4.37}$$

In order to be able to describe mixed Frenkel and CT eigenstates we introduce creator operators involving the respective part $u_{\xi\nu_e}$, $v_{\xi\gamma_+\eta_+}$, and $v_{\xi\gamma_+\eta_-}$ of the eigenstate j obtained from the diagonalization of eq. (4.36):

$$d^\dagger_{\mathbf{k}j\xi} = \sum_{\nu_e=0}^{\nu_e^{max}} u_{j\xi\nu_e} b^\dagger_{\mathbf{k}\xi\nu_e} + \frac{1}{\sqrt{2}} \Big(\sum_{\gamma_+,\eta_-=0}^{\gamma_+^{max}\eta_-^{max}} v_{j\xi\gamma_+\eta_-} c^\dagger_{\mathbf{k}\gamma_+\eta_-,+} + v_{j\xi\gamma_+\eta_-} c^\dagger_{\mathbf{k}\gamma_+\eta_-,-} \Big) \tag{4.38}$$

where $u_{j\xi\nu_e}$ ($v_{j\xi\gamma_+\eta_-}$) are the corresponding Frenkel (CT) eigenvalues of the matrix H^{tot} and ξ represents either x or y. Now, for an excitation carrying a momentum **k**, we can use eq. (4.37) to write the transition dipole moment for the Frenkel and CT states

$$\boldsymbol{\mu}_{\mathbf{k}j\xi} = \langle g \mid \hat{\boldsymbol{\mu}} \mid d^\dagger_{\mathbf{k}j\xi} g \rangle \tag{4.39}$$

For optical excitation corresponding to essentially vanishing photon momentum $\mathbf{k}$, the transition dipole moment can be expressed as a sum of Frenkel and CT transition dipoles at $\mathbf{k} = 0$:

$$\boldsymbol{\mu}_{\mathbf{0}j\xi} = \boldsymbol{\mu}_{\mathbf{0}j\xi}^{\mathrm{F}} + \boldsymbol{\mu}_{\mathbf{0}j\xi}^{\mathrm{CT}} = \sum_{\nu_e=0}^{\nu_e^{max}} u_{\mathbf{0}j\xi\nu_e}\langle g \mid \hat{\boldsymbol{\mu}} \mid b_{\mathbf{0}\xi\nu_e}^{\dagger} g\rangle + \sum_{\eta_-\gamma_+}^{\eta_-^{max}\gamma_+^{max}} v_{\mathbf{0}j\xi\eta_-\gamma_+}\langle g \mid \hat{\boldsymbol{\mu}} \mid (\frac{c_{\mathbf{0}\xi\eta_-\gamma_+,+}^{\dagger} + c_{\mathbf{0}\xi\eta_-\gamma_+,-}^{\dagger}}{\sqrt{2}})g\rangle$$

$$(4.40)$$

We divide this into a Frenkel and a CT part. When neglecting intermolecular exchange effects, $\boldsymbol{\mu}_{\mathbf{0}j\xi}^{\mathrm{F}}$ can be written as

$$\boldsymbol{\mu}_{\mathbf{0}j\xi}^{\mathrm{F}} = \sum_{\nu_e=0}^{\nu_e^{max}} \underbrace{\frac{1}{\sqrt{N}}\sum_n}_{=\sqrt{N}} u_{j\xi\nu_e}\underbrace{\langle \chi_n^{e\nu_e} \mid \chi_n^{g0_g}\rangle}_{=S_{0_g\nu_e}}\underbrace{\langle\prod_n \chi_n^{g0_g} \mid \chi_n^{g0_g}\rangle}_{=1}\underbrace{\langle\phi_n^e \prod_{m\neq n}\phi_m^g \mid \hat{\boldsymbol{\mu}} \mid \prod_{n'}\phi_{n'}^g\rangle}_{=\boldsymbol{\mu}_{ME}} =$$

$$= \sqrt{N}\boldsymbol{\mu}_{ME}\sum_{\nu_e=0}^{\nu_e^{max}} u_{\mathbf{0}j\xi\nu_e}S_{0_g\nu_e} \tag{4.41}$$

where $\boldsymbol{\mu}_{ME}$ is the transition dipole moment of an intra-molecular excitation. As discussed in Sec. 4.3, in the excitonic eigenstates the molecular transition dipoles $\boldsymbol{\mu}_A$ and $\boldsymbol{\mu}_B$ are superimposed, defining two orthogonal Cartesian direction x and y:

$$\boldsymbol{\mu}_{\mathbf{0}jx}^{\mathrm{F}} = \sqrt{\frac{N}{2}}(\boldsymbol{\mu}_A - \boldsymbol{\mu}_B)\sum_{\nu_e=0}^{\nu_e^{max}} u_{\mathbf{0}jx\nu_e}S_{0_g\nu_e}$$

$$\boldsymbol{\mu}_{\mathbf{0}jy}^{\mathrm{F}} = \sqrt{\frac{N}{2}}(\boldsymbol{\mu}_A + \boldsymbol{\mu}_B)\sum_{\nu_e=0}^{\nu_e^{max}} u_{\mathbf{0}jy\nu_e}S_{0_g\nu_e}$$

Neglecting exchange of electrons and holes between CT dimers and the other molecules in their ground states we get, using the same reasoning as for the Frenkel dipole, the charge transfer dipole moment

$$\boldsymbol{\mu}_{\mathbf{0}j\xi}^{\mathrm{CT}} =$$

$$= \sum_{\gamma_+\eta_-} v_{\mathbf{0}j\xi\gamma_+\eta_-}\frac{1}{\sqrt{N}}\sum_n\frac{1}{\sqrt{2}}\Big(\langle\phi_n^+\chi_n^{+\gamma}\phi_{n+1}^-\chi_{n+1}^{-\eta} \mid \prod_{\substack{m\neq n\\m\neq n+1}}\phi_m^g\chi_m^{g0_g} \mid \hat{\boldsymbol{\mu}} \mid \sum_{n'}\phi_{n'}^g\chi_{n'}^{g0_g}\rangle +$$

$$\langle\phi_n^+\chi_n^{+\gamma}\phi_{n-1}^-\chi_{n-1}^{-\eta} \mid \prod_{\substack{m\neq n\\m\neq n-1}}\phi_m^g\chi_n^{g0_g} \mid \hat{\boldsymbol{\mu}} \mid \prod_{n'}\phi_{n'}^g\chi_{n'}^{g0_g}\rangle\Big) =$$

$$= \sum_{\gamma_+\eta_-} v_{\mathbf{0}j\xi\gamma_+\eta_-}\sqrt{N}\sqrt{2}S_{\gamma_+0_g}^+S_{\eta_-0_g}^-\boldsymbol{\mu}_{MCT}, \tag{4.42}$$

where $\boldsymbol{\mu}_{MCT}$ is the transition dipole moment of a charge transfer towards the stack neighbor. The total expression of all the possible transition dipole moments can be written as

$$\boldsymbol{\mu}_{\mathbf{0}j\xi} = \sqrt{N}\Big(\sum_{\nu_e=0}^{\nu_e^{max}} \boldsymbol{\mu}_{ME} u_{\mathbf{0}j\xi\nu_e} S_{0_g\nu_e} + \sum_{\gamma_+\eta_-} \sqrt{2} S_{\gamma_+0_g}^+ S_{\eta_-0_g}^- \boldsymbol{\mu}_{\mathrm{MCT}} v_{\mathbf{0}j\xi\gamma_+\eta_-}\Big). \tag{4.43}$$

Since the total dipolar coupling strength is unaffected by the unitary transformations to the excitonic eigenstates, we can use the relation

$$\sum_{j\xi} \Big(|\boldsymbol{\mu}_{\mathbf{0}j\xi}^{\mathrm{F}}|^2 + |\boldsymbol{\mu}_{\mathbf{0}j\xi}^{\mathrm{CT}}|^2\Big) = N\Big((\boldsymbol{\mu}_A^{\mathrm{F}})^2 + (\boldsymbol{\mu}_B^{\mathrm{F}})^2 + (\boldsymbol{\mu}_A^{\mathrm{CT}})^2 + (\boldsymbol{\mu}_B^{\mathrm{CT}})^2\Big).$$

as an additional test to confirm the validity of the sums involved in the definition of the transition dipoles ν_ξ of the excitonic states. The contribution of each eigenstate $|d_{\mathbf{k}j\xi}^\dagger g\rangle$ to the optical spectrum is governed by the oscillator strength depending on the square of the transition dipole moment

$$f_{\mathbf{0}j\xi} = \frac{2m_e}{e^2\hbar^2} E_{\mathbf{0}j\xi} |\boldsymbol{\mu}_{\mathbf{0}j\xi}|^2. \tag{4.44}$$

As discussed in Sec. 3.3.4, the transition dipole moment of the CT state is typically less than one seventh of the molecular transition dipole, which gives a contribution below 2% to the oscillator strength. However, if the Frenkel and CT basis states are strongly mixed, the resulting mixed eigenstates can have a significant Frenkel character. Therefore, even excitonic eigenstates containing mainly CT transitions can acquire a substantial oscillator strength arising from the admixture of the large molecular transition dipole involved in the part coming from Frenkel excitons.

4.5 Sum rules

The vibronic progression observed for molecular crystals is subject to two types of sum rules, one concerning the transition dipoles and one regarding moments of the line shape as a function of energy.

4.5.1 Sum rules for transition dipoles

In a model where only Frenkel excitons contribute to the absorption, the overall strength of the HOMO-LUMO transition can be expressed as

$$\int dE \Im[\epsilon_{xx}(E)] = \frac{2\pi Z \mu_x^2}{\epsilon_0 V_0} \tag{4.45}$$

where the intergration shall extend over an interval of about $1.8-3.2$ eV, excluding higher transitions, and Z is the number of molecules in the unit cell, and V_0 the volume, and μ the transition dipole involved in the optical excitation. The values of the transition dipole

for each molecule can be found in Table 3.10 and the calculated area $\int dE tr[\Im(\epsilon_{\xi\xi})]$ in Table 4.1.

For DIP the experimental results gives a value of 4.2 eV [11] and a transition dipole of $\mu = 6.6\ D$ while our calculation gives a value of 7.2 eV and a transition dipole of $\mu = 8.1\ D$. From this we draw the conclusion that the calculated values are the upper bounds, whereas the experimentally determined transition dipole can work as a lower bound since the roughness of the film reduces the filling factor below 100%. Still, the experimental value is expected to be closer to the real value since measurements with atomic force microscopy (AFM) and X-ray data shows that the roughness defines by the root-mean-square error of the mean thickness is rms≈4.3 nm, which is still small compared to the mean film thickness of 33 nm.

compound	Fit: dielectric response		Fit: dipole		TD-DFT	
	$\int dE\Im\left[\epsilon_{xx}(E)\right]$ [eV]	$\int dE\Im\left[\epsilon_{yy}(E)\right]$ [eV]	$\boldsymbol{\mu}_x$ [D]	$\boldsymbol{\mu}_y$ [D]	$\boldsymbol{\mu}_x$ [D]	$\boldsymbol{\mu}_y$ [D]
α-PTCDA ϵ_{xx} [141]	2.905	-	4.711	-	4.653	-
α-PTCDA ϵ_{yy} [141]	-	3.241	-	5.005	-	5.135
PTCDA [110]	2.055	2.473	3.962	4.372	4.653	5.135
Me-PTCDI [127]	0.568	4.510	2.204	6.321	2.441	7.002
Me-PTCDI [14]	0.732	5.811	1.968	5.645	2.441	7.002
Me-PTCDI [142]	0.419	3.320	1.891	5.424	2.441	7.002
PB31 [14]	4.861	2.590	8.386	6.120	6.694	5.082
PTCDI [143]	5.965	0.177	6.964	1.162	7.553	1.268
PR149 [14]	2.183	2.084	5.259	5.107	4.850	4.710
DIP [11]	7.200	0.015	8.099	0.375	8.194	0.380

Table 4.1: Values of the fitted relative strength of the dielectric response (column two and three), and fitted (column four and five) and calculated dipole moment using TD-DFT (column six and seven).

4.5.2 Sum rules for exciton transfer

In the following, the transfer matrix elements $T_{AA}(\mathbf{k} = 0) \pm T_{AB}(\mathbf{k} = 0)$ occurring in the Frenkel part of the Hamiltonian will be abbreviated as T. According to Briggs *et al.* [133, 134, 132] a sum rule gives that the mean energy of the Frenkel spectra is

$$\langle E^{\mathrm{F}}\rangle = E_{00}^{\mathrm{F}} + S\hbar\omega + T \tag{4.46}$$

where $\langle E^{\mathrm{F}}\rangle$ can be expressed as the center of mass of the imaginary part of the dielectric function in the crystalline phase. From similar reasoning follows that the pure CT states have the center of mass of their optical transition line shape mass at a position given by

$$\langle E^{\mathrm{CT}}\rangle = E_{00}^{\mathrm{CT}} + (S_+ + S_-)\hbar\omega. \tag{4.47}$$

In the F-CT model the average energy of the HOMO-LUMO transition will be at

$$\langle E \rangle = \frac{\langle E^{\mathrm{F}} \rangle + \langle E^{\mathrm{CT}} \rangle \cdot p_{rel}^2}{1 + \mu_{rel}^2} \tag{4.48}$$

where the $\boldsymbol{\mu}_{rel} = |\boldsymbol{\mu}_{CT}|/|\boldsymbol{\mu}_F|$ is the weighting of the CT transition dipole relative to the molecular transition dipole. As discussed below, for the perylene pigments analyzed in the present work, the difference $|E_{00}^{\mathrm{CT}} - E_{00}^{\mathrm{F}}|$ never exceeds 0.3 eV, and $\mu_{rel}^2 = |\boldsymbol{\mu}_{CT}|^2/|\boldsymbol{\mu}_F|^2$ remains below 0.02, so that the CT transitions do not affect the average (4.48) by more than 0.006 eV. As this energy scale is irrelevant with respect to uncertainties arising from the analysis of measured data, in a further sum rule for the second moment, the influence of the small CT transition dipole will be ignored.

In a pure Frenkel model, it was shown previously that the second moment of the optical response does not depend on exciton transfer [134]

$$\langle (\Delta E)^2 \rangle = S(\hbar\omega)^2. \tag{4.49}$$

In the limit of vanishing transition dipole of the CT states, our mixed Frenkel-CT model gives a simple equation for the change in the second moment,

$$\langle (\Delta E)^2 \rangle = S(\hbar\omega)^2 + 2(t_e + t_h)^2, \tag{4.50}$$

where the contribution arising from electron and hole transfer reproduces the second moment obtained in a single particle picture.

4.6 Optical properties

To obtain the frequency-dependent elements of the dielectric tensor it is necessary to include the broadening of the vibronic subbands in a physically meaningful way. From the Lorentzian broadening of resonant Raman spectra and the decay of vibrational oscillations observed in pump-probe experiments, it can be estimated that the lifetime of optical excitations is of the order of a few picoseconds, corresponding to a FWHM of about 1 meV. Nevertheless, the strong coupling of the transitions to the elongation of low-frequency molecular vibrations and external phonons results in a Gaussian broadening with a FWHM of the order of 100 meV. Therefore, the imaginary part of each element of the dielectric tensor has to account for normalized Gaussian lineshapes of each transition

$$\Im[\epsilon_{xx}(\omega)] = \frac{2}{\epsilon_0 V \hbar} \sum_j \boldsymbol{\mu}_{\mathbf{0}jx}^2 f(\omega, \omega_{\mathbf{0}jx}, \sigma_{jx}) \tag{4.51}$$

and similar for $\epsilon_{yy}(\omega)$ and where the normalized Gaussian can be written as

$$f(\omega, \omega_{\mathbf{0}jx}, \sigma_{jx}) = \frac{1}{\sqrt{2\pi}\sigma_{jx}} exp\Big(\frac{-(\omega - \omega_{\mathbf{0}jx})^2}{2\sigma_{jx}^2}\Big). \tag{4.52}$$

Here $\omega_{\mathbf{0}jx} = E_{\mathbf{0}jx}/\hbar$ are the transition frequencies obtained from the diagonalization of the model Hamiltonian, the prefactor 2 represent spin degeneracy, and V is the volume of the crystal. To obtain the real part we apply the Kramers-Kronig transform

$$Re(\omega) = \frac{2}{\pi} P \int_0^\infty \frac{\omega' Im[\omega']}{\omega^2 - \omega'^2} d\omega' \tag{4.53}$$

where P denotes the Cauchy principal value. In the real part the frequency-dependent background from higher lying transitions $\chi_b(\omega)$ has to be accounted for as

$$\chi_b(\omega) = \chi(0)\frac{\Omega_g^2}{\Omega_g^2 - \omega^2} \tag{4.54}$$

where we assume a single transition frequency Ω_g and a contribution $\chi(0)$ to the static susceptibility. From this follows the real part of the dielectric tensor element ϵ_{xx}

$$\Re[\epsilon_{xx}(\omega)] = 1 + \chi_b(\omega) + \frac{2}{\epsilon_0 V \hbar} \sum_j \boldsymbol{\mu}_{\mathbf{0}jx}^2 \sqrt{\frac{2}{\pi^3 \sigma_j}} P \int_0^\infty \frac{\omega' e^{-(\omega' \pm \omega_{\mathbf{0}j})^2/2\sigma_j^2}}{\omega^2 - \omega'^2} d\omega' \tag{4.55}$$

From the dielectric function other optical properties can be derived, such as the refractive index through the relations $n = \Re(n) + i\Im(n) = \sqrt{\epsilon}$ and $\Im(\epsilon) = 2\Re(n)\Im(n)$. Furthermore, the absorption coefficient can be deduced from the extinction coefficient $\Im(n)$ using the relation

$$\alpha(\omega) = 2\frac{\omega}{c}\Im(n) \tag{4.56}$$

where the factor 2 comes from the fact that we square the wave amplitude to get the light intensity and its decay.

Optical density (OD) and reflectivity R provide complementary information on the real and imaginary parts of the refractive index. The optical density depends logarithmically on the transmission T

$$\text{OD} = -\log_{10}(T) \tag{4.57}$$

with the transmission given by

$$T = e^{-\alpha d}(1 - R)^2 \tag{4.58}$$

where d is the film the thickness, R the reflectivity and α the absorption given in eq. (4.56). When the organic film is grown on a substrate like glass, this formula can be generalized to different reflectivities of the front and rear surfaces of the film, but such differences will be ignored in the following. From the exponential in the definition of T, one expects the optical density to be proportional to the extinction coefficient, but the correction factor $(1 - R)^2$ generates energy-dependent deviations. Moreover, published values for the optical density tend to suppress an energy dependent slope in order to have a closer analogy to the extinction coefficient.

4.7 Data analysis

For the reference case of Me-PTCDI films studied at room temperature, digitized published data for the optical density and the reflectivity are presented in Fig. 4.5 [14].

In the fitting procedure a Kramers-Kronig consistent model function was defined for the complex refractive index n, and then all parameters were optimized. The extinction coefficient $\Im(n)$ was modelled with a sum of Gaussians. In order to perform an analytical Kramers-Kronig transform, each Gaussian was replaced by four superimposed Lorentzians with weights and relative widths kept at the same values with respect to a normalized Gaussian. For the real part of the refractive index a background coming from a sharp transition at a much higher values is included. Since this is similar to the background contribution of $Re(\epsilon)$, this background function does not generate a contribution $\Im(n)$ in the energetic range of interest.
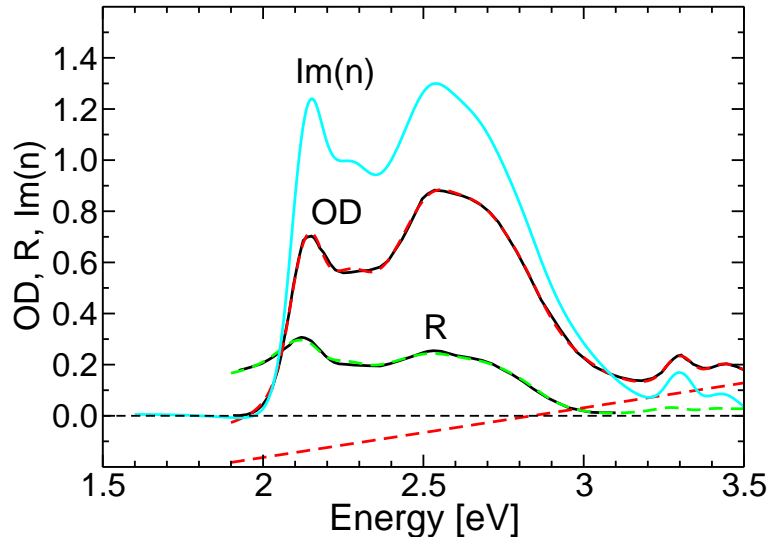
Figure 4.5: Optical density (OD), reflectivity (R), and extinction coefficient $\Im(n)$ of Me-PTCDI, at room temperature. Black: observed optical density of thin film with a thickness of about 100 nm and reflectivity of a single crystal with electric field polarized along the lattice vector **b** [14], red: fit to optical density, and assumed linear baseline underlying the published data, green: fit to reflectivity, blue: extinction coefficient $\Im(n)$. The fits are relying on a Kramers-Kronig consistent model for the refractive index.

We found clear evidence that the published optical density was corrected for a frequency-dependent background, compare Fig. 4.5, and we assumed that this background was described by a linear dependence on energy. The area and broadening of the different subbands can easily be obtained from the optical density, but without additional information on the reflectivity, it would not be possible to determine reliable values for the background of $\Re(n)$. Therefore, we alternated between fits of the Gaussian subbands contributing to $\Im(n)$ and an adjustment of the background of $\Re(n)$. As a result of this fitting procedure, we have determined a Kramers-Kronig consistent model for the complex

refractive index, and as visualized in Fig. 4.5, optical density and reflectivity calculated from this model give excellent agreement with the observed data. The optical density was measured on a polycrystalline film with random azimuthal orientation of the crystallites, so that about 90% of the absorption arises from the large diagonal component ϵ_{yy} of the dielectric tensor, and 10% from the small component ϵ_{xx}, compare Table 3.1. In the fit, we have assumed that both components have the same energy dependence. The modulation of the calculated reflectivity curve depends on the film thickness assumed in the fit of the optical density, and we found the best agreement at the reflectivity extrema occuring at 2.12 and 3.10 eV for a fixed film thickness of 86 nm in the fit of the optical density, in reasonable agreement with the experimental estimate of about 100 nm. Our best value for the film thickness was based on visual inspection of the agreement between calculated and measured reflectivity curve, as opposed to a fit of a free thickness parameter. Therefore, we give a conservative estimate of $d = 86 \pm 5$ nm for the film thickness underlying our analysis, excluding uncertainties of the absolute scale of the measured data which were not reported. Fig. 4.5 demonstrates that the reflectivity corrections in the definition to the optical density are responsible for small deviations between the shape of the observed optical density and the underlying extinction coefficient $\Im(n)$.

Chapter 5

Application to perylene compounds

In this chapter we will apply the exciton model to observed optical spectra of several molecular crystals. The first part discusses sample properties and measurements of optical spectra, including their temperature dependence. The following sections present a comparsion between calculated and observed line shapes of the dielectric function in PTCDA, DDTP, Me-PTCDI, PB31, PTCDI, PR149 and DIP, with two different degrees of sophistication of the exciton model.

5.1 Crystal preparation and optical measurements

The **PTCDA** single crystal measured by Alonso *et al.* was grown with temperature step sublimation under vacuum and the specific (102) crystal face used for optical measurements was obtained by cleavage. These spectra were obtained at room temperature using a spectral ellipsometer with rotating polarizer. The data set analysed in this thesis has been obtained from a reinterpretation of existing ellipsometry data [141] with a refined model for the propagation of light in a monoclinic medium because the exciton model discussed in this thesis has demonstrated that the dielectric tensor published earlier cannot be reproduced with model calculations.

The **Me-PTCDI** and **PR149** single crystals were grown from source material purified by vacuum sublimation using a two-zone furnace. PR149 was sublimed at 740 K and Me-PTCDI at 620 K. The thin films were prepared from evaporation and crystallization onto plain glass slides using conventional vacuum equipment. For the measurements, a spectrophotometer was used to collect the UV-Vis transmission and reflection spectra over a winde range of temperatures [14].

The **PB31** single crystal was grown from the vapor phase using argon as the carrier gas in the same sublimation equipment [109] and the measurements were carried out as for Me-PTCDI and PR149.

PTCDI was purified by a train sublimation method and the crystals were produced using a multisource-type molecular beam deposition system and the optical spectra were measured using a spectrophotometer.

DIP films were grown by organic molecular beam deposition (OMBD) on oxidized silicon wafers. To collect the data, the dielectric response including its anisotropy was obtained with variable-angle spectroscopic ellipsometry (VASE) [11].

The **DDTP** powder was purified twice by vacuum sublimation. The single crystals were then grown from the vapor phase sublimed at about 635 K using argon for 48 hours. The evaporated sample was then prepared under high vacuum using conventional evaporation equipment. A subsequent vapor treatment was performed using acetone vapor for 1 hour. The absorption spectra were performed using a UV/NIT Lambda 9 spectrophotometer [144].

5.1.1   Temperature dependence of optical observables

Previous studies of the temperature dependence of the lattice vectors have revealed that the stacking vector of Me-PTCDI and PR149 shrinks by at least 1% when going from room temperature to low temperature [14]. At room temperature, the anisotropic thermal expansion coefficient is of the order of 1×10^{-4} K^{-1}, and for PTCDA, the expansion coefficient of the stacking vector even exceeds this value [14, 138]. Assuming that the temperature dependence of the stacking vector in PTCDA remains particularly large when cooling the material, it can be estimated that its reduction should be around 1.5% when going to very low temperature. The calculated dependence of the CT transition energy on the stacking vector of 0.5 eVÅ^{-1} [118] gives an estimate of about 0.02 to 0.03 eV for the resulting red shift of the CT transition. Energetic shifts in this range are consistent with the temperature dependence of photoluminescence from CT states [139]. Concerning absorption spectra of PTCDA, a line shape analysis of low-temperature spectra reveal a red shift of the lowest Frenkel subband by about 0.02 eV with respect to ellipsometry data obtained at room temperature [127, 140]. For Me-PTCDI, the observed optical density at $T = 20$ K contains sharper structures, consistent with a red shift of the neutral molecular excitation by about 0.02 eV with respect to room temperature, and a reduced broadening. For simplicity, we assume that neutral molecular excitations and CT transitions shift in the same way as a function of temperature, or by -0.02 eV when reducing the temperature to $T = 20$ K. In the following, we shall analyse room temperature optical data for selected materials, where the sharper observed structures at low temperature allow for a more precise determination of the model parameters.

5.2   Modelling of optical spectra with Frenkel excitons

Before coming to the F-CT model we will first discuss the parameters for the pure Frenkel model presented in Sec. 4.2, determined from a comparison of eq. (4.46) with the average transition energy. The lowest dispersion branch at the Γ point of the Brillouin zone, $E_{00}^{\mathrm{F}}(\mathbf{0})$, corresponds to the lowest transition contributing to the dielectric function. The

difference between the molecular parameter E_{00}^{F} and the observed transition at $E_{00}^{\mathrm{F}}(\mathbf{0})$ can be determined by calculating the optical spectra of the pure Frenkel model.

We compare the dielectric tensor element $\Im(\epsilon_{yy})$ of Me-PTCDI with the Frenkel exciton model with parameters resulting in the same average transition energy $\langle E \rangle$ together with the observed value for the lowest subband which is assigned to $E_{00}^{\mathrm{F}}(\mathbf{0})$ in Fig. 5.1. This procedure allows us to determine an approximate exciton transfer $T = T_{AA}(\mathbf{0}) + T_{AB}(\mathbf{0})$ governing this element of the dielectric tensor. As the only evidence for the shape of the perpendicular diagonal element ϵ_{xx} is restricted to a reflectivity curve with similar shape as the one included in Fig. 4.5, but with reduced modulation, we assume that both tensor elements ϵ_{xx} and ϵ_{yy} coincide except for the size related to the respective dipolar coupling strength. This corresponds to a vanishing Davydov splitting since the exciton transfer between the differently aligned basis molecules $T_{AB}(\mathbf{0})$ is assumed to vanish.
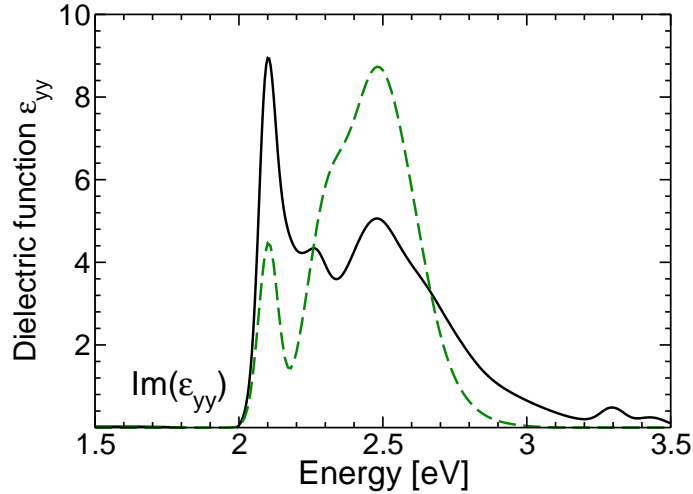
Figure 5.1: Imaginary part of the dielectric tensor element ϵ_{yy} derived from the measured optical density at $T = 20K$ [14] (black solid), and calculation based on a pure Frenkel exciton model (green dashed) with parameters chosen according to the sum rule in eq. (4.46), compare Table 5.1.

By reproducing the observed value of $\langle E \rangle$ and the position of the lowest subband $E_{00}^{\mathrm{F}}(\mathbf{0})$ one obtains the parameter set summarized in Table 5.1. From Fig. 5.1 it is obvious that this model is not flexible enough for obtaining a quantitative agreement with the observed intensities of the various subbands. However, this approach provides approximate starting values for E_{00}^{F} and the matrix element governing the transfer of neutral excitations. Moreover, for PTCDA, the anisotropy of the the optical observables measured by spectroscopic ellipsometry allows to determine reasonable parameters both for $T_{AA}(\mathbf{0})$ and $T_{AB}(\mathbf{0})$ [140, 141].

	T	$\langle E \rangle$	E_{00}^{F}	$S\hbar\omega$	$T_{AA}(\mathbf{0})$	$T_{AB}(\mathbf{0})$	$E_{00}^{\mathrm{F}}(\mathbf{0})$
	K	eV	eV	eV	eV	eV	eV
PTCDA ϵ_{xx} [141]	300	2.40	2.20	0.15	0.095	0.045	2.22
PTCDA ϵ_{yy} [141]	300	2.49	2.20	0.15	0.095	0.045	2.25
PTCDA [110]	300	2.49	2.16	0.15	0.18	0.11	2.23
DDTP [144]	12	2.12	1.76	0.15	0.25	–	1.82
Me-PTCDI [14]	20	2.43	2.05	0.15	0.23	–	2.10
Me-PTCDI [14]	300	2.46	2.08	0.15	0.23	–	2.13
PB31 [14]	12	2.36	1.96	0.15	0.25	–	2.01
PTCDI [143]	300	2.42	2.06	0.14	0.22	–	2.14
PR149 [14]	20	2.51	2.14	0.15	0.22	–	2.19
DIP [11]	300	2.48	2.22	0.15	0.11	–	2.25

Table 5.1: Model parameters for a pure Frenkel exciton model. The effective mode and its Huang-Rhys factor S are taken from Table 5.2, and the exciton transfer parameters are determined according to the sum rule in eq. (4.46) and the lowest observed subband, assigned to $E_{00}^{\mathrm{F}}(\mathbf{0})$ at Γ. The average observed excitation energy $\langle E \rangle$ of the HOMO-LUMO transition is obtained from an analysis of measured spectra, excluding the higher transition around 3.3 eV. The parameter $T_{AB}(\mathbf{0})$ responsible for Davydov splitting can only be addressed for PTCDA where a pronounced anisotropy of the dielectric tensor was observed [140, 141].

5.3 Modelling of optical spectra with interference of Frenkel excitons and CT transitions

5.3.1 Model parameters

In this refined exciton model containing both Frenkel excitons and CT states, the microscopic parameters can be divided into several groups. The first set of parameters addresses molecular deformations in excited or charged molecular states. As discussed in Sec. 2.3.4, these deformations can be calculated with DFT, and their parametrization in terms of an effective internal vibration is a well controlled procedure. Therefore, the respective parameters in Table 2.5 will be applied without modification. The second set of parameters consists of the electron transfer t_e and the hole transfer t_h. As discussed in Sec. 3.3.1 in more detail, Hartree-Fock and the hybrid functional B3LYP give somewhat different results, and in the present section, it will be shown that the B3LYP/TZ values in Table 3.6 are the better choice. However, from visual inspection of the agreement between model line shapes and measured data, and from a comparison with the analytical sum rule eq. (4.50) for the second moment, small modifications of the B3LYP/TZ starting values will be required in selected cases. The third group of parameters contains the lowest molecular transition E_{00}^{F} and the transfer parameters $T_{AA}(\mathbf{0})$ and $T_{AB}(\mathbf{0})$ governing the Frenkel excitons. As discussed in Sec. 5.2, the model containing only Frenkel excitons

together with the sum rule eq. (4.46) gives easy access to reasonable starting values, but the resulting line shape may be in rather poor agreement with the observations. Therefore, in cases of strong mixing of Frenkel and CT states with large transfer parameters of electron and hole, this simplistic model may give misleading parameters, and in the full exciton model, some modification will be unavoidable. Nevertheless, the sum rule eq. (4.46) will remain particularly useful. As will be demonstrated below in some detail, the difference $\Delta_{00} = E_{00}^{\mathrm{CT}} - E_{00}^{\mathrm{F}}$ between the lowest CT subband and the lowest molecular transition has a tremendous influence on the computed line shapes. At the present time, microscopic calculations of this difference are not yet very precise so that this difference Δ_{00} will be considered as a completely free fitting parameter.

On site energies: E_{00}^{F} and E_{00}^{CT}

The transition energies of neutral excitations (E_{00}^{F}) and CT states (E_{00}^{CT}) can be estimated from quantum chemical analysis but the resulting values are not precise enough for our purposes. However, the E_{00}^{CT} is expected to depend linearly on the intermolecular distance [145]. This argument builds on a parallel plate condensator with opposite charges on both plates. For PTCDA, the energies E_{00}^{F} and E_{00}^{CT} are consistent with the range deduced in previous model calculations [129, 122, 118]. For PTCDA and PTCDI, sign and size of the transfer parameters t_e and t_h seem to be arranged in a way that they counterfeit and weaken the influence of the CT state on the optical properties, once for $E_{00}^{\mathrm{CT}} - E_{00}^{\mathrm{F}} < 0$ (PTCDA), and once for $E_{00}^{\mathrm{CT}} - E_{00}^{\mathrm{F}} > 0$ (PTCDI). We found that for all molecules excluding PTCDA, the dependence on the stacking distance d is approximately $\partial(E^{\mathrm{CT}} - E^{\mathrm{F}})/\partial d \approx 0.06$ eV/Å, see Fig. 5.2. Possibly small deviations from linearity arise from different values for the effective dielectric function along the stacking vector. For PTCDA, the presence of the anhydride groups induces stronger hydrogen bridges between adjacent molecules and larger quadropole moments of each molecule. It remains unclear how the increased intermolecular interactions determine the deviation of the CT energy from the trend observed in the other perylene compounds.

Transfer of neutral excitations: T_{AA} and T_{AB}

The exciton transfer integrals can be estimated by the interaction between the transition dipoles of $\boldsymbol{\mu}_\alpha$ and $\boldsymbol{\mu}_\beta$ for sufficiently large distances between the corresponding molecules, see Sec. 3.4 for details. These parameters will be treated as quasi-free fitting parameters since they are neither calculated nor deduced from experiments because the static ϵ-tensor is unknown, except for PTCDA. As experimental information on the anisotropy of the optical properties is not available for all other compounds, $T_{AB}(0) = 0$ will be assumed throughout. However, the exciton transfer $T_{AA}(0)$ is restricted by sum rules discussed in Sec. 4.5, so that an approximate value can be obtained by studying the experimental spectra.

In cases where the long axes of the two basis molecules are close to parallel, one element of the dielectric tensor is dominating. In these cases, an effective transfer parameter $T = T_{AA} + T_{AB}$ is sufficient. In the case of PB31, the angle between the long axes of the
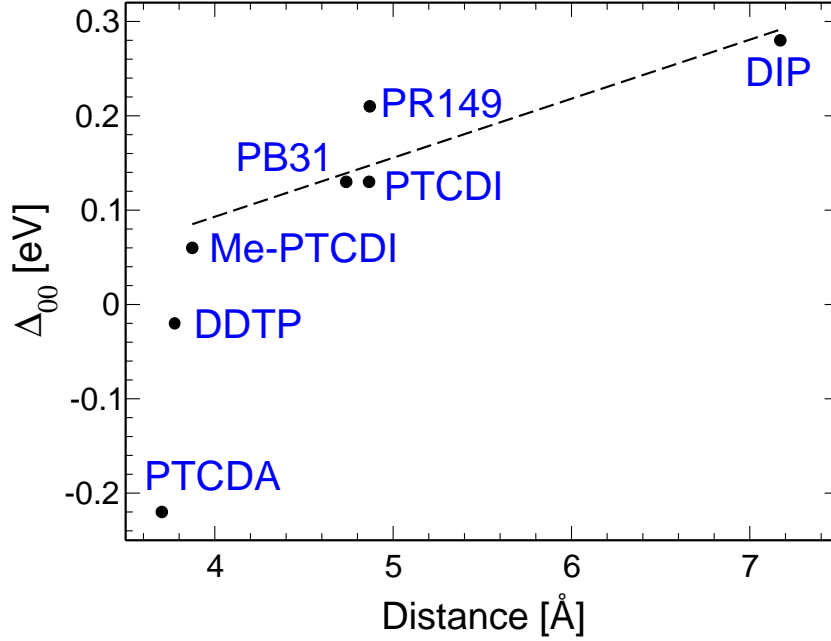
Figure 5.2: Dependence of the difference between the lowest vibronic subbands of the CT transition and the neutral molecular excitation $\Delta_{00} = E_{00}^{CT} - E_{00}^{F}$ on the stacking vector of the perylene compounds, together with a linear slope fitted through the values of all compounds except for PTCDA and DDTP. Their exact values can be found in Tables 3.4 and 5.5.

molecules is quite large, compare Table 3.4, so that a non-vanishing value for the exciton transfer T_{AB} might result in a pronounced anisotropy of the line shape of the refractive index.

The lowest transition contributing to the dielectric function corresponds to the lowest dispersion branch at the Γ point of the Brillouin zone, $E_{00}^{F}(\mathbf{k} = 0)$, not to the molecular parameter E_{00}^{F} occurring in the sum rule. Its position can be estimated by

$$E_{00}(\Gamma) \approx E_{00}^{F} + e^{-S}T + O(T^2) \tag{5.1}$$

and a more precise value can easily be obtained from a numerical diagonalization of the Frenkel Hamiltonian.

Ab initio parameters

The calculated parameters are summarized in Tables 3.10, 5.2 and 5.3. The dipole moments are taken from Table 3.11 and scaled in order to reproduce the area of the observed line shapes, compare Table 3.10.

compound	mode $\hbar\omega_{\text{eff}}$ eV	cation S_+ 1	anion S_- 1	excited S 1
PTCDA	0.171	0.348	0.649	0.880
DDTP	0.165	0.379	0.462	0.722
Me-PTCDI	0.170	0.336	0.625	0.867
PB31	0.175	0.166	0.635	0.873
PTCDI	0.170	0.276	0.552	0.816
PR149	0.170	0.191	0.730	0.882
DIP	0.165	0.311	0.560	0.929

Table 5.2: Effective internal vibration for the perylene compounds, with Huang-Rhys factors S_- and S_+ of the ionized states obtained with DFT, and the Huang-Rhys factor in the relaxed excited geometry with constrained DFT, all at the B3LYP/TZ level and with a frequency scaling of 0.973.

compound	t_e eV	t_h eV
PTCDA [141]	0.024	-0.034
PTCDA [110]	0.024	-0.034
DDTP [144]	0.044	-0.080
Me-PTCDI [127]	-0.080	-0.035
Me-PTCDI [14]	-0.090	-0.020
Me-PTCDI [142]	-0.090	-0.030
PB31 [14]	0.053	0.144
PTCDI [143]	0.019	0.076
PR149 [14]	0.015	0.088
DIP [11]	-0.033	-0.056

Table 5.3: Electron transfer and hole transfer used in the Frenkel-CT exciton model.

5.3.2 Optical spectra of perylene compounds

Since the pure Frenkel exciton model was only able to reproduce the energy of the lowest vibronic subband and the average transition energy $\langle E \rangle$, but failed to reproduce the observed dielectric function displayed in Fig. 5.1, the second moment of the calculated line shape remains much too narrow. This indicates that the pure Frenkel model is ignoring a fundamental interaction mechanism leading to an additional spreading of the calculated dielectric function over a larger energetic range. This section will be used to demonstrate that the Frenkel-CT interference via electron and hole transfer can account quantitatively for these features.

compound	$\boldsymbol{\mu}^{\mathrm{F}}_{x;y}$ D	μ^{F}_x D	μ^{F}_y D	$\boldsymbol{\mu}^{\mathrm{CT}}_{x;y}$ D	μ^{CT}_x D	μ^{CT}_y D
PTCDA ϵ_{xx} [141]	7.016	4.711	5.199	0.573	0.548	-0.169
PTCDA ϵ_{yy} [141]	6.754	4.535	5.005	0.552	0.527	-0.163
PTCDA [110]	6.481	4.352	4.803	0.530	0.506	-0.156
Me-PTCDI [14]	5.979	1.968	5.646	0.392	0.381	0.093
Me-PTCDI [127]	7.322	2.410	6.914	0.480	0.466	0.114
Me-PTCDI [142]	5.864	1.930	5.537	0.385	0.374	0.091
PB31 [14]	10.381	8.386	6.120	0.824	0.788	0.242
PTCDI [143]	7.061	6.964	1.169	0.632	0.561	-0.292
PR149 [14]	7.332	7.280	0.877	0.260	0.100	0.240
DIP [11]	8.099	8.091	0.375	0.018	-0.015	0.010

Table 5.4: Scaled dipole moments used in the fits, assuming that $\boldsymbol{\mu}^{\mathrm{F}}$ is oriented exactly along the long axis of the perylene core, and an orientation of $\boldsymbol{\mu}^{\mathrm{CT}}$ as obtained from a calculation of a stacked dimer.

In the Frenkel-CT model, for $E^{\mathrm{F}}_{00} < E^{\mathrm{CT}}_{00}$, the interaction between both types of excitations pushes the lowest vibronic subband down in energy, so that the lowest molecular transition E^{F}_{00} is required to be higher in energy than in the pure Frenkel model parameters given in Table 5.1. The sum rule (4.46) implies that the exciton transfer $T_{AA}(\mathbf{0})$ has to be reduced in order to keep the average transition energy $\langle E \rangle$ consistent with observations. The resulting model parameters used are summarized in Table 5.5.

Compund	T (K)	E^{F}_{00} (eV)	E^{CT}_{00} (eV)	Δ_{00} (eV)	$T_{AA}(\mathbf{0})$ (eV)	$T_{AB}(\mathbf{0})$ (eV)	$\boldsymbol{\mu}^{\mathrm{F}}$ (D)
PTCDA [141]	300	2.17	1.95	-0.22	0.14	0.05	7.02
PTCDA [110]	300	2.17	1.95	-0.22	0.14	0.05	6.75
DDTP [144]	12	1.86	1.84	-0.02	0.145	0.00	-
Me-PTCDI [14]	20	2.18	2.24	0.06	0.08	0.00	5.98
Me-PTCDI [14]	300	2.20	2.26	0.06	0.08	0.00	5.98
Me-PTCDI [127]	300	2.18	2.24	0.06	0.09	0.00	7.32
Me-PTCDI [142]	300	2.31	2.25	0.06	0.05	0.00	5.86
PB31 [14]	12	2.195	2.325	0.13	0.01	0.00	10.38
PB31 [14]	293	2.195	2.325	0.13	0.01	0.00	10.02
PTCDI [143]	300	2.18	2.31	0.13	0.06	0.00	7.06
PR149 [14]	20	2.155	2.365	0.21	0.12	0.00	7.33
DIP [11]	300	2.255	2.535	0.28	0.095	0.00	8.10

Table 5.5: Parameters of the Frenkel-CT model, with $\Delta_{00} = E^{\mathrm{CT}}_{00} - E^{\mathrm{F}}_{00}$.

PTCDA

Even though previous studies have shown that the mixing between Frenkel and CT states is rather small for PTCDA [122], we found evidence that the CT interference still has a significant influence on the optical line shape. An interesting feature of PTCDA is the anisotropy of the material, and by using data collected by Alonso *et al.* we can include this feature in our model fit. The calculation will also be compared to line shapes measured by Djurisic *et al.* [110] in order to access the quality of our model parameters for different sets of measured data.

For PTCDA, in contrast to DIP, the large angle between the transition dipoles of the two basis molecules results in an oscillator strength of similar size in both components of the dielectric tensor. Therefore, it is particularly interesting to analyze the impact of the relatively small mixing between Frenkel and CT states onto the optical response of this model compound. By applying second order perturbation theory to the off-diagonal matrix elements proportional to t_e and t_h according to eq. (4.31) we obtain a shift of the Frenkel exciton subband $E_{00}^{\mathrm{F}}(\mathbf{0})$ of less than 0.02 eV, so that the parameters resulting from a pure Frenkel model given in Table 5.1 should remain reasonable up to small changes within a similar energetic range.
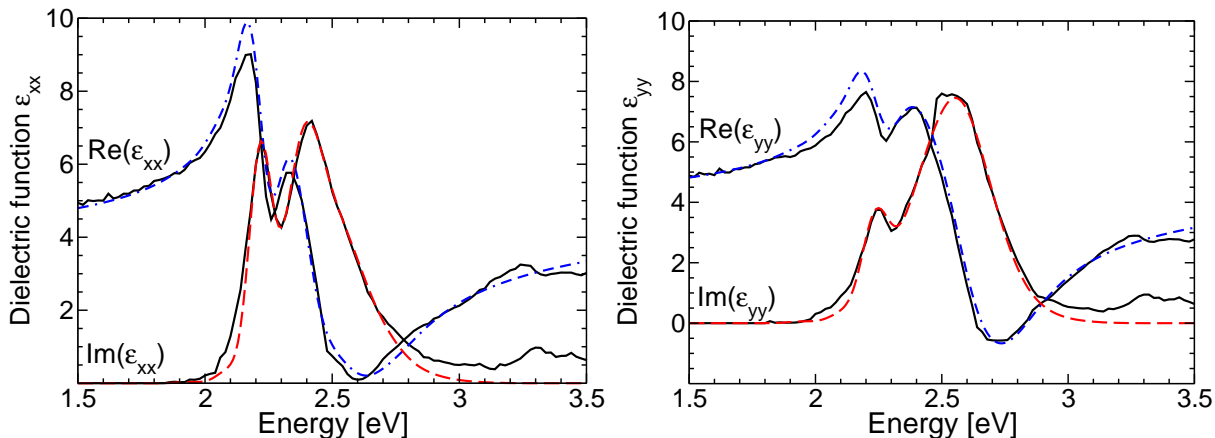
Figure 5.3: Comparison of the measured line shape of the elements of the dielectric tensor, obtained from a (102) face of a single crystal of α-PTCDA [141], and calculated (dashed) dielectric function for light polarization orthogonal (left) and parallel (right) to the **b**-axis of the crystal unit cell.

In Alonso's measurement for polarization along the **b**-axis, or parallel to the y axis of our Cartesian reference system, there are two prominent peaks, the first at $\sim$2.24 eV corresponding to a single vibronic subband, whereas the broad structure around 2.55 eV consists of several superimposed subbands, see Fig. 5.3. Both for ϵ_{xx} and ϵ_{yy}, the calculation reproduces the key features appearing in the experimental spectra, including in each case position and relative height of the lowest vibronic subband and the main band around 2.5 eV. The transition dipoles from Table 5.5 used in the calculated line shapes are close to the TD-DFT value of 6.93 D. Small deviations between the chosen

transition dipoles can be related to an energy-dependent slope contained in the observed data which may arise from unknown contributions such as non-specular diffuse reflection, so that the data analysis of spectroscopic ellipsometry gives a small positive value $\Im(\epsilon)$ in specific energetic regions where no Frenkel or CT transitions are expected, *e.g.* around 3 eV.

In the full F-CT model, the lowest transitions occur at 1.948 eV, slightly shifted down with respect to $E_{00}^{CT} = 1.95$ eV via the F-CT mixing. The size of these structures depends sensitively on the interference between the small values for the CT transition dipole obtained from TD-DFT calculations of a stacked dimer and the large transition dipole of the neutral molecular excitations. Even though these calculated absorption features are hardly visible in Fig. 5.3, recent PL excitation studies have demonstrated that excitation in this energetic region can selectively produce PL from CT states, confirming that our value of E_{00}^{CT} is realistic [139]. Moreover, at room temperature, in the region of the first excited vibronic level of the CT transition at $E_{01}^{CT} = E_{00}^{CT} + \hbar\omega = 2.12$ eV, PL excitation spectra show a resonance allowing selective excitation of PL from excimers [12], a further indication that weakly absorbing CT transitions play a key role for the excitation of PL from self-trapped CT excitons.

Due to the Frenkel transfer between differently aligned molecules the spectra for the two orthonogal polarizations are quite different. The center of mass of the calculated imaginary part of the dielectric tensor element $\Im(\epsilon_{xx})$ at $\langle E \rangle_x = 2.40$ eV, is lower than for the average over $\Im(\epsilon_{yy})$ at $\langle E \rangle_y = 2.49$ eV, which leads to a pronounced anisotropy, with $T_{AB}(\mathbf{0}) = (\langle E \rangle_y - \langle E \rangle_x)/2 = 0.045$ eV.

The small influence of CT states can also be observed by inspecting the first peak at 2.20 eV in the left panel and at 2.24 eV in the right panel of Fig. 5.3. These peaks contain little CT weight, due to the small Frenkel-CT mixing via the transfer matrix elements $t_e = 0.026$ eV and $t_h = -0.034$ eV. Furthermore, for PTCDA the relative size of the calculated CT transition dipole is very small, $\mu^{CT}/\mu^F = 0.06$, reducing the influence of the CT states on the optical response.

For PTCDA the CT energy of $E_{00}^{CT} = 1.95$ eV is well below the $E_{00}^{F} = 2.17$ eV, because the stacking distance in the crystal is particularly small. This large difference between the on-site energies can also explain why the CT state is not very prominent since it cannot efficiently borrow oscillator strength from the much stronger Frenkel transitions. As shown in Fig. 5.4 using the parameters in Table 5.1 for the pure Frenkel excitons according to the sum rules discussed in Sec. 4.5, the agreement with the observed dielectric tensor deteriorates significantly. Therefore, even though in PTCDA the mixing between Frenkel and CT states is particularly small, the adjustment of E_{00}^{CT} with respect to E_{00}^{F} in the full F-CT model still improves the calculated shapes of the two elements of the dielectric tensor. The sensitivity of the calculated lineshape on the energetic difference $E_{00}^{CT} - E_{00}^{F}$ is visualized in Fig. 5.5, where $E_{00}^{F} = 2.17$ eV was kept fixed, but E_{00}^{CT} was modified by ± 0.07 eV. From the significant deviation between the calculated line shapes for $\Im(\epsilon_{xx})$ and the observed data we conclude that our exciton model allows to determine the CT energy within an uncertainty range of $E_{00}^{CT} = 1.95 \pm 0.07$ eV, or less than half of the effective internal vibration.
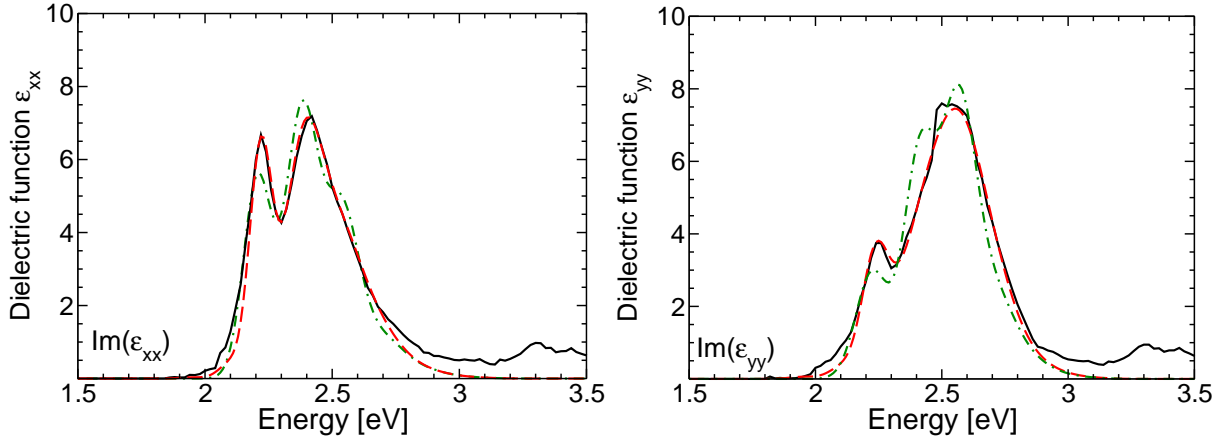
Figure 5.4: Comparison of revised values of the dielectric functions ϵ_{xx} and ϵ_{yy} [141] comparing the line shapes computed with the pure Frenkel (green dash-dotted) and the F-CT (red dashed) model, with parameters according to Tables 5.1 and 5.5, respectively.
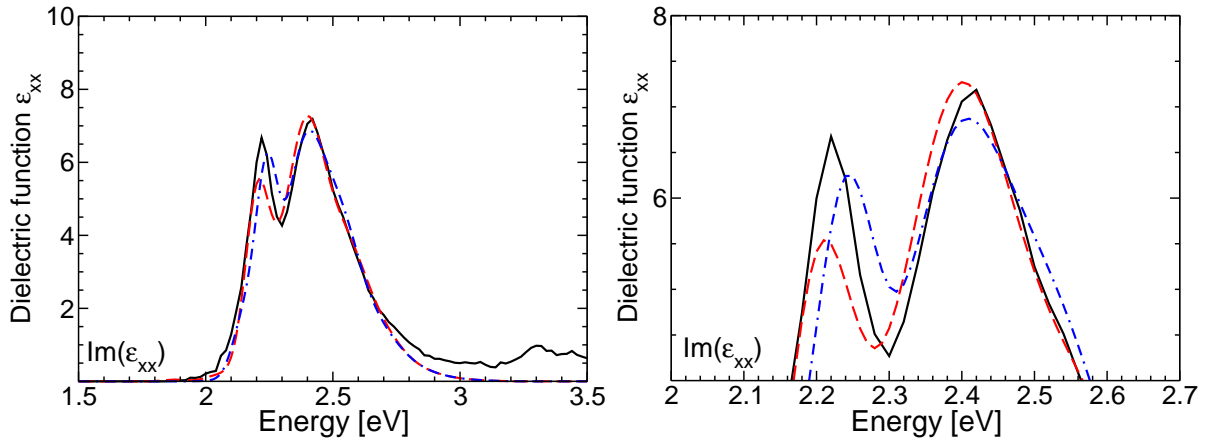
Figure 5.5: Left: as Fig. 5.3, but calculated with $E_{00}^{\mathrm{CT}} = 1.88$ eV (red dashed) and $E_{00}^{\mathrm{CT}} = 2.02$ eV (blue dash-dotted). Right: higher resolution, revealing substantial deviations for the lowest subbands.

In data obtained by Djurišić *et al.* [110] the higher transitions are lying around 3.3 eV and the dipolar coupling strength of the HOMO-LUMO transition is about 2/3 as strong as for the ellipsometry study of single crystals [141]. Except for the modified size of the dipole moments these data can be qualitatively reproduced with the same set of parameters. Residual deviations are partly related to the fact that the experimental data are not entirely Kramers-Kronig consistent, as opposed to the elements of the dielectric tensor deduced from spectroscopic ellipsometry, compare Fig. 5.3.

In summary, for PTCDA, the availability of the anisotropic dielectric tensor allows to deduce the parameters for transfer of neutral excitations $T_{AA}(\mathbf{0})$ and $T_{AB}(\mathbf{0})$ in a model relying exclusively on Frenkel excitons. The refined model including the mixing between Frenkel excitons and CT states can determine the energetic position of the CT transition
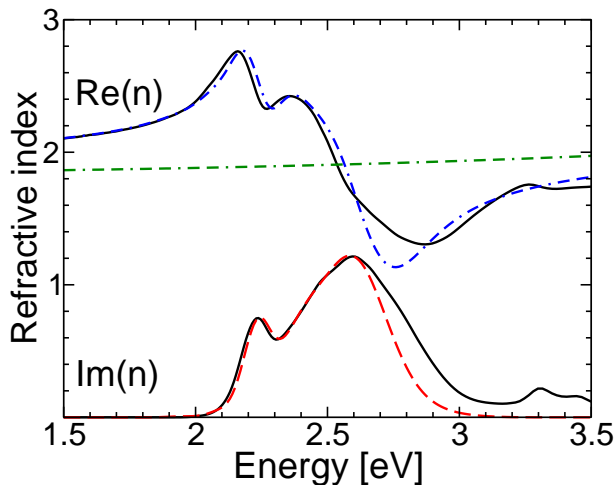
Figure 5.6: Refractive index of PTCDA thin films [110], and calculated values based on the average of the diagonal elements of the dielectric tensor, $(\epsilon_{xx} + \epsilon_{yy})/2$. The essential model parameters correspond to the fit of published ellipsometry data in Fig. 5.3, but we assumed an overall reduction of the dipolar coupling strength by a factor of 2/3. Broadenings of the various subbands were adjusted to the observed line shape.

within a precision of better than 0.07 eV, resulting in a quite remarkable agreement between calculated and measured line shapes. Due to the smallness of electron transfer t_e and hole transfer t_h, and due to their destructive interference, the full model does not require significant changes of the Frenkel parameters determined beforehand. Furthermore, PTCDA seems to be the only perylene compound studied in this report where the CT transition E_{00}^{CT} is placed significantly below the neutral excitation of a molecule in the crystalline phase, E_{00}^{F}. Therefore, weak transitions around 1.95 eV and 2.12 eV arising from E_{00}^{CT} and E_{01}^{CT}, respectively, allow the selective excitation of PL from CT states [139]. The value of $E_{00}^{\mathrm{CT}} = 1.95 \pm 0.07$ eV deduced from the Frenkel-CT model corresponds to an average CT transition energy of $\langle E^{\mathrm{CT}} \rangle = E_{00}^{\mathrm{CT}} + (S_+ + S_-)\hbar\omega = 2.12 \pm 0.07$ eV, in good agreement with an earlier estimate based on excimer PL arising from a self trapped CT exciton modeled as a deformed dimer, indicating a value in the range $\langle E^{\mathrm{CT}} \rangle = 2.14 \pm 0.08$ eV for the undeformed crystal [118].

Me-PTCDI

Among the compounds studied, Me-PTCDI has the largest electron transfer parameter t_e, so that the the calculated line shape $\Im(\epsilon_{yy})$ in Fig. 5.1 obtained from the pure Frenkel exciton model deviates strongly from the observed line shape. Indeed, the particularly large energetic difference between the strongest observed features at about 2.12 eV and 2.5 eV can only be reproduced with a very large value for t_e, so that the entire line shape is separated into two large bands, with weaker features in between. Irrespective of the position of the CT transition E_{00}^{CT} we found clear evidence that the B3LYP/TZ values of $t_e = -0.104$ eV and $t_h = -0.041$ eV are slightly too large in absolute size.

106
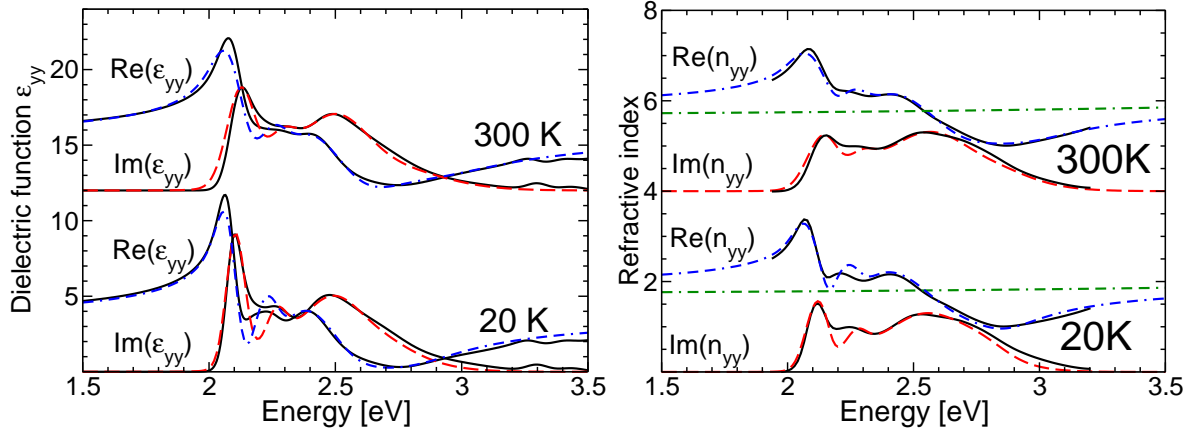
Figure 5.7: Me-PTCDI calculated line shapes compared with digitized observed spectra [14] at temperatures of 20K and 300K with parameters obtained from Tables 5.2 to 5.5. Left: comparison of calculated measured dielectric function for light polarization along y. The curves for 300K are shifted upwards by $+12.0$ for clarity. Right: comparison of calculated and measured refractive index. The curves for 300K are shifted upwards $+4.0$ for clarity. The green dot-dashed line is the background for the higher lying transitions for the real part of the refractive index, $\sqrt{1 + \chi_b(\omega)}$.

The measured spectra show a quite strongly absorbing lowest peak well separated from the band around 2.5 eV (Fig. 5.7), a direct consequence of the large electron transfer integral. When setting this parameter to zero the area of the lowest peak decreases significantly, resulting in a graph looking more similar to *e.g.* PTCDA. Even though the contribution to the peak at 2.10 eV from the CT states remains small, the removal of mixing would decrease it to a relative height of one fourth with respect to the subbands at higher energy. The hole transfer integral is rather small, so that it has only a minor impact on the overall lineshape.

As shown in Fig. 5.7, slightly reduced parameters for electron transfer of $t_e = -0.090$ eV and hole transfer of $t_h = -0.020$ eV provide a line shape in good agreement with the experimental curve when Frenkel and CT transitions are close to degenerate, $\Delta_{00} = 0.06$ eV. From eqs. (4.25 - 4.27), it can be deduced that at $\mathbf{k} = \mathbf{0}$, the off-diagonal matrix element between these two transitions is determined by the sum $t'_h + t'_e$. The deformation parameters in Table 5.2 together with $t_e = -0.090$ eV and $t_h = -0.020$ eV yield $t'_e = t_e S_{0_e 0_+} S_{0_g 0} = -0.062$ eV and $t'_h = t_h S_{0_e 0} S_{0_g 0_+} = -0.017$ eV, or $t'_h + t'_e = -0.079$ eV. In contrast to the simpler Frenkel exciton model, the lowest observed subband is no more placed slightly above the lowest molecular transition E^{F}_{00}. Instead, the particularly large interaction between Frenkel and CT manifold pushes it to 0.08 eV below E^{F}_{00}, but it still derives the main part of its oscillator strength from this molecular transition. According to the sum rule eq. (4.46), the increase in E^{F}_{00} by 0.13 eV with respect to the value estimated in the pure Frenkel model corresponds to a reduction in $T_{AA}(\mathbf{0})$ by a similar amount, so that the F-CT model is now based on a much smaller exciton transfer parameter of only

$T_{AA}(\mathbf{0})$=0.08 eV. Therefore, Me-PTCDI can serve as a prototype for a material where the mixing between Frenkel and CT states has the largest influence on the line shape of the optical response, as opposed to PTCDA, where the transfer of neutral excitations represents the most important intermolecular interaction.

The transition dipole μ^{F}=5.98 D used for the calculated line shape is below a previous experimental estimate of 6.8 $\pm$ 0.7 D [127] and our TD-DFT value of 7.42 D; compare Tables 5.5 and 3.11. Such a rather large deviation indicates a questionable absolute scale of the reflectivity and optical density underlying our experimental model line shape of ϵ_{yy} [14].

In the region of the first valley in the imaginary part of the dielectric function around 2.2 eV, the exciton model cannot provide an optical response of similar size. At the present stage, we do not know if this reveals a principal limitation of our approach or merely contributions from a slightly different crystal phase to the measured spectra, *e.g.*, based on different orientations of the methyl groups [146].

Similarly to the opposite limit of very small electron and hole transfer parameters realized for PTCDA, the position of the lowest CT transition can be determined quite accurately. In Fig. 5.8, the deviation of the calculated spectra from the experimental reference curve obtained for variations in the CT energy by ± 0.05 eV demonstrates that an uncertainty range of E_{00}^{CT}=2.24$\pm$0.05 eV at low temperature or E_{00}^{CT}=2.26$\pm$0.05 eV at room temperature is a conservative estimate.
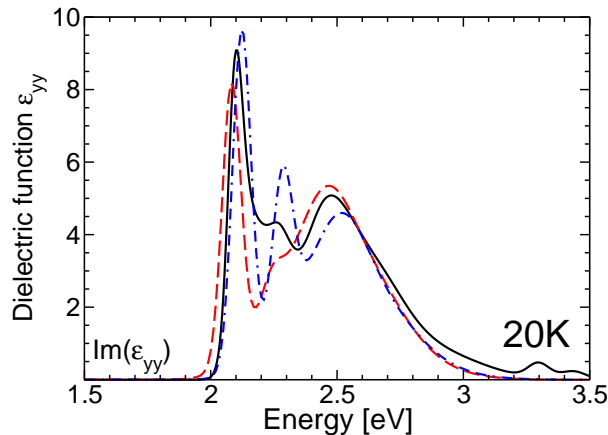
Figure 5.8: Me-PTCDI, with different values for the on-site energies using the best fit as a starting point and increasing and decreasing it by 50 meV, compared to the line shape ϵ_{yy} deduced from measured data, compare Sec. 4.7.

As Mizuguchis papers have also addressed the reflectivity of Me-PTCDI single crystals, we have digitized these data to analyze reflectivity with our model. The resulting line shape can be found in Fig. 5.9, showing good agreement between exciton model and measured spectra.

Two other groups have done measurements on the optical spectra of Me-PTCDI: Hoffmann *et al.* [57] and Lehmann *et al.* [142]. The Me-PTCDI spectra from Hoffmann
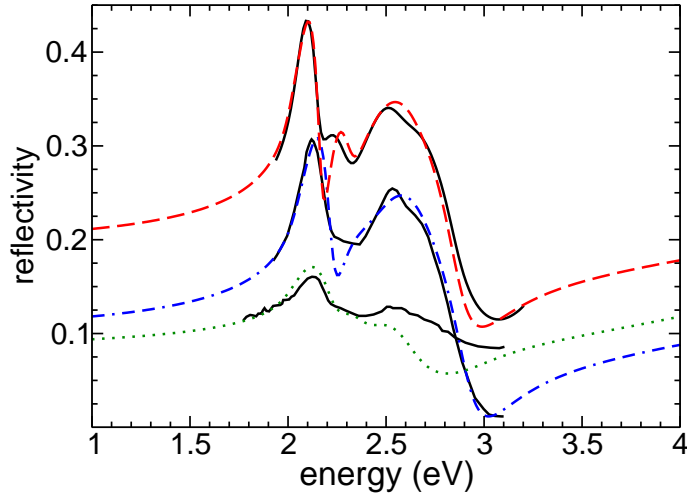
Figure 5.9: Measured reflectivity of Me-PTCDI (black solid) digitized from [14] compared with calculations using the Frenkel-CT model: unpolarized reflectivity (red dashed), reflectivity for polarization $\mathbf{E} \parallel \mathbf{b} \parallel y$ (blue dash-dotted), and for $\mathbf{E} \parallel x \perp \mathbf{b}$ (green dotted). For clarity, the curves for the unpolarized reflectivity are shifted upwards by $+0.1$.

et al. [127] have a center of mass for the imaginary part of the dielectric function at $\langle E \rangle = 2.44$ eV. The parameters used were close the ones used in the comparison with Mizuguchis data set, compare Table 5.5.
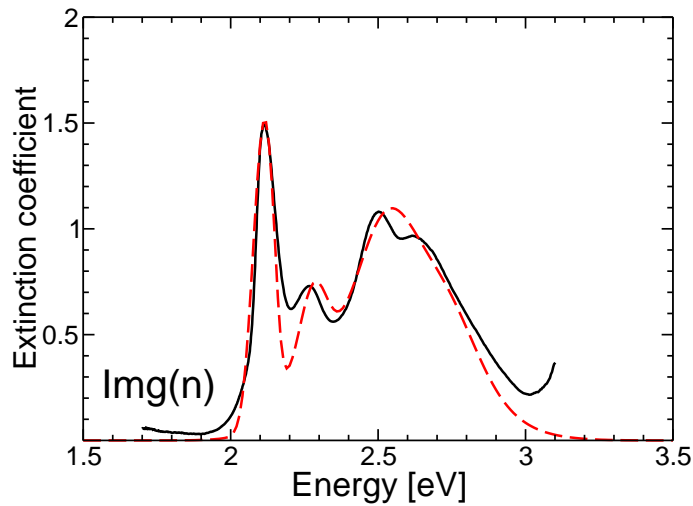
Figure 5.10: Comparison of the measured (black solid) by Hoffmann *et al.* [127], and calculated (red dashed) refractive index of Me-PTCDI.

Lehmann *et al.* have derived a Kramers-Kronig consistent dielectric function from spectroscopic ellipsometry [142], compare Fig. 5.11. The essential features of the dielectric function obtained by Lehmann *et al.* can be reproduced with a similar size of $\Delta_{00} = 0.06$ eV, but shifted E_{00}^{F}, using $E_{00}^{\mathrm{F}} = 2.25$ eV, $E_{00}^{\mathrm{CT}} = 2.31$ eV, and $T_{AA}(\mathbf{0}) = 0.05$ eV. The

shift in the energetic positions of the dielectric response indicates an influence of strain on the optical observables of thin film grown under different conditions.
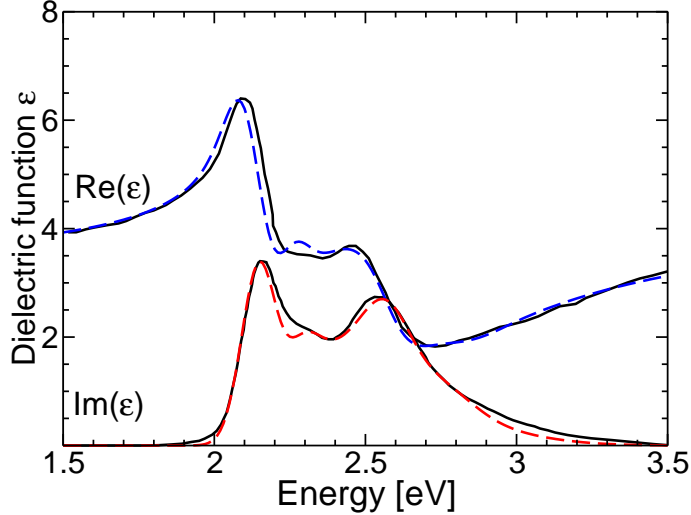
Figure 5.11: Calculated model line shapes for Me-PTCDI (dashed), superimposed to the measured dielectric function deduced from spectroscopic ellipsometry [142]. The calculation results from an average over the two diagonal components of the dielectric tensor, $(\epsilon_{xx} + \epsilon_{yy})/2$.

PB31

The spectrum of PB31 resembles the one of Me-PTCDI, but in PB31, the very large splitting between the two strongest features at 2.01 and 2.64 eV is realized by an extraordinarily large hole transfer parameter interfering constructively with a somewhat smaller electron transfer. In contrast to Me-PTCDI, the relatively large angle between the two long axes of the two basis molecules in the PB31 unit cell assigns substantial coupling strengths both to ϵ_{xx} and to ϵ_{yy}; compare Table 4.1. The published data for the optical density were measured on polycrystalline films, so that both diagonal elements of the calculated dielectric tensor have to be averaged. Based on the values t_h=0.144 eV and t_e=0.053 eV, the latter slightly reduced with respect to the B3LYP/TZ reference, our model can reproduce the experimental line shape quite well; compare Fig. 5.12. Together with the deformation parameters from Table 5.2, we obtain t'_h=0.131 eV and t'_e=0.034 eV, interfering constructively as $t'_h + t'_e$=0.165 eV in the off-diagonal matrix element between E_{00}^{CT} and E_{00}^{F}. Therefore, the lowest subband contributing to the dielectric function has again mixed Frenkel-CT character. The resulting line shape of the average between ϵ_{xx} and to ϵ_{yy} is visualized in Fig. 5.12 reproducing all details of the experimental reference. The best agreement with the experimental line shape is found if the CT transitions are significantly above the neutral excitations, with a difference of $E_{00}^{CT} - E_{00}^{F}$=0.13 eV. From modified values for the CT transition, we deduce again an uncertainty range of ±0.05

eV for E_{00}^{CT}. The transition dipole of μ^F=10.38 D underlying the calculated line shape deviates rather strongly from the TD-DFT reference of μ^F=8.62 D in Table 5.5 presumably due to a problem in the determination of the measured film thickness of 100 nm underlying our data analysis [14]. The black color of PB31 is a direct consequence of the exceptionally large contribution of $t_e + t_h$ to the second moment of $\Im(\epsilon)$ according to eq. (4.50), so that this material absorbs over a quite wide energetic region covering the entire visible range of the spectrum.
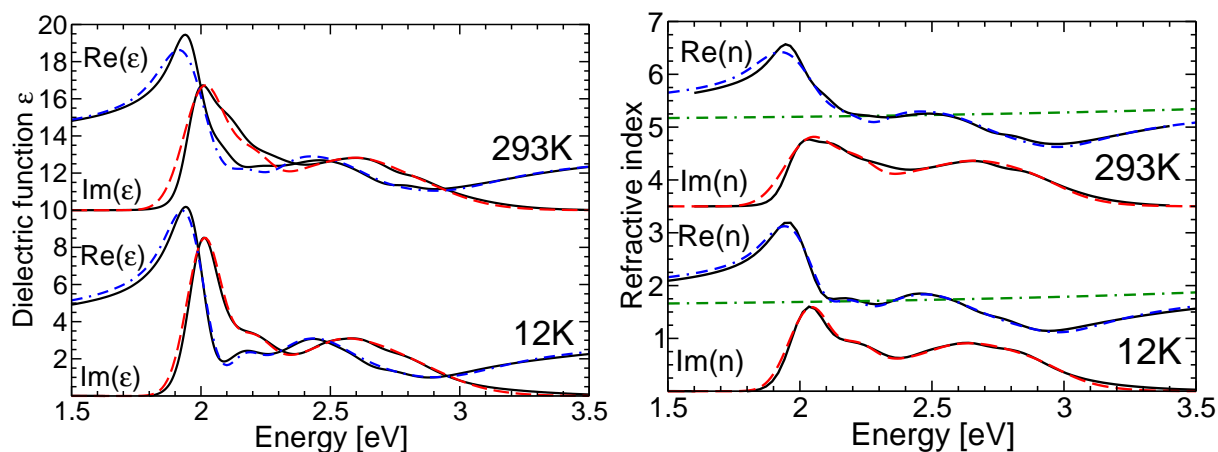
Figure 5.12: Comparison of calculated dielectric function (left) and refractive index (right) of PB31 (blue dashed, red dashed) and Kramers-Kronig consistent fit of measured data (black) [14].

PTCDI

PTCDI shows a quite large broadening of the lowest subband whose FWHM corresponds roughly to the energy of the calculated effective internal mode of 0.175 eV, see Table 5.2 [143], indicating a particularly large elongation of external vibrational phonons or low frequency internal vibrations after optical excitation.

The calculated hole transfer integral is fairly large, $t_h = 0.076$ eV, and due to the relative small electron transfer t_e =0.019 eV the off-diagonal matrix element between E_{00}^{CT} and E_{00}^{F} is still rather large, $t_h' + t_e' = 0.079$ eV. This leads to a strongly modulated optical response, as in Me-PTCDI and PB31, but the larger broadening gives this peak a broader base instead of a large height. To identify the subbands contributing we have recalculated the dielectric function for a reduced broadening. This reveals that the subsequent peaks do not follow a monotonous rise and then decrease when going to higher energies, but just as for Me-PTCDI and PB31, there is an intermediate "valley" region with reduced oscillator strength of the subbands. Although the electron transfer parameter remains the largest intermolecular interaction as in Me-PTCDI, the larger splitting $E_{00}^{CT} - E_{00}^{F} = 0.13$ eV reduces the impact of F-CT interaction onto the relative strength of adjacent vibrational subbands.
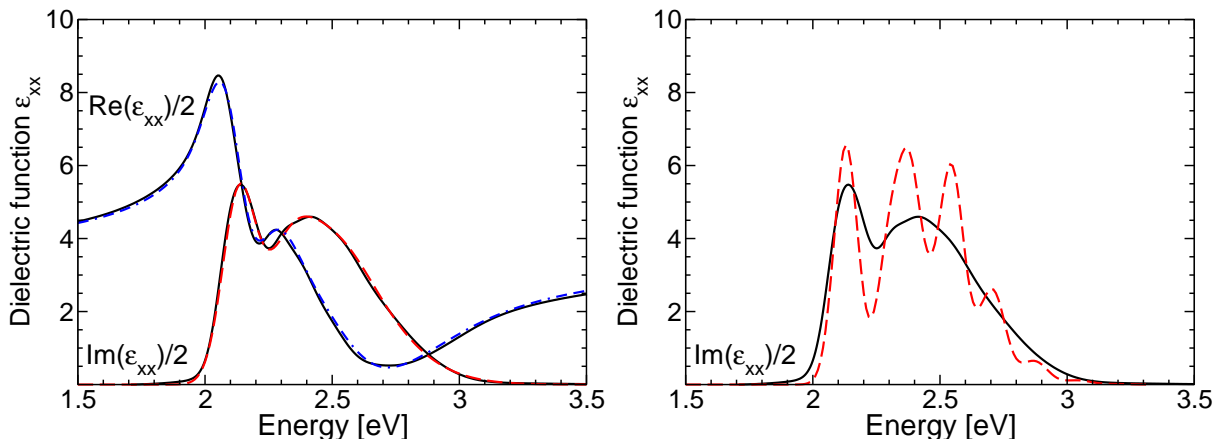
Figure 5.13: Left: comparison of the calculated dielectric function of PTCDI (blue dashed and red dashed) with a reference curve (black) obtained from a Kramers-Kronig consistent fit of measured data [143]. Right: the same fit parameters but with lower broadenings to emphasize the individual contributions.

The right panel of Fig. 5.13 reveals that in PTCDI the lowest subband is fairly prominent, larger than for PTCDA and PR149, but with less weight than for Me-PTCDI and PB31. In the left panel, the large broadening of the higher peaks makes the main features merge together, so that all the calculated peaks at 2.30 2.38 and 2.47 eV merge into a broad absorption band.

The anisotropy is found to be negligible due to the vanishing value of T_{AB}. The relative strength of the CT transition dipole $\mu^{CT}/\mu^F = 0.09$ is close to PTCDA. However, due to the rather large hole transfer integral $t_h = 0.076$ eV, the lowest peak is pushed quite far away from the main absorption band. We have checked that both structures move closer together when assuming vanishing electron and hole transfer, producing a calculated line shape resembling ϵ_{xx} in the case of PTCDA.

PR149

When using parameters for electron transfer and hole transfer in the range obtained from B3LYP/TZ the agreement of the model calculation in Fig. 5.14 with the dielectric function deduced from experimental data is fairly good, but the shape of the lowest vibronic subband cannot be reproduced quantitatively. In the experiment the distance between the first two peaks is 0.110 eV while for the model it is as large as 0.160 eV. This failure might indicate that charge transfer between the two basis molecules results in a substantial redistribution of oscillator strength between the lowest two subbands, an interaction mechanism not included in our approach. A model calculation with modified Huang-Rhys factors can improve on this situation, but we do not think such modified parameters can still have a sound microscopic foundation. Instead, from the TD-DFT results of the stacked dimer, we found that other low-lying dipole-active transitions occur rather close to the HOMO-LUMO transition. Therefore, it seems that a more complicated

exciton model based on several molecular transitions would be required in order to improve the agreement between calculated and measured line shapes.
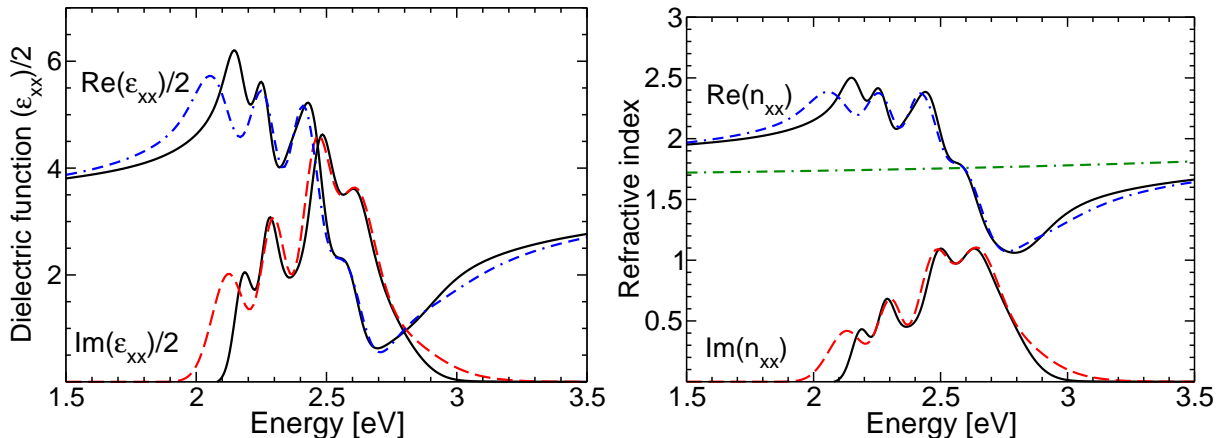
Figure 5.14: Left: model calculation of the dielectric function ϵ_{yy} of PR149 (red dashed, blue dashed) superimposed to Kramers-Kronig consistent dielectric function fitted to the published optical density [14]. The background of the real part of the dielectric function was assumed to correspond to Me-PTCDI. Right: refractive index where the green dot-dashed line is the background for the higher lying transitions for in real part of the refractive index $\sqrt{1 + \chi_b(\omega)}$.

DIP

Since the geometric overlap between adjacent DIP molecules in the thin film phase is almost negligible, all the intermolecular parameters remain particularly small, so that the crystal spectra are expected to resemble the free molecule. As we have shown in Fig. 5.15 the crystal spectra resemble a Poisson progression with Huang-Rhys factor around $S \approx 1$. With our transfer integrals $t_e = -0.033$ eV and $t_h = -0.056$ eV close to the B3LYP/TZ values, the model reproduces all experimental features. The transition dipole of the CT state is particularly small compared to the other molecules with p^{CT}/p^F=0.004.

As discussed in Sec. 3.1, in the thin film phase of DIP the orientation of the transition dipoles of the two basis molecules determines relative weights of 10^{-4} and 1 for the two components ϵ_{xx} and ϵ_{yy} of the dielectric tensor. From the tilting angle of $\theta = 19.8^0$ of the molecular long axes with respect to the substrate normal, we expect the large component to contribute with a relative weight of $\cos^2 \theta = 0.885$ to the component of the dielectric tensor along the substrate normal, and with $(\sin^2 \theta)/2 = 0.057$ to each of the components in the substrate plane, where the factor 1/2 arises from the random azimuthal orientation of the crystallites [11]. In this picture, both observable components of the dielectric tensor in the Cartesian reference frame of the substrate should be dominated by the large component ϵ_{yy} in the Cartesian reference frame defined by the two molecular transition dipoles oriented along long axes of the basis molecules, so that the tiny component ϵ_{xx}

cannot be observed separately. In addition, the components of the dielectric tensor in the substrate plane contain significant contributions from other transitions at energies somewhat above E_{00}^{F} of the HOMO-LUMO transition, presumably CT transitions arising from other pairs of molecular orbitals [11]. As a result, our model can only address the component of the dielectric tensor along the substrate normal in the form $\epsilon_{yy} \cos^2 \theta$, so that a comparison between calculated and observed optical line shape yields only $T_{AA} + T_{AB}$. As a calculation of ϵ_{xx} based on an exciton transfer $T_{AA} - T_{AB}$ cannot be compared to the observed in plane component of the dielectric tensor, the transfers T_{AA} and T_{AB} cannot be determined separately. Instead, we found that $T_{AA} + T_{AB} = 0.095$ eV together with $\Delta_{00} = E_{00}^{\mathrm{CT}} - E_{00}^{\mathrm{F}} = 0.28$ eV gives excellent agreement with the observed out of plane component of the dielectric tensor, compare Fig. 5.15.

By changing the energy difference $E_{00}^{\mathrm{CT}} - E_{00}^{\mathrm{F}}$ by ± 0.05 eV we find a large deterioration of the line shape. In this way we can pinpoint the difference between the two types of crystal excitations to be in the range $\Delta_{00} = E_{00}^{\mathrm{CT}} - E_{00}^{\mathrm{F}} = 0.28 \pm 0.05$ eV.
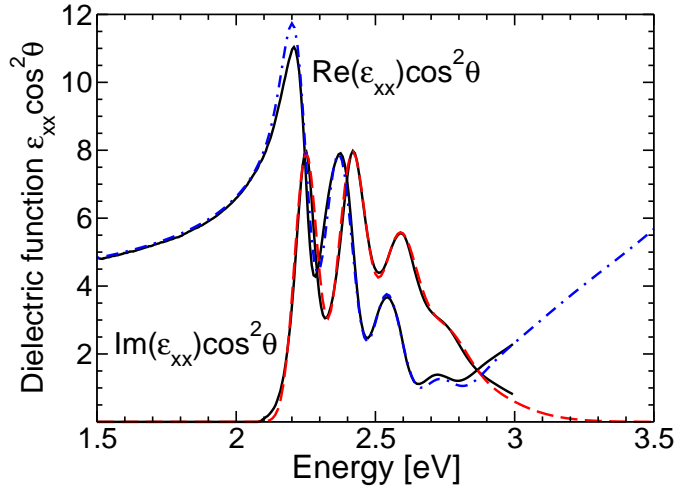
Figure 5.15: Dielectric function along the normal of the thin film phase of DIP ([11]), and calculated dielectric function ϵ_{xx}, scaled down by a prefactor $cos^2\theta$ calculated from the tilting of the long axis of DIP molecules from the substrate normal by $\theta = 19.8°$.

DDTP

Among the two crystal phases of DDTP, a detailed geometry of the molecular geometry in the crystal unit cell has only been presented for phase II, whereas for phase I, it has not been reported [103]. Therefore, the derivation of microscopically founded transfer parameters among stack neighbors can only be performed for phase II, so that in the following, the comparison between calculated and measured optical spectra will be restricted to this phase.

As mentioned before in Sec. 2.3.1 the geometric arrangement of DDTP can be seen as two pentacene molecules crossing each other. When studying the individual valence

orbitals the resemblance is further accentuated, compare Fig. 5.16 where the HOMO and LUMO character of pentacene can be identified. The similarity between the frontier
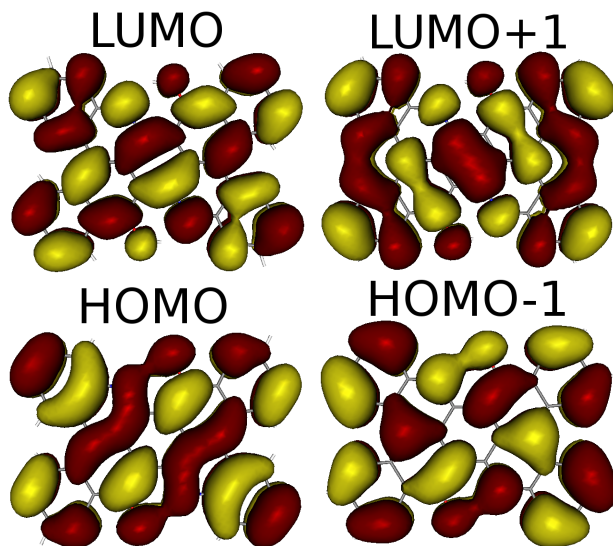
Figure 5.16: Valence orbitals of DDTP.

orbitals in DDTP and in pentacene raises the question how far the optical spectra of this compound will resemble crystalline pentacene. On the other hand, the stacking vector of only 3.775 Å reported in Table 3.4 is among the shortest of all perylene compounds investigated in this thesis, far below the stacking vector of pentacene which is as long as 6.14 Å [147].

In the exciton model, we found that the hole transfer parameter t_h yielding the best agreement with the observed spectra are still close to the B3LYP/TZ values, but the respective value for t_e is somewhat too large, compare Tables 3.6 and 5.3 and the absorption line shape in Fig. 5.17. The lowest observed peak at 1.88 eV is remarkably close to the lowest absorption band in crystalline pentacene at 1.85 eV [148]. However, from the parameters of the exciton model summarized in Table 5.5, this energy cannot be identified with E_{00}^{F}.

The coincidence between the energy of the lowest absorption band in DDTP and in crystalline pentacene raises the question how far this perylene compound can be used as a model for pentacene. From band structure calculations of pentacene, there is clear evidence that electron and hole transfer between the different basis molecules dominates, so that a Frenkel-CT model for pentacene should definitely include the respective entries. Modulation spectroscopy has helped to assign the energy of the CT state in crystalline pentacene to 2.12 eV, an energy representing presumably E_{00}^{CT}. However, since DDTP has a smaller distance of only 3.78 Å along the stacking direction compared to the shortest intermolecular separation in pentacene of 5.01 Å [147], we expect the value $\Delta_{00} = E_{00}^{\mathrm{CT}} - E_{00}^{\mathrm{F}}$ to be higher in pentacene, compare Fig. 5.2. This is just a rule of thumb while the DDTP perylene core is both bended and two OH-groups are attached, so that

DDTP does not necessarily follow the same dependence of Δ_{00} on distance as the other perylene molecules. Even though in pentacene the dominating interaction mechanism of Frenkel excitons and CT states will definitely require both basis molecules, the key parameters like E_{00}^{F} and the effective values for the interference between the electron and hole transfer parameters required in an exciton model seem to be quite similar to the respective values in DDTP. On the other hand, DDTP has a very high transfer parameter $T_{AA}(\mathbf{k}=0) = 0.145$ eV for Frenkel excitons, below the respective value of about 0.25 eV expected from line shape analysis according to the sum rule eq. (4.46).
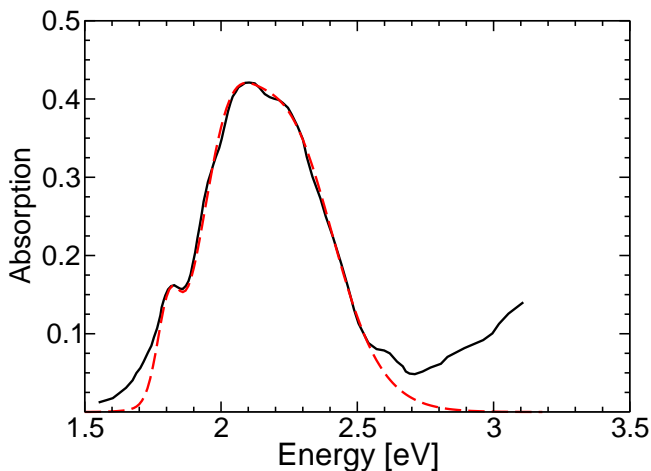
Figure 5.17: Measured (black solid lines) [144] and calculated (red dashed line) absorption of DDTP in phase II.

5.3.3 Summary

For all perylene compounds investigated, the F-CT model could reproduce the essential features of the observed spectra [149]. In most cases, the B3LYP values for the transfer parameters t_e and t_h are close to the values used to fit the observed line shapes. The constrained DFT method used for parameterizing the elongation of the effective internal mode in the relaxed excited state produces a Huang-Rhys parameter S lying systematically slightly above the value deduced from solution spectra. Therefore, the contribution of internal deformations to the second moment of the absorption band in somewhat too large, a fact we have compensated by reducing the size of the relevant transfer parameter $t_e + t_h$ by a small amount with respect to the B3LYP reference. Including these minor modifications of the DFT parameters for transfer of electrons and holes we have demonstrated that an exciton model accounting for the interference between Frenkel excitons and charge transfer transitions can quantitatively reproduce the observed optical spectra of several perylene compounds.

For compounds with relatively small electron and hole transfer, in this report PTCDA and DIP, the mixing of Frenkel and CT states results only in marginal modifications

of the neutral molecular excitation energy and the respective transfer matrix elements derived from a sum rule for the average transition energy of the Frenkel excitons. For crystals with stronger mixing of Frenkel and CT features, which was the case for all the other perylene compounds studied, the complete exciton model is needed to quantify the progression over the various vibronic subbands, and the preliminary parameters obtained in the Frenkel model have to be refined.

At this level, for compounds with substantial sum of fermionic transfer parameters $t_e + t_h$, the exciton model allows to determine the energies of CT transitions along the stacking direction within a precision better than 0.05 eV, an uncertainty range far below systematic deviations occurring in HF, DFT, or microelectrostatic calculations.

5.4   Photoluminescence excitation of PTCDA

The physical origin of the excitonic emission in polycrystalline molecular films and in polymers has been the subject of intense research for more than 20 years. In this context, photoluminescence excitation spectroscopy (PLE) has become a powerful optical technique allowing to establish a correspondence between specific absorption resonances and the resulting radiative recombination channels. For twisted molecules like para-hexaphenyl and various conjugated polymers, PLE has demonstrated a dependence of the photoluminescence (PL) bands on the excitation energy: When exciting above a certain threshold energy, the PL bands do not depend on the excitation energy, but below this threshold, they follow the excitation energy with a constant Stokes shift [150, 151]. This finding has been interpreted as a consequence of an inhomogeneously broadened distribution of transition energies, so that excitation at sufficiently high energy allows the exciton to migrate to any other site before eventually recombining under emission of a PL photon, whereas excitation in the lower part of the distribution addresses specific sites with low transition energies, so that the exciton remains in the same spatial region before eventually emitting in the region of the red edge of the inhomogeneously broadened PL band. This corresponds to a red shift with respect to the entire distribution of recombination energies which would become available when exciting above the threshold energy. Therefore, this threshold is interpreted as a localization energy, defining the demarcation between high energy excitons migrating between sites, and low energy excitons remaining confined in the spatial region where they have been excited [150].

Due to the rigidity of perylene-based chromophores and pentacene compared to polymers, a variation of the conjugation length or an internal twisting of the molecule can be excluded as a source of inhomogeneous broadening. Instead, external phonon modes are strongly elongated by optical excitations, resulting eventually in a pronounced Raman activity and correspondingly to rather broad absorption features [152, 153, 154].

Among these materials, the emission from molecular PTCDA single crystals and polycrystalline films shows a particularly rich variety of excitonic bands at low temperatures (10-100 K) [12, 155] and the identification of these recombination channels is still subject of intense debate. In this section, we analyze PLE spectra obtained on this compound,

allowing eventually to corroborate previous assignments of the various PL channels by identifying the respective PLE resonances.

Early PL investigations of PTCDA at low temperatures [12, 155] assign the high energy emission to Frenkel exciton transitions and attribute emission bands at lower energy to non-relaxed as well as to self-trapped charge transfer (CT) excitons. Several theoretical models that include Frenkel excitons, CT excitons and self-trapped excitons [126, 57, 59, 156] have been developed to describe and support the experimental observations.

More recent investigations use time-resolved PL (TRPL) measurements on α-PTCDA single crystals and on polycrystalline films to differentiate various recombination channels [157, 158, 159, 160]. The TRPL studies were performed in the temperature range from 10 to 300 K. From the recombination times that were detected within the emission band, five different exciton emission channels have been isolated at low temperature [58, 159]: (1) A high energy emission band around 1.95 eV due to a non-relaxed charge transfer transition (CT2-nr) between two PTCDA molecules stacked along the **a** direction, (2) a pronounced Frenkel exciton transition with emission maximum at ~1.82 eV starting from a minimum of the excitonic dispersion at the surface of the Brillouin zone, (3) a relaxed charge transfer transition between two PTCDA basis molecules within the same unit cell (CT1) with a peak energy at ~1.85 eV, (4) a self-trapped CT2 exciton involving a reduced distance between stacked PTCDA molecules with peak energy at ~1.71 eV, and (5) the respective excimer transition with a PL maximum at ~ 1.76 eV which is weak at low temperature but becomes the dominant band at higher temperatures (T > 200 K). Accordingly, the E-band is attributed to excimer-like states that are preferentially formed at stacking defects in PTCDA layers. For 650 nm thick polycrystalline PTCDA films, in the region around 2.1 eV, a twentyfold enhancement of the PL efficiency was observed with respect to excitation into the Frenkel exciton manifold above 2.2 eV, revealing a particular excitation resonance [12]. A resonance of the photocurrent in the same region around 2.1 eV indicates an excitation resonance favoring charge separation [161]. These band assignments are supported by recent PL measurements under uniaxial pressure [162]. With increasing pressure, the CT2 gains intensity relative to the Frenkel exciton emission, and the CT2 transition reveals a shift to lower energies. Both observations are attributed to an increased exciton trapping probability and to an enhanced binding energy at a reduced distance between stacked molecules. These interpretations as well as the above mentioned band assignments are further supported by theoretical models that handle pure Frenkel exciton transitions [129, 122, 163] and CT states separately [118].

In addition to the PL investigations, only a few studies have applied the technique of photoluminescence excitation (PLE) to PTCDA films [108, 164]. In these investigations the tunable excitation source covers the PTCDA absorption band from ~2.0 eV up to ~3.0 eV. The change of the PLE signal as a function of the substrate temperature [108] and of the growth temperature [164] of deposited films was used to study the influence of the α- and β-phase growth morphology on the optical properties rather than to identify different PL lines according to their electronic nature. In particular, investigations on PTCDA films deposited on different substrates like quartz, KCl, and NaCl attribute the energy band at ~1.85 eV (Y-line) to the β-phase of PTCDA, whereas the low energy

band at ∼1.71 eV (E-band) is assigned to the α-phase [108]. More recent investigations on PTCDA films deposited on Ag(111) [164] at different growth temperatures show a weak dependence of the Y-line as a function of the PTCDA growth morphology whereas the E-band shows an intensity maximum in a temperature regime where the α- and β-phase coexist. Accordingly, the E-band is attributed to excimer-like states that are preferentially formed at stacking defects in PTCDA layers.

The PLE measurements analysed in the following have been obtained on α-PTCDA single crystals and polycrystalline films grown on naturally oxidized Si(100) substrate. The optical excitation energy was varied below the 0-0 Frenkel exciton absorption band, allowing the selective excitation of Frenkel excitons as well as of various CT excitons.

The interpretation of the PL and PLE spectra discussed in the following is based on existing calculations concerning the dispersion of pure Frenkel excitons [129] and investigations of PL from self-trapped CT excitons involving two stack neighbors at reduced intermolecular distance [118]. Moreover, the full Frenkel-CT exciton model will be applied to an assignment of the PLE resonances, and the excitonic dispersion derived from the Hamiltonian according to eq. (4.36) corroborates previous assignments of the various radiative recombination channels.

5.4.1 Experimental results

The PLE measurements were performed with an Ar-ion laser ($\lambda = 514$ nm) pumped dye laser as variable excitation source. The covered energies ranged from 1.88 eV to 2.15 eV. Details on the experimental setup can be found in [139]. Fig. 5.18 shows the PL of a PTCDA single crystal at 5 K at various excitation energies ranging from 1.878 to 2.149 eV and at a laser power of 100 μW.

At the lowest excitation energy (1.878 eV), significantly below the 0-0 transition of the CT2 exciton assigned to 1.95 eV in Fig. 5.18, a broad emission band with a peak at 1.72 eV can still be excited. As this excitation energy does not correspond to any excitonic state in the ideal periodic crystal, this excitation channel is assigned as a defect in the crystal, *e.g.* a stacking fault . Since this PL band around 1.72 eV is close to the CT2 transition energy identified by time-resolved PL measurements on PTCDA crystals at low temperatures [58, 158], this is assigned to the self-trapped CT2 exciton transition between oppositely charged stacked PTCDA molecules at a reduced distance. The CT2 band reaches its intensity maximum at an excitation energy of 1.893 eV and then decreases at higher excitation energies up to 1.92 eV. When exciting above 1.90 eV, a second PL band with rapidly increasing intensity emerges at energies above 1.8 eV. With increasing energy, the center energy of this band shifts linearly to higher values and reaches a constant value (∼ 1.86 eV) at excitation energies larger than 1.968 eV. This emission band is assigned to the relaxed CT1 transition between PTCDA molecules within the same unit cell. In addition a weaker emission band appears in the PL spectra, separated from the CT1 band by ∼160 meV to lower energy. This weak PL band shows the same excitation energy dependence as the CT1 emission. Accordingly, it is attributed to the first vibronic subband of the CT1 transition where the energy difference of ∼160 meV corresponds to the effective internal
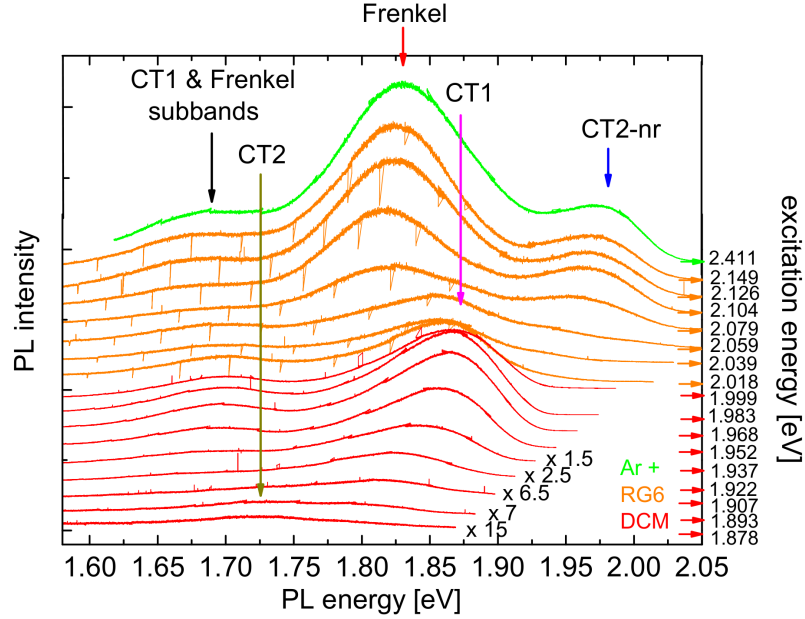
Figure 5.18: Excitation PL spectra of a PTCDA single crystal at 5 K at excitation energies ranging from 1.878 to 2.149 using DCM and Phodamine 6G dye lasers as labeled [139]. The topmost spectrum is excited with an Ar ion laser at an excitation energy of 2.411 eV. The PL spectra are offset to each other for clarity and the weakest spectra at low excitation energy are multiplied by different magnification factors as labeled.

vibrational mode of the molecule at about 170 meV [12, 57].

Above 2.018 eV excitation energy, the CT1 emission decreases, and two new PL bands appear at ∼1.79 and at ∼1.92 eV. With increasing excitation energy the intensities of both bands increase rapidly. The emission at ∼1.92 eV shows a blue shift with increasing excitation energy similar to that of the CT1 transition and its vibronic subband at lower energy. The 1.79 eV emission band also shows a shift to higher energy, but with a significantly lower rate. For higher excitation energies (>2.12 eV) consult [139].

Figs. 5.19 and 5.20 summarize the shifts of the spectral positions and the PL intensities (Gaussian areas) of the different recombination channels, respectively, as a function of the excitation energy ranging from 1.878 to 2.149 eV. The center energies E_j and the Gaussian areas a_j of the emission bands were deduced from Fig. 5.18.

Fig. 5.19 clearly reveals a blue shift of the CT1 emission and its vibronic subband when the laser starts to excite the low energy part of the inhomogeneously broadened distribution of the CT1 states. Since the density of these low energy states is small, the PL intensity is initially weak but rapidly grows with increasing excitation energy due to the rising number of accessible states, as shown in Fig. 5.20. When the laser excitation exceeds the maximum of the CT1 state distribution, the optically excited states start to relax into energetically lower lying states. Therefore, the CT1 emission resembles the density of states distribution leading to constant PL center energies of ∼1.86 and ∼1.70 eV
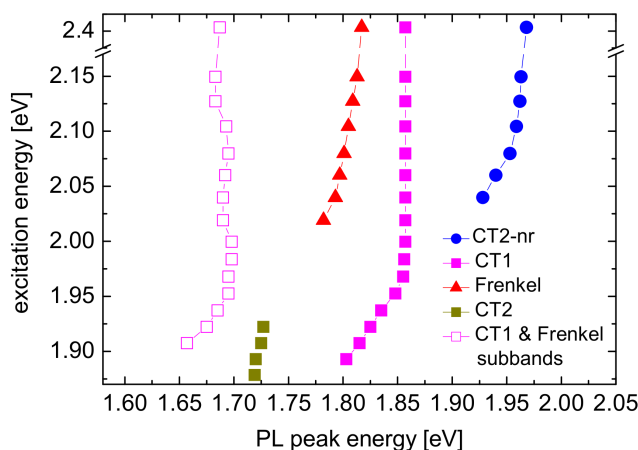
Figure 5.19: Different exciton emission channels in a PTCDA crystal at 5 K as a function of the excitation energy ranging from 1.878 to 2.149 eV. The emission channels are obtained from the spectra in Fig. 5.18 by a multi-Gaussian decomposition of the observed line shape as described in the text.
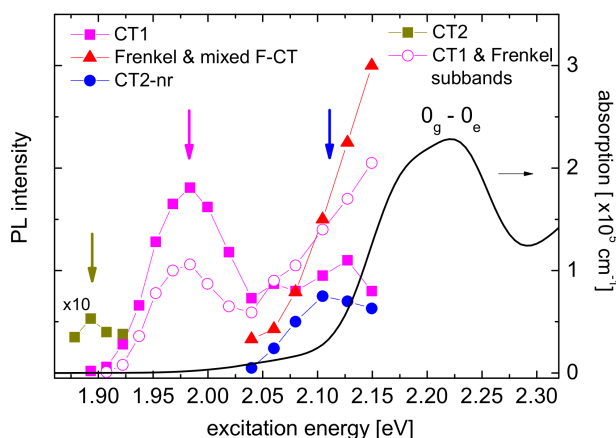
Figure 5.20: PL intensity (Gaussian areas) of different emission channels in PTCDA crystals at 5 K as a function of the excitation energy ranging from 1.878 to 2.149 eV obtained from the spectra in Fig. 5.18. Arrows indicate the energy positions of the distribution maxima of CT2, CT1 and CT2-nr states, respectively. In addition an absorption curve derived from the optical density of a 36 nm thick PTCDA film on Pyrex at 10 K using a Kramers-Kronig consistent model for the complex refractive index is shown as black solid line.

for the CT1 and its vibronic subband, respectively. Since the density of states decreases at energies above the peak of the CT state distribution, the PL intensity of the CT1 transition and its vibronic subband decreases for excitation energies higher than 1.983 eV (see Fig. 5.20).

For excitation energies larger than ∼2.04 eV the indirect Frenkel exciton and the CT2-nr start to occur in the PL spectra. While the CT2-nr transition energy shows a similar dependence as the CT1 transition for laser energies that are below the maximum of the state distribution, the Frenkel exciton transition reveals an unexpectedly weak excitation energy dependence (see Fig. 5.19). Although the optical excitation energies are significantly lower than the $|0_g\rangle \rightarrow |0_e\rangle$ absorption energy of ∼2.20 eV [129, 122, 163] the relaxed Frenkel exciton transition energy reached its final value of 1.82 eV already at ∼2.15 eV excitation energy.

5.4.2 Excitonic dispersion

In accordance to Chap. 4, the exciton model discussed in the following includes neutral molecular excitations and CT transitions between stack neighbors. In order to remain compatible with previous assignments of PL spectra summarized in Sec. 5.4.2 [158], in the present section 5.4.2, the CT state along the stack will be called CT2, whereas a further CT state involving both basis molecules in the unit cell will be called CT1. According to Sec. 4.3, neutral molecular excitations and CT2 states are coupled via electron transfer t_e and hole transfer t_h as to eq. (4.33).

Due to momentum conservation, the small wave vector of the photon results in an excitonic Bloch wave close to the Γ point of the Brillouin zone, or $\mathbf{k} = 0$. For this particular wave vector, electron and hole transfer interfere constructively according to $t'_h + t'_e$, but for PTCDA with its nearly parallel valence and conduction bands, t_e and t_h have opposite signs, so that the contribution of the Frenkel-CT mixing to the second moment of the absorption band according to

$$(\Delta E)^2 = S(\hbar\omega)^2 + 2(t_e + t_h)^2 \tag{5.2}$$

remains much smaller than the second moment of the Poisson progression over the effective internal mode, $S(\hbar\omega)^2$. In the calculation of the optical line shape, the energy of a CT2 state involving two stacked molecules in the undeformed crystal remains the only relevant fitting parameter required for an optimum agreement with published optical data [140, 110, 141]. As discussed in Sec. 5.3.2, the comparion of this model with the dielectric tensor of α-PTCDA single crystals obtained at room temperature provides values $E_{00}^{\mathrm{F}} = 2.17$ eV and $E_{00}^{\mathrm{CT2}} = 1.95 \pm 0.07$ eV for the fundamental 0-0 transitions of the neutral molecular excitation and of charge transfer along the stack, respectively [149]. Due to the particularly small mixing between Frenkel excitons and CT2 states via electron transfer t_e and hole transfer t_h according to $t_e + t_h = -10$ meV, the influence of the CT2 state on the linear optical properties remains rather small, so that a comparison between calculated and observed spectra does not allow for a more precise determination of the CT2 transition energy.

At low temperatures, the stacking vector of PTCDA is reduced by about 1.5 %, resulting in a red shift of the absorption band by about 0.02 eV [14, 51]. Assuming that the CT2 transition shifts by the same amount, this would place the fundamental transitions at $E_{00}^{\mathrm{F}} = 2.15$ eV and $E_{00}^{\mathrm{CT2}} = 1.93 \pm 0.07$ eV. In the following, we choose a value

of $E_{00}^{\text{CT2}} = 1.95$ eV for the CT2 transition along the stack, still within the conservative uncertainty range derived from the comparison between the calculated dielectric tensor and the observed values deduced from spectroscopic ellipsometry [141].
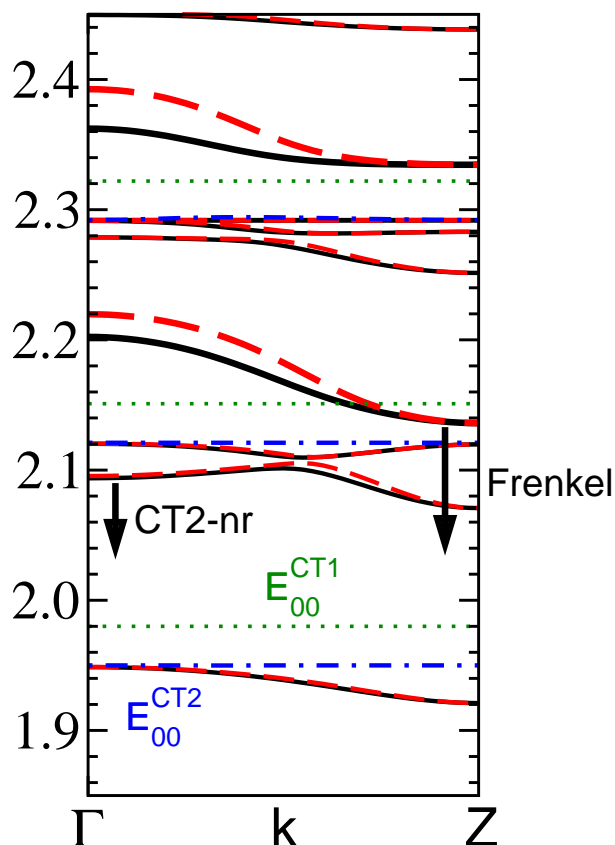
Figure 5.21: Excitonic dispersion in α-PTCDA at low temperature. Blue dash-dotted: dipole-forbidden vibronic levels of CT2 exciton involving stack neighbours; black, red dashed: dispersion branches of dipole-allowed mixed Frenkel-CT2 states, black for light polarized along x (in ac plane) and red dashed for light polarized along y (parallel to $\mathbf{b}$ lattice vector); green dotted: vibronic levels of CT1 exciton involving both basis molecules.

With these ingredients, the previous calculation of the excitonic states in the center of the Brillouin zone can easily be generalized to finite wave vectors. Fig. 5.21 shows the calculated excitonic dispersion branches at low temperatures, where the calculated optical properties derived from the dipole-allowed states at Γ are again in good agreement with the observed spectra [127, 165]. The dispersion branches with a large Frenkel exciton parentage are highlighted, and the lowest pair with maxima around 2.20 and 2.22 eV can be analysed further in terms of the Davydov splitting between the lowest absorption peaks occurring for orthogonal polarizations [141], compare Sec. 5.3.2. Moreover, the minima of these dispersion branches at the surface of the Brillouin zone close to 2.14

eV give rise to vertical radiative recombination to excited vibronic levels of the effective internal vibration, as indicted by the arrow downwards [122, 163]. Due to the low-lying CT transitions, several excitation resonances below the lowest Frenkel dispersion branch are worth mentioning: The fundamental $E_{00}^{CT2} = 1.95$ eV for charge transfer along the stack, the region between 2.10 and 2.12 eV in resonance with $E_{01}^{CT2} = 2.12$ eV, and the fundamental $E_{00}^{CT1} = 1.98$ eV for charge transfer between the two basis molecules in the crystal unit cell. As the electron or hole transfer between the two basis molecules is expected to be smaller than the respective transfers along the stack, the CT1 states are not included in the exciton model, so that their dispersion branches are visualized by horizontal lines. From the PLE spectra summarized in Sec. 5.4.1 above, a suitable CT1 energy in the crystal can be obtained, as visualized in Fig. 5.21.

5.4.3 Interpretation of PLE and PL resonances

According to model calculations of the excitonic dispersion in Sec. 5.4.2 [149], the minimum of the lowest dispersion branch dominated by Frenkel excitons at the surface of the Brillouin zone occurs about 70 meV below the dispersion maxima at Γ [129, 166], compare Fig. 5.21. After thermal relaxation into this energetic minimum the lowest accessible final state for recombining excitons is the $|1_g\rangle$ state which lowers the transition energy by about 170 meV, corresponding to the energy of an effective internal vibration. The PL energy from this dispersion minimum is further reduced by about 110 meV caused by low frequency modes [163, 166] resulting in a total Stokes shift of $\sim$0.39 eV for optical excitation resonant to the 0-0 dispersion branch of the Frenkel exciton at the Γ-point. Even at the highest excitation energy of $\sim$2.15 eV in our PLE measurements, the expected Stokes shift of the Frenkel exciton emission amounts to only 0.33 eV. Therefore, opposite to the CT transitions at lower energies, excitation at 2.15 eV in the low-energy edge of the 0-0 Frenkel resonance allows the observation of the entire density of states of the respective PL channel. On the other hand, at energies ranging from $\sim$2.05 to 2.15 eV, the PL from Frenkel excitons shows a red shift similar to the excitation of CT states below their absorption resonance. We therefore suggest that in this energetic range, the observed Frenkel exciton PL band is generated by selective excitation of spatial regions with a particularly low-lying transition energy.

Moreover, in this energetic region, excitation into the mixed Frenkel-CT2 states dominated by E_{00}^{CT2} basis states at 2.10 and 2.12 eV might still contribute to emission from the dispersion minimum of the lowest branch dominated by Frenkel excitons at 2.14 eV.

The mixed F-CT2 states around $2.10 - 2.12$ eV discussed above seem to be the relevant excitation channel resulting in the CT2-nr PL band occurring at a constant emission energy of $\sim$1.97 eV at an excitation energy above $\sim$2.10 eV. As for the relaxed CT2 transition, the observed Stokes-shift of $\sim$130 $-$ 150 meV exceeds the shift of $\sim$110 meV caused by low energy modes [163, 166].

In contrast to the Frenkel exciton band the CT2-nr band does not further increase it Gaussian area for excitation above $\sim$2.10 eV, indicating that the distribution maximum of these states has been reached by the exciting laser line.

Excitation around 2.10 eV also leads to an enhanced PL of self-trapped CT2 states which additionally contribute to the PL intensity and spectral width of the low energy band at ∼1.69 eV that is eventually composed by the non-resolved CT1 and Frenkel exciton subbands as well as by the PL band of CT2 states generated by the relaxation of CT2-nr states into self-trapped CT2 excitons involving a reduced stacking distance between an anionic and cationic molecule.

5.4.4   Summary photoluminescence

Photoluminescence excitation studies on α-PTCDA single crystals and polycrystalline PTCDA films were compared to the calculated excitonic dispersion deduced from an exciton model including the coupling between Frenkel excitons and charge transfer along the stacking direction. For excitation energies below the 0-0 Frenkel exciton absorption band at 5 K, these measurements enable the selective excitation of several CT states. The CT2 state involving stacked PTCDA molecules gives an excitation resonance for photoluminescence from the self-trapped CT2 exciton and from the non-relaxed CT2-nr state. Moreover, the fundamental transition of the CT1 involving both basis molecules in the crystal unit cell can be determined from the respective excitation resonance. The excitation energy dependence of the different emission bands allows the assignment of the fundamental transition energies of the CT2 and CT1 excitons to 1.95 eV and 1.98 eV, respectively. When the excitation energy exceeds ∼2.10 eV, we observe a dominating emission channel related to the indirect minimum of the lowest dispersion branch dominated by Frenkel excitons. Temperature-dependent PL measurements between 10 and 300 K at an excitation energy of 1.88 eV further allow a detailed investigation of the relaxation behavior of the isolated CT2 and its vibronic subband.

Chapter 6

Conclusion

So far, the crystallochromy of perylene pigments has not been fully understood. Therefore the aim of this thesis was to combine a theoretical model and a physically well founded parameter set obtained with *ab initio* methods, and to compare these model calculations to experimental results, allowing us to describe the physical mechanisms behind the optical attributes of perylene pigments.

The calculated deformation patterns, reorganization energies and vibrations of the single molecule were found to be in excellent agreement with observed solution spectra and resonant Raman cross sections. From these properties the effective vibrational modes and Huang-Rhys factors for three different electronic configurations were extracted, including neutral excited, anionic and cationic states. In total a number of ten different organic molecules were studied in their dissolved state. Calculations could also reproduce pre-resonant Raman spectra giving further support to the *ab initio* approaches used. We found that for the planar organic molecules such as the perylene compounds and pentacene where the lowest transition contains nearly 100% of HOMO-LUMO excitation, a constrained DFT approach could describe the deformation pattern better than TD-DFT. On the other hand, for the non-planar molecules such as TPD and rubrene, the TD-DFT approach was found to be more consistent with experiments.

Concerning crystalline perylene pigments the calculated values of the transfer parameter along the stacking direction could be verified experimentally for crystals of PTCDA and Me-PTCDI, and the approximate values of electron and hole transfer obtained with the B3LYP functional could reproduce the observed optical spectra for all seven compounds investigated. However, the calculated values for the exciton transfer along the stack were not in agreement with the values obtained from the exciton model. Instead a sum rule was applied to the experimental spectra, allowing to deduce the transfer parameter $T_{AA}(\mathbf{k} = 0)$ directly from the observations.

The model itself includes Frenkel excitons and charge transfer states. The different deformation patterns from the ionized states are taken into consideration, allowing to study in detail the contribution of charge transfer transitions to the optical spectra. The model is a quasi one-dimensional model motivated by the fact that the stacking geometry of the molecules results in a much larger electronic or excitonic interaction along the stacking

direction than between the two basis molecules. According to the traditional theoretical tools applied to periodic crystals, the exciton Hamiltonian based on localized electronic excitations was block-diagonalized by applying a Fourier transform to the wave vector $\mathbf{k}$ of an excitonic Bloch wave. By using calculated transition dipole moments for neutral excitations of the two molecules in the unit cell, and of the CT transition dipoles along the respective stacks, the optical anisotropy in the xy-plane could be investigated. For most compounds, the model allows to determine the energies of CT transitions along the stacking direction in the crystalline phase within a precision better than 0.05 eV, an uncertainty range far below systematic deviations occuring in Hartree-Fock, DFT, or microelectro-static calculations. The energy of the lowest CT state is crucial for optoelectronic device applications of semiconducting crystalline molecular materials. Furthermore, in the future, these improved values for the CT energies should allow for a deeper understanding of device related observables like photocurrents and a refinement of existing microscopic models for photoluminescence along the lines discussed in this thesis.

We have demonstrated that an exciton model accounting for the interference between Frenkel excitons and charge transfer transitions can quantitatively reproduce the observed optical spectra for a set of perylene pigments, including the pronounced anisotropy of the dielectric tensor, and related optical observables like reflection, optical density and extinction coefficient. The excellent agreement obtained corroborates the validity of the assumptions underlying the exciton model and the reliability of the microscopic parameters derived with DFT. This work demonstrates the high relevance of a theoretical model for quantifying the color generation mechanism in pigments.

We have found that DDTP shows properties inbetween perylene and pentacene. Even though it has a perylene core its geometrical arrangement and orbitals resembles two pentacene molecules crossing each other at an angle of 60°. In the DDTP crystal, the lowest subband arising from the HOMO-LUMO transition is reasonably close to the respective feature observed in crystalline pentacene, but the lowest CT transition energies differ significantly. Nevertheless, it seems realistic that an extension of the exciton model discussed in this thesis to charge transfer between the two basis molecules will contribute to a deeper understanding of the optical spectra of pentacene crystals.

Bibliography

[1] W. Herbst and K. Hunger, *Industrial Organic Pigments*, Wiley-VCH (Berlin 2005).

[2] E. Hädicke and F. Graser, *Acta Cryst. C* **42**, 189 (1986).

[3] E. Hädicke and F. Graser, *Acta Cryst. C* **42**, 195 (1986).

[4] D. Knipp, R. A. Street, B. Krusor, and J. Ho, *Res. Soc. Symp. Proc.* **725**, P5.2 (2002).

[5] C. Li, J. Yum, S. Moon, A. Herrmann, F. Eickemeyer, N. Pschirer, P. Erk, J. Schöneboom, K. Müllen, M. Grätzel, and M. Nazeeruddin, *ChemSusChem* **1**, 615 (2008).

[6] C. W. Tang, *Appl. Phys. Lett.* **48**, 183 (1986).

[7] K. Sato, J. Mizuguchi, Y. Sakai, and S. Aramaki, *J. Appl. Phys.* **103**, 013702 (2008).

[8] J. Mizuguchi, *J. Appl. Phys.* **84**, 4479 (1998).

[9] K. Hirao, Y. Tsukada, S. Suzuki, H. Takahashi, and J.Mizuguchi, *J. Appl. Phys.* **103**, 053706 (2008).

[10] K.-Y. Law, *Chem. Rev.* **93**, 449 (1993).

[11] U. Heinemeyer, R. Scholz, L. Gisslén, M. I. Alonso, J. O. Ossó, M. Garriga, A. Hinderhofer, M. Kytka, S. Kowarik, A. Gerlach, and F. Schreiber, *Phys. Rev. B* **78**, 085210 (2008).

[12] V. Bulović, P. E. Burrows, S. R. Forrest, J. A. Cronin, and M. E. Thompson, *Chem. Phys.* **210**, 1 (1996).

[13] U. Gomez, M. Leonhardt, H. Port, and H. C. Wolf, *Chem. Phys. Lett.* **268**, 1 (1997).

[14] J. Mizuguchi and K. Tojo, *J. Phys. Chem. B* **106**, 767 (2002).

[15] E. Engel, K. Schmidt, D. Beljonne, J.-L. Brédas, J. Assa, H. Fröb, K. Leo, and M. Hoffmann, *Phys. Rev. B* **73**, 245216 (2006).

[16] G. Klebe, F. Graser, E. Hädicke, and J. Berndt, *Acta Cryst. B* **45**, 69 (1989).

[17] M. Born and R. Oppenheimer, *Annalen der Physik* **84**, 457 (1927).

[18] A. Szabo and N. S. Ostlund, *Modern Quantum Chemistry*, Dover/MacGraw-Hill, New York, 1996.

[19] F. Jensen, *Introduction to Computational Chemistry*, Wiley (Wiltshire 1999).

[20] E. Runge and E. K. U. Gross, *Phys. Rev. Lett.* **52**, 997 (1984).

[21] P. Hohenberg and W. Kohn, *Phys. Rev.* **136**, B864 (1964).

[22] W. Kohn and L. J. Sham, *Phys. Rev.* **140**, A1133 (1965).

[23] M. Dierksen and S. Grimme, *J. Chem. Phys.* **120**, 3544 (2004).

[24] M. Dierksen and S. Grimme, *J. Phys. Chem.* **108**, 10225 (2004).

[25] M. Andrzejak, G. Mazur, and P. Petelenz *J. Mol. Struct. (Theochem)* **527** (2000).

[26] D. Becke, Phys. Rev. A 38, 3098 (1988); C. Lee, W. Yang, R. G. Parr, *Phys. Rev. B* **37**, 785 (1988).

[27] R. Ahlrichs, M. Bär, M. Häser, H. Horn, and C. Kölmel, *Chem. Phys. Lett.* **162**, 165 (1989).

[28] S. H. Vosko, L. Wilk, and M. Nusair, *Can. J. Phys.* **58** , 1200 (1980).

[29] R. M. Dreizler and E. K. U. Gross, *Density Functional Theory*, Springer (1990).

[30] J. M. L. Martin, J. El-Yazal, and J.-P. Francois, *J. Phys. Chem.* **100**, 15358 (1996).

[31] M. Rummi, G. Zerbi, and K. Müllen, *J. Chem. Phys.* **108**, 8662 (1998).

[32] K. K. Ong, J. O. Jensen, and H. F. Hameka, *J. Mol. Str.* **459**, 131 (1999).

[33] C. W. Bauschlicher, *Chem. Phys. Lett.* **246**, 40 (1995).

[34] M. D. Halls, J. Velkovski, and H. B. Schlegel, *Theor. Chem. Acc.* **105**, 413 (2001).

[35] O. Treutler and R. Ahlrichs, *J. Chem. Phys.* **102**, 346 (1995).

[36] R. Bauernschmitt and R. Ahlrichs, *Chem. Phys. Lett.* **256**, 454 (1996).

[37] F. Furche and J. Ahlrichs, *J. Chem. Phys.* **117**, 7433 (2002). **100**, 5829 (1994).

[38] A. J. Sobolewski and W. Domcke, *Phys. Chem. Chem. Phys.* **1**, 3065 (1999).

[39] R. Burcl, R. D. Amos, and N. C. Handy, *Chem. Phys. Lett.* **355**, 8 (1999).

[40] A. Schäfer, H. Horn, and R. Ahlrichs, *J. Chem. Phys.* **97**, 2571 (1992).

[41] A. Schäfer, C. Huber, and R. Ahlrichs, *J. Chem. Phys.*

[42] R. J. Glauber, *Phys. Rev.* **131**, 2766 (1963).

[43] J. Franck, *Transactions of the Faraday Society* **21**, 536 (1926).

[44] C. V. Raman, *Nature* **121**, 619 (1928).

[45] A. C. Albrecht and M. C. Hutley, *J. Chem. Phys.* **44**, 4438 (1971).

[46] B. B. Johnson and W. L. Peticolas, *Ann. Rev. Phys. Chem.* **27**, 465 (1976).

[47] A. Warschel and P. Dauber, *J. Chem. Phys.* **66**, 5477 (1977).

[48] R. Loudon, *The Quantum Theory of Light*, Oxford University Press (Oxford 2000), ch. 8.

[49] A. C. Albrecht, *J. Phys. Chem.* **34**, 1476 (1961).

[50] A. B. Myers, R. A. Mathies, D. J. Tannot, and E. J. Heller, *J. Chem. Phys.* **77**, 3857 (1982).

[51] A. C. Dürr, F. Schreiber, M. Mnch, N. Karl, B. Krause, V. Kruppa, and H. Dosch, *Appl. Phys. Lett.* **81**, 2276 (2002).

[52] S. Kowarik, A. Gerlach, S. Sellner, F. Schreiber, L. Cavalcanti, and O. Konovalov, *Phys. Rev. Lett.* **96**, 125504 (2006).

[53] A. K. Tripathi and J. Pflaum, *Appl. Phys. Lett.* **89**, 082103 (2006).

[54] L. M. Ramaniah and M. Boero, *Phys. Rev. A* **74**, 042505 (2006).

[55] V. Coropceanu, J. M. André, M. Malagoli, and J. L. Brédas, *Theor. Chem. Acc.* **110**, 59 (2003).

[56] G. Mazur, P. Petelenz, and M. Slawik, *J. Chem. Phys.* **118**, 1423 (2003).

[57] M. Hoffmann and Z. G. Soos, *Phys. Rev. B* **66**, 024305 (2002).

[58] A. Yu. Kobitski, R. Scholz, D. Tenne, T. U. Kampen, H. P. Wagner, and D. R. T. Zahn, *Appl. Surf. Sci.* **190**, 386 (2002).

[59] M. H. Hennessy, Z. G. Soos, R. A. Pascal, and A. Girlando, *Chem. Phys.* **245**, 199 (1999).

[60] R. Scholz, A. Yu. Kobitski, T.U. Kampen, M. Schreiber, D. R. T. Zahn, G. Jungnickel, M. Elstner, M. Sternberg, and Th. Frauenheim, *Phys. Rev. B* **61**, 13659 (2000).

[61] K. Akers, R. Aroca, A. M. Hor, and R. O. Loutfy, *Spectrochim. Acta* **44A**, 1129 (1988).

[62] C. Wöll, *Physical and Chemical Aspects of Organic Electronics*, Wiley-VHC (Weinheim 2009).

[63] D. R. T. Zahn, G. N. Gavrila, and G. Salvan, *Chem. Rev.* **107**, 1161 (2007).

[64] V. Chis, G. Mile, Stiufiuc, N. Leopold, and M. Oltean, *J. Mol. Struc.* **924**, 47 (2009).

[65] V. Presser, B.-E. Schuster, M. B. Casu, U. Heinemeyer, F. Schreiber, K. G. Nickel, and T. Chassé, *J. Raman Spec.* (2009).

[66] V. Coropceanu, M. Malagoli, D. A. da Silva Filho, N. E. Gruhn, T. G. Bill, and J. L. Brédas, *Phys. Rev. Lett.* **89**, 275503 (2002).

[67] K. Akers, R. Aroca, A. M. Hor, and R. O. Loutfy, *J. Phys. Chem.* **91**, 2954(1987).

[68] L. Gisslén, C. Himcinschi, J. Pflaum, and R. Scholz, *in preparation* (2009).

[69] V. Podzorov, S. E. Sysoev, E. Loginova, V. M. Pudalov, and M. E. Gershenson, *Appl. Phys. Lett.* **83**, 3504 (2003).

[70] Y. Y. Noh and D. Y. Kim, *Solid-State Elec.* **51**, 1052 (2007).

[71] B. A. Paez, I. Thurzo, G. Salvan, R. Scholz, H. von Seggern, and D. R. T. Zahn *Proc. SPIE* **5940**, 73 (2005).

[72] R. Signerski, G. Jarosz, and J. Godlewski, *Synth. Met.* **94**, 135 (1998).

[73] S. S. Kim, S. P. Park, J. H. Kim, and S. Im, *Thin Solid Films* **19**, 420-421 (2002).

[74] J. Lee, D. K. Hwang, C. H. Park, S. S. Kim, and S. Im, *Thin Solid Films* **12**, 451-452 (2004).

[75] A. C. Mayer, M. T. Lloyd, D. J. Herman, T. G. Kasen, and G. G. Malliaras, *Appl. Phys. Lett.* **85**, 6272 (2004).

[76] D. M. N. M. Dissanayake, A. A. D. T. Adikaari, and S. R. P. Silva, *Appl. Phys. Lett.* **92**, 093308 (2008).

[77] T. Ji, S. Jung and V. K. Varadan, *IEEE Elec. Dev. Lett.* **28**, 1105 (2007).

[78] D. Knipp, R. A. Street, A. Völkel, and J. Ho, *J. Appl. Phys.* **93**, 347 (2003).

[79] D. Kumaki, M. Yahiro, Y. Inoue, and S. Tokito, *Appl. Phys. Lett.* **90**, 133511 (2007).

[80] A. Hinderhofer, U. Heinemeyer, A. Gerlach, S. Kowarik, R. M. J. Jacobs, Y. Sakamoto, T. Suzuki, and F. Schreiber. *J. Chem. Phys.* **127**, 194705 (2007).

[81] H. L. Cheng, W. Y. Chou, C. W. Kuo, and F. C. Tang, and Y. W. Wang, *Appl. Phys. Lett.* **88**, 161918 (2006).

[82] V. Coropceanu, D. A. da Silva Filho, O. Kwon, R. S. Sanchez-Carrera, and J. L. Brédas, *Proc. Int. Symp. Super-Functionality of Organic Devices, IPAP Conf. Series 6*, p. 15-18.

[83] M. Banasiewicz, I. Deperasińska, D. Fabjanowicz, and B. Kozankiewicz, *J. Phys. Chem. A* **107**, 662 (2003).

[84] M. Banasiewicz, I. Deperasińska, and B. Kozankiewicz, *J. Phys. Chem. A* **107**, 662 (2003).

[85] A. Amirav, U. Even, and J. Jortner, *Chem. Phys. Lett.* **72**, 21 (1980).

[86] M. Malagoli, V. Coropceanu, D. A. da Silva Filho, and J. L. Brédas, *J. Chem. Phys.* **120**, 7490 (2004).

[87] M. Hartmann, A. Lindinger, J. P. Toennies, and A. F. Vilesov, *Phys. Chem. Chem. Phys.* **4**, 4839 (2002).

[88] P. M. Borsenberger, and D. S. Weiss, *Organic Photoreceptors for Xerography*, Marcel Dekker, (New York 1998).

[89] E. Bellmann, S. E. Shaheen, S. Thayumanavan, S. Barlow, R. H. Grubbs, S. R. Marder, B. Kippelen, and N. Peyghambarian, *Chem. Mater.* **10**, 1668 (1998).

[90] W. Holzer, A. Penzkofer, H.-H. Hörhold, *Synth. Met.* **113**, 281 (2000).

[91] E. M. Calzado, J. M. Villavilla, P. G. Boj, J. A. Quintana, M. A. Díaz-García, *Org. Electron.* **7**, 319 (2006).

[92] M. A. Díaz-García, S. F. de Ávila, M. Kuzyk, *Appl. Phys. Lett.* **80**, 4486 (2002).

[93] M. A. Díaz-García, E. M. Calzado, J. M. Villavilla, P. G. Boj, J. A. Quintana, and M. J. Kuzyk, *Nonlin. Opt. Phys. Mater.* **13**, 621 (2004).

[94] E. M. Calzado, J. M. Villavilla, P. G. Boj, J. A. Quintana, and M. A. Díaz-García, *J. Appl. Phys.* **97**, 093103 (2005).

[95] I. Vragović, E. M. Calzado, M. A. Diaz Garcia, C. Himcinschi, L. Gisslén, and R. Scholz, *J. Lumin.* **128**, 845 (2007).

[96] R. Scholz, L. Gisslén, C. Himcinschi, I. Vragović, E. M. Calzado, E. Louis, E. S. F. Maroto, and M. A. Díaz-García, *J. Phys. Chem. A* **113**, 315 (2009).

[97] O. Brafman, C. K. Chan, B. Khodadoost, J. B. Page, C. T. J. Walker, *J. Chem. Phys.* **80**, 5406 (1984).

[98] M. Malagoli and J. L. Brédas, Chem. *Phys. Lett.* **327**, 13 (2000).

[99] A. R. Kennedy, W. E. Smith, D. R. Tackley, W. I. F. David, K. Shankland, B. Brown, and S. J. Teat, *J. Mater. Chem.* **12**, 168 (2002).

[100] I. Vragović, E. M. Calzado, M. A. Díaz-García, *Chem. Phys.* **48**, 332 (2007).

[101] M. Kytka, L. Gisslén, A. Gerlach, U. Heinemeyer, J. Kovác, R. Scholz, and F. Schreiber, *J. Chem. Phys.* **113**, 315 (2009).

[102] A. J. Lovinger, S. R. Forrest, M. L. Kaplan, P. H. Schmidt, and T. Venkatesan, *J. Appl. Phys.* **55**, 476 (1984).

[103] J. Mizuguchi, *Acta Cryst. C* **52**, 2315 (1996).

[104] J. Mizuguchi, *Acta Cryst. C* **54**, 1479 (1998).

[105] K. Tojo and J. Mizuguchi, *Z. Krist. NCS* **217**, 45 (2002).

[106] J. Mizuguchi and K. Tojo, *Z. Krist. NCS* **216**, 375 (2001).

[107] M. A. Heinrich, J. Pflaum, A. K. Tripathi, W. Frey, M. L. Steigerwald, and T. Siegrist, *J. Phys. Chem. C* **111**, 18878 (2007).

[108] M. Leonhardt, O. Mager, H. Port, *Chem. Phys. Lett.* **313**, 24 (1999).

[109] J. Mizuguchi, *Acta Cryst. C* **54**, 1479 (1998).

[110] A. B. Djurisić, T. Fritz, and K. Leo, *Opt. Commun.* **183**, 123 (2000).

[111] H. Yamane and S. Kera, Phys. Rev. B **68**, 033102 (2003).

[112] G. N. Gavrila, H. Mendez, T. U. Kampen, D. R. T. Zahn, D. V. Vyalikh, and W. Braun, *Appl. Phys. Lett.* **85**, 4657 (2004).

[113] N. Ishikawa, O. Ohno, Y. Kaizu, and H. Kobayashi, *J. Phys. Chem.* **96**, 8832 (1992).

[114] I. G. Hill, A. Kahn, Z. G. Soos, and R. A. Pascal, *Chem. Phys. Lett.* **327**, 181 (2000).

[115] E. V. Tsiper and Z. G. Soos, *Phys. Rev. B* **64** 195124 (2001).

[116] E. V. Tsiper, Z. G. Soos, W. Gao W, and A. Kahn, *Chem. Phys. Lett.* **360**, 47 (2002).

[117] M. Wewer and F. Stienkemeier, *J. Chem. Phys.* **120**, 1239 (2004).

[118] R. Scholz, A. Y. Kobitski, D. R. T. Zahn, and M. Schreiber, *Phys. Rev. B* **72**, 245208 (2005).

[119] A. Dreuw, J. L. Weisman, and M. Head-Gordon, *J. Chem. Phys.* **119**, 2943 (2003).

[120] A. S. Davydov, *Theory of Molecular Excitons*, Plenum Press (New York 1971).

[121] A. S. Davydov and E. F. Sheka, *Phys. Stat. Sol.* **11**, 877 (1965).

[122] I. Vragović and R. Scholz, *Phys. Rev. B* **68**, 155202 (2003).

[123] L. D. Landau and E. M. Lifshitz, *Electrodynamics of Continuous Media*, Pergamon (Oxford 1984).

[124] F. F. So and S. R. Forrest *Phys. Rev. Lett.*, **66**, 2649 (1991).

[125] E. I. Haskal, Z. Shen, P. E. Buttows, and S. R. Forrest, *Phys. Rev. B* **51**, 4449 (1995).

[126] Z. G. Soos, M. H. Hennessy, and G. Wen, *Chem. Phys.* **227**, 19 (1998).

[127] M. Hoffmann, K. Schmidt, T. Fritz, T. Hasche, V. M. Agranovich, and K. Leo, *Chem. Phys.* **258**, 73 (2000).

[128] *Frenkel and Charge-Transfer Excitons in Quasi-One-Dimensional Molecular Crystals with Strong Intermolecular Orbital Overlap*, M. Hoffmann, PhD. thesis (Dresden 2000).

[129] I, Vragović, R. Scholz, and M. Schreiber, *Europhys. Lett.* **57**, 288 (2002).

[130] M. I. Alonso, M. Garriga, N. Karl, J. O. Ossó, and F. Schreiber, *Org. Electron.* **3**, 23 (2001).

[131] V. M. Agranovich, K. Schmidt, and K. Leo, *Chem. Phys. Lett.* **325**, 308 (2000).

[132] R. Fulton and M. Gouterman, *J. Chem. Phys.* **41**, 2289 (1964).

[133] J. S. Briggs and A. Herzenberg, *Proc. Phys. Soc.* **92**, 159 (1967).

[134] J. S. Briggs and A. Herzenberg, *J. Phys. B: Atom. Molec. Phys.* **3**, 1663 (1970).

[135] V. M. Agranovich and M. D. Galanin, *Electronic Excitation Energy Transfer in Condensed Matter*, North-Holland (Amsterdam 1982).

[136] M. H. Hennessy, Z. G. Soos, V. Bulović, and S. R. Forrest, *Mat. Res. Soc. Symp. Proc.* **488**, 171 (1998).

[137] A. La Magna and R. Pucci, *Phys. Rev. B* **53**, 8449 (1996).

[138] B. Krause, A. C. Dürr, F. Schreiber, H. Dosch, and O. H. Seeck, *J. Chem. Phys.* **119**, 3429 (2003).

[139] V. R. Gangilenka, L. V. Titova, L. M. Smith, H. P. Wagner, L. Gisslén, and R. Scholz, submitted to *Phys. Rev. B* (2009).

[140] M. I. Alonso, M. Garriga, N. Karl, J. O. Ossó, and F. Schreiber, *Organic Electronics* **3**, 23 (2002).

[141] M. I. Alonso, M. Garriga, J. O. Ossó, F. Schreiber, L. Gisslén and R. Scholz, revised evaluation of ellipsometry data of PTCDA (unpublished).

[142] D. Lehmann and D. R. T. Zahn, *Appl. Phys. A* **95**, 203 (2009).

[143] S. Tokito, J. Sakata, and Y. Taga, *J. Appl. Phys.* **77**, 1985 (1995).

[144] J. Mizuguchi, Dyes and Pigments **35**, 347 (1997).

[145] P. M. Kazmaier and R. Hoffmann, *J. Am. Chem. Soc.* **116**, 9684 (1994).

[146] CSD (Cambridge structural database) file for Me-PTCDI corresponding to Refs. [2, 3].

[147] R. B. Campbell, J. M. Robertson, J. Trotter, *Acta Crys.* **14**, 705 (1961).

[148] K. Kim, Y. K. Yoon, M.-O. Mun, S. P. Park, S. S. Kim, S. Im, and J. H. Kim, *J. Superconductivity* **15**, 595 (2002).

[149] L. Gisslén and R. Scholz, *Phys. Rev. B* **80**, 115309 (2009).

[150] H. Baessler and B. Schweitzer, *Acc. Chem. Res.* **32**, 177 (1999).

[151] A. Piaggi, G. Lanzani, G. Bongovianni, A. Mura, W. Graupner, F. Meghdadi, G. Leising, and M. Nisoli, *Phys. Rev. B* **56**, 10133 (1997).

[152] R. G. Della Valle, E. Venuti, L. Farina, A. Brillante, M. Masino, and A. Girlando, *J. Phys. Chem. B* **108**, 1822 (2004).

[153] G. Salvan, D. A. Tenne, A. Das, T. U. Kampen, and D. R. T. Zahn, *Org. Electron.* **1**, 49 (2000).

[154] R. Scholz and M. Schreiber, *Chem. Phys.* **325**, 9 (2006).; R. Scholz, I. Vragović, A. Yu. Kobitski, G. Salvan, T. U. Kampen, M. Schreiber, and D. R. T. Zahn, *Proc. Int. School "E. Fermi," course CXLIX: Organic Nanostructures: Science and Applications*, edited by V. M. Agranovich and G. C. La Rocca, IOS Press (Amsterdam 2002) p. 379.

[155] S. R. Forrest, *Chem. Rev.* **97**, 1793 (1997).

[156] M. H. Hennessy, R. A. Pascal, and Z. G. Soos, *Mol. Cryst. Liq. Cryst.* **355**, 41 (2001).

[157] A. Y. Kobitski, R. Scholz, I. Vragovic, H. P. Wagner, and D. R. T. Zahn, *Phys. Rev. B* **66**, 153204 (2002).

[158] A. Y. Kobitski, R. Scholz, D. R. T. Zahn, and H. P. Wagner, *Phys. Rev. B* **68**, 155201 (2003).

[159] H. P. Wagner, A. DeSilva, and T. U. Kampen, *Phys. Rev. B* **70**, 235201 (2004).

[160] H. P. Wagner, A. DeSilva, V. R. Gangilenka, and T. U. Kampen, *J. Appl. Phys.* **99**, (2006).

[161] V. Bulović, P. E. Burrows, S. R. Forrest, J. A. Cronin, and M. E. Thompson, *Chem. Phys.* **210**, 13 (1996).

[162] V. R. Gangilenka, A. DeSilva, H. P. Wagner, R. E. Tallman, B. A. Weinstein, and R. Scholz, *Phys. Rev. B* **77**, 115206 (2008).

[163] R. Scholz, I. Vragovic, A. Y. Kobitski, M. Schreiber, H. P. Wagner, and D. R. T. Zahn, *phys. stat. sol. (b)* **234**, 402 (2002).

[164] M. Schneider, E. Umbach, and M. Sokolowski, *Chem. Phys.* **325**, 185 (2006).

[165] H. P. Wagner, V. R. Gangilenka, A. DeSilva, H. Schmitzer, R. Scholz, and T. U. Kampen, *Phys. Rev. B* **73**, 125323 (2006).

[166] R. Scholz, M. Schreiber, I. Vragovic, A. Y. Kobitski, H. P. Wagner, and D. R. T. Zahn, *J. Lumi.* **108**, 121 (2004).

Appendix A

Appendix

A.1   Fourier transform of the infinite stack

Since we assume periodic boundary conditions for a cyclic stack of N molecules, or in other words a infinite chain, we can convinient Fourier transform the operators of the model. Fourier transform of the Frenkel operator can be written as

$$b^\dagger_{\mathbf{k}\alpha\nu_e} = \frac{1}{\sqrt{N}} \sum_{\mathbf{n}} e^{-i\mathbf{k}\mathbf{R}_{\mathbf{n},\alpha}} b^\dagger_{\mathbf{n}\alpha\nu_e;\mathbf{n}\alpha 0}, \tag{A.1}$$

which gives the back transform

$$b^\dagger_{\mathbf{n}\alpha\nu_e} = b^\dagger_{\mathbf{n}\alpha\nu_e;\mathbf{n}\alpha 0} = \frac{1}{\sqrt{N}} \sum_{\mathbf{k}} e^{i\mathbf{k}\mathbf{R}_{\mathbf{n},\alpha}} b^\dagger_{\mathbf{k}\alpha\nu_e}. \tag{A.2}$$

Since we have periodic boundary conditions we can write

$$\sum_{\mathbf{n}} e^{i(\mathbf{k}-\mathbf{k}')\mathbf{n}} = N\delta_{\mathbf{k}\mathbf{k}'} \tag{A.3}$$

Inserting the operators $b^\dagger_{\mathbf{n}\alpha\nu_e}$ according to eq. (A.2) together with a similarly defined adjoint operator $b_{\mathbf{n}\alpha\nu_e}$, the Frenkel Hamiltonian will then transform to

$$H^{\mathrm{F}} = \sum_{\mathbf{n}\alpha\nu_e} E_{0\nu_e} \Big(\frac{1}{\sqrt{N}} \sum_{\mathbf{k}} e^{-i\mathbf{k}R_{\mathbf{n}}} b^\dagger_{\mathbf{k}\alpha\nu_e} \frac{1}{\sqrt{N}} \sum_{\mathbf{k}'} e^{i\mathbf{k}'R_{\mathbf{n}}} b_{\mathbf{k}'\alpha\nu_e} \Big) +$$

$$\sum_{\mathbf{n}\alpha\nu_e} \sum_{\mathbf{m}\beta\mu} t_{\mathbf{n}\alpha\nu_e,\mathbf{m}\beta\mu} \Big(\frac{1}{\sqrt{N}} \sum_{\mathbf{k}\mathbf{k}'} e^{-i\mathbf{k}R_{\mathbf{n}}} \frac{1}{\sqrt{N}} e^{i\mathbf{k}'R_{\mathbf{m}}} b^\dagger_{\mathbf{k}\alpha\nu_e} b_{\mathbf{k}'\beta\mu} \Big) =$$

$$= \sum_{\alpha\nu_e} E_{0\nu_e} \sum_{\mathbf{k}\mathbf{k}'} \frac{1}{N} \sum_{\mathbf{n}} e^{-i(\mathbf{k}-\mathbf{k}')R_{\mathbf{n}}} b^\dagger_{\mathbf{k}\alpha\nu_e} b_{\mathbf{k}'\alpha\nu_e} +$$

$$\sum_{\alpha\nu_e} \sum_{\beta\mu} \sum_{\mathbf{k}\mathbf{k}'} \frac{1}{N} \sum_{\mathbf{m}\mathbf{n}} t_{\mathbf{n}\alpha\nu_e,\mathbf{m}\beta\mu} e^{i\mathbf{k}R_{\mathbf{n}}+i\mathbf{k}'R_{\mathbf{m}}} b^\dagger_{\mathbf{k}\alpha\nu_e} b_{\mathbf{k}'\beta\mu} =$$

139

$$\sum_{\alpha\nu_e} E_{0\nu_e} \sum_{\mathbf{kk'}} \delta_{\mathbf{kk'}} b^\dagger_{\mathbf{k}\alpha\nu_e} b_{\mathbf{k'}\alpha\nu_e} + \sum_{\alpha\nu_e}\sum_{\beta\mu}\sum_{\mathbf{kk'}}\sum_{\mathbf{m}} \frac{1}{N} \{\sum_{\mathbf{n}} t_{\alpha\beta}(R_\mathbf{m}-R_\mathbf{n}) e^{i\mathbf{k}(R_\mathbf{m}-R_\mathbf{n})}\} e^{-i(\mathbf{k}-\mathbf{k'})R_\mathbf{m}} b^\dagger_{\mathbf{k}\alpha\nu_e} b_{\mathbf{k'}\beta\mu} =$$

$$= \sum_{\alpha\nu_e} E_{0\nu_e} \sum_{\mathbf{k}} b^\dagger_{\mathbf{k}\alpha\nu_e} b_{\mathbf{k'}\alpha\nu_e} + \sum_{\alpha\nu_e}\sum_{\beta\mu}\sum_{\mathbf{kk'}} \frac{1}{N}\{\sum_{\mathbf{n}} t_{\alpha\beta} R_l e^{i\mathbf{k}R_l}\} \underbrace{\sum_{\mathbf{m}} e^{-i(\mathbf{k}-\mathbf{k'})R_\mathbf{m}}}_{N\delta_{\mathbf{kk'}}} b^\dagger_{\mathbf{k}\alpha\nu_e} b_{\mathbf{k'}\beta\mu} =$$

$$= \sum_{\alpha\nu_e} E_{0\nu_e} \sum_{\mathbf{k}} b^\dagger_{\mathbf{k}\alpha\nu_e} b_{\mathbf{k}\alpha\nu_e} + \sum_{\alpha\nu_e}\sum_{\beta\mu}\sum_{\mathbf{kk'}}\sum_{m} \frac{1}{N} t_{\alpha\beta\mathbf{k}} N\delta_{\mathbf{kk'}} b^\dagger_{\mathbf{k}\alpha\nu_e} b_{\mathbf{k'}\beta\mu} \tag{A.4}$$

where

$$t_{\alpha\beta}(\mathbf{k}) = \sum_l e^{i\mathbf{k}R_l} t_{\alpha\beta}(\mathbf{R}_l). \tag{A.5}$$

so that blocks for different wave vectors decouple,

$$H^{\mathrm{F}} = \sum_{\alpha\nu_e} E_{0\nu_e} \sum_{\mathbf{k}} b^\dagger_{\mathbf{k}\alpha\nu_e} b_{\mathbf{k}\alpha\nu_e} + \sum_{\alpha\nu_e}\sum_{\beta\mu}\sum_{\mathbf{k}} t_{\alpha\beta\mathbf{k}} b^\dagger_{\mathbf{k}\alpha\nu_e} b_{\mathbf{k}\beta\mu}. \tag{A.6}$$

With the same reasoning using the operators described in eq. (4.28) and (4.29) the Fourier transform of the CT Hamiltonian becomes

$$H^{\mathrm{CT}} = \sum_{\gamma\eta} E_{c\gamma\eta} \sum_{\mathbf{m}} (\frac{1}{N} \sum_{\mathbf{k}} e^{-i\mathbf{k}R_\mathbf{m}} c^\dagger_{\mathbf{k}\gamma\eta,-1} \sum_{\mathbf{k'}} e^{i\mathbf{k'}R_\mathbf{m}} c_{\mathbf{k'}\gamma\eta,-1} +$$

$$\frac{1}{N} \sum_{\mathbf{k}} e^{-i\mathbf{k}R_\mathbf{m}} c^\dagger_{\mathbf{k}\gamma\eta,+1} \sum_{\mathbf{k'}} e^{i\mathbf{k'}R_\mathbf{m}} c_{\mathbf{k'}\gamma\eta,+1}) =$$

$$= \sum_{\gamma\eta} E_{c\gamma\eta} \sum_{\mathbf{kk'}} (\frac{1}{N} \sum_{\mathbf{m}} e^{-i(\mathbf{k}-\mathbf{k'})R_\mathbf{m}} c^\dagger_{\mathbf{k}\gamma\eta,-1} c_{\mathbf{k'}\gamma\eta,-1} +$$

$$\frac{1}{N} \sum_{\mathbf{m}} e^{-i(\mathbf{k}-\mathbf{k'})R_\mathbf{m}} c^\dagger_{\mathbf{k}\gamma\eta,+1} c_{\mathbf{k'}\gamma\eta,+1}) =$$

$$= \sum_{\gamma\eta} E_{c\gamma\eta} \sum_{\mathbf{k}} (c^\dagger_{\mathbf{k}\gamma,-1} c_{\mathbf{k}\gamma\eta,-1} + c^\dagger_{\mathbf{k}\gamma\eta,+1} c_{\mathbf{k}\gamma\eta,+1}), \tag{A.7}$$

or

$$H^{\mathrm{CT}}(\mathbf{k}) = \sum_{\gamma\eta} E_{c\gamma\eta} (c^\dagger_{\mathbf{k}\gamma,-1} c_{\mathbf{k}\gamma\eta,-1} + c^\dagger_{\mathbf{k}\gamma\eta,+1} c_{\mathbf{k}\gamma\eta,+1}). \tag{A.8}$$

Finally the Fourier transform of the F-CT Hamiltonian reads:

$$H^{\mathrm{F-CT}} = \sum_{\mathbf{n}\nu_e}\sum_{\mathbf{m}\gamma\eta} (\frac{1}{N} \sum_{\mathbf{kk'}} e^{-i\mathbf{k}R_\mathbf{m}} e^{i\mathbf{k'}R_\mathbf{n}} c^\dagger_{\mathbf{k}\gamma\eta,-1} b_{\mathbf{k'}\nu_e} (\delta_{\mathbf{mn}} t'_h + \delta_{\mathbf{m,n+1}} t'_e) +$$

$$\frac{1}{N} \sum_{\mathbf{kk'}} e^{-i\mathbf{k}R_\mathbf{m}} e^{i\mathbf{k'}R_\mathbf{n}} c^\dagger_{\mathbf{k}\gamma\eta,+1} b_{\mathbf{k'}\nu_e} (\delta_{\mathbf{mn}} t'_h + \delta_{\mathbf{m,n-1}} t'_e)) + h.c. =$$

$$= \sum_{\mathbf{k}\mathbf{k}'} \sum_{\nu_e} \sum_{\gamma\eta} (\sum_{\mathbf{m}} \frac{1}{N} t'_n e^{-i(\mathbf{k}-\mathbf{k}')R_\mathbf{m}} c^\dagger_{\mathbf{k}\gamma\eta,-1} b_{\mathbf{k}'\nu_e} + \sum_{\mathbf{m}} \frac{1}{N} t'_e e^{-ikR_\mathbf{m}+ik'R_{\mathbf{m}-1}} c^\dagger_{\mathbf{k}\gamma\eta,-1} b_{\mathbf{k}'\nu_e} +$$

$$\sum_{\mathbf{m}} \frac{1}{N} t'_h e^{-i(\mathbf{k}-\mathbf{k}')R_\mathbf{m}} c^\dagger_{\mathbf{k}\gamma\eta,+1} b_{\mathbf{k}'\nu_e} + \sum_{\mathbf{m}} \frac{1}{N} t'_e e^{-ikR_\mathbf{m}+ik'R_{\mathbf{m}+1}} c^\dagger_{\mathbf{k}\gamma\eta,+1} b_{\mathbf{k}'\nu_e}) + h.c. =$$

$$= \sum_{\nu_e} \sum_{\gamma\eta} \sum_{\mathbf{k}\mathbf{k}'} (t'_h \delta_{\mathbf{k}\mathbf{k}'} c^\dagger_{\mathbf{k}\gamma\eta,-1} b_{\mathbf{k}'\nu_e} + t'_e \sum_{\mathbf{m}} \frac{1}{N} e^{-i(\mathbf{k}-\mathbf{k}')R_\mathbf{m}} e^{-i\mathbf{k}'\mathbf{r}} c^\dagger_{\mathbf{k}\gamma\eta,-1} b_{\mathbf{k}'\nu_e} +$$

$$t'_h \delta_{\mathbf{k}\mathbf{k}'} c^\dagger_{\mathbf{k}\gamma\eta,+1} b_{\mathbf{k}'\nu_e} + t'_e \underbrace{\sum_{\mathbf{m}} \frac{1}{N} e^{-i(\mathbf{k}-\mathbf{k}')R_\mathbf{m}}}_{\delta_{\mathbf{k}\mathbf{k}'}} e^{i\mathbf{k}'\mathbf{r}} c^\dagger_{\mathbf{k}\gamma\eta,+1} b_{\mathbf{k}'\nu_e} + h.c. =$$

$$= \sum_{\nu_e} \sum_{\gamma\eta} \sum_{\mathbf{k}} (t'_h c^\dagger_{\mathbf{k}\gamma\eta,-1} b_{\mathbf{k}\nu_e} + t'_e e^{-i\mathbf{k}\mathbf{r}} c^\dagger_{\mathbf{k}\gamma\eta,-1} b_{\mathbf{k}'\nu_e} + t'_h c^\dagger_{\mathbf{k}\gamma\eta,+1} b_{\mathbf{k}\nu_e} + t'_e e^{i\mathbf{k}\mathbf{r}} c^\dagger_{\mathbf{k}\gamma\eta,+1} b_{\mathbf{k}\nu_e}) + h.c. =$$

$$= \sum_{\nu_e} \sum_{\gamma\eta} \sum_{\mathbf{k}} (c^\dagger_{\mathbf{k}\gamma\eta,-1} b_{\mathbf{k}\nu_e} (t'_h + e^{-i\mathbf{k}\mathbf{r}} t'_e) + c^\dagger_{\mathbf{k}\gamma\eta,+1} b_{\mathbf{k}\nu_e} (t'_h + e^{i\mathbf{k}\mathbf{r}} t'_e)) + h.c. \quad (A.9)$$

A.2 Transition dipole moments

The Frenkel transition dipole moment can be derived using eq. (4.41):

$$\boldsymbol{\mu}^{\mathrm{F}}_{\mu_e \xi} = \sum_{\nu_e} \frac{1}{\sqrt{N}} \sum_n e^{i\mathbf{k}n} u_{\nu_e \mu_e \xi} \langle g \mid \boldsymbol{\mu} \mid b^\dagger_{\mathbf{k}\xi\nu_e} g \rangle \overset{\mathbf{k}=0}{=}$$

$$\overset{\mathbf{k}=0}{=} \sum_{\nu_e} \frac{1}{\sqrt{N}} \sum_n u_{\nu_e \mu_e \xi} \langle g \mid \boldsymbol{\mu} \mid b^\dagger_{\mathbf{0}\nu_e \xi} g \rangle =$$

$$= \sum_{\nu_e} \frac{1}{\sqrt{N}} \sum_n u_{\nu_e \mu_e \xi} \langle \phi^e_n \chi^{e\nu_e}_n \mid \prod_{m \neq n} \phi^g_m \chi^{g0_g}_m \mid \boldsymbol{\mu} \mid \prod_{n'} \phi^g_{n'} \chi^{g0_g}_{n'} \rangle =$$

$$= \sum_{\nu_e} \underbrace{\frac{1}{\sqrt{N}} \sum_n}_{=\sqrt{N}} u_{\nu_e \mu_e \xi} \underbrace{\langle \chi^{e\nu_e}_n \mid \chi^{g0_g}_n \rangle}_{=S_{0\nu_e}} \underbrace{\prod_n \langle \chi^{g0_g}_n \mid \chi^{g0_g}_n \rangle}_{=1} \underbrace{\langle \phi^e_n \prod_{m \neq n} \phi^g_m \mid \boldsymbol{\mu} \mid \prod_{n'} \phi^g_{n'} \rangle}_{=\boldsymbol{\mu}_{ME}} =$$

$$= \sum_{\nu_e} \sqrt{N} u_{\nu_e \mu_e \xi} \boldsymbol{\mu}_{ME} S_{0\nu_e} \quad (A.10)$$

and for the CT dipole we use eq. (4.42):

$$\boldsymbol{\mu}^{\mathrm{CT}}_\xi = \sum_{\gamma\mu} v_{\xi\gamma\mu} \langle g \mid \boldsymbol{\mu}_\xi \mid \frac{1}{\sqrt{2}} (c^\dagger_{\mathbf{k}\gamma\mu,+1} + c^\dagger_{\mathbf{k}\gamma\eta,-1}) g \rangle \overset{\mathbf{k}=0}{=}$$

$$= \sum_{\gamma\eta} v_{\xi\gamma\eta} \frac{1}{\sqrt{N}} \sum_n e^{i0n} \frac{1}{\sqrt{2}} \langle g \mid \boldsymbol{\mu}_\xi \mid (c^\dagger_{0\gamma\eta,+1} + c^\dagger_{0\gamma\eta,-1}) g \rangle =$$

$$= \sum_{\gamma\eta} v_{\xi\gamma\eta} \frac{1}{\sqrt{N}} \sum_n \frac{1}{\sqrt{2}} (\langle \phi_n^+ \chi_n^{+\gamma} \phi_{n+1}^- \chi_{n+1}^{-\eta} \mid \prod_{\substack{m\neq n \\ m\neq n+1}} \phi_m^g \chi_m^{g0_g} \mid \boldsymbol{\mu} \mid \sum_{n'} \phi_{n'}^g \chi_{n'}^{g0_g} \rangle +$$

$$\langle \phi_n^+ \chi_n^{+\gamma} \phi_{n-1}^- \chi_{n-1}^{-\eta} \mid \prod_{\substack{m\neq n \\ m\neq n-1}} \phi_m^g \chi_n^{g0_g} \mid \boldsymbol{\mu} \mid \prod_{n'} \phi_{n'}^g \chi_{n'}^{g0_g} \rangle =$$

$$= \sum_{\gamma\eta} v_{\xi\gamma\eta} \frac{1}{\sqrt{N}} \sum_n \frac{1}{\sqrt{2}} \cdot$$

$$\left(\langle \chi_n^{+\gamma} \mid \chi_n^{g0_g} \rangle \langle \chi_{n+1}^{-\eta} \mid \chi_{n+1}^{g0_g} \rangle \langle \prod_{\substack{m\neq n \\ m\neq n+1}} \chi_m^{g0_g} \mid \chi_m^{g0_g} \rangle \langle \phi_n^+ \phi_{n+1}^- \mid \boldsymbol{\mu} \mid \phi_n^g \phi_{n+1}^g \rangle \prod \phi_m^g \mid \phi_m^g \rangle + \right.$$

$$\left. \langle \chi_n^{+\gamma} \mid \chi_n^{g0_g} \rangle \langle \chi_{n-1}^{-\eta} \mid \chi_{n-1}^{g0_g} \rangle \langle \prod_{\substack{m\neq n \\ m\neq n-1}} \chi_m^{g0_g} \mid \chi_m^{g0_g} \rangle \langle \phi_n^+ \phi_{n-1}^- \mid \boldsymbol{\mu} \mid \phi_n^g \phi_{n-1}^g \rangle \prod \phi_m^g \mid \phi_m^g \rangle \right) =$$

$$= \sum_{\gamma\eta} v_{\xi\gamma\eta} \sqrt{N} S_{\gamma 0}^+ S_{\eta 0}^- \boldsymbol{\mu}_{\text{MCT}} \tag{A.11}$$

where

$$\boldsymbol{\mu}_{\text{MCT}} = \frac{1}{\sqrt{2}} \langle \phi_n^g \phi_{n-1}^g \mid \boldsymbol{\mu} \mid \phi_n^+ \phi_{n+1}^- + \phi_n^+ \phi_{n-1}^- \rangle \tag{A.12}$$

A.3   Huang-Rhys factor

Starting from the expression $|\chi^{e0}\rangle = e^{-g^2/2}e^{ga_g^\dagger} \mid \chi^{g0_g}\rangle$, we derive the Huang-Rhys factor $S_{\mu\nu}$ for transition between an electronic ground state in vibronic level μ and an electronic excited state in vibronic level ν, by studying the overlap between these states

$$
\begin{aligned}
S_{\mu\nu} \quad &= \langle \chi^{g\mu} \mid \chi^{e\nu} \rangle \\
&= \langle \chi^{g\mu} \mid \frac{1}{\sqrt{\nu!}}(a_e^\dagger)^\nu \mid \chi^{e0} \rangle \\
&= \langle \chi^{g\mu} \mid \frac{(a_g^\dagger - g)^\nu}{\sqrt{\nu!}} \mid e^{-g^2/2}e^{ga_g^\dagger}\chi^{g0_g} \rangle \\
&= \langle \chi^{g\mu} \mid \frac{(a_g^\dagger - g)^\nu}{\sqrt{\nu!}}e^{-g^2/2}\sum_{k=0}^{\infty}\frac{g^k(a_g^\dagger)^k}{k!} \mid \chi^{g0_g} \rangle \\
&= e^{-g^2/2}\sum_{k=0}^{\infty}\frac{g^k}{k!}\langle \chi^{g\mu} \mid \frac{(a_g^\dagger - g)^\nu}{\sqrt{\nu!}}(a_g^\dagger)^k \mid \chi^{g0_g} \rangle \\
&= \frac{e^{-g^2/2}}{\sqrt{\nu!}}\sum_{k=0}^{\infty}\frac{g^k}{k!}\langle \chi^{g\mu} \mid \sum_{i=0}^{\mu}\binom{\nu}{i}(a_g^\dagger)^i(-g)^{\nu-i}(a_g^\dagger)^k \mid \chi^{g0_g} \rangle \\
&= \frac{e^{-g^2/2}}{\sqrt{\nu!}}\sum_{i=0}^{\nu}\frac{\nu!}{i!(\nu-i)!}(-g)^{\nu-i}\sum_{k=0}^{\infty}\frac{g^k}{k!}\langle \chi^{g\mu} \mid (a_g^\dagger)^{i+k} \mid \chi^{g0_g} \rangle \\
&= \frac{e^{-g^2/2}}{\sqrt{\nu!}}\sum_{i=0}^{\nu}\frac{\nu!}{i!(\nu-i)!}(-g)^{\nu-i}\sum_{k=0}^{\infty}\frac{g^k}{k!}\langle \chi^{g\mu} \mid \sqrt{(k+i)!} \mid \chi^{g(k+i)} \rangle \\
&= \frac{e^{-g^2/2}}{\sqrt{\nu!}}\sum_{i=0}^{min(\nu,\mu)}\frac{\nu!}{i!(\nu-i)!}(-g)^{\nu-i}\frac{g^{\mu-i}}{(\mu-i)!}\sqrt{\mu!}\langle \chi^{g\mu} \mid \chi^{g\mu} \rangle \\
&= \frac{e^{-g^2/2}}{\sqrt{\nu!\mu!}}\sum_{i=0}^{min(\nu,\mu)}\frac{(-1)^{\nu-i}g^{\mu+\nu-2i}\mu!\nu!}{i!(\mu-i)!(\nu-i)!}.
\end{aligned}
\tag{A.13}
$$

A.4 Visualization of orbitals in molecule pairs
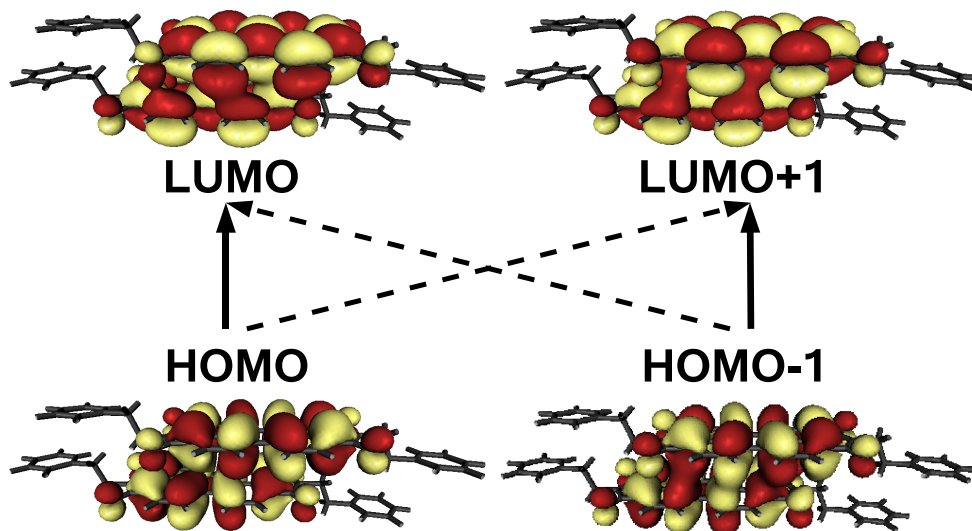
Figure A.1: PB31 orbitals
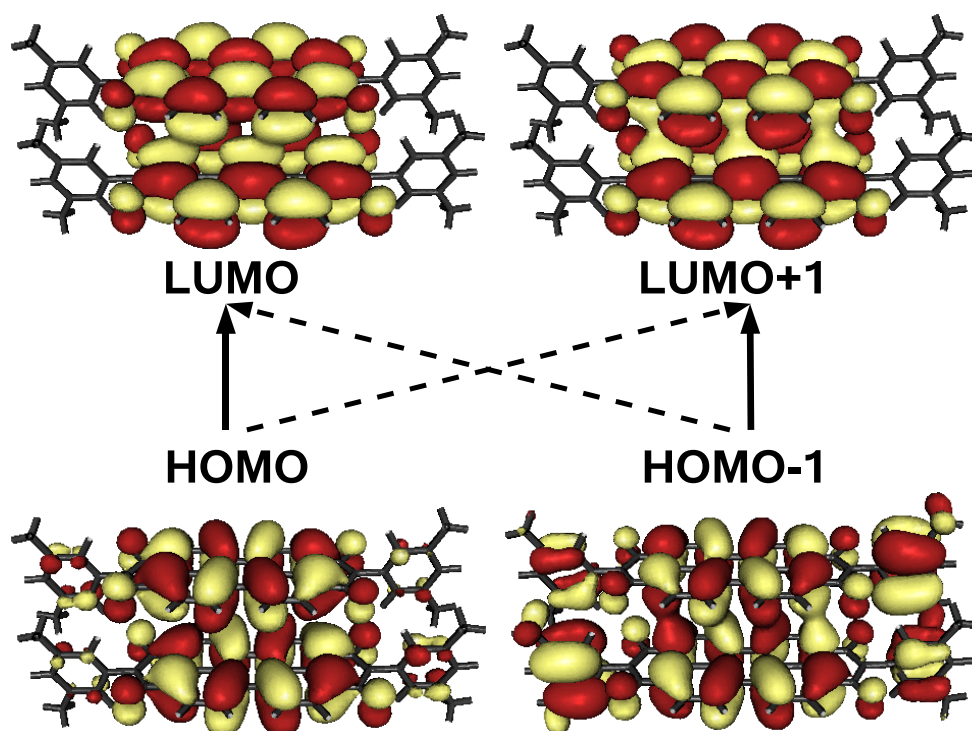
Figure A.2: PR149 orbitals, revealing HOMO and HOMO-1 wave functions containing a hybridization between π orbitals localized on the core region and on the xylyl groups.

LUMO   **LUMO+1**

HOMO   **HOMO-1**
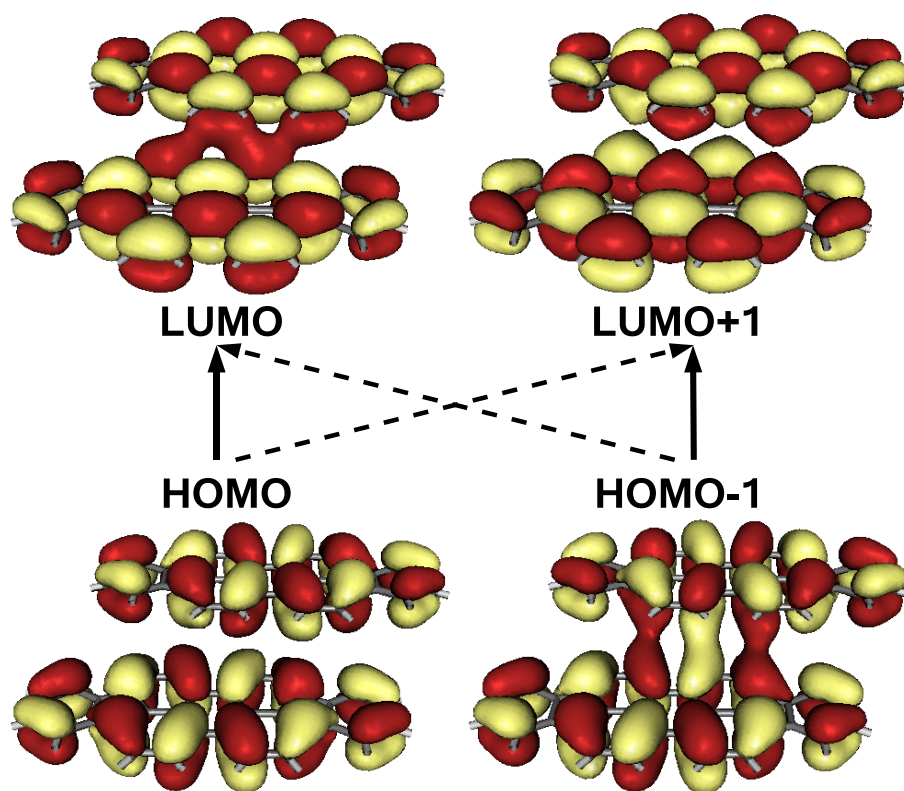
Figure A.3: DIP orbitals

A.5 Tables of vibronic modes

This section contains the calculated modes for single molecules.

mode		cation		anion		neutral		neutral	
B3LYP	Raman [63]	DFT		DFT		c-DFT		TD-DFT	
		λ_j	S_j	λ_j	S_j	λ_j	S_j	λ_j	S_j
(cm^{-1})	(cm^{-1})	(1)	(cm^{-1})	(1)	(cm^{-1})	(1)	(cm^{-1})	(1)	
211	220	18	0.090	21	0.104	84	0.421	59	0.296
351	239	4	0.012	2	0.007	0	0.000	0	0.000
401	390	65	0.171	60	0.159	0	0.000	0	0.000
467	435	6	0.013	0	0.001	4	0.010	3	0.007
524	538	8	0.016	68	0.137	16	0.031	16	0.032
556	569	40	0.077	7	0.013	57	0.109	50	0.096
708	720	5	0.008	4	0.005	1	0.002	2	0.003
943	961	33	0.037	0	0.000	16	0.018	11	0.012
1056		1	0.001	1	0.001	0	0.000	0	0.000
1074	1085	2	0.002	28	0.028	5	0.005	0	0.000
1193	1181	2	0.001	4	0.003	6	0.006	5	0.005
1195	1203	1	0.001	7	0.007	10	0.009	8	0.007
1277	1290	0	0.000	7	0.006	4	0.004	2	0.001
1284	1301	4	0.003	39	0.032	49	0.040	25	0.020
1298	1318	168	0.137	153	0.125	460	0.375	304	0.247
1351	1370	2	0.002	141	0.110	87	0.068	51	0.040
1361	1381	49	0.038	17	0.013	83	0.064	42	0.033
1420	1455	3	0.002	45	0.034	41	0.030	26	0.019
1445		28	0.021	3	0.002	10	0.007	6	0.004
1552	1570	73	0.050	123	0.084	272	0.185	190	0.129
1557	1581	12	0.008	241	0.163	76	0.052	52	0.035
1596	1588	47	0.031	18	0.012	6	0.004	3	0.002
Sum:			0.336		0.625		0.867		0.558

Table A.1: As Table 2.6, but for Me-PTCDI.

mode		cation		anion		neutral	
B3LYP	Raman [64]	DFT		DFT		c-DFT	
		λ_j	S_j	λ_j	S_j	λ_j	S_j
(cm^{-1})	(cm^{-1})	(1)	(cm^{-1})	(1)	(cm^{-1})	(1)	(cm^{-1})
227	247	5	0.025	39	0.180	81	0.377
385		63	0.174	38	0.104	4	0.010
472		0	0.000	7	0.015	5	0.011
539	551	63	0.124	1	0.001	48	0.094
651	654	3	0.005	46	0.075	17	0.028
731		6	0.009	21	0.031	7	0.010
830		4	0.005	8	0.010	0	0.000
1059	1066	20	0.020	1	0.001	12	0.012
1178	1178	0	0.000	9	0.008	8	0.007
1278	1285	30	0.025	4	0.003	8	0.007
1311	1302	98	0.079	145	0.117	357	0.288
1366	1377	162	0.125	1	0.000	112	0.087
1383		36	0.028	64	0.049	143	0.109
1438		17	0.013	23	0.017	51	0.037
1567	1572	130	0.088	71	0.048	285	0.192
1587	1585	222	0.148	1	0.000	113	0.075
1644		42	0.027	49	0.031	1	0.001
3144		0	0.000	0	0.000	1	0.000
3392		1	0.000	1	0.000	0	0.000
Sum:			0.552		0.276		0.816

Table A.2: As Table 2.6, but for PTCDI.

		anion		cation		neutral
	λ_j	S_j	λ_j	S_j	λ_j	S_j
cm^{-1}	cm^{-1}	1	cm^{-1}	1	cm^{-1}	1
96	15	0.155	0	0.000	0	0.000
122	11	0.086	1	0.007	1	0.007
166	2	0.010	0	0.002	0	0.002
214	13	0.061	4	0.020	4	0.020
272	0	0.000	8	0.028	8	0.028
325	3	0.008	1	0.003	1	0.003
387	15	0.038	2	0.006	2	0.006
389	3	0.007	1	0.003	1	0.003
434	49	0.113	15	0.034	15	0.034
539	79	0.146	9	0.016	9	0.016
563	11	0.020	23	0.041	23	0.041
730	6	0.008	2	0.003	2	0.003
846	3	0.004	9	0.010	9	0.010
976	0	0.000	9	0.009	9	0.009
1024	0	0.000	2	0.002	2	0.002
1033	0	0.000	3	0.003	3	0.003
1101	26	0.024	1	0.001	1	0.001
1220	0	0.000	5	0.004	5	0.004
1222	4	0.004	2	0.002	2	0.002
1232	1	0.001	5	0.004	5	0.004
1313	51	0.039	0	0.000	0	0.000
1333	168	0.126	78	0.058	78	0.058
1381	106	0.077	3	0.002	3	0.002
1394	13	0.010	0	0.000	0	0.000
1396	63	0.045	12	0.009	12	0.009
1422	6	0.004	4	0.003	4	0.003
1463	37	0.025	5	0.004	5	0.004
1504	13	0.009	5	0.003	5	0.003
1595	122	0.077	34	0.021	34	0.021
1598	264	0.165	6	0.003	6	0.003
1629	1	0.000	22	0.013	22	0.013
1639	15	0.009	21	0.013	21	0.013
3136	1	0.000	2	0.001	2	0.001
Sum:		0.618		0.162		0.849

Table A.3: As Table 2.6, but for PB31.

	anion		cation		neutral	
	λ_j	S_j	λ_j	S_j	λ_j	S_j
cm^{-1}	cm^{-1}	1	cm^{-1}	1	cm^{-1}	1
132	37	0.278	1	0.011	48	0.360
268	7	0.026	7	0.025	37	0.136
313	35	0.111	23	0.074	8	0.026
461	41	0.088	0	0.000	4	0.008
482	2	0.004	11	0.023	14	0.029
544	124	0.227	1	0.002	57	0.104
552	215	0.389	0	0.000	12	0.021
694	1	0.001	4	0.005	10	0.014
741	8	0.010	8	0.011	13	0.017
842	4	0.004	2	0.002	0	0.000
948	0	0.000	6	0.006	8	0.008
1024	39	0.038	17	0.017	2	0.001
1039	67	0.065	4	0.004	22	0.021
1091	1	0.001	0	0.000	3	0.002
1158	91	0.079	1	0.001	4	0.003
1224	33	0.027	3	0.002	25	0.020
1295	35	0.027	7	0.005	16	0.012
1331	112	0.084	81	0.061	348	0.261
1338	37	0.028	14	0.010	160	0.119
1386	141	0.101	0	0.000	70	0.050
1398	31	0.022	21	0.015	119	0.085
1464	26	0.018	9	0.006	51	0.035
1595	159	0.100	36	0.022	323	0.202
1600	180	0.113	3	0.002	50	0.031
1622	4	0.002	16	0.010	0	0.000
1645	10	0.006	40	0.024	9	0.005
3001	30	0.010	0	0.000	4	0.001
3002	128	0.043	0	0.000	22	0.007
3081	19	0.006	0	0.000	2	0.001
3082	20	0.006	0	0.000	3	0.001
3137	3	0.001	1	0.000	0	0.000
3159	49	0.015	0	0.000	9	0.003
3205	3	0.001	0	0.000	3	0.001
Sum:		0.710		0.186		0.859

Table A.4: As Table 2.6, but for PR149.

mode		cation		anion		neutral	
B3LYP	Raman [65]	DFT		DFT		c-DFT	
		λ_j	S_j	λ_j	S_j	λ_j	S_j
(cm^{-1})	(cm^{-1})	(1)	(cm^{-1})	(1)	(cm^{-1})	(1)	(cm^{-1})
215	220	8	0.040	29	0.144	69	0.339
449		1	0.002	0	0.001	1	0.003
529	535	37	0.074	11	0.021	64	0.127
626	632	35	0.059	0	0.001	31	0.052
697		0	0.000	1	0.002	1	0.002
833		0	0.000	5	0.006	1	0.001
995		0	0.000	0	0.000	0	0.000
1021	1068	1	0.001	3	0.003	2	0.002
1089	1089	62	0.060	0	0.000	19	0.018
1155		7	0.007	7	0.007	0	0.000
1208		7	0.006	4	0.003	1	0.001
1277	1284	143	0.118	153	0.127	449	0.371
1312		3	0.003	59	0.047	68	0.054
1314	1323	17	0.013	6	0.004	1	0.001
1387	1399	206	0.157	4	0.003	179	0.137
1421		10	0.008	80	0.060	107	0.080
1447	1459	175	0.128	13	0.010	195	0.142
1567		0	0.000	10	0.007	7	0.005
1584		4	0.002	16	0.011	35	0.024
1592	1611	84	0.056	43	0.029	142	0.094
3084		0	0.000	0	0.000	0	0.000
3086		1	0.000	1	0.000	0	0.000
3105		1	0.000	1	0.000	0	0.000
3110		0	0.000	1	0.000	1	0.000
Sum:			0.560		0.311		0.929

Table A.5: As Table 2.6, but for DIP.

Appendix B

List of Abbreviations

1D	one-dimensional
3D	three-dimensional
α, β	indices for the differently aligned molecules in a unit cell
$\mathbf{a}$, a	unit-cell vector and its length
AO	atomic orbital
α, β	summation indices for basis molecules in unit cell
A, B	indices of basis molecules in unit cell
$\alpha(\omega)$	absorption
AFM	atomic force microscopy
$\mathbf{b}$, b	unit-cell vector and its length
$b^\dagger_{\boldsymbol{n}\alpha\nu_e;\boldsymbol{n}\alpha 0_g}$	creation operator for neutral excitation on specific molecule
$b^\dagger_{\boldsymbol{k}\xi\nu}$	creation operator for Frenkel exciton with wave vector $\mathbf{k}$ and transition dipole along $\xi = x$ or $\xi = y$
$b^\dagger_{\boldsymbol{k}\alpha\nu_e}$	creation operator for Frenkel exciton with wave vector $\mathbf{k}$ and transition dipole along α molecule
B3LYP	hybrid functional with three adjusted parameters according to Becke and Lee-Yang-Parr
$\mathbf{c}$, c	unit-cell vector and its length
$c^\dagger_{\boldsymbol{n}\alpha\gamma\eta,\sigma}$	creation operator for localized CT state
$c^\dagger_{\boldsymbol{k}\alpha\gamma\eta,\sigma}$	creation operator for CT exciton in $\mathbf{k}$-space
$\chi^s_{\mathbf{n}\alpha}$	vibronic wave function in electronic state s on molecule α in unit cell $\mathbf{n}$.
CGTO	contracted Gaussian-type orbital
CI	configuration interaction
CT	charge-transfer
D	environment shift of the transition energies
DFT	density functional theory
δ	angle between the molecular HOMO-LUMO transition dipole and the lattice vector $\mathbf{b}$
DIP	diindenoperylene
DZ	double-ζ basis set

DZVP	double-ζ valence polarized basis set
E_{00}	energy distance between the lowest vibronic state in the electronic ground state and the lowest vibronic state in the electronic excited state
E_{00}^{CT}	transition energy of the CT exciton
E_{00}^{F}	transition energy of the Frenkel exciton
F	Frenkel
F-CT	Frenkel exciton and charge transfer state
GGA	generalized gradient approximation
GTO	Gaussian-type orbital
H^{F}	Frenkel Hamiltonian
$H^{\mathrm{F-CT}}$	part of Hamiltonian mixing Frenkel and CT states
H^{CT}	CT Hamiltonian
HF	Hartree-Fock
$\hbar\omega_{\mathrm{eff}}$	effective internal vibration factor
HOMO	highest occupied molecular orbital
H_g	superposition of HOMOs of two stacked molecules with even parity
H_u	superposition of HOMOs of two stacked molecules with odd parity
$\boldsymbol{k}$	k-space representation
λ	reorganization energy
LCAO	linear combination of atomic orbitals
LDA	local density approximation
LUMO	lowest unoccupied molecular orbital
L_g	superposition of LUMOs of two stacked molecules with even parity
L_u	superposition of LUMOs of two stacked molecules with odd parity
$\boldsymbol{\mu}$	dipole moment
$\boldsymbol{\mu}_A, \boldsymbol{\mu}_B$	transition dipole moments for A and B basis vectors respectively
Me-PTCDI	N,N-dimethyl-3,4,9,10-perylenetetracarboxylic diimide
MO	molecular orbital
ν, μ	vibronic level of the Frenkel state
γ_+	vibronic level for the cationic state
η_-	vibronic level for the anionic state
$\mathbf{n}, \mathbf{m}$	unit cell
OD	optical density
OLED	organic light emitting diode
OMBD	organic molecular beam deposition
Ω_g	transition frequency
ω	internal vibrational mode
φ	angle between basis molecules in the unit cell
PB31	pigment black 31: N,N-bis(2-phenylethyl)-perylene-3,4,9,10-bis(dicarboximide)
PES	potential energy surface
PL	photoluminescence
PR149	pigment red 149: N,N-Bis(3,5-xylyl) perylene-3,4,9,10-bis(dicarboximide)
PTCDA	3,4,9,10-perylene tetracarboxylic dianhydride

PTCDI	3,4,9,10-perylene-bis(dicarboximide)
$\chi(0)$	static susceptibility
RHF	restricted Hartree-Fock
$\mathbf{R_{n\alpha;m\beta}}$	distance vector between two molecules
$S_{\nu\mu}$	Franck-Condon overlap factor
S	Huang-Rhys factor for the neutral excited state
S_-	Huang-Rhys factor for the anionic state
S_+	Huang-Rhys factor for the cationic state
σ_ν	Gaussian broadening for vibronic mode ν
SCF	self-consistent field
STO	Slater type orbitals
SVP	single valence polarized basis set
t_e	electron transfer parameter
t_h	hole transfer parameter
t_H	HOMO transfer parameter
t_L	LUMO transfer parameter
$t_{\boldsymbol{n}\alpha\nu_e;\boldsymbol{m}\beta\mu_e}$	transfer matrix element
T_{AA}	Frenkel transfer parameter between same basis molecules
T_{AB}	Frenkel transfer parameter between different basis molecules
TD-DFT	time-dependent density functional theory
TZ	triple-ζ basis set
TZVP	triple-ζ valence polarized basis set
UV	ultra violet
V	crystal volume
VASE	variable angle spectroscopic ellipsometry

Appendix C

Acknowledgement

The people of Prof. Dr. Michael Schreibers group: Dr. Afshin Abbasi, Davoud Pouladsaz, Luis Mancera, Dr. Markus Schröder, Peter Karmann, Dr. Ulrich Kleinekathöfer, Dr. Philipp Cain, Soroosh Pezeshki, Dr. Qi Guang Li and Dr. Viktor Cerovski for the warm and pleasant atmosphere during the time I spend at Technische Universität Chemnitz.

All the friends that I knew before or met during my thesis time, from Sweden, Chemnitz, München and everywhere else. You all know who you are and thanks to your friendship and support my days were much more fun and pleasant during this period.

Last, but mostly my family: Kerstin, Leif and Petter Gisslén, for the unconditioned and loving support throughout all of my life.

Appendix D

List of Publications

in preparation:

12. **Modeling of optical spectra of crystalline organic perylene molecules involving Frenkel and charge transfer interactions**
    L. Gisslén and R. Scholz

11. **The vibronic structure of higher excitations of pentacene: Analysis of pre-resonant Raman spectra with time-dependent density functional theory**
    L. Gisslén, C. Himcinschi, J. Pflaum, and R. Scholz

10. **Resonant Raman spectra of diindenoperylene thin films**
    R. Scholz, L. Gisslén, B. Casu, T. Chassé, U. Heinemeyer, and F. Schreiber

9. **Revised evaluation of the anisotropic dielectric tensor of PTCDA**
    M. I. Alonso, M. Garriga, J. O. Ossó, F. Schreiber, L. Gisslén, and R. Scholz

submitted:

8. **Selective excitation of exciton transitions in PTCDA crystals and films**
   V. R. Gangilenka, L. V. Titova, L. M. Smith, H.P. Wagner, L. A. A. DeSilva, L. Gisslén, and R. Scholz
   Submitted to Phys. Rev. B (2009).

7. **Intermolecular interactions in molecular crystals and chemisorption at molecule-metal interfaces**
   R. Scholz, L. Gisslén, and A. Abbasi
   Conference proceedings: High Performance Computing in Science and Engineering (2009).

published:

6. **Crystallochromy of perylene pigments: Interference between Frenkel excitons and charge transfer states**
   L. Gisslén and R. Scholz
   Phys. Rev. B **80**, 115309 (2009).

5. **Optical spectra obtained from amorphous films of rubrene: Evidence for predominance of twisted isomer**
   M. Kytka, L. Gisslén, A. Gerlach, U. Heinemeyer, J. Kovác, R. Scholz, and F. Schreiber
   J. Chem. Phys. **130**, 214507 (2009).

4. **Asymmetry between absorption and photoluminescence line shapes of TPD: Spectroscopic fingerprint of the twisted biphenyl core**
   R. Scholz, L. Gisslén, C. Himcinschi, I. Vragović, E. M. Calzado, E. Louis, E. S. Maroto, and M. A. Diaz-Garcia
   J. Phys. Chem. A **113**, 315 (2009).

3. **Metal/organic interface formation studied in situ by resonant Raman spectroscopy**
   G. Salvan, B. A. Paez, D. R. T. Zahn, L. Gisslén, and R. Scholz
   Physical and Chemical Aspects of Organic Electronics by C. Wöll, Chap. 13, Wiley-VHC (Weinheim 2009).

2. **Exciton phonon coupling in diindenoperylene thin films**
   U. Heinemeyer, R. Scholz, L. Gisslén, M. I. Alonso, J.O. Osso, M. Garriga, A. Hinderhofer, M. Kytka, S. Kowarik, A. Gerlach, and F. Schreiber
   Phys. Rev. B **78**, 085210 (2008).

1. **Modelling absorption and photoluminescence of TPD**
   I. Vragović, E. M. Calzado, M. A. Diaz Garcia, C. Himcinschi, L. Gisslén, and R. Scholz
   J. Lumin. **128**, 845-7 (2007).